SOLUTION-PROCESSED METAL OXIDES AND THEIR THIN FILMS/COATINGS TOWARDS ANTIFOULING AND GAS SENSING APPLICATIONS

Thesis

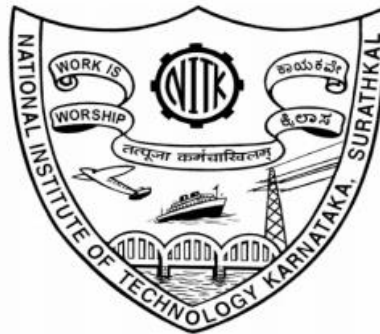Submitted in partial fulfilment of the requirements for the degree of

DOCTOR OF PHILOSOPHY

By

ROBBI VIVEK VARDHAN

(177006MT007)

DEPARTMENT OF METALLURGICAL AND MATERIALS ENGINEERING

NATIONAL INSTITUTE OF TECHNOLOGY KARNATAKA SURATHKAL, MANGALURU – 575025

JANUARY, 2023

SOLUTION-PROCESSED METAL OXIDES AND THEIR THIN FILMS/COATINGS TOWARDS ANTIFOULING AND GAS SENSING APPLICATIONS

Thesis

Submitted in partial fulfilment of the requirements for the degree of

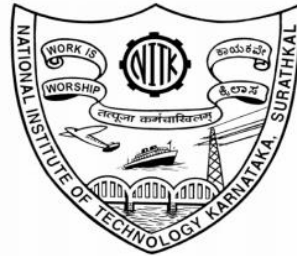## DOCTOR OF PHILOSOPHY

By

ROBBI VIVEK VARDHAN

(177006MT007)

Under the guidance of

Dr. Saumen Mandal

Assistant Professor

Department of Metallurgical and Materials Engineering

NITK Surathkal

DEPARTMENT OF METALLURGICAL AND MATERIALS ENGINEERING

NATIONAL INSTITUTE OF TECHNOLOGY KARNATAKA SURATHKAL, MANGALURU – 575025

DECLARATION

I hereby *declare* that the Research Thesis entitled "**Solution-processed metal oxides and their thin films/coatings towards antifouling and gas sensing applications**" which is being submitted to the National Institute of Technology Karnataka, Surathkal in partial fulfillment of the requirements for the award of the Degree of Doctor of Philosophy in the Department of Metallurgical and Materials Engineering, is a *bonafide report of the research work carried out by me*. The material contained in this Research Thesis has not been submitted to any University or Institution for the award of any degree.

R.Vivek Vardhan

Name: ROBBI VIVEK VARDHAN

Registration Number: 177006MT007
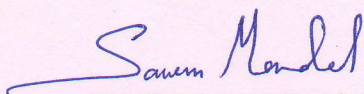
Department of Metallurgical and Materials Engineering

Place: NITK Surathkal

Date: 31-01-2023

CERTIFICATE

This is to certify that the Research Thesis entitled "**Solution-processed metal oxides and their thin films/coatings towards antifouling and gas sensing applications**" submitted by Mr. Robbi Vivek Vardhan (Registration Number: 177006MT007) as the record of the research work carried out by him, is *accepted as the Research Thesis submission* in partial fulfillment of the requirements for the award of degree of Doctor of Philosophy.
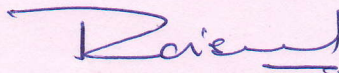
Research supervisor

Dr. Saumen Mandal

Assistant Professor

Department of Metallurgical and Materials Engineering

NITK Surathkal

Chairman- DRPC

Chairman - DRPC
Dept. of Metallurgical and Materials Engineering
National Institute of Technology Karnataka, Surathkal
Post Srinivasnagar, Mangaluru - 575 025
Karnataka, India

DEDICATED TO

THE ALMIGHTY GOD……

ACKNOWLEDGEMENTS

Late. Mr. Robbi Hemarao and my mother Mrs. Robbi Annapurna, who supported me throughout my life and during this study. I am grateful to my parents, siblings, friends and relatives for their care and love.

Finally, I thank all my friends, well-wishers, and anonymous souls for their love and regards, prayers and wishes, that directly and indirectly helped me for completing this research work.

<div align="right">ROBBI VIVEK VARDHAN</div>

ABSTRACT

In the current study, metal oxides and their thin films/coatings were developed through solution-phase methods as an approach to antifouling and gas sensing applications. Thermal decomposition-processed facile spray pyrolyzed pure WO_3 films were successfully fabricated by utilizing minimal sophisticated facilities. Compared to uncoated substrates, all the coated substrates exhibited an enhancement in scratch hardness. The attained relatively better scratch hardness was ascribed to the existence of a well-established WO_3 film. The demonstrated WO_3 films were hydrophilic natured (WCA < 31°) and after chemical modification with OTS, the films revealed hydrophobicity (WCA > 120°) due to the formation of water-repellant OTS-SAM on the surface. Solution-combustion-processed spin coated pristine and Ti-doped ZnO films responded to NH_3 gas at room temperature. Pristine ZnO film revealed better gas sensing performance than doped films at all concentrations of NH_3 gas. The maximum gas response of 34.7 and high selectivity were perceived in pristine ZnO film at 100 ppm of NH_3 gas. Room temperature detection of NH_3 gas was also accomplished in respective spin-coated air and vacuum-annealed pristine, Nb-doped TiO_2 films fabricated through the solution combustion method. Compared to other films, a relatively superior gas response was traced at all NH_3 gas concentrations by vacuum-annealed pristine TiO_2 film. The film exhibited the highest gas response of ~16 and selectivity towards 100 ppm of NH_3 gas. Solution-combustion-derived spin coated Ti and Zn co-doped In_2O_3 films were polycrystalline without any secondary dopant oxide phases, and the films revealed transparency (>85%) in the visible region. Screen-printable particle-free aqueous solution combustible inks with a combustion temperature of ~280 °C were utilized to fabricate undoped In_2O_3, Sn doped In_2O_3, Zn doped In_2O_3, Sn and Zn co-doped In_2O_3 screen-printed films. All the screen-printed films sensed ethanol gas at room temperature, and the undoped screen-printed film performed comparatively better gas sensing. A maximum gas response of 17.3 and high selectiveness towards 100 ppm of ethanol gas were discerned in the stated film. The evolution of the BSO/LBSO phase from the intermediate phases was evidenced between 500 ℃ and 600 ℃. The pure BSO/ LBSO

phase with non-appearance of intermediate phases was recognized at 800 ºC and above, in La_xBa_{1-x} $SnO_{3-\delta}$ (x = 0, 0.05, 0.1 and 0.15) powders, synthesized through the polymerized complex method. A progressive augmentation in the electrical conductivity of BSO-based pellets was recognized with La doping.

CONTENTS

NOMENCLATURE

AFM	:	Atomic Force Microscopy
BSO	:	Barium Stannate
BSSO	:	Antimony doped Barium Stannate
CA	:	Citric Acid
CBM	:	Conduction Band Minimum
CVD	:	Chemical Vapor Deposition
DSC	:	Differential Scanning Calorimetry
DTG	:	Derivative of Thermogravimetric
ρ	:	Density of the Liquid
DC	:	Direct Current
m*	:	Effective Mass of Electron
EG	:	Ethylene glycol
EDL	:	Electron Depletion Layer
σ	:	Electrical Conductivity
μ	:	Electrical Mobility
EDAX	:	Energy Dispersive X-Ray Analysis
E_f	:	Formation Energy
ϕ	:	Fuel to Oxidizer ratio
F_N	:	Normal Load
FTIR	:	Fourier Transform InfraRed
FWHM	:	Full Width Half Maximum
G/L	:	Gaussian/Lorentzian
H_S	:	Scratch Hardness
HAL	:	Hole Accumulation Layer

ICDD	:	International Centre for Diffraction Data
LBSO	:	Lanthanum doped Barium Stannate
M	:	Molarity
N	:	Carrier Concentration
OTC	:	Organotin compounds
OTS	:	Octadecyltrichlorosilane
α	:	Optical Absorption Coefficient
E_g	:	Optical Energy Band Gap
OV	:	Oxidizing Valency
λ_p	:	Plasma Wavelength
h	:	Plank's Constant
$h\upsilon$	:	Photon Energy
PCM	:	Polymerized Complex Method
α_o	:	Proportionality Constant
R_a	:	Resistance in air
R_g	:	Resistance in target gas
RF	:	Radio Frequency
RTP	:	Rapid Thermal Processing
RV	:	Reducing Valency
S	:	Gas Response
SAM	:	Self-assembled Monolayer
SEM	:	Scanning Electron Microscopy
SCS	:	Solution Combustion Synthesis
SHS	:	Superhydrophobic Surfaces
SMO	:	Semiconducting Metal Oxide
SS	:	Stainless Steel

TBT	:	Tributyltin
TGA	:	Thermogravimetric Analysis
TPT	:	Triphenyltin
TSO	:	Transparent Semiconducting Oxide
UV-Vis	:	Ultraviolet-Visible
VOC	:	Volatile Organic Compound
ϕ	:	Volume Fraction of Gas
WCA	:	Water contact angle
XRD	:	X-Ray Diffraction
XPS	:	X-ray Photoelectron Spectroscopy

The page was left intentionally blank

CHAPTER 1

INTRODUCTION

Metal oxides are the most plentiful materials in the crust of the earth and they are the ingredients in traditional ceramics (Yu et al. 2016). Over the years, metal oxides have received a lot of interest due to their versatile electronic, optical, mechanical, chemical, and ferromagnetic properties that are suitable for a broad range of applications. The functional characteristics of the metal oxides are highly dependent on their crystal structure, native defects, composition, doping, etc. Metal oxides in the form of thin films/coatings exhibit an outstanding diversity of properties that make them ideal in optoelectronic devices, gas sensors, solar cells, energy storage, fouling and corrosion protection, high-temperature shields etc. (Pasquarelli et al. 2011) (Grilli 2020; Stojanovic et al. 2018).

Despite the metal oxide of interest, the fabrication of them in the form of thin films/coatings is a crucial entity. In common, the fabrication of metal oxide-based thin films is categorized into (i) vapor-phase and (ii) solution-phase methods. Vapor-phase methods such as thermal deposition, sputtering, pulsed laser deposition and atomic layer deposition necessitate high vacuum usage. These methods deliver compositionally robust films, but they are extremely expensive, time-consuming, require high-precision equipment and the substrate size is limited. Continuous research has been performed to develop simple, low-cost thin film fabrication methods. Solution-phase methods, namely, dip coating, spray coating, spin coating, screen printing, inject printing, aerosol printing etc., have emerged as a decent substitute for the vapor-phase methods. These methods are relatively simple, quick, and low-cost, with minimal utilization of capital-intensive equipment, and the vacuum requirement is not essential (Pasquarelli et al. 2011) (Yu et al. 2016). Here, an initial solution called precursor, which contains metal salts (as starting materials of the desired oxide), stabilizers, binders and solvents etc., is formulated and deposited on a substrate of interest by the mentioned techniques. Thereafter, thermal processing is conducted for the as-deposited wet films, which assists in evaporation of solvents, removal of

undesired organics, decomposition of precursor, prompting of crystallization and subsequent formation of uniform, dense metal oxide film.

Biological fouling, usually called biofouling, is a noteworthy concern all over the world because of an unwanted accumulation of species, namely, microorganisms, plants (seaweeds) and animals (barnacles and mussels) on submerged surfaces in the water (Callow and Callow 2011). Biofouling generates significant operational problems in maritime industries, such as enhancement in weight, consequent decrement in manoeuvrability and speed of the ships, and also leads to excess fuel consumption. It also has serious unfavourable effects on underwater pipelines, oceanographic equipment, heat exchangers, desalination plants etc. (Yebra et al. 2004). To retard the biofouling, antifouling coatings with tributyltin (TBT), triphenyltin (TPT) and organotin compounds (OTC) were utilized initially, but they were recognized as biocides which polluted the aquatic environment. The continuity of TBT, TPT and other tin-comprised materials in antifouling coatings was intensively opposed by the environment protection committees. This opposition led to an immediate need for the antifouling paint industries and researchers to find a replacement for toxic coatings (Krishnan et al. 2015). Many alternate approaches were introduced for designing antifouling coatings, like micro or nanostructuring and photoactivation of the surfaces, etc., but most of the approaches comprised substantial disadvantages in adhesion, mechanical weakness, uniformity, and long-lasting stability. To prevail over the mentioned challenges, transition and rare earth metal oxides have turned up as an exciting category of materials because of their versatility in mechanical, chemical and physical properties. Among them, in particular, tungsten oxide (WO_3) has emerged as a new potential material because of its high mechanical durability, high chemical stability, excellent corrosive resistance in acidic and basic conditions, very minimal toxicity and environmental friendliness (Tesler et al. 2015) (Mardare and Hassel 2019).

Nowadays, besides biofouling, the world is facing another major issue in terms of the emission of intense harmful and pollutant gases into the environment due to the speedy development of urbanization and industrialisation. The emission of harmful gases has become a considerable global threat to human existence and the surrounding environment. The emitted pollutants comprise plentiful toxic gases such as CO_2, CO,

NH_3, NO_2, NO, H_2S and volatile organic compound (VOC) gases, namely methane, ethanol, LPG, formaldehyde, and many others. Exposure to these gases severely hazards human health (Manohar et al. 2020) (Eranna et al. 2004). Therefore, detecting these harmful gases is becoming progressively crucial in several industries, mines, public safety places, and so on. In this scenario, the effective and continuous tracing or monitoring of these dangerous gaseous by using gas sensors is a substantial necessity (Zhu and Zeng 2017). Numerous gas sensing techniques, namely catalytic combustion, electrochemical, infrared absorption, and thermal conductive techniques, were utilized for this need (Korotcenkov 2007). Nevertheless, the mentioned techniques have certain limitations, such as minimal sensitivity, low selectivity, deficiency in portability, sophisticated design, and comparatively high price. In constant research to subdue the specified challenges, gas sensors that are based on semiconducting metal oxides (SMOs) have been achieved much attention around the globe due to their unique features such as higher gas response, high stability, less response/recovery time, fair selectivity, compact size, abundant availability of raw materials, and minimal fabrication cost (Manohar et al. 2020) (Wang et al. 2010b). Among the SMOs, n-type SMOs are the most frequently utilized sensing materials. Metal oxides, namely, zinc oxide (ZnO), titanium oxide (TiO_2), indium oxide (In_2O_3) and barium stannate ($BaSnO_3$), which are n-type semiconductors, can serve as effective SMO-based gas sensors (Eranna et al. 2004) (Tian et al. 2021) (Reddy et al. 2001). One of the top design preferences of SMO-based sensors is now to develop smart sensors in handheld devices with cost-efficient fabrication, like printing. The smart sensors with decent gas sensing capability and high transparency at visible ranges generate opportunities for their usage in optoelectronic devices and transparent electronic circuitries. Transparent semiconducting oxides (TSOs) have the ability to be used as efficient optically transparent and high-performance gas sensors, which can be potentially integrated into automobile windshields, transparent electronics, and several other miniaturized transparent devices (Moon et al. 2012).

CHAPTER 2 is dedicated to the existing literature in the current area of research. **CHAPTER 3** is assigned to the fabrication and characterization studies of thermal decomposition-processed spray pyrolyzed scratch-resistant, hydrophobic

tungsten oxide films on steel and glass substrates, respectively. **CHAPTER 4** is allocated to the fabrication of solution combustion-processed spin-coated zinc oxide-based, titanium oxide-based, and indium oxide-based films, and their characterization studies. **CHAPTER 5** is devoted to the development of screen-printable particle-free aqueous solution combustible indium oxide-based inks, films, and their characterization studies. **CHAPTER 6** is allotted to barium stannate-based metal oxide powders and electrically conducting pellets developed through the polymerized complex method, and their characterization studies. Lastly, **CHAPTER 7** is dedicated to the conclusion as well as the future scope of the current studies.

CHAPTER 2

LITERATURE REVIEW

2.1 Metal oxides

Metal oxides are chemical compounds which are formed due to the reaction between metals and oxygen; they comprise a metal cation as well as an oxide anion. For example, zinc reacts with oxygen and forms zinc oxide. Metal oxides have grasped much interest because of their tailorable versatile electrical, optical, mechanical, and magnetic properties, which can be utilized in a wide range of applications. The preparation and synthesis of metal oxides have initiated 100 years ago. Since then, several new techniques and methods have emerged for the preparation of metal oxides (Voon et al. 2020). Metal oxides in bulk, thin film form, and metal oxide nanostructures display a wide variety of functional properties and are used in applications like optoelectronic devices, solar cells, gas sensors, catalysis, passive optics, energy conversion and storage, corrosion, and environmental protection etc. The processing methods and growth parameters of metal oxides highly determine their physical-chemical properties and morpho-structural characteristics (Grilli 2020). A substantial advancement in the preparation and synthesis of various metal oxides has been accomplished from many years. The methods for the metal oxides' preparation and synthesis can be broadly classified into physical and chemical methods. The physical methods mostly rely on mechanically and thermally induced chemical reactions (mechanochemical reactions and solid-state synthesis). In contrast, chemical methods are relied on the decomposition and precipitation of precursors (sol-gel, hydrothermal, solvothermal, coprecipitation, polymeric precursor synthesis, auto-combustion processing etc.) to generate new compounds (Stojanovic et al. 2018). The preparation and synthesis of metal oxides are employed by two approaches; they are (i) the top-down approach and (ii) the bottom-up approach. The top-down method contains mechanical crushing, grinding, milling, pulverisation, mechanochemical reactions and mechanical activation to etch or remove bulk matter in order to create the smaller desirable structure. On the contrary, the bottom-up approach, often acknowledged as

the self-assembly process, entails assembling smaller building parts (initiating from atoms or molecules) to create the desired structure of metal oxides. This approach demonstrates the potential for developing materials that are specifically designed to possess the required properties. Both approaches are utilised in physical and chemical methods for preparation and synthesis of the metal oxides. Most of the metal oxides that are developed through chemical methods rely on solution processing routes (Voon et al. 2020) (Stojanovic et al. 2018).

2.2 Solution-processing routes

Solution-processing routes initiate with a precursor, which is a chemical reagent that comprises the target cation and reacts to produce the target material and phase. The choice of a precursor relies on solvent, formulation, and preferred processing route (Pasquarelli et al. 2011). Basically, the common method of solution-processing is of two kinds: (i) via colloidal nanoparticle precursor and (ii) through molecular precursor deposition. The precursor is developed according to the kind and deposited through various techniques. It is essential to mention about the sequences of the solution-processing routes to deposit the thin films/coatings; they are (a) design of precursor, (b) deposition of thin films and (c) thermal annealing of thin films/coatings. The beneath sections are devoted to these sequences of processing thin films/coatings through solution-processing routes.

2.2.1 Designing the precursor

In this session, the design of the precursor is initially discussed and followed by certain solution-processing routes such as sol-gel, thermal decomposition processing, solution-combustion synthesis and polymerized complex method are described, which are utilized to prepare metal oxide thin films/coatings. In colloidal dispersions, nanoparticles along with the surfactants, are generally dispersed in the solvent, and the obtained precursor is utilized for fabrication of thin films/coatings. However, in the case of molecular precursors, designing the precursors is relatively complex and requires more chemistry understanding. The used reagents in the precursor that comprise the required cations undertake a chemical reaction, which outcomes as the dense metal oxide film when an appropriate thermal processing is applied. As

6

mentioned earlier, the selection of the precursor relies on the solvent type and the processing route. The selected chemical reagents (solute) should dissolve in a certain solvent to attain a stable, clear, and homogeneous precursor. In many cases, two or more solvents are also essential to accomplish a stable, clear, and homogeneous solution. Here, most of the chemical reagents will be metal salts such as nitrates, acetates, chlorides and acetylacetonates. For instance, zinc acetate is the favoured precursor for Zn compared to nitrate. In the case of In and Sn, nitrates and chlorides are favoured over acetylacetonates and acetates due to their ease of compatibility and dissolution with the other metal salts and solvents. To generate metal oxides through solution routes, nitrates, chlorides, or acetates are typically employed due to their ease of availability and low cost. Along with them, laboratory-synthesized complex precursors such as carboxylates, homometallic alkoxides, heterometallic alkoxides, beta-diketonates, oxo-alkoxides, organometallics and ammine hydroxy nitrates also have been utilized (Pasquarelli et al. 2011). Another important feature to be considered while designing the precursor to fabricate metal oxide thin films/coatings is the processing route, and a few processing routes are described below.

2.2.1.1 Sol-gel

Sol-gel process, also termed wet-chemical or soft-chemistry, is an appropriate wet route for synthesising metal oxides. The reaction typically includes the linkage of metal alkoxides into the polymer matrix. It is a simple method and depends on the hydroxylation and poly-condensation of molecular precursors, which is the formation of 'sol'. The sol evolves as a porous polymeric network termed 'gel' after the solvent (water or alcohol) elimination. The gelation phenomenon depends on time, and the time span is termed as 'aging'. The aging results in the creation of oxo (M-O-M) or hydroxo (M-OH-M) bridging through condensation, which comprises water or alcohol removal. The precursors that experience such events are categorized as the 'sol-gel' precursors (Pierre 1998). Base catalysis yields the generation of a colloidal gel; in contrast, acid catalysis causes the polymeric form of a gel. These reactions can occur at room temperature conditions, but thermal treatments are required to attain the crystalline state of metal oxides (Stojanovic et al. 2018) (Pasquarelli et al. 2011).

2.2.1.2 Polymerized complex method

Pechini method is another gel route which was initiated by Pechini in the year 1967 (Pechini 1967). The basic chemistry in this method is the dehydration reaction between a carboxylic acid and an alcohol which is termed esterification. The in-situ formation of the polymeric resin generated via polyesterification reactions in between metal chelate complexes by using alpha-hydroxycarboxylic acids (namely, citric acid (CA)) and polyhydroxy alcohol (namely, ethylene glycol (EG)) is the characteristic feature in this method. CA and EG is the couple which is most widely utilized here and the esterification reaction between them happens at 100 to 150 °C, and it is shown in Fig. 2.1 (Kakihana 1996) (Kakihana and Yoshimura 1999).
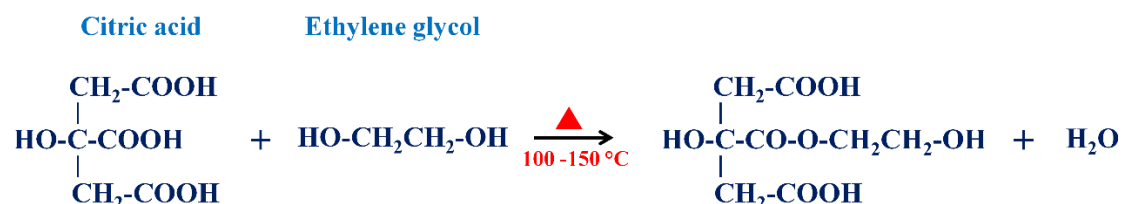
Fig. 2.1: Esterification reaction between CA and EG.

In this method, metal ions from initial materials like hydroxides, carbonates, and alkoxides are chelated in solution with CA. As CA is a polybasic compound that comprises one alcoholic group and three carboxylic acid groups in one molecule, many metallic ions can establish stable chelate complexes with CA. The addition of EG generates polyesterification reactions and causes organic ester. The formed ester still contains two carboxylic groups and two hydroxyls, which can also further react with another EG or CA to create the next polymer branch. The development and branching of these polymer chains cause immobilization of the metal cations and preserve the original stoichiometry (Pasquarelli et al. 2011). The calcination (heat treatment) of the polymer resin at > 300 °C consequences the breakage of chains, the removal of organics and the formation of the desired metal oxides as the residue. The flow chart of the process is shown in Fig. 2.2. (Kakihana and Yoshimura 1999).

Further research was conducted to utilize the other initial materials, such as nitrates in the Pechini method, to develop desired metal oxides, which termed as the modified Pechini process. The polymerized complex method (PCM) in which nitrates

can be used as starting material comes under the category of the modified Pechini process. The concept of chelation and polyesterification reactions between metal ions, CA and EG, and the heat treatment process for synthesizing metal oxides in PCM is exactly similar to the Pechini method (Kakihana et al. 1992) (Udawatte et al. 1998) (Olav et al. 2016).
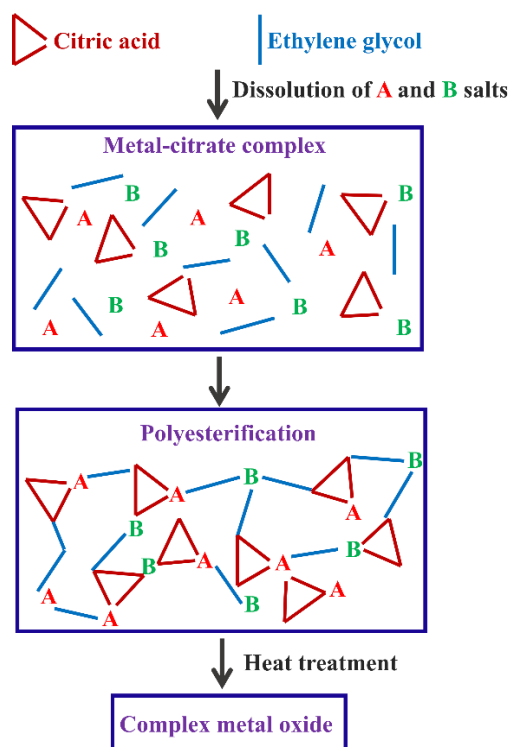
Fig. 2.2: The flow chart of the formation of metal oxide through polyesterification in the PCM method.

The idea beneath the "in-situ" polymerization in PCM/Pechini method is to lessen the individualities of various metal ions. It can be accomplished by steadily holding stable metal-chelate complexes through a growing organic polymer chain. In a rigid polymer chain, the immobilization or no movement of these metal-chelate complexes can minimize the possible segregations of metal ions during the heat treatment at high temperatures, thus ensures compositional homogeneity. This offers a benefit over sol-gel in which hydrolysis and condensation reactions in each metal compound lead to phase and chemical inhomogeneities (Kakihana 1996). It is used as a favoured method in the synthesis of complex multicomponent metal oxides, such as perovskites because it diminishes the chances of segregation (Sunde et al. 2018). This

method also eliminates additional steps such as centrifugation, filtration, cleaning, drying, or controlling pH (Kakihana et al. 1992).

2.2.1.3 Solution-combustion synthesis
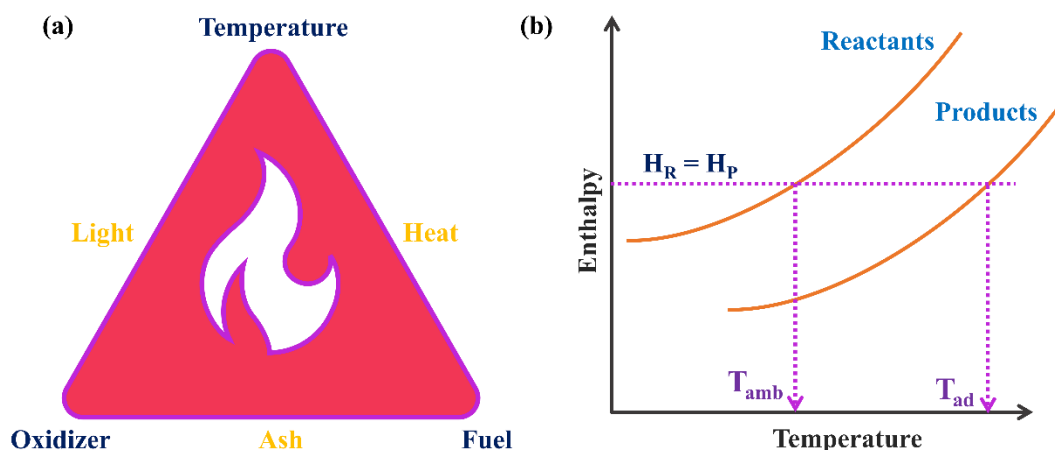
Fig. 2.3: (a) Fire triangle showing required elements and (b) enthalpy vs temperature plot for the combustion reaction, respectively.

Solution combustion synthesis (SCS) appeared as a simple, fast, versatile, and efficient method for the development of metal oxides with high purity and homogeneity for a wide number of applications (Carlos et al. 2020). SCS is a self-sustained redox exothermic reaction that occurs between the metal nitrates (oxidizers) and the fuel (usually composed of the organics comprising carbon and hydrogen) with a low externally supplied thermal energy (< 200 °C) (Kim et al. 2011). Three elements are essential to produce a combustion reaction, which are an oxidizer, a fuel, and the appropriate temperature, as displayed in Fig. 2.3 (a). In this method, the precursors are designed to be combustible, which means that the precursor comprises the oxidizers and fuel. The redox reaction between oxidizer and fuel generates a change in the enthalpy, which produces localized high temperatures and results in the formation of desired metal oxides (Varma et al. 2016).

The enthalpy for the combustion reaction ($\Delta H_{reaction}$) can be estimated from the Hess law. The first law of thermodynamics for an open system is shown in equation 2.1.

$$\delta Q - \delta W = dH_{reaction} \qquad 2.1$$

10

here, δQ, δW, and dH are denoted as heat transfer, work transfer, and enthalpy change of the reaction, respectively. The combustion reaction occurs spontaneously and it is exothermic. The increment in the temperature in the combustion reaction in a short time creates the system adiabatic; therefore, $\delta Q = 0$. In the combustion processing of materials, there is no work transfer; hence $\delta W = 0$. Therefore, the resulting equation can be written as equation 2.2. Upon integrating equation 2.2, within limits of enthalpy of reactants (H_R) and enthalpy of products (H_P), it turns into equation 2.3.

$$dH_{reaction} = 0 \qquad\qquad 2.2$$

$$\Delta H_{reaction} = (H_P - H_R) = 0 \qquad\qquad 2.3$$

Upon plotting equation 2.2 as enthalpy vs temperature in the thermodynamic plane (Fig. 2.3 (b)), it is noticed that the products achieve higher temperature (adiabatic temperature, T_{ad}) after the combustion reaction. In equation 2.1, the transfer of heat from the system to the surrounding is negative (considering the sign convention). Hence, equation 2.3 can be modified as equation 2.4.

$$-\delta Q = dH_{reaction}$$

$$Q_{R \to P} = \Delta H_{reaction} = (H_P - H_R) < 0 \qquad\qquad 2.4$$

For the exothermic reaction, it can be noticed from equation 2.4 that the enthalpy of reactants (H_R) is more than the enthalpy of products (H_P) and the difference is the quantity of heat transfer from system to surrounding. The T_{ad} is denoted as the combustion reaction's exothermicity. The exothermicity will be maximum when the reactants are mixed with a balanced stoichiometry. Any deviation in stoichiometric quantities of oxidizers and fuel may divert to the reduction in exothermicity. The stoichiometric amounts of the combustible elements are specified by the fuel-to-oxidizer ratio (ϕ), shown in equation 2.5.

$$\phi = \left(\frac{RV}{OV}\right) \times n \qquad\qquad 2.5$$

here, RV is reducing valency (fuel), OV is oxidizing valency (OV) and n is the number of moles of fuel required for one mole of oxidizer. When $\phi = 1$, then the combustible elements are in stoichiometry; when $\phi < 1$, it is considered that the fuel is lean; and

when $\phi > 1$, it is considered that the fuel is excess. The effect of ϕ on the combustion reaction is pictorially represented in Fig. 2.4.
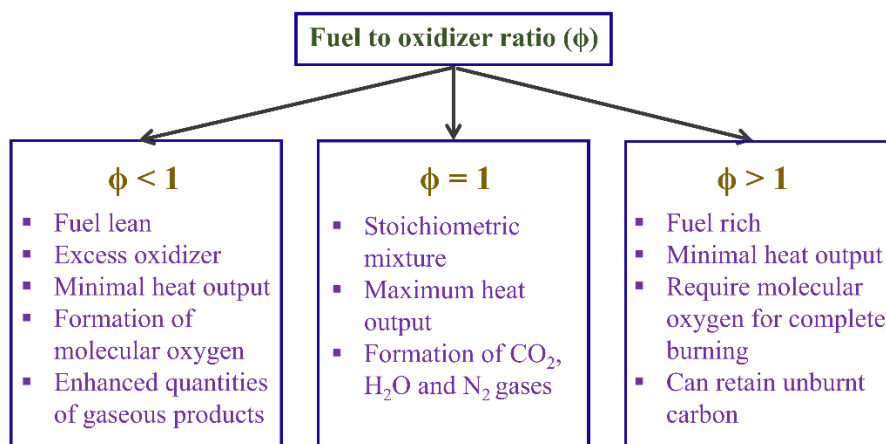
Fig. 2.4: The effect of fuel to oxidizer ratio (ϕ) on the combustion reaction.

In this method, fuel and oxidizer (metal nitrate) are dissolved in the solvent, that can be aqueous or organic. Many solvents like water, ethanol, methanol, 2-methoxyethanol etc., have been reported in earlier studies. An ideal solvent should have the ability to dissolve many metal nitrates and should have an extensive solubility range. Another crucial ingredient in this method is fuel. There is a wide range of fuels that dissolve in various solvents and also present compatibility with metal nitrates. The properties that fuels should possess are low ignition temperature, high calorific value, preferably soluble in water, compatibility with metal nitrates, and must not produce residual mass after combustion reaction. All the hydrocarbons can be treated as fuels. Some of them are urea, glycine, citric acid, acetylacetone, acetic acid, oxalic acid, etc. (Patil et al. 2008). The precursor containing all the combustible elements is defined as the combustible precursor, and it should possess compositional homogeneity and optical clearness. The combustible precursor can be utilized to synthesize bulk powder or to fabricate thin film. The development of metal oxides has been reported by many studies (Patil et al. 2008; Varma et al. 2016). However, the fabrication of thin films through the combustion method is comparatively new, and the initially reported study was in the year 2011 (Kim et al. 2011). It has emerged as a promising method for the fabrication of metal oxide thin films/coatings at relatively low temperatures (Pujar et al. 2020).

2.2.1.4 Thermal decomposition method

Thermal decomposition, also termed thermolysis, occurs due to the chemical decomposition of the material at high-temperature conditions. Decomposition temperature of the material is denoted as the temperature where the material decomposes chemically. This process is considered as a subclass of the solution-processing routes. The decomposition of the precursor (generally an organometallic compound) is performed at high temperatures and normal ambient pressure in an open atmosphere. The components such as precursor, solvent, and ligands are commonly utilized in the thermal decomposition process. Here, the precursor refers to the metal source for preparing metal oxides and they are usually metal acetylacetonates, chlorides or acetates. The solvent is utilized to deliver the environment for the processing of the reaction. Generally, organic solvents with a high boiling point, namely, phenyl ether, 1-octadecene, benzyl ether etc., are used. Ligands denote the molecular moieties or molecules which are efficient in binding with the metal atom or centre ion. The ligands can govern or limit the growth of metal oxides, can stabilize the nanocrystals, and also can modify metal oxides' properties. The ligands are also normally referred to as surfactants in the thermal decomposition process. Ratios of the starting materials, along with surfactant and solvent can control the growth, but temperature, reaction time and aging period can also be crucial. (Pasquarelli et al. 2011) (Voon et al. 2020). In the literature, many metal oxides such as ZnO (Darezereshki et al. 2011; Jing et al. 2002; Salavati-Niasari et al. 2008), WO$_3$ (Yan et al. 2011), CuO (Al-Gaashani et al. 2011), NiO (Salavati-Niasari et al. 2010) etc. have been developed through the thermal decomposition method (Guo et al. 2013; Voon et al. 2020).

2.2.2 Deposition of thin films

The deposition of metal oxide thin films/coatings has been performed by various techniques and the following section discusses it. The thin films/coatings of metal oxides have been initiated through the chemical solution process, which is spray pyrolysis. However, with the arrival of physical vapor deposition technologies (vapor-phase methods), which are vacuum-based (namely pulsed vapor deposition, sputtering), these technologies have turned as principal tools for research as well as for industrial purposes with time. These commercial vapor-phase methods persist as ideal for the

investigation of new materials due to their ability to deposit morphologically robust coatings with benchmark properties (Pasquarelli et al. 2011) (Pujar et al. 2020). Commonly, vapor-phase methods include thermal evaporation, direct current and radio frequency magnetron sputtering, pulsed laser deposition and atomic layer deposition. Although the stated vapor-phase methods offer compositionally robust coatings, they also comprise very specialised equipment and targets, which enhances an extra cost for the fabrication. Also, limitations like small area of deposition, poor utilization of the materials (most of the material to be deposited lands up on the walls of the chamber) and slow rates of deposition are connected with vapor-phase methods. Additionally, these vapor-phase methods comprise a prolonged processing time for the generation of the high vacuum and for the deposition of the films, which mandate a high energy consumption (power). And also, significant energy is expended to heat or sputter from the target. Consequently, the overall consumption of energy is very high to deposit a coating through these methods, which is not compatible as far as the ecological routes are considered (Mitzi 2009).

In comparison with the related inherent limitations of vapor-phase methods, there is a new drive to return the processing of coatings to its root, i.e., chemical solution processing (Pasquarelli et al. 2011). Solution-phase methods, namely, spray coating, spin coating, dip coating, screen printing, inkjet printing, aerosol printing, slot casting and chemical bath, are a facile substitute to the conventional vapor-phase methods in depositing the coatings due to their low equipment cost, ease of fabrication, efficient materials utilization, and scalability at atmospheric pressure conditions (Pujar et al. 2020). The solution-phase methods also have the potential to replicate as a more ecological or green route in terms of the conservation of resources and energy. Substantial continuous efforts have been pivoted on the progress of these inexpensive solution-phase methods (Ahn et al. 2015) (Mitzi 2009).

In general, the solution-phase methods are classified into two groups: in the first group, the material is directly grown on the given substrate during the time of deposition, whereas in the latter case, the deposited liquid coatings need an extra processing step to evaporate the solvent and yield the desired phase. Chemical bath deposition comes in the group of direct growth method and this method depends on

controlled reaction as well as precipitation of reagents in the solution. The nucleation and the growth of the coating generate on the immersed surface of the substrate in the precursor reservoir. The critical limitation associated with chemical bath deposition is the wastage of the solution quantity (Hodes 2007) (Pasquarelli et al. 2011). In the liquid coating group, the spin coating method is highly utilized; and in this method, the solution is spun on the substrate to form a thin layer (Sahu et al. 2009). The details of the spin coating method are addressed in beneath section. Another method, named dip coating, involves depositing a layer of solution on the dipped substrate during the withdrawal from the precursor reservoir. Dip coating offers coverage of coating on both sides of the immersed substrate (Brinker et al. 1991). Whereas other scalable techniques (such as doctor blade or metering rod) exist for depositing a coating on the single side of the substrate. In the doctor blade method (also called knife-over-roll coating), the thickness of the coating is managed by the gap existing between the substrate and the blade (Pasquarelli et al. 2011). In contrast, a wire-wound metering rod [60] is utilized instead of the blade in the metering rod method. The diameter of the wire determines the amount of the coating that remains on the substrate. These methods comprise distribution, smoothening and thinning across the substrate surface with the help of a blade or rod, respectively, after applying the precursor (Shim 2018). In slot-die casting, the solution is allowed to flow by a syringe pump through a slotted head positioned near the substrate (Patidar et al. 2020). In these methods, the line speed is maintained faster than the extrusion speed so that the obtained coating becomes thinner than the slot width; they are used for high viscous solids-loading solutions with a viscosity of 5 to 50000 cP. Discussing spray coating, it can be utilized as a liquid coating method. It can also be used as a direct growth method. In the second case, when the temperature of the substrate is maintained above the decomposition of the precursor in spray coating, the process is usually termed spray pyrolysis (Pasquarelli et al. 2011).

The deposition of the coating through the spray pyrolysis process involves the following crucial steps; the atomization of the precursor, the transportation of the resultant atomized droplets with the help of carrier gas and finally, their thermal decomposition on the preheated substrate. For the atomization of the precursor, air blast, electrostatic and ultrasonic atomizers are commonly utilized (Perednis and

Gauckler 2005). Post atomization, the droplets of very small sizes are transported through a nozzle by a carrier gas (air/nitrogen/argon/oxygen) onto a preheated substrate. During this step, the transportation of the maximum droplets towards the hot substrate without the formation of the particles is important. When the droplets hit the substrate surface, the evaporation of the solvent, followed by the spreading of the droplets, occurs. Finally, the thermal decomposition of the precursor happens where the chemical constituents in the precursor react to form the desired compound (Perednis and Gauckler 2005) (Patil 1999).

Furthermore, printing is considered as an additive deposition process in which the deposition and the patterning can be performed simultaneously; therefore, a reduction in chemical and energy consumption is attained. Screen printing, inkjet printing and aerosol printing come into this category (Yu et al. 2016). Screen printing is a contact method performed with a mask or stamping; it requires solutions with high viscosity. Here, force is applied to the solution to deposit on the given substrate through the mesh pores (Riemer 1989). The screen-printing method is elaborately detailed in the following section. Attractive substitutes for screen printing are inject printing and aerosol jet, which deliver many advantages, such as multi-layer deposition without photolithography and non-contact deposition on fragile substrates (Pasquarelli et al. 2011).

2.2.2.1 Spray coating

Spray coating received much attention because it is a simple, non-contact, inexpensive, as well as large-area deposition method. As stated previously, it has the feasibility to be utilized either as a liquid coating method or as a direct growth of the coating when the temperature of the substrate is maintained well above the decomposition temperature of the atomized precursor. The latter approach is generally denoted as spray pyrolysis (Pasquarelli et al. 2011). It delivers good productivity and viability for depositing coatings of any composition on comparatively large substrates. Spray pyrolysis equipment typically encompasses an atomizer, precursor and preheated substrate. The generally used atomizers in spray pyrolysis methods are (i) air blast (the precursor is exposed to a high-velocity air stream), (ii) electrostatic (the precursor is exposed to a high electric field) and (iii) ultrasonic (fine atomization is generated by

ultrasonic frequencies). The deposition of the film on any given preheated substrate through the spray pyrolysis process includes initial spraying of precursor, impact of droplets on the surface of the substrate, spreading of the droplets and final thermal decomposition. These processes can happen either simultaneously or sequentially (Perednis and Gauckler 2005). The noteworthy variables that impact the morphology and properties of the final coating in the spray pyrolysis process are ambient temperature, distance between nozzle and substrate, flow rate of carrier gas and solution, radius of the droplet and its momentum, process of atomization, temperature of the substrate surface, type of solvents, type of salts and additives, decomposition of the precursor, concentration of the solution, motion of the substrate (in the case of the continuous process), available time for a particular drop to react before the strike of the second drop on the same surface (Perednis and Gauckler 2005) (Mooney and Radding 1982).

The most important variable in spray pyrolysis is the temperature of the substrate surface. The substrate temperature plays a vital role in the solvent evaporation rate and the precursor decomposition, which subsequently determines the morphology of the coating. If it is higher, the coatings can be rougher and porous, whereas if it is too low, the coatings can generate cracks (Perednis and Gauckler 2005) (Stelzer and Schoonman 1996). Commenting on the substrate at high-temperature conditions, the heat generated from the substrate act not only on the substrate surface but also on the arriving droplets by enhancing droplets' temperature through the radiative heat transfer, which leads to the evaporation of the solvent in air. The higher the substrate temperature, the higher the radiative heat transfer, which causes an excessive solvent evaporation rate in the droplets before they hit the hot substrate. Due to the high rate of evaporation of solvent at this condition, the tiny droplets dry before striking the substrate and they reach as the dried particles on the surface of the substrate. When the dried particles are in relatively large numbers, they accumulate on the substrate's surface due to their preferential landing. Their accumulation will ultimately cause a rough and porous coral-like coating on the substrate. When the substrate is maintained at a low temperature and the spray is still active, a certain amount of precursor solution droplets approaches and deposits on the substrate. At this instant, the amount of solvent evaporated from the droplets is too minimal compared to the amount of solution that

reaches the substrate. The lower the substrate temperature, the larger the solution amount exists on the substrate's surface because of the low solvent evaporation rate during the droplets transport. The solution tends to establish as a thin liquid layer on the top of the forming base layer. The temperature of the established thin liquid layer speedily increases when the spraying ends, and it causes rapid solvent evaporation. In this condition, the base layer of the coating adheres to substrate. Whereas the upper drying layer experiences a volume shrinkage due to the rapid solvent loss (here, the solvent loss by evaporation at the surface is quicker than the diffusional migration of the solvent in the coating). The difference in shrinkage between the shrinking surface and the adhered base leads to mechanical (tensile) stresses in the speedily shrinking upper layer. The higher the amount of solvent evaporated, the higher will be the generation of the stresses. If the generated stresses are more, cracks originate at the surface and spread through the entire coating. In the extreme scenario, the excessive stresses may shatter the adherence of the coating to the substrate and delaminate the coating (Neagu et al. 2006).

Most spray pyrolysis methods are generally performed through an aqueous-based solvent (Mooney and Radding 1982). Here the water is used without added organic catalysts and additives. The aqueous-based solvent is non-toxic, safe, has no detrimental impact on the environment (environmentally benign), is abundantly available, and is cost-effective (Pasquarelli et al. 2011). It meets the current ecological awareness by restricting the usage of environmentally hazardous organic content in the precursor (Liu et al. 2015). Nevertheless, research is also performed through nonaqueous solutions because the solvent in the aqueous solution evaporates before reaching the preheated surface and leaves the vapors to react at the surface (Mooney and Radding 1982).

2.2.2.2 Spin coating

Spin coating is a widely used method because it offers simplicity and reproducibility. The process of spin coating is categorized into four stages, namely, deposition, spin-up, spin-off and evaporation (Scriven 1988). In this method, the solution is deposited on the surface of a substrate, which is held to the holder with the help of a vacuum chuck. The holder can either be in static or-speed spinning mode (Yu

et al. 2016) (Pasquarelli et al. 2011). Later, the substrate on the holder is allowed to rotate at a high spinning speed (several thousand rpm). The centrifugal forces generated by the spinning substrate are used to spread the solution on the substrate surface. During spin-off, the rotation of the substrate decelerates and it comes to its initial static position. After the solvent evaporation, a uniform and thin coating develops on the substrate (Yu et al. 2016) (Birnie 2001). The thickness and quality of the resulting coating depend on several factors such as spinning acceleration, solution volatility, viscosity, concentration and surface tension of the solute, mass of the precursor, hydrophilicity of the substrate, substrate size, eccentricity of the vacuum chuck, ramp-up time, elapsed-time between coating and annealing (Scriven 1988).

2.2.2.3 Screen-printing

Printing is considered as one of the most noteworthy technical developments in human history. In general, printing is a reproductive technique that duplicates the information (like text or graphics or pictures) by depositing inks on the substrate (image-carrying medium). Screen-printing, also called stencil printing, is one of the printing processes in which an information is passed by using an ink via the openings in the stencil onto the substrates (Michel et al. 2001). The screen-printing method is being utilized for mass production because of its advantages like simplicity, versatility, reliability, miniaturization, has no restrictions on the type of substrates (plastics, papers, ceramics) and it can be executed at ambient conditions. The screen-printing process does not necessitate a sophisticated environment that leads to minimal investment and low-cost manufacturing (Schüler et al. 2009). Nowadays, screen-printing is used in manufacturing numerous electronic appliances such as electronic circuits, thin film transistors, gas sensors and fuel cell printing (Faddoul et al. 2012b).

Screen-printing has mainly three key components, they are (i) screen with frame and mesh, (ii) coater and (iii) squeegee, as shown in Fig. 2.5. As stated, the screen has two parts which are frame and mesh; generally, the screen frame is made up of metals like stainless steel, aluminum, or wood. Whereas the screen mesh is made of silk, polyester, nylon, or stainless steel. Here, the mesh counts range from 10 to 600 openings per inch. Screen mesh is fixed effectively on a screen frame under a tension of 20-30 N/cm using appropriate adhesives or glues. After proper adhesion of tensile-state mesh

19

on the frame, it is coated with a photosensitive emulsion. Post-coating, it is dried for a few minutes in a drying chamber. Later, a transparent photographic film containing the pattern (to be printed) is placed on the dried screen mesh, which is coated with a photosensitive emulsion. The set-up is exposed to UV light finally for some time (in minutes). During this step, the places where the film with the pattern exists, will not be exposed to UV light. Later, the emulsion layer of the unexposed areas will be removed by applying a high-stream water jet. At this point, the pattern (to be printed) will be left out on the screen mesh mounted on the frame.
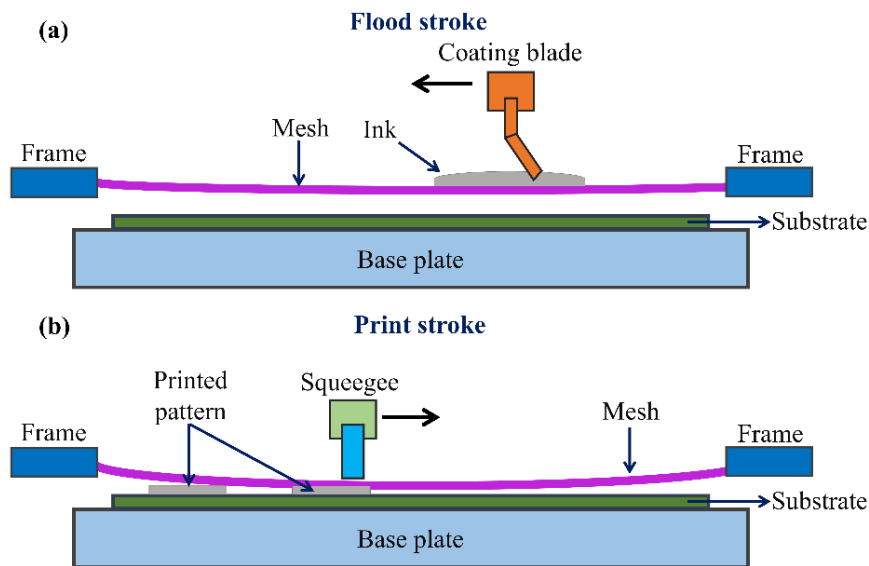
Fig. 2.5: Schematic representation of screen-printing process during (a) flood stroke and (b) print stroke, respectively.

The screen-printing process involves pushing the ink with viscosity (5-50 poise) to deposit on the substrates via a permeable patterned screen. Screen-printing is normally conducted in two strokes, (i) flood stroke and (ii) print stroke. During the flood stroke, the screen-printing ink spreads over the fixed screen mesh by filling the pores with the ink. In this stroke, a coating blade is utilized to spread the ink. In the flood stroke, the screen mesh will not be in contact with the substrate. The flood stroke is schematically represented in Fig. 2.5 (a). The print stroke occurs after the flood stroke. During the print stroke, a squeegee is used, which presses the ink and transfers it onto the substrate through the screen mesh pores. In the print stroke, the screen mesh

comes in contact with the substrate. The print stroke is schematically denoted in Fig. 2.5 (b).

In the screen-printing process, there are many factors related to squeegee load, squeegee speed, mesh type and snap-off distance, which influence the quality of the screen-printed film (Pan et al. 2012). It has been suggested that the respective load and speed of the squeegee must be in the range of 6 to 9 kg and 20 to 50 mm/s. When the squeegee load is enhanced, then the speed of squeegee must be reduced and it should be maintained, and vice versa. The load of the squeegee can be augmented if the inks have too sticky nature and the required thickness is low (Somalu et al. 2017). In their report, Phair et al. stated that the thickness of the films diminished with enhancing the squeegee load. The authors observed that the squeegee load of 5 and 9 kg resulted in film thickness of ~40 and 20 µm, respectively (Phair et al. 2009). The snap-off distance should be kept in the range of 1.5 to 2 mm. The distance can be adjusted depending on the requirement of film thickness. It has been advised that a high snap-off distance is essential to fabricate a film with high thickness. In general, squeegees with a rectangular shape, made of polyurethane polymer with hardness shore-B, are utilized to deposit the metal and metal oxide films through the screen-printing. In their study, Dollen and Barnett observed that the films attained precise dimensions when they deposited by utilizing a softer squeegee (60 durometers) and lesser squeegee speed (25.4 mm/s), in contrast to the films deposited by utilizing a more rigid squeegee (80 durometers) and higher speed (55.8 mm/s) (von Dollen and Barnett 2005). As far as the film quality is concerned, it is determined that low squeegee speed enhances the surface levelling and quality of the films by offering ample time for the flow of ink, specifically in the case of high viscous screen-printing inks. In their report, Mücke et al. found that the thickness of the films was in the range of 23 to 100 µm when the squeegee speed, squeegee pressure and snap-off distance maintained at 150 mm/s, 0.3 MPa and 2 mm, respectively (Mücke et al. 2014). In their study, Somalu et al. observed that the films were of thickness ~10 µm when a squeegee speed of 20 mm/s, squeegee load of 6 kg and snap-off distance of 2 mm was maintained (Somalu and Brandon 2012). The aforementioned outcomes approve that the thickness of films can be altered by changing the parameters of screen-printing, primarily squeegee load, squeegee speed and snap-off. Screen meshes with mesh number varying from 300 to 600 are generally

used. A high mesh number is favoured when the sharp edge lines of the film are required to be printed. The overall screen-printing parameters, suggested conditions and remarks are presented in Table 2.1 (Somalu et al. 2017).

Table 2.1: The overall screen-printing parameters, suggested conditions and remarks (Somalu et al. 2017) (Information from the reference is used with permission from Elsevier).

Screen-printing parameters	Suggested conditions	Remarks
Squeegee load	6 to 9 kg	To be enhanced when the ink is too sticky.
Squeegee speed	20 to 50 mm/s	To be decreased when the ink is too sticky.
Snap-off distance	1.5 to 2 mm	To be enhanced to enhance the thickness of the film.
Screen-printing angle	45°	Appropriate for good ink filling onto the substrate
Squeegee's geometry and type	Rectangular and polyurethane polymer	The thickness of the film decreases by enhancing the hardness of the squeegee
Type of screen mesh	305 to 325	It controls the thickness of films (10 to 50 µm).

Discussing screen-printing inks, they are made of three chief components, (a) the functional material, (b) the organic vehicle and (c) the additives like promoter and dispersant. The functional materials can be added into the solution containing organic vehicle and additives. Nano or micro-sized particles of several classes of materials like metal, metal oxides, polymers, graphene, hydrides, and nitrides can be used as functional materials (Do et al. 2003; Faddoul et al. 2012a; Joseph et al. 2016; Manjunath et al. 2020b). The loading of the functional material in the screen-printing inks is generally in the range of 60 to 70 wt. %. To attain smooth printed patterns, particles with a diameter lesser than 3 to 5 µm are normally utilized. In the case of conductive inks, particles of noble metals, namely silver, gold, palladium, and platinum, are

utilized. Also, the preparation of conductive inks from the particles of non-noble metals such as nickel and copper is reported in the literature. However, these particles can oxidize during sintering in the air atmosphere. To prevent oxidation, sintering must be conducted in the inert gas atmosphere (Faddoul et al. 2012a). Apart from the metal-based particles, non-metal-based particles like carbon nanotubes, graphene, graphite, polyaniline etc., have also been utilized as functional materials for preparing conductive inks (Faddoul et al. 2012a; Stampino et al. 2010). Several metal-oxide-based screen-printable inks have also been developed to fabricate metal oxide screen-printed films such as zinc oxide, tin oxide, barium stannate, tungsten oxide etc., which are potentially applied in several areas, including gas sensors, thin film transistors, solid oxide fuel cells etc.

Based on the kind of functional material, the screen-printing ink can be called particle-based or particle-free ink. The name itself suggests that the functional material in ink can be in the form of particles or directly in the form of molecular precursor. In the first case, as explained in the former paragraph, the functional material (metal or metal oxide) will be in the form of nano or microparticles, termed as the particle-based approach. The latter case is a novel-particle-free approach where the molecular precursors are considered directly. Here, the extra particle processing steps, such as synthesis and their calcination, which consume excess time for preparing the functional material, can be sidestepped. The issues like the agglomeration of the particles can occur in the particle-based approach. Also, the clogging of the mesh pores happens in the particle-based approach due to the sticking of the particles to the pores of the screen mesh. Further, it leads to deformity in the patterns during printing. However, in the particle-free approach, the problem of particle agglomeration and clogging of the pores can be entirely eradicated, and the films with lower thickness can also be attained (Manjunath et al. 2019, 2021a).

Commenting on the organic vehicle, it is one of the main components in screen-printing inks. Approximately 20 to 45 wt.% of the inks are encompassed with the organic vehicle. Phenomena like wetting of the particles, formation, and adhesion of the film onto the substrate occur due to the presence of the organic vehicle in ink. The organic vehicle comprises organic binders and solvents. It assists in flowing of the ink

via the screen mesh. The organic vehicle must contain chemical inertness; it should not react with the substrate as well as the functional particles. Its decomposition temperature must be lesser than the melting temperature of the functional materials and the softening point of additives. Binder is one of the main parts of the organic vehicle, which enhances the particle network, avoids defects, and permits the ink adhesion onto the substrates. Long chained molecular organic compounds such as carboxy methyl cellulose, hydroxyethyl cellulose, butyl cellulose, polyvinyl butyral, polyvinyl acetal, polymethyl methacrylate, etc., can be served as a binder. The type of solvent also has a crucial role in defining the maximum content of solid in ink. Solvents such as diethyl glycol, diethylene glycol, acetone, cyclohexane, texanol, terpineol, methyl ethyl ketone, butyl carbitol, carbitol acetate, N-methyl-2- pyrrolidone, glycol ethers (propylene and Di-propolyene), butyl carbitol acetate, epoxy and phenoxy resin, etc. can be utilized in the formulation of screen-printable inks. Recently, water, an ecologically friendly solvent, is also utilized to subdue the contrary effects on the atmosphere caused by the usage of formerly categorized solvents. The use of non-polar solvents and non-degradable binder causes the production of toxic elements that can lead to adverse consequences on the atmosphere. To diminish the production of toxic elements, the practice of polar solvents and bio-degradable binders must be uplifted (Faddoul et al. 2012a; Somalu et al. 2017).

Discussing the additives, it contains inorganic promoters and dispersants, which improve the ink's functionality during the screen-printing process and also during the sintering. The loading of the additives varies from 3 to 5 wt. % in the screen-printing inks. The inorganic promoters are added when the sintering process is realized to occur at high temperatures (> 400 °C). They activate the process of sintering at relatively lesser temperatures. Generally, glass frits are utilized as inorganic promoters. Nowadays, to eliminate the lead which is conventionally present in glass frits, a mixture of bismuth, magnesium, alumina, calcium, and sodium carbonates is utilized (Faddoul et al. 2012a). Dispersants are long-chain molecules and the function of dispersants is to expand the solid particles' separation. They form as a stearic or an electrostatic barrier around the surfaces of the particle so that the optimization of the interparticle forces among neighbouring particles is possible to a satisfactory extent. It subsequently

decreases the viscosity of the ink. Due to this consequence, the solid content can be augmented in ink, and the density of the printed films can also be enhanced. Also, the addition of dispersants can avoid particle agglomeration and stabilize the ink for a longer duration. Phosphoric acid ester, oleic acid, stearic acid, pentastearic acid oligomer and oligomeric polyester are utilized as dispersants in the literature (Somalu et al. 2017).

2.2.3 Thermal processing of thin films

The last and crucial step for thin film fabrication is thermal processing. It is performed after the deposition of precursor on the substrate of interest through any of the aforementioned deposition techniques. The thermal processing step is conducted for primarily three reasons: (i) to decompose the precursor and simultaneous elimination of organic impurities, (ii) to encourage crystallization and formation of required phase (phase transformations), and (iii) to govern carrier concentration via tailoring of the defects. The initial step is the most required and pivotal when the purity as well as densification of the film are concerned. Regardless of colloidal nanoparticle-based or molecular-based precursor, the impurity elimination and decomposition steps are to be essentially fulfilled with better yield. The thermal processing step can be conducted either on a hotplate or under restricted surroundings in a tubular furnace or with the help of a rapid thermal processing (RTP) system. Furthermore, secondary annealing or post-processing can also be processed where the heating step (annealing) is performed in a vacuum atmosphere or reducing (mixture of N_2 and H_2) or N_2 atmosphere. Usually, the annealing in a vacuum/reducing/N_2 atmosphere is conducted for the generation of more carrier concentration. During the thermal processing of thin films deposited via colloidal nanoparticle-based precursor, the terms curing and sintering are generally used. The curing temperature is denoted as the temperature at which the organic capping agents are eliminated from the particles, and the particles tend to contact each other. If the density is required in the films instead of nanoparticulate networks, then further heating is essential, which is defined as sintering. The sintering process happens at higher temperatures which generates necks in between the particles (Pasquarelli et al. 2011). The overall fabrication, i.e., starting from the

designing of the precursor to the development of metal oxide thin films through solution-phase methods, is pictorially summarized and is represented in Fig. 2.6.
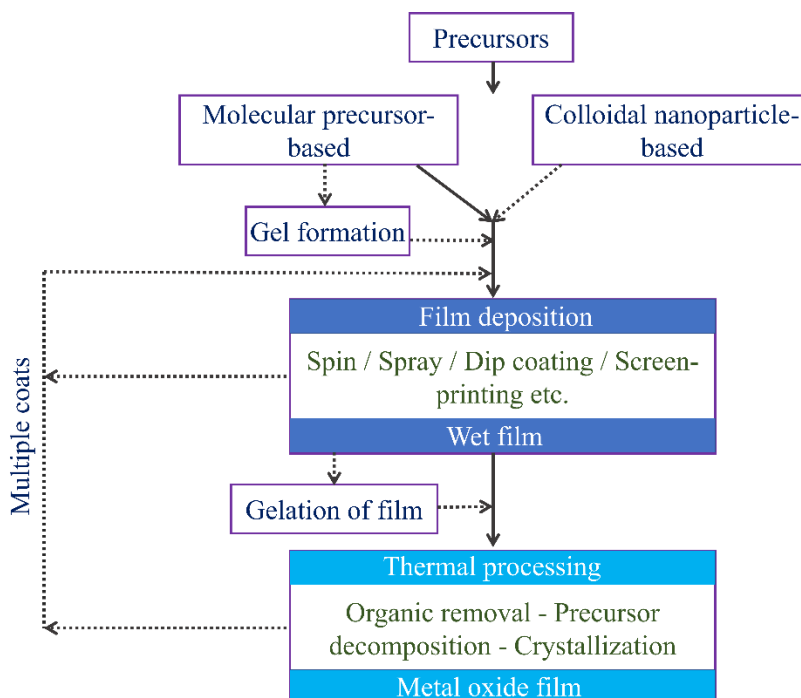
Fig. 2.6: Flow chart showing the fabrication of film through solution-phase methods. (Solid line denotes the simplest route, whereas the dotted line indicates alternate paths).

2.3 Antifouling coatings

2.3.1 Antifouling

As mentioned in the previous chapter, biofouling can be elucidated as the uninvited accretion of microorganisms, plants and animals on the surfaces that are submerged in the water (Yebra et al. 2004). In the aquatic environs, competition for living is high, and all the surfaces are influenced by biofouling. The micro and macro-organisms generally stick to the natural or man-made surfaces and create multicellular communities called biofilms. When a fresh surface is submerged in seawater, it instantly begins to adsorb a molecular 'conditioning' film mainly comprised of dissolved organic material. The attachment of bacteria and other unicellular organisms occurs next. It is followed by the attachment of spores of macroalgae (seaweeds) and protozoa within a week, and in turn, by larvae of invertebrates, such as barnacles, within several weeks (Krishnan et al. 2015; Pistone et al. 2021). A schematic representing the

26

attachment of biofouling on the submerged surface is shown in Fig. 2.7. It is often mentioned that the formation of biofouling proceeds as a linear successional model. But in reality, instead of the linear model, the dynamic model delivers a balanced view in a better manner. In some cases, spores of seaweeds have the ability to settle within a few minutes of immersion; and larvae of few species of barnacles adhere within a few hours on an immersed surface. Henceforth, fouling is categorized as a highly dynamic process (Callow and Callow 2011).
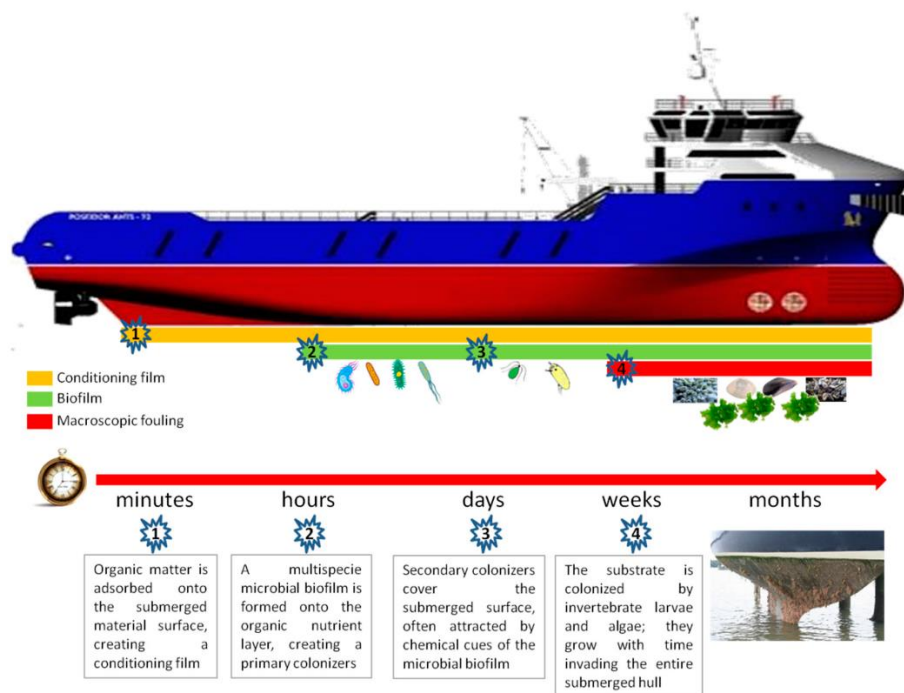
Fig. 2.7: Schematic representing the attachment of biofouling on the submerged surface (Pistone et al. 2021).

Biofouling is a serious concern globally because it leads to significant problems along with economic losses. In the case of ships/boats, the unfavourable effects triggered by the biological settlement cause various issues. High frictional resistance produced by the roughness causes an increment in the weight of the ships and a consequent reduction in the speed and loss of manoeuvrability. To recompense this effect, high consumption of fuel is required and it originates enhanced emissions of threatful greenhouse gases in the environment. Biofouling also has adverse effects on industrial equipment, shipping industries, underwater pipelines, offshore platforms, desalination plants, oceanographic equipment etc. (Krishnan et al. 2018; Yebra et al.

2004). Most of the mentioned industries, pipelines etc., use stainless steel as one of the common materials. The interaction of stainless steel with the aquatic environment leads to biofouling, which assists in a significant reduction of functionality and causes contamination (Tesler et al. 2015). The usage of glasses is also common in oceanographic equipment such as sensors, cameras and torch lights to obtain data for underwater research. These glasses are also often affected by biofouling, as there is no protection to restrict biofouling. Therefore, this equipment has to be cleaned frequently to preserve their standard functionality. In the aquatic environment, despite the material (steel or glass), every arrangement is planned to be utilized uninterruptedly for a long time without much maintenance. Nevertheless, biofouling creates detrimental effects to limit this goal (Xue et al. 2015).

To restrict biofouling, antifouling coatings containing biocides that deter or kill settling organisms were developed firstly. Chemical agents comprising organotin biocides like tributyltin, triphenyltin, organotin compounds and booster biocides like diuron and irgarol were utilized as components of effective antifouling coatings in the past. Nevertheless, they were observed to be extremely toxic and speedily producing a negative influence on the aquatic environment. Global organizations such as International Maritime Organization (IMO) and Marine Environmental Protection Committee (MEPC) intensively opposed the practice of these tin-based biocides in the antifouling coatings during an International Convention conducted on 5 October 2001. After 1st January 2003, environmentally harmful tin-based coatings were banned. The ban on these products was the reason for the significant transformation in the antifouling paint industries. The antifouling paint industries were advised to progress with TBT-free products that are capable of substituting the TBT-based products, and simultaneously produce economic advantages and cause minimal detrimental effects on the surroundings. Major antifouling paint industries like Hempel's Marine Paints, International Marine Coatings, Jotun, Chugoku Marine Paints and Ameron have agreed to obey the regulation by eradicating all TBT-based products from 1 January 2003. The shipping companies such as A.P. Møller, Leif Höegh have also reacted to the legislative changes towards tin-free paints. After 1st January 2008, the existence of such kind of coatings on the surfaces of ships/boats was totally restricted. For this cause, an urgent

requirement has originated to develop ecologically minimal harmful, non-toxic antifouling coatings as a replacement for detrimental tin-based coatings (Krishnan et al. 2018; Yebra et al. 2004).

Many approaches have been developed in the proposal of anti-fouling materials. Coating with artificially or inherently equipped antimicrobial materials, micro-nano structuring, cationic or antibiotic polymer grafting and photoactivation of surfaces come under this category (Banerjee et al. 2011). However, most of the mentioned approaches included considerable limitations like mechanical weakness, non-uniformity in the coating, weak adhesion to the substrate and deficiency in longstanding stability. Henceforth, a facile, inexpensive method to develop robust coatings with uncompromised mechanical properties and simultaneous repelling of fouling contaminants has an instantaneous importance in the applications which suffer from the mentioned challenges (Tesler et al. 2015). Recently, superhydrophobic surfaces (SHS) that replicate the lotus architecture, where the water droplets roll off from the nanoscopically rough surface of the leaf, have been appeared as a possible solution for the creation of antifouling materials (Verho et al. 2011). Several techniques have been tested to develop non-wetting SHS by utilizing a variety of materials (Feng et al. 2002). However, the micro/nano surface topography of SHS, which is important for attaining high water contact angles, comprises deficient mechanical stability (Celia et al. 2013). Though SHS have technological significance, neither naturally obtained SHS nor artificially developed analogues have decent mechanical robustness. So, they cannot be effectively utilized in abrasion-heavy applications, particularly when they are deposited on metallic surfaces like stainless steel (SS) (Tesler et al. 2015).

2.3.2 Metal oxide-based antifouling coatings

To overcome the above limitations, transition and rare earth metal oxides have appeared as vital materials because of their versatility in their properties (Parreira et al. 2006). Metal oxides such as titanium oxide (Dineshram et al. 2009; Ruffolo et al. 2013; Szeto et al. 2020), zinc oxide (Al-Fori et al. 2014; Miller et al. 2010; Sathe et al. 2016) have been utilized to prevent the antifouling. Most of the approaches have utilized metal oxide nanoparticles in the antifouling coatings. It is known that tungsten oxide possesses the properties such as excellent mechanical durability, outstanding corrosive

29

resistance in acidic and basic conditions, good chemical stability, very low toxicity, and environmental friendliness (Mardare and Hassel 2019; Tesler et al. 2015). In the literature, it is found that antifouling coatings based on tungsten oxide are limited. Recently, for the first time, Tesler et al. developed exceptionally robust antifouling tungsten oxide coatings directly (avoiding the nanoparticle route) on steel substrates through the electrochemical deposition technique. In their study, Tesler et al. displayed that tungsten oxide coatings were mechanically durable and also chemically modified tungsten oxide coatings exhibited anti-wettability properties simultaneously by eradicating fouling formation. The innovative idea of Tesler et al. was to develop coatings with an outstanding combination of mechanical and hydrophobic properties. Such an approach makes the coatings mechanically durable and concurrently repels the water, which helps in avoiding the adhesion of biofilm in the fouling arenas (Tesler et al. 2015).

Before discussing tungsten oxide and its coatings, the important properties such as mechanical and water-repellant properties that are primarily required for antifouling coatings, are explained here. As stated, mechanical properties play a vital role in antifouling coatings to generate durability and stability in resisting mechanical damage in the fouling vicinities (Tesler et al. 2015). Among several mechanical properties, the hardness of the films is one of the predominant properties. Commonly, hardness measures the resistance of films against permanent or plastic deformation induced by either scratches, indentation, or abrasion. Scratch hardness measurement is considered as one of the types of measuring the hardness of the surface of the coatings against the scratches. It is measured through a scratch test, which is an easy and commonly used technique. In some aspects, scratch hardness is different from normal hardness. The normal hardness or indentation hardness is described as the resistance provided by the material against the deformation by vertical penetrating material (known as indenter) (Misra et al. 2018) (Sinha et al. 2009). Scratch hardness is defined as resistance offered by the surface of the coating to the surface deformation, which is caused by passing the scratching indenter tangentially along the surface of the coating under a fixed load and speed. Scratch hardness is generally called as the load (force) per unit load-bearing area at the time of scratching. As finding the load-bearing area during the test is tough, the

scratch hardness is measured from the width of the leftover scratch, which is obtained after the completion of the scratch test. A relative advantage of measuring scratch hardness over normal hardness is the feasibility of investigating the hardness variations by making only a single scratch; the absolute value of the scratch hardness can be obtained at any specific position on the single scratch track. Also, by a single scratch, the hardness of different constituent phases can be determined by just measuring the width of the scratch and applying the scratch hardness equation (Beegan et al. 2007) (Misra et al. 2018). For an indenter tip with a circular area of cross-section, the value of the scratch hardness (H_s) is calculated from equation 2.6.

$$H_s = \frac{8\,F_N}{\pi b^2} \qquad\qquad 2.6$$

where F_N is the normal force used and b is the average scratch width, according to the ASTM G171-03 norm (Beegan et al. 2007) (Augustin et al. 2016). A summary of previously reported scratch hardness values of several metal oxide coatings that are deposited through different processing techniques is presented in Table 2.2.

Table 2.2: A summary of formerly reported scratch hardness values of various metal oxide coatings deposited through different processing techniques.

Coating material	Substrate	Deposition technique	Thickness of the film (µm)	Indenter material	Indenter tip radius (µm)	Normal load applied (N)	Scratch hardness (GPa)	Reference
TiO_2	Microscope glass	RF reactive magnetron sputtering	~0.315 to 0.345	Rockwell sharp spherical diamond	25	~2.5 (maximum)	5.5 to 8.4	(Hasan et al. 2010)
TiO_2	Microscope glass	RF reactive magnetron sputtering	~0.315 to 0.345	Rockwell sharp spherical diamond	25	~1.7 (maximum)	11.5 to 13.6	(Haseeb et al. 2010)
TiO_2	Aluminium & SS	Suspension plasma spraying	8 to 33	Rockwell diamond	200	~10 to 30	0.58 to 3.6	(Jaworski et al. 2008)
TiO_2	Aluminium alloy (AA1350) & mild steel (S235GJ)	Low pressure cold spraying	10 to 55	Rockwell diamond	200	5	0.5 to 1.5	(Winnicki et al. 2021)
YSZ (Yttria stabilized zirconia)	316L SS	Suspension plasma spraying	~58 to 62	Rockwell diamond	100	15	~6.19 to 6.65	(Łatka et al. 2020)

YSZ	SS	Suspension plasma spraying	70 to 110	Rockwell diamond	200	30	~0.5 to 4.8	(Kozerski et al. 2011)
YSZ & CeYSZ	SS	Suspension plasma spraying	70 to 110	Rockwell diamond	200	30	~2.8 to 5.5	(Łatka et al. 2013)
Pb(Zr, Ti)O_3	Strontium titanate & strontium ruthenate	Powder magnetron sputtering	--	Rockwell conical diamond	25	--	2.32 to 3.02	(Zavareh et al. 2020)
SiO_2	316L SS	Plasma enhanced chemical vapour deposition	0.66	Rockwell C diamond	100, 200 & 800	0.5 to 3	~0.9 to 2.1	(Benayoun et al. 1999)
Al_2O_3	Aluminium alloy (AA3003-H14)	Electrochemical anodization	0.382 to 0.8	Diamond	25 ± 2	~2 N	0.21 to 0.25	(Sarraf et al. 2020)
Al_2O_3	Aluminium alloy (Al5052)	Anodization	6 to 7	Conical diamond	--	~5 N	~0.9	(Sundararajan et al. 2020)
WO_3	Microscope glass	RF reactive magnetron sputtering	0.335 to 0.425	Rockwell sharp spherical diamond	25	~1.2 (maximum)	10.8 to 19.5	(Hasan et al. 2012)

Discussing water-repellant properties, these properties are also concurrently taken into consideration as a notable feature of antifouling coatings along with mechanical properties. Water repellent, i.e., hydrophobic surfaces, are the surfaces that deliver a high value of water contact angle (WCA), due to which the water does not spread onto the surface. Usually, a self-assembled monolayer (SAM) is a high-ordered molecular assembly that spontaneously forms on a surface submerged in a solution of amphifunctional molecules (Mundev and Turyan 1996). A schematic representing the establishment of SAM on the surface of a substrate is shown in Fig. 2.8. SAMs possess excellent characteristics such as stability in chemical and physical properties, outstanding covalent bonding with the surface, minimal thickness and can be easily prepared. SAMs are inherently manufacturable and technologically attractive as a vital tool for surface engineering (Ulman 1996) (Satyanarayana et al. 2005). On a metal oxide surface, three types of molecules are broadly utilized for the formation of SAMs; they are silanes ($RSiX_3$, where $X = Cl$, OC_2H_5, OCH_3), alcohols (ROH) and organometallics (RMgX or RLi). Here R is an alkyl group (Aswal et al. 2006). Due to the stable and dense structure of SAMs, they have been used in many potential applications; one among them is the hydrophobic surface.
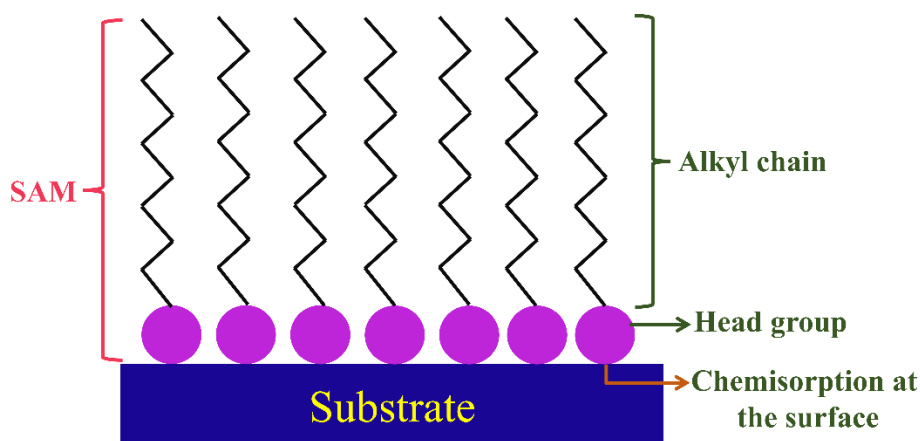
Fig. 2.8: Schematic representing the establishment of SAM on the surface of a substrate.

Octadecyltrichlorosilane (OTS), an organosilane molecule, which is commonly used as a modifier to produce SAM on the surface, which transmutes the hydrophilic surface to the hydrophobic surface and assists in repelling water (Kwak et al. 2010). OTS molecule comprises a long-chained alkyl ($C_{18}H_{37}-$) and a polar head group ($SiCl_3-$

). It has the ability to establish well-arranged SAMs on diverse kinds of substrates and has good substrate coverage ability (Ke et al. 2010) (Pomerantz et al. 1985). OTS-SAMs have good stability due to the covalent bonding with the substrates and the presence of in-plane networks of polysiloxane with the neighbouring molecules within the vicinity of the substrate (Turgman-Cohen et al. 2009). Additionally, fluoro-octyl-trichloro-silane is also often utilized as a substitute due to its (a) higher vapor pressure for vapor-phase deposition and (b) fluorines produce much lower energy surfaces with higher contact angle (better hydrophobicity) (Fan and Stebe 2005) (Reynolds et al. 2010). The most commonly used technique for the development of SAMs of silanes is the wet chemical process, in which the substrates are immersed in a solution containing silane molecules. Apart from wet chemical processing, modification of the surface by the silanes is also performed by vapor phase deposition methods (Schoell et al. 2012) (Jönsson et al. 1985).

2.3.3 Tungsten oxide (WO$_3$) coatings

Tungsten (VI) oxide, also called tungsten trioxide (WO$_3$), is a naturally abundant low-cost transitional metal oxide, possessing low toxicity, high chemical stability, excellent corrosive resistance and environmentally friendliness. Stoichiometric WO$_3$ exhibits transitions in the phase and polymorphism in crystal structure by varying the temperature. Generally, WO$_3$ crystalizes in the form of corner and edge-shared octahedral WO$_6$. Phases of WO$_3$ (in bulk form), namely, monoclinic II (ε-WO$_3$), triclinic (δ-WO$_3$), monoclinic I (γ-WO$_3$), orthorhombic (β-WO$_3$) and tetragonal (α-WO$_3$) are reported to be transformed at temperatures < -43 °C, -43 °C to 17 °C, 17 °C to 330 °C, 330 °C to 740 °C and > 740 °C, respectively, in a sequence. The phase transformation of WO$_3$ with temperature is schematically represented in Fig. 2.9. Among these phases, monoclinic I is stated to be the most steady phase at ambient temperature, and in some cases, triclinic is also noticed. The high-temperature phases, such as orthorhombic and tetragonal of WO$_3$, are incapable of retaining their phases and usually transform into monoclinic I phase during cooling. Hexagonal (h-WO$_3$), a metastable phase, is also synthesized through some chemical techniques. However, this phase is reported to be metastable and transforms into the monoclinic I phase when heated at a temperature > 400 °C. Along with the fore-mentioned phases, another phase

named cubic (c-WO₃) is also noticed, but it is reported to be not commonly found in experiments. The behaviour of phase transition of nanostructured tungsten oxide involves complexity since phase transition is highly dependent on the morphology of the material, which is mainly influenced by the synthesis process and usage of initial precursors (Zheng et al. 2011).

Monoclinic II ▲ → Triclinic II ▲ → Monoclinic I ▲ → Orthorhombic ▲ → Tetragonal
ε-WO$_3$ < –43 to 17°C δ-WO$_3$ 17 to 330 °C γ-WO$_3$ 330 to 740 °C β-WO$_3$ >740 °C α-WO$_3$

Fig. 2.9: Schematic representing the phase transformation of WO₃ with temperature.

Tungsten oxide attained substantial attention as a functional metal oxide over the past 50 years due to its promising combination of crystalline structures, bandgap, optical and electrical properties. This material is extensively used in many applications, such as electrochromic devices, photocatalysis, etc. It is also well known as a solid lubricant applied at elevated temperatures due to its admirable lubrication performance associated with minimal tribo-oxidation sensitivity (Zheng et al. 2011) (Lugscheider et al. 1999). Thin films/coatings of tungsten oxide are also remarkably investigated over the years and utilized in many widespread technological applications such as electrochromic switchable glazing smart windows, pH sensors and photoanodes for water splitting due to its versatile electro and photochromic properties, semiconducting properties, and chemical stableness (Mardare and Hassel 2019). Tungsten oxide coatings also own hydrophilic and gasochromic properties. These coatings are moreover exploited as solid lubricants possessing admirable oxidation stability in atmospheric conditions (Parreira et al. 2007). The application of these films is also extended in multi-layered heat mirror coatings used on building and automotive glasses. Most of the former studies on tungsten oxide coatings emphasized electrochromic, photochromic and gasochromic applications, optoelectronic and iontronic applications, photoelctrocatalytic and optical applications (Mardare and Hassel 2019) (Mehmood et al. 2020) (Hai et al. 2019) (Zhu et al. 2014b). Only limited studies were conducted on the mechanical properties of the tungsten oxide coatings. These coatings are well known for their good wear resistance and hardness (Ziakhodadadian and Ren 2020). It is very essential to have adequate information on mechanical properties like durability of these films on metallic or glass substrates, which are used in practical purposes like

antifouling appliances (Hasan et al. 2012). The earlier reports on the mechanical properties of tungsten oxide films are presented in Table 2.3.

Table 2.3: A summary of the earlier reports on the mechanical properties of tungsten oxide coatings.

Deposition technique	Substrate	Studied mechanical properties	Reference
Electron beam evaporation	Sapphire	Wear and friction	(Greenwood et al. 1999)
DC magnetron sputtering	High speed steel and carbide	Hardness, wear, and friction	(Lugscheider et al. 2000)
Thermal evaporation and magnetron sputtering	ITO-coated glass	Hardness and elastic modulus	(Ong et al. 2001)
DC magnetron sputtering	High speed steel and carbide	Hardness and elastic modulus	(Lugscheider et al. 2001)
RF magnetron sputtering	Silicon	Hardness	(Maillé et al. 2005)
DC magnetron sputtering	SS and high-speed steel	Hardness and Young's modulus	(Parreira et al. 2006)
DC magnetron sputtering	Steel, glass, and silica	Hardness and Young's modulus	(Parreira et al. 2007)
DC magnetron sputtering	High-speed steel	Hardness and Young's modulus	(Polcar et al. 2007)
DC magnetron sputtering	High-speed steel	Hardness, residual stress, wear, and friction	(Polcar and Cavaleiro 2010)
RF magnetron sputtering	Glass	Scratch hardness and wear	(Hasan et al. 2012)
Electrochemical deposition	Austenitic, ferritic, and naval	Hardness, Young's modulus, and wear	(Tesler et al. 2015)

	construction grade SS		
Atomic layer deposition	Silicon	Hardness and Young's modulus	(Mamun et al. 2015)
DC magnetron sputtering	Silicon	Hardness and elastic modulus	(Enriquez-Carrejo et al. 2016)
Chemical vapor deposition	Silicon	Hardness, elastic modulus, and friction	(Ziakhodadadian and Ren 2020)
RF magnetron sputtering	Silicon	Hardness and elastic modulus	(Ramana et al. 2020)
Pulsed laser deposition	Silicon	Elastic modulus	(Besozzi et al. 2019)

SS = Stainless steel

Discussing the surface wettability properties of tungsten oxide coatings, they are inherently hydrophilic in nature. The hydrophilic natured surfaces of tungsten oxide coatings are transformed into hydrophobic surfaces by chemical modification. Tesler et al. in their work observed that the deposited tungsten oxide coatings on SS were superhydrophylic with a water contact angle, WCA of ~ 0 °, due to inherent hydrophilic nature, and they were surface modified with perfluoroalkyl-bearing phosphate to form superhydrophobic surfaces, resulted in an increment of a WCA of 169 ° ± 4 ° (Tesler et al. 2015). In another report, Hui et al. fabricated tungsten oxide coatings on wood surfaces and they were found to be hydrophilic with a WCA of ~ 0 °. The coatings were chemically treated with OTS and post-treatment, the surfaces displayed a WCA of ~ 127 ° and proved hydrophobic behaviour (Hui et al. 2015). In their study, Jiang et al. developed superhydrophobic coatings of OTS-based tungsten oxide coatings on glass substrates with a WCA of 155 ° (Jiang and Guo 2016). In another study, Yang et al. developed perfluorodecyltriethoxysilane-treated tungsten oxide coatings and the surfaces showed hydrophobicity with a WCA ~ 160 ° (Yang et al. 2016). The details are summarized in Table 2.4.

Table 2.4: A summary of WCA before and after surface treatment of tungsten oxide coatings in the previous studies.

WCA (°), before surface treatment	Chemical used	WCA (°), after surface treatment	Reference
~0 °	Perfluoroalkyl-bearing phosphate	169 ° ± 4 °	Tesler et al. 2015
~0 °	OTS	~127 °	Hui et al. 2015
Not reported	OTS	155 °	Jiang and Guo 2016
~10 °	Perfluorodecyltriethoxysilane	~ 160 °	Yang et al. 2016

Commenting on the antifouling properties of tungsten oxide coatings, as mentioned before, the report presented by Tesler et al. is the first study which utilized the combination of accomplished mechanical and water-repellent properties of tungsten oxide coatings for antifouling applications. In this report, mechanically durable and water-repellent tungsten oxide on steel substrate was tested against a green alga named chlamydomonas reinhardtii (model organism) along with an uncoated steel substrate. During the removal from the culture, the tungsten oxide-coated steel sample revealed an instant delamination of 93 ± 6 % of biofilm which resulted in a high clean surface by forbidding the fouling attachment. Whereas a strong attachment of biofilm on the untreated sample was detected with a fouled surface of 99 ± 1 %. The authors concluded that the pioneering idea of utilising these surfaces that offer a supreme combination of pronounced mechanical durability with antifouling properties could be beneficial, particularly in applications that necessitate mechanical actions under severe fouling and environmental conditions (Tesler et al. 2015). In fact, the report by Tesler et al. provides an opportunity to investigate the tungsten oxide coatings developed through various deposition techniques and to explore their application as antifouling coatings.

2.4 Gas-sensors

As stated in the preceding chapter, over the last few decades, due to the rapid growth of industries and urbanization, extreme air pollution which is due to the emission of vast quantities of harmful and pollutant gases from factory productions and automobile exhausts, has developed a significant hazard to the human survival and the environment. Also, leakage of explosive and flammable gases can out-turn in the loss of life as well as property damage (Manohar et al. 2020; Zhu and Zeng 2017). For example, nearly 3.8 million people per year suffer from extreme illnesses that can cause fatality due to air pollution. Furthermore, approximately 20 % of cardiovascular stokes and deaths can be ascribed to household pollution (Schraufnagel et al. 2019). Moreover, extreme air pollution may lead to damage to the lungs. Also, the toxic gases can remarkably hurt the respiratory tract and even can be threatful to the immune and nervous systems. To lessen the potential hazard to human health, these toxic and volatile organic compounds (VOC) gases in the air should be continuously and adequately detected as well as monitored by using effective and reliable gas sensors (Manohar et al. 2020). The applications of gas sensors in various fields are schematically projected in Fig. 2.10.
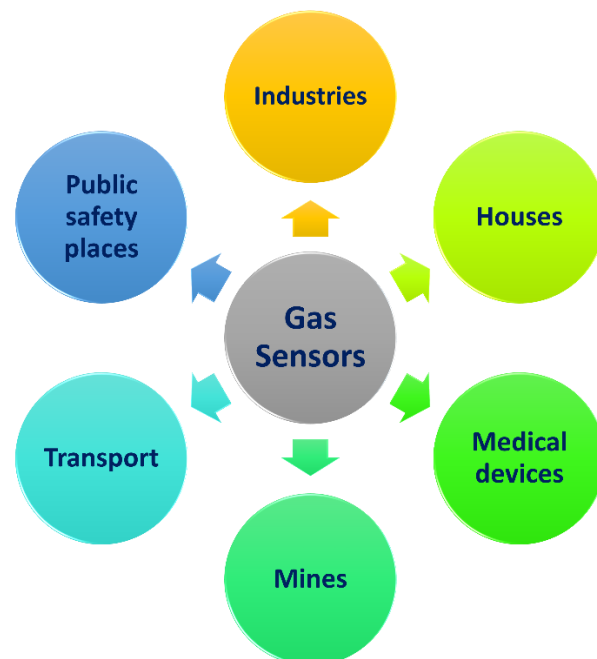
Fig. 2.10: Schematic showing the applications of gas sensors in various fields.

2.4.1 Different types of gas sensors

Over the past 20 years, considerable research has focused on developing gas sensing devices that aim for practical applications ranging from the detection of toxic gases to the monitoring of manufacturing process. Most of the industries are emitting harmful gases enormously; therefore, it has become highly crucial to develop gas-detecting devices. Such devices must permit incessant tracking of the concentration of specific gases in a quantitative and selective mode (Eranna et al. 2004). Also, the gas detection has become extremely vital in mines, public safety paces, and so on (Manohar et al. 2020). Henceforth, several kinds of gas sensors have progressed based on various sensing materials and methods. Many investigations have noticed the reversible interactions among the surface of solid-state material and target gas, which is a characteristic of gas sensors. These interactions between solid and gas can be sensed by measuring the variation in electrical resistance, work function, capacitance, optical, mass characteristics or energy of reaction released during the interaction etc. The variations are recorded through the electrodes, transistors, diode arrangements, optical arrangements, thickness mode transducers etc. In such gas sensing devices, several materials that are developed in the form of porous ceramics (pellets) and thin or thick films can be utilized as active layers. Korotcenkov has defined the gas sensors based on their different sensing measurements and classified them as catalytic combustion gas sensors, electro-chemical gas sensors, infrared absorption gas sensors, thermal conductive gas sensors and semiconducting metal oxide (SMO) gas sensors. A comparison between the mentioned gas sensors has been performed by Korotcenkov and it is presented in Table 2.5 (Korotcenkov 2007).

The SMO gas sensors are acknowledged as the most studied gas sensors compared to others because they satisfy the necessities of an ideal sensor to a decent extent. The SMO gas sensors provide high sensitivity, simplicity in functioning and they are low cost. Additionally, in SMO gas sensors, combining the sensitive element, signal converter and control electronics in the same device can be easily possible, and it markedly simplifies the sensor design, which can be considered as the main advantage of SMO sensors over other gas sensors (Dey 2018; Korotcenkov 2007). The following section focuses on the SMO gas sensors in detail.

Table 2.5: A brief comparison between various kinds of gas sensors (Korotcenkov 2007) (Information from the reference is used with permission from Elsevier).

Parameters	Catalytic combustion gas sensors	Electro-chemical gas sensors	Infrared absorption gas sensors	Thermal conductive gas sensors	SMO gas sensors
Sensitivity	G	G	E	B	E
Accuracy	G	G	E	G	G
Selectivity	B	G	E	B	P
Response time	G	P	P	G	E
Stability	G	B	G	G	G
Durability	G	P	E	G	G
Maintenance	E	G	P	G	E
Cost	E	G	P	G	E
Portability	G	P	B	G	E

B = Bad; P = Poor; G = Good; E = Excellent

2.4.2 Semiconducting metal oxide-based gas sensors

SMO gas sensor is a chemiresistive-type sensor where the change in the electrical resistance of the sensing layer is noticed when it interacts with the target gases. The reactions with the target gas molecules occur at the SMO surface and these reactions alter the density of charge carriers in SMO. In these sensors, the sensing element generally contains a semiconducting oxide deposited on an insulating substrate with two separated metallic electrodes (Au/Pt/Ag). SMO, in the form of a pellet with deposited metallic electrodes on either side, can also be utilized for gas sensing measurements (Korotcenkov 2007).

Discussing the mechanism, as stated earlier, the variation in the electrical resistance in a target gas atmosphere is treated as the primary gas sensing mechanism of the SMO gas sensor. The electrical resistance of the SMO can either enhance or

decline on exposure to the target gas. It relies on the type of dominant charge carriers and the type of gases that interact with the SMO surface. Several SMOs, namely, ZnO, TiO$_2$, Ta$_2$O$_5$, SnO$_2$, In$_2$O$_3$, MoO$_3$, WO$_3$, MgO, ZrO$_2$, Al$_2$O$_3$, Ga$_2$O$_3$ and BaSnO$_3$ display n-type gas sensing characteristics. Other SMOs like CuO, NiO, PdO, Cr$_2$O$_3$, Mn$_2$O$_3$, Co$_3$O$_4$, Y$_2$O$_3$, CeO$_2$, La$_2$O$_3$ and Bi$_2$O$_3$ exhibit p-type gas sensing behaviour (Dey 2018; Korotcenkov 2007; Reddy et al. 2001). The gas sensing mechanism is explained here by considering an n-type SMO. Under normal (ambient) atmospheric conditions, significant oxygen molecules get adsorbed on surface of SMO. Post-adsorption, the oxygen molecules dissociate, and every oxygen atom accepts a charge carrier (electron) from the surface of SMO (if n-type) and forms chemisorbed oxygen species (like O$_2^-$, O$^-$ and O^{2-}). The chemisorbed oxygen species type relies on the operating temperature of the SMO sensor. Generally, molecular (O$_2^-$) species form at room temperature operating conditions or < 150 °C, whereas atomic (O$^-$ and O^{2-}) species occur at high-temperature operating conditions. This results in the decrement of the electron density in SMO and, subsequently, the increment in the electrical resistance of SMO. The electrons can be extracted by adsorbed oxygen molecules only to a specific depth from the SMO surface and it is called Debye length (λ). The layer/region within a Debye length is denoted as the electron depletion layer (EDL) due to the depletion of their charge carriers. At this stage, when the SMO is introduced to a reducing gas, the gas molecules interact with the chemisorbed oxygen species by pulling them from the surface of the SMO. This interaction between gas molecules and chemisorbed oxygen species causes a simultaneous donation of electrons back into the conduction band of SMO, which leads to a decrement in the electrical resistance (Miller et al. 2014; Yu-Feng Sun 2012).

When an n-type SMO is exposed to the reducing gas, the electrical resistance decreases, whereas its electrical resistance increases when it is exposed to the oxidizing gas. In case of p-type SMO, a hole accumulation layer (HAL) will be formed. When the p-type SMO is exposed to a reducing gas, its electrical resistance increases, whereas its electrical resistance declines when it is exposed to an oxidizing gas (Dey 2018; Manohar et al. 2020). The respective variation in the electrical resistance in n-type and

p-type SMOs when exposed to reducing/oxidizing gas is detailed in Table 2.6 (Miller et al. 2014).

Table 2.6: Variation in resistance of n-type and p-type SMOs, when exposed to reducing/oxidizing gas (Miller et al. 2014) (Information from the reference is used with permission from Elsevier).

Gas type	SMO type	
	n-type (ZnO, TiO$_2$, In$_2$O$_3$, SnO$_2$, Ga$_2$O$_3$, Ta$_2$O$_5$, Al$_2$O$_3$, MgO, MoO$_3$, BaSnO$_3$) (Dominant charge carriers: electrons, e$^-$)	p-type (CuO, NiO, PdO, Cr$_2$O$_3$, Mn$_2$O$_3$, Co$_3$O$_4$, Y$_2$O$_3$, La$_2$O$_3$, CeO$_2$, Bi$_2$O$_3$) (Dominant charge carriers: holes, h$^+$)
Reducing gases Examples: NH$_3$, C$_2$H$_5$OH, HCHO, etc.,	Decrease in the resistance	Increase in the resistance
Oxidizing gases Examples: O$_2$, O$_3$, CO$_2$, SO$_2$ etc.,	Increase in the resistance	Decrease in the resistance

The gas response is defined in several ways according to the SMO type (n or p-type) and the gas type (reducing or oxidizing). Most regularly, it is considered as the ratio of the electrical resistance in the presence of air to the electrical resistance in the presence of target gas, i.e., (R_a/R_g), for an n-type SMO with a reducing gas (Miller et al. 2014). In some reports, the gas response is also considered as ((R_a/R_g)-1). It is also denoted in percentage as ((R_a/R_g)-1) × 100 (Pandeeswari and Jeyaprakash 2014). The gas response is considered as (R_g/R_a) or ((R_g/R_a)-1) for an n-type SMO with an oxidizing gas. The ratios are reversed in p-type SMOs. The gas response is a unitless parameter. Gas selectivity is called as the ability of the gas sensor to trace a specific gas in presence of a mixture of gases. The response and recovery times are generally denoted as the time (in seconds) the gas sensor takes for the electrical resistance to attain 90% of its steady-state value post-exposure or exclusion of the target gas, respectively. Operating temperature is termed as the temperature at which the gas

sensor is operated for gas sensing characterizations. The operating temperature can vary from room temperature to 300-500 °C (Dey 2018; Miller et al. 2014).

2.4.2.1 Zinc oxide (ZnO)

Zinc oxide (ZnO) is a typical n-type SMO in group II-VI. It has unique physical and chemical properties like outstanding thermal and chemical stability, high electron mobility, wide band gap of ~3.37 eV, and high bond energy of 60 meV, which put together it as attractive in several potential applications in electronics and optoelectronics. Furthermore, ZnO is attractive because of its non-toxicity, low-cost, ease of synthesis and scalability of production. ZnO exists mostly in the hexagonal wurtzite crystal structure (Kolodziejczak-Radzimska and Jesionowski 2014). ZnO is considered as a typical chemiresistive sensing material. It is also widely used as an SMO gas sensor in the literature to trace numerous kinds of harmful gases, which include ammonia, formaldehyde, hydrogen sulphide, carbon monoxide etc. (Zhu and Zeng 2017). Table 2.7 shows the details of previously examined SMO gas sensors based on ZnO (Zhu and Zeng 2017).

2.4.2.2 Titanium oxide (TiO$_2$)

Titanium dioxide (TiO$_2$), also called titania, is a high-resistance n-type SMO. It has achieved significant attention because of its catalytic properties, chemical stability, environmental friendliness, and the variation in its structural, optical and transport properties. It is widely utilized in many applications, namely, solar cells, photocatalysis and gas sensors. It possesses a band gap of ~3 eV. TiO$_2$ comprises three phases; they are anatase, brookite, and rutile. It is reported that the rutile is the most stable phase, whereas the anatase and brookite phases are reported to be metastable. These phases can be transformed irreversibly to rutile phase at a high-temperature range of 600 to 800 °C. Anatase is noticed as the most broadly used gas sensor because of its eminent capacity of gas reaction and high oxygen vacancy formation. The phase transformation from anatase phase to rutile phase may lead to an extreme decrement in the gas sensing properties. Thus, efforts are being performed to stabilize the anatase phase and restrict its transformation to the rutile phase at higher temperatures. Doping of pentavalent atoms such as Nb, Ta, or trivalent atoms like La to TiO$_2$ prevents the transformation

from the anatase phase to the rutile phase. The similar ionic radii of Nb^{5+} and Ti^{4+} can allow Nb atoms to substitute Ti atoms in the lattice. This replacement results in the inhibition of phase transformation and grain growth (Singh et al. 2012; Tian et al. 2021). Pristine and doped TiO_2 in various forms (nanostructures/thin films) have been utilized to detect various types of gases in the literature (Tian et al. 2021). Table 2.8 presents the details of earlier reported SMO gas sensors based on TiO_2 (Tian et al. 2021).

2.4.2.3 Indium oxide (In_2O_3)

Indium oxide (In_2O_3) is another n-type SMO with excellent features such as low resistivity, broad band gap (3.5 to 3.8 eV) and high catalytic activity. In_2O_3 exhibits three types of crystal structures; they are cubic bixbyite crystal structure (c-In_2O_3), hexagonal corundum crystal structure (h-In_2O_3) and orthorhombic Rh_2O_3(II) crystal structure. Among them, c-In_2O_3 is the most stable structure at ambient conditions, whereas the other structures are stable at only high temperatures and pressures (Liu et al. 2013a). The thin films based on In_2O_3 have been used as transparent conductive electrodes in numerous electronic and optoelectronic devices like liquid crystal displays, solar cells, photovoltaics, and solid electrolyte cells due to their decent electrical conductivity and excellent transmittance in the visible and near-infrared regions (Y. Niu et al. 2022). In the past few years, the gas sensing characteristics of In_2O_3 as an SMO gas sensor have been thoroughly investigated (Shankar et al. 2016). Generally, In_2O_3 exits in a non-stoichiometric form because of native or intrinsic defects such as oxygen vacancies and In interstitials. The basis and nature of these defects primarily rely on the utilized approach during the synthesis. The electrons are released by these defects or vacancies to the conduction band of In_2O_3 and encourage a significant change in the band structure and electrical resistance in contrast to the perfect one. Because of these factors, In_2O_3 has been served widely as a gas sensor (Anand et al. 2016). In the literature, pristine as well as doped In_2O_3 have been utilized to detect several types of gases such as ethanol, acetone, hydrogen sulphide etc. The formerly investigated details of SMO gas sensors based on In_2O_3 are presented in Table 2.9.

Table 2.7: Details such as dopants, morphology, fabrication/synthesis method, target gas and its concentration, operation temperature and gas response of ZnO-based SMO gas sensors (Zhu and Zeng 2017) (Information from the reference is used with permission from Elsevier).

Material	Dopant	Morphology	Method	Target gas	Gas Conc. (ppm)	Operation temp. (°C)	Gas response	Reference
ZnO	--	Flower-like	Hydrothermal	C_2H_5OH	400	350	30.4	(Zhu et al. 2018)
ZnO	--	Nanoparticles	Hydrothermal	NH_3	46	100	3.96 %	(Rawal 2014)
ZnO	--	Quantum dots	Wet chemical	H_2S	68.5	90	567	(Deng et al. 2016)
ZnO	--	Thin film	Sol-gel	NH_3	600	150	57.5 %	(Li et al. 2014)
ZnO	--	Nanofibers	Electrospinning	CH_3NO_2	30	170	29	(Cao et al. 2016)
ZnO	--	3D hierarchical porous	Precipitation	C_2H_5OH	50	250	36.6	(Fan et al. 2015)
ZnO	--	Nanorods	Carbothermal	C_2H_5OH	200	RT	4.24	(Park et al. 2016)
ZnO	--	Nanorods	Spray pyrolysis	H_2S	100	RT	110	(Mani and Rayappan 2015b)

ZnO	--	Nanowires	CVD	C_2H_5OH	20	RT	~10%	(Zou et al. 2016)
ZnO	--	Nanopetals	Chemical precipitation	NO_2	20	RT	~119	(Sonker et al. 2015)
ZnO	--	Nanofibres	Electrospinning	HCHO	100	RT	12.61	(Cui et al. 2016)
ZnO	--	Nanoflates	Hydrothermal	HCHO	100	RT	1.88	(Cui et al. 2016)
ZnO	--	Nanonails	Hydrothermal	H_2S	100	RT	70.4	(Lin et al. 2017)
ZnO	--	Nanoflowers	Hydrothermal	HCHO	100	RT	4.95	(Cui et al. 2016)
ZnO	--	Thin film	Spray pyrolysis	H_2	450	RT	81	(Vijayalakshmi and Gopalakrishna 2014)
ZnO	--	Thin film	Magnetron sputtering	NH_3	100	RT	~300	(Dhivya and Sridharan 2014)
ZnO	Cr	Nanorods	Hydrothermal	C_2H_5OH	400	300	45	(Zhu et al. 2017)
ZnO	Al	Thick film	Sol-gel	CO	80	250	~6	(Dhahri et al. 2016)

ZnO	Ga	Thick film	Sol-gel	CO	80	200	~5.5	(Dhahri et al. 2015)
ZnO	W	Thin film	Magnetron sputtering	HCHO	10	150	~350	(Tesfamichael et al. 2015)
ZnO	Au	Nanoparticles	Sol-gel	HCHO	5	RT	10.57	(Chung et al. 2014)
ZnO	Cu	Nanorods	Hydrothermal	NH_3	100	RT	~30%	(Mhlongo et al. 2016)
ZnO	Co	Thin film	Spray pyrolysis	NH_3	100	RT	3.48	(Mani and Rayappan 2015a)
ZnO	Ni	Nanorods	Spray pyrolysis	H_2S	100	RT	321	(Mani and Rayappan 2015b)
ZnO	Mg	Nanorods	Magnetron sputtering	H_2	200	RT	~30	(Vijayalakshmi and Karthick 2014)
ZnO	La	Thin film	Sol-gel	H_2	1000	RT	51%	(Venkatesh et al. 2014)
ZnO	Ti	Thin film	Spray pyrolysis	H_2S	30	200	0.36	(Shewale and Yu 2016)
ZnO	In	Nanobelts	Thermal evaporation	C_3H_6O	37.5	275	714	(Qi et al. 2015)

RT = Room temperature; CVD = Chemical vapor deposition

Table 2.8: Details such as dopants, morphology, fabrication/synthesis method, target gas and its concentration, operation temperature and gas response of TiO_2-based SMO gas sensors (Tian et al. 2021).

Material	Dopant	Morphology	Method	Target gas	Gas Conc. (ppm)	Operation temp. (°C)	Gas response	Reference
TiO_2	--	Nanoparticles	Hydrothermal	C_3H_6O	500	270	9.19	(Navale et al. 2018)
TiO_2	--	Nanoflowers	Hydrothermal	C_3H_6O	700	60	66.58	(Bhowmik et al. 2016)
TiO_2	--	Nanotubes	Electrochemical anodization	C_2H_5OH	100	150	75.4%	(Gakhar and Hazra 2020)
TiO_2	--	Nanorods	AVO	O_2	40000	RT	1.68	(Wang et al. 2016)
TiO_2	--	Nanosheets	--	C_3H_6O	200	400	21.6	(Ge et al. 2020)
TiO_2	--	Thin film	Blade coating	H_2S	5	200 (UV)	6	(Chinh et al. 2019)
TiO_2	--	Nanoflowers	Hydrothermal	C_2H_5OH	400	350	22.9	(Gao et al. 2017)
TiO_2	--	Nanoflowers	Hydrothermal	C_2H_5OH	100	RT	24	(Wang et al. 2020b)

TiO$_2$	Nb	Thin film	Sol-gel	CO	250	400	1.1	(Duta et al. 2016)
TiO$_2$	Fe	Nanopowders	MCBM	H$_2$	500	270	94.5%	(Eadi et al. 2017)
TiO$_2$	Y	Thin film	Spray pyrolysis	NH$_3$	300	150	1.31	(Gopala Krishnan et al. 2018)
TiO$_2$	Y	Nanoparticles	Sol-gel	C$_2$H$_5$OH	100	RT	225.46	(Nithya et al. 2019)
TiO$_2$	Sn	Nanoparticles	Hydrothermal	C$_3$H$_6$O	100	240	21.19	(Zhang et al. 2019)
TiO$_2$	W	Nanoporous	Hydrothermal	C$_3$H$_6$O	500	240	173.67	(Wang et al. 2020a)
TiO$_2$	Ni	Nanoparticles	Co-precipitation	H$_2$	10000	600	73%	(Fomekong et al. 2020)
TiO$_2$	Cr	Nanotubes	Anodization	NO$_2$	100	500	3.5	(Gönüllü et al. 2015)
TiO$_2$	F	Nanosheets	Hydrothermal	C$_3$H$_6$O	400	RT	12.5	(Feng et al. 2020)
TiO$_2$	Fe	Nanotubes	Anodization	H$_2$S	50	100	32.5	(Tong et al. 2020)

RT = Room temperature; AVO = Acid vapor oxidation; MCBM = Mechanochemical ball milling.

Table 2.9: Details such as dopants, morphology, fabrication/synthesis method, target gas and its concentration, operation temperature and gas response of In_2O_3-based SMO gas sensors.

Material	Dopant	Morphology	Method	Target gas	Gas Conc. (ppm)	Operation temp. (°C)	Gas response	Reference
In_2O_3	La	Nanowires	Nanocasting	HCHO	10	210	39.51	(Y. Niu et al. 2022)
In_2O_3	--	Thin film	SG & HVTE	NO_2	0.7 to 7	250	NR	(Cantalini et al. 2000)
In_2O_3	--	Thin film	SG	CO/H_2	1000	350	44/88	(Chung et al. 1998)
In_2O_3	Sn	Thin film	MS	H_2	1000	300	0.008	(Yoo et al. 2005)
In_2O_3	Sn	Thick film	PBI-screen-printing	NO	1200	210	~15	(Mbarek et al. 2007)
In_2O_3	Sn	Thick film	PBI-screen-printing	NH_3	1000	120	~4.25	(Mbarek et al. 2006)
In_2O_3	Sn	Thick film	PBI-screen-printing	C_7H_8	NR	RT	~4 to5%	(Maslik et al. 2018)
In_2O_3	--	Nanowires	Electrospinning	C_3H_6O	100	200	37.9	(Che et al. 2021)
In_2O_3	Mn	Nanoparticles	Co-precipitation	CH_3OH C_2H_5OH	50	300 300	~17 ~23	(Anand et al. 2016)

				NH$_3$		400	~3.5	
				LPG		400	~8	
				C$_3$H$_6$O		350	~15	
In$_2$O$_3$	Sn	Nanoparticles	Combustion	C$_2$H$_5$OH	1000	200	24	(Ayeshamariam et al. 2014)
In$_2$O$_3$	Fe	Nanospheres	OSI	C$_2$H$_5$OH	100	350	133	(Chen et al. 2019)
In$_2$O$_3$	Pr	Nanoparticles	Solvothermal	C$_2$H$_5$OH	50	240	106	(Ma et al. 2020)
In$_2$O$_3$	Ag	Nanoparticles	SG	HCHO	25	100	~28	(Wang et al. 2009)
In$_2$O$_3$	Ce	Microspheres	Hydrothermal	C$_3$H$_6$O	200	250	~42	(Wei et al. 2018)
In$_2$O$_3$	Pb	Nanoparticles	Sonochemical	C$_2$H$_5$OH	100	250	~33	(Montazeri and Jamali-Sheini 2017)
In$_2$O$_3$	--	Thick film	PBI-screen-printing	H$_2$S	200	150	~58	(Kulkarni and Borse 2011)

RT = Room temperature; NR = Not reported: SG = Sol-gel; HVTE = High vacuum thermal evaporation; MS = Magnetron sputtering: PBI = Particle-based ink; OSI = One-step impregnation.

2.5 Perovskite metal oxides

Perovskite is the general name for a mineral called calcium titanium oxide ($CaTiO_3$) which was initially discovered in the mid-19th century in the Ural Mountains. Lev Perovski, a mineralogist, is the root for the name 'perovskite'. Meanwhile, the term 'perovskite' has been utilized to denote the materials that exhibit similar crystal structure of $CaTiO_3$. A schematic representation of the $CaTiO_3$ crystal structure is displayed in Fig. 2.11. It must be noted that $CaTiO_3$ indicates the perovskite crystal structure but not the composition of $CaTiO_3$. In detail, these perovskites have a common stoichiometry of ABX_3. Here, the sites A and B denote different cations; the elements in the A site are mostly rare earth or alkaline earth metals, whereas the elements in the B site are transition metals. Moreover, the site X signifies the anions. Usually, most of the common perovskites are metal oxides (here X = O), also other halogens (Br, Cl, F, I) and chalcogens (S, Se, Te) are also possible (Bhalla et al. 2016; Postiglione and Leighton 2017). It has been reported that, due to the structural features of perovskite oxides, nearly 90% of metallic elements from the periodic table can possibly be included solely or partially at the A or B sites of perovskite oxides without disrupting their crystal structure. Because of many probable elemental combinations and the exhibition of a broad range of properties such as ferroelectricity, piezoelectricity, ferromagnetism and photoelectrochemical sensitivity etc., research interest on perovskite oxides has emerged vastly. Perovskite oxides are utilized widely in many technological applications, which comprise gas sensors, transparent electronics, thermoelectrics, solid oxide fuel cells, photocatalysis etc.(Liu et al. 2013; Postiglione and Leighton 2017; Zhu et al. 2014a).
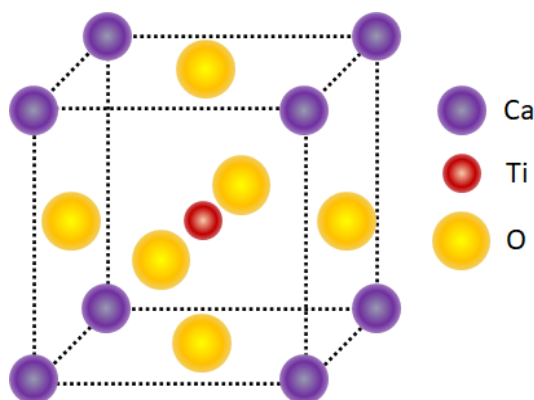

Fig. 2.11: Schematic representation of the $CaTiO_3$ crystal structure.

Perovskite oxides (ABO_3) contain a fundamental and functional unit cell, which has a corner-sharing BO_6 octahedra with a central B atom of transition metal cations surrounded by six oxygen ligands. Any changes in the shape (unequal B–O bonds number), size (B–O bond lengths) and connectivity (pattern and magnitude of octahedral rotations) of octahedral units offer access to a broad range of multifunctional properties. The ABO_3 perovskite structure is basically assembled by tiling the vital BO_6 octahedral blocks on the Cl site in a simple cubic CsCl structure. The A site cations are at the Cs sites in this cubic CsCl structure. The absence of octahedral distortions and rotations produces the cubic perovskite structure. In this structure, the A site cation is generally twelve-fold coordinated, whereas the B site cation is six-fold coordinated with oxygen anions. Here, the reported bottom limits for the cation radii r_A is greater than 0.09 nm, while r_B is greater than 0.051 nm (Rondinelli et al. 2012; Zhu et al. 2014a). Moreover, relying on the comparative size of the constituent atoms, the BO_6 octahedra can tilt to employ the space efficiently and to minimize lattice energy. This phenomenon leads to the generation of perovskites with non-cubic symmetric structures, which has an extreme impact on the properties of the perovskites. Apart from the cubic crystal structure, orthorhombic and rhombohedral are also detected crystal structures in perovskites; besides, tetragonal and hexagonal crystal structures are noticed as well (Postiglione and Leighton 2017; Rondinelli et al. 2012).

2.5.1 Alkaline earth stannates

Conducting oxides are broadly studied for their potential applications in the technological fields comprising transparent electrodes, gas sensors, superconductors, etc. Choosing suitable materials necessitates a decent familiarity of electronic properties like transport properties and their relations with structural features and chemical composition (Trari et al. 1994). One of the significant material features for numerous oxide applications is high carrier mobility (μ) at room temperature. Indeed, a high electron mobility perovskite oxide would indisputably perceive widespread application as electrically conducting oxide in many electronic devices. Earlier, some perovskites, such as strontium titanate ($SrTiO_3$), have been utilized as the n-type conducting oxides, but its conduction band minimum (CBM) is mostly obtained from localized Ti 3d states, that causes high electron effective mass and subsequently

minimal μ in doped SrTiO$_3$. In order to develop a perovskite conducting oxide with relatively better μ, the CBM of SrTiO$_3$ should be modified so that the CBM encompasses extra delocalized atomic characters like the 's' character. It can be accomplished by replacing Ti in SrTiO$_3$ (at the B site) with an alternative group IV element which contains small s orbital energy. A respectable choice for this is to substitute Ti with Sn. For the element Sn, the 5s orbitals are at relatively low energy levels. Hence it causes the hybridization of Sn 5s and O 2p orbitals, which generate the anti-bonding states at CBM. It origins comparatively more electron density and significantly lower electron effective mass (m*) than the other perovskite oxides with 'd' state conduction bands (Liu et al. 2013b; Postiglione and Leighton 2017).

Discussing perovskite-type alkaline earth stannates, they have a common formula, ASnO$_3$ (where A = Ba, Sr, and Ca) (Stanulis et al. 2012). In ASnO$_3$ perovskites, the valence band maximum (VBM) is made up mainly from O 2p energy levels and the CBM comprises Sn 5s energy levels that are separated by forbidden band energy of minimum 3 eV (Zidi et al. 2010).

2.5.2 Barium stannate (BaSnO$_3$)

Barium stannate, BaSnO$_3$ (BSO), is an n-type semiconducting material from the family of alkaline earth stannate. It is a vital metal oxide material in pure and also in doped forms. BSO possesses electrical resistivity of >10^6 Ω-cm at room temperature. The optical energy band gap of BSO was reported to be 3.1 eV (indirect band gap). These properties aid in the usage of this material in gas sensors and optoelectronic applications (Deepa et al. 2011). BSO usually exists in an ideal cubic perovskite crystal structure with a space group Pm$\overline{3}$m at room temperature. In the crystal structure, the A site is occupied by Ba^{2+} cations and the B site is engaged by Sn^{4+}, forming the SnO$_6$ octahedra. The lattice parameter of BSO is ~ 4.1 Å. BSO is stable up to high temperatures (~1000 °C). It exhibits low thermal expansion of 0.93 to 0.96 × 10^{-5} K^{-1}. These thermoelectric properties generate BSO as a versatile material in numerous high temperature, high power applications (Postiglione and Leighton 2017; Yasukawa et al. 2010). According to the Drude model, μ has an inverse relation with m*. The decrement in the m* leads to the increment in the μ. It is reported that BSO owns Sn 5s – O 2p antibonding orbitals with m* (Postiglione and Leighton 2017). The μ and electrical

conductivity (σ) of doped n-type BSO can be dramatically improved because of its small m*. One of the broadly investigated dopants in BSO is La. The dopant La^{3+} substitutes the element Ba^{2+} (A site) and forms a stable ion with a +3-oxidation state. The dopant La can donate one extra electron to the conduction band (CB) of BSO; henceforth, it is termed an electron donor. $La_xBa_{1-x}SnO_3$ (LBSO) shows n-type conduction because of the existence of one extra electron from dopant La. Replacing Ba with La mostly conserves the 's' character of the CB, hence preserving the high μ of the host material. BSO doped with a few % of La has been reported with a high μ of 320 $cm^2V^{-1}s^{-1}$, which is the maximum value attained in perovskite oxides. The σ was enhanced up to 10^5 S m^{-1} by La doping (Kim et al. 2012; Li et al. 2017). The details of previously reported studies which demonstrated the σ of LBSO (thin film/bulk), developed through various processing techniques, are represented in Table 2.10. Generally, in the case of bulk (pellets), σ would be strongly dependent on the porosity. Noteworthy that the mere mentioning of the density measurements via Archimedes's principle is a wrong practice. For all such sintered pellets, density measurements must be carried out as per the guidelines given in **ASTM C20** or **ASTM C373**.

While La is utilized in BSO as the typical 'A' site dopant, the most investigated 'B' site dopant is Sb. Here, Sb^{5+} replaces Sn^{4+} in the B site and contributes one extra electron to the CB, producing an n-type conductor. Sb-doped BSO (BSSO) exhibited much inferior μ than LBSO. BSSO single crystals exhibited an μ of ~ 80 $cm^2V^{-1}s^{-1}$ at a carrier concentration of ~ 1×10^{20} cm^{-3} (Mizoguchi et al. 2013). The decrement in the μ is because of the enhancement of the scattering effect by the dopant Sb. It is reported that the dopant La does not make any impact on the distortion of SnO_6 octahedra, whereas the dopant Sb makes the distortion which disturbs the conduction pathway. It is also stated that further scattering mechanisms are generated in the form of defect-complex neutral impurities or in the form of ionized impurities (Kim et al. 2013). In his study, Slassi calculated the formation energies (E_f) of LBSO and BBSO. Generally, the most stable structure contains low formation energy. It is observed that LBSO possesses E_f of ~ –0.63 eV, which proves that LBSO system has more stability than pure BSO. The noticed E_f of BBSO system is ~ +0.46 eV, which shows that BBSO system is relatively less stable than pure BSO (Slassi 2015).

Table 2.10: Details of previous reports which showed the electrical conductivity of LBSO that are developed through various processing techniques.

Processing technique	Processing conditions	Thin films/bulk	Conductivity (S cm^{-1})	Reference
Sol-gel	800 ℃ (Rapid thermal annealing)	Thin film	~ 6.6	(Shan et al. 2014)
Pulsed laser deposition	630 ℃ (Deposition pressure: 0.375 mTorr of O_2)	Thin film	9	(James et al. 2015)
Pulsed laser deposition	750 ℃ (Deposition pressure: 0.1 Torr of O_2)	Thin film	4928	(Kim et al. 2012)
Pulsed laser deposition	850 ℃ (Deposition pressure: 1 mTorr of O_2)	Thin film	1707	(Sallis et al. 2013)
RF magnetron sputtering	800 ℃ (RF power intensity: 2.5 W/cm^2, Deposition pressure: 20 mTorr of Ar and O_2)	Thin film	444	(Luo et al. 2016)
Chemical solution deposition	1000 ℃ (Film annealed in N_2 atmosphere)	Thin Film	555	(Wei et al. 2015)
Polymerized complex method	1000 ℃ (Spark plasma sintering)	Bulk	330 - 660	(Yasukawa et al. 2010)
Solid state reaction	1300 ℃ (Solid state sintering)	Bulk	0.7	(Luo et al. 2015)

Solid state reaction	1300 ℃ (Solid state sintering)	Bulk	~ 1.5 x 10^{-3}	(Ansaree and Upadhyay 2015)
Solid state reaction	1352 ℃ (Solid state sintering)	Bulk	~ 1.2 x 10^{-4}	(Upadhyay et al. 2004)
Solid state reaction	1300 ℃ (Solid state sintering)	Bulk	~ 2 x 10^{-3}	(Upadhyay and Kavitha 2007)

2.6 Objectives of the present study

- To develop spray pyrolyzed tungsten oxide thin films on stainless steel and glass substrates through the thermal decomposition process.

- To fabricate facile solution-combustion synthesized, doped zinc oxide, doped titanium oxide, and co-doped indium oxide-based thin films, respectively, by spin coating method on glass substrates.

- To formulate screen-printable particle-free aqueous combustible inks and to develop mono-doped and co-doped indium oxide-based screen-printed films on glass substrates.

- To synthesize La-doped barium stannate-based metal oxides through the polymerized complex method.

CHAPTER 3

FABRICATION AND CHARACTERIZATION OF THERMAL DECOMPOSITION PROCESSED SPRAY PYROLYZED SCRATCH-RESISTANT, HYDROPHOBIC TUNGSTEN OXIDE (WO₃) FILMS ON STEEL AND GLASS SUBSTRATES

3.1 Introduction

This chapter deals with the tungsten oxide (WO_3) films deposited on stainless steel (SS) substrates and glass substrates, respectively, through a facile spray pyrolysis method using a low-cost equipment. Initially, the thermal behaviour of the precursor is inspected in this study. The appropriate temperature for the successful fabrication of the films is examined and after the examination, the films are fabricated at that particular temperature. After the fabrication, the scratch hardness of the respective films on SS and glass substrates is inspected and it is compared with the scratch hardness of the uncoated substrates. The films are chemically treated with octadecyltrichlorosilane (OTS) for the conversion from hydrophilic to hydrophobic nature; the wettability properties of the films before and after chemical treatment are studied through water contact angle (WCA) measurements.

3.2 Experimental procedure

3.2.1 Materials

All the reagents were of analytical grade and utilized without additional purification. Tungsten hexachloride (WCl_6) (Sigma-Aldrich), 2-methoxyethanol ($C_3H_8O_2$) (Molychem), toluene (C_7H_8) (Molychem) and octadecyltrichlorosilane ($C_{18}H_{37}Cl_3Si$) (Sigma-Aldrich) were used in this study.

3.2.2 Preparation of precursor and its characterization

1 g of WCl_6 was dissolved in 20 ml of $C_3H_8O_2$ and allowed to stir (at 250 rpm) for 30 min at room temperature to achieve the precursor with a concentration of 0.05

g/ml (0.1 M). To find the thermal response of the precursor, thermogravimetric analysis (TGA, PerkinElmer, Thermo-Gravimetric Analyser TGA 4000), differential scanning calorimetry (DSC, NETZSCH-DSC-404F1) were performed from the room temperature to 450 °C at a heating rate of 10 °C/min in the nitrogen atmosphere.

3.2.3 Fabrication of the WO$_3$ film on SS substrate

Polished 316L SS (stainless steel) substrates were initially washed with aqueous detergent and ultrasonically cleaned for 10 min, respectively, in de-ionized water followed by acetone and later dried under the nitrogen gas flow. Before depositing the film, the substrates were preheated at a temperature of 400 °C. The prepared precursor was deposited on the preheated substrate through the spray pyrolysis method using a low-cost and simple spray gun. During the spraying process, a distance of 10 cm was kept between the substrate and the spray gun. The precursor was continuously sprayed for 5 s. An intermediate annealing time of 2 min was maintained after every spray for simultaneous film formation and by-product gases evaporation. This way, the precursor was sprayed ten times on the substrate. After spraying, the WO$_3$ film was annealed at 400 °C for 2 h. During preheating the substrate, spraying the precursor, and annealing the film, the substrate temperature was regularly cross-checked with an infrared thermal gun and the substrate temperature was maintained at nearly 400 °C. A solution comprising a 15 ml quantity of toluene with 450 μl quantity of OTS was prepared and it was maintained at a temperature of 6 °C. The fabricated film was immersed in the solution for 3 h. Post immersion, the film was taken out and thoroughly rinsed with the toluene. Finally, the film was further dried with the help of nitrogen gas.

3.2.4 Characterization of the WO$_3$ film on SS substrate

The fabricated film was examined under PANalytical multi-purpose high-resolution XRD (Empyrean) utilising Cu Kα radiation source (1.54 Å) with a step size of 0.06° and a grazing angle of 3° to inspect the crystal structure of the film. An X-ray photoelectron spectroscopic study (XPS, Kratos Axis Ultra DLD) was executed to inspect the chemical state of the elements on the surface of the film. The calibration of the obtained spectra was performed by using the C-H peak of adsorbed carbon located at a binding energy of 284.6 eV. The fitting of the spectra was performed with XPS

curve fitting software (XPSPEAK41). During the fitting, the full-width half maximum (FWHM) and the Gaussian/Lorentzian (G/L) ratio were fixed, and the minimum chi-square was selected after subtracting the Shirley background. The details of fitting parameters are provided in Appendix I. Atomic force microscopy (AFM, Innova SPM) was engaged to observe the surface topography and estimate the surface roughness of the film, and the scanning area used was 2×2 μm. A scratch hardness tester (LINEARTESTER-249, Erichsen) with variable normal loads of 5 N, 10 N and 15 N was used for scratch testing the coated and uncoated SS substrates. A gap of 0.5 cm was maintained between each scratch. Here, the indenter with a tip diameter of 1 mm, made of tungsten carbide, was drawn at 25 mm s^{-1}, and the drawing speed was kept constant. The test was performed according to the ASTM G171-03 standard. Scanning electron microscopy (SEM, JSM 6380, JEOL) was used to explore the surface morphology of the fabricated film and to measure the scratch width. The average grain size of the film was estimated by randomly selecting 150 grains on the surface of the film obtained in the SEM image with the help of ImageJ software. The elemental composition of the film was examined through the energy dispersive X-ray analysis (EDAX, AMETEK). The thickness of the film was measured through field emission scanning electron microscopy (FESEM, GeminiSEM 300) in cross-section mode. To investigate the surface wettability, the WCA of the film was measured before and after OTS chemical treatment by dropping de-ionized water of 1 μl quantity on randomly selected places on the film, with the help of contact angle system (Krüss, Drop Shape Analyzer, DSA 100). Further, the OTS-treated film was stored in an ambient atmosphere for 100 days, and the surface wettability was re-analyzed after the mentioned period to inspect the stability. The sessile drop mode was utilized to measure all the WCAs.

3.2.5 Fabrication of the WO$_3$ films on glass substrates

Soda-lime-silica glass substrates (Blue Star; thickness ~1 mm) were properly cleaned with soap water, followed by cleaning with de-ionized water. For further cleaning, the substrates were immersed in the solution comprising 50 ml of de-ionized water, 10 ml of liquid ammonia and 10 ml of hydrogen peroxide, and later the solution was heated at 70 °C for 15 min. By spray pyrolysis technique, the

precursor was sprayed as fine droplets through a low-cost and simple spray gun on the glass substrates maintained at 400 °C on a hot plate. Similar spraying parameters were used as mentioned previously, i.e., a distance of 10 cm was maintained between the spray gun nozzle and the substrate. The solution was sprayed for 5 s and after every spray, a gap of 2 min was maintained for the formation of film and evaporation of by-product gases. In this manner, the solution was sprayed 5, 10 and 15 times, respectively, on three different glass substrates. After spraying, the substrates were annealed at 400 °C for 2 h. The fabricated films were submerged in the solution consisting of 15 ml of toluene and 450 µl of OTS for 3 h at 6 °C, as stated previously. Later, the films were thoroughly rinsed with toluene and dried under nitrogen gas. The schematic representation of fabricating WO_3 film on SS/glass substrates is shown in Fig. 3.1.
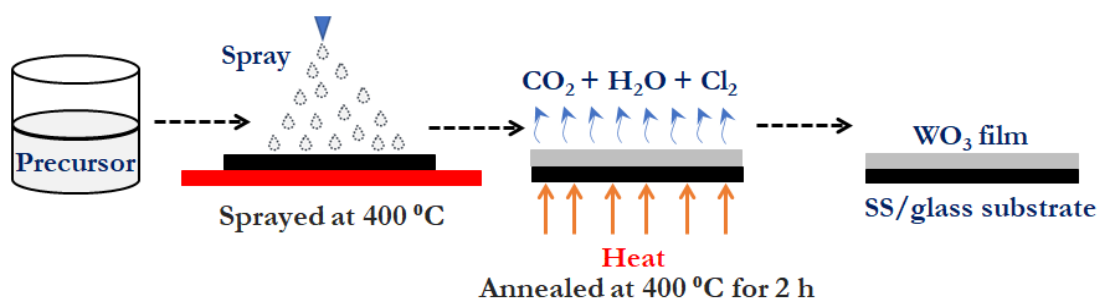
Fig. 3.1: Schematic representation of fabricating WO_3 film on SS/glass substrates.

3.2.6 Characterization of the WO₃ films on glass substrates

For structural characterization, the fabricated films on glass substrates were inspected under the X-Ray diffraction technique (XRD, JEOL-JPX 8) by Cu Kα radiation source (1.54 Å) with a step size of 0.02º and a scanning rate of 2º min^{-1}. The surface topography and roughness of the films were assessed by atomic force microscopy (AFM, Innova SPM). The average grain size of the films was measured with ImageJ software by choosing 30 grains randomly from their corresponding AFM image. UV-visible spectrometer (Shimadzu UV-3600 Spectrophotometer) was utilised to examine the transparency of the films in the visible region. The thickness of the films was measured by using a near normal spectroscopic reflectometer (HO-NNSR-01). X-ray photoelectron spectroscopic studies (XPS, Kratos Axis Ultra DLD) were performed

to examine the chemical state of elements on the surface of the films. The resultant spectra were calibrated by the C-H peak of adventitious carbon located at the binding energy of 284.6 eV. The fitting of the spectra was carried out using XPS curve fitting software (XPSPEAK41) by fixing the Gaussian/Lorentzian (G/L) ratio and the full-width half maximum with the selection of minimum chi-square after the subtraction of Shirley background. The details of the fitting parameters are given in Appendix II. The scratch test was conducted on the films as well as on the uncoated glass by using a scratch hardness tester (LINEARTESTER-249, Erichsen). In this test, a stylus tip indenter of tungsten carbide with a 1 mm tip diameter was drawn on the films at a steady speed of 25 mm s^{-1} with varying normal loads of 5, 10 and 15 N side by side with a gap of 0.5 cm (as mentioned previously). Scratch width on the films and surface morphology of the films were inspected under scanning electron microscopy (SEM, JSM 6380, JEOL). The surface wettability of films before and after treatment with OTS was assessed by measuring the WCA with 1 μl of de-ionized water on different areas on the films by using contact angle system (Krüss, Drop Shape Analyzer, DSA 100). The OTS-treated films were stored for a year in an ambient atmosphere. Later, the WCA of these one-year stored OTS-treated films were re-inspected to observe the stability. All the WCAs were measured in the sessile drop mode.

3.3 Results and discussion

3.3.1 Thermal analysis of the precursor

To understand the thermal behaviour of the precursor, thermal analysis (TGA and DSC) is performed. The TGA curve, its derivate DTG, and the DSC curve are subdivided into four regions with respect to temperature. They are named as region I (32 °C to 165 °C), region II (165 °C to 206 °C), region III (206 °C to 290 °C) and region IV (290 °C to 450 °C). Fig. 3.2 (a) shows the TGA and DTG curves of the precursor. The region I is accompanied by a 24.5 % major weight loss in the TGA curve and a broad peak in the DTG curve, and it can be credited to the evaporation of the solvent. A minor weight loss of 2.4 % is observed in the region II of the TGA curve with no peak in the DTG, and it can be dedicated to the release of organic residues present in the precursor. In the next region, i.e., region III, another major weight loss of 14.4 % is detected with a sharp peak at 230 °C in the DTG curve. It can be ascribed to the thermal

decomposition of the precursor and formation of the respective oxide (WO_3) with the release of by-product gases. Further, in the region IV, no noticeable weight loss or change in the TGA and DTG curves is observed with a 58.5 weight % of retained material.
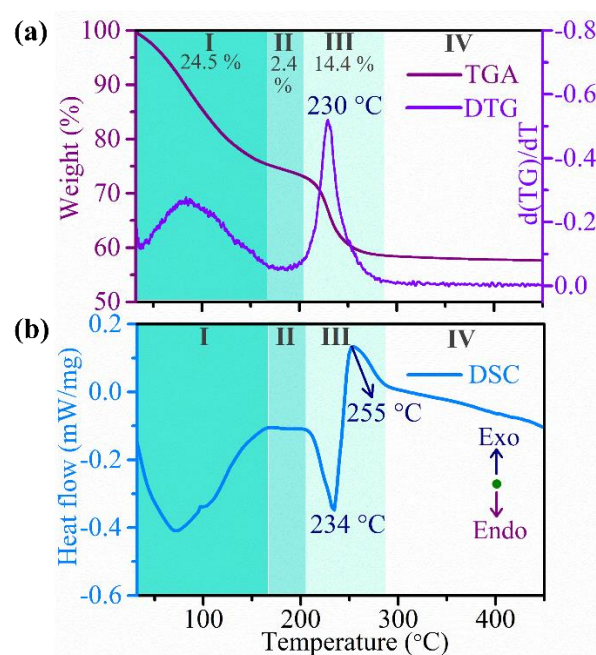
Fig. 3.2: (a) TGA, DTG and (b) DSC thermal curves of the precursor.

Fig. 3.2 (b) displays the DSC curve of the precursor. The region I has comprised a broad endothermic peak, which can be dedicated to the evaporation of the solvent, and it is in accordance with TGA/DTG curves. Further, no substantial change in the DSC curve is detected in the region II. A sharp endothermic peak is found at 234 °C in the region III, and it can be attributed to the thermal decomposition of the precursor and the formation of the oxide (WO_3). It is observed that the temperature for the thermal decomposition of the precursor (~230 °C) is almost the same, though they are exposed separately from TGA/DTG and DSC thermograms. In the region III of the DSC curve, after the endothermic peak, an exothermic response is also found at the temperature of 255 °C, which could have resulted from the crystallization of the WO_3. It can be concluded from the thermal analysis that thermal decomposition followed by crystallization of the precursor has occurred in the region III, i.e., 206 °C to 290 °C.

3.3.2 Analysis of the WO₃ film on SS substrate

Fig. 3.3 displays the schematic representation of the probable WO_3 film formation mechanism on the SS substrate. During the initial spraying of precursor for 5 s, presumably, the droplets might be in a wet condition and have spread quickly on the surface of the SS substrate due to the high surface tension of SS (Chen et al. 1996). During the intermediate annealing of 2 min, as the underlying SS is in the preheated state, the droplets might have thermally decomposed into WO_3 with the release of by-product gases, as presented in equation 3.1.

$$WCl_6 \xrightarrow[\text{air}]{\Delta\ 400\ °C,} WO_3 + Cl_2\uparrow \qquad (3.1)$$
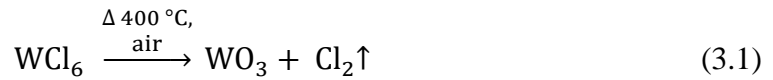
The resultant initial layer might be discontinuous and porous due to the escape of by-product gases. During the second spray, the droplets might have spread on the initial layer, and some of the droplets might have penetrated the discontinued areas and pores by capillary action. These droplets might have thermally decomposed into WO_3 and formed a stacked-layer above, during intermediate annealing time. Therefore, the previously arisen defects are rectified in this manner (Chen et al. 1996). This process might have continued till ten sprays, and the layers might have stacked one above the other, as shown in Fig. 3.3. In the last stage of annealing for 2 h, the stacked layers might have combined during the provided annealing time and temperature, and consequently might have formed a WO_3 film on the SS substrate, as shown in Fig. 3.3.
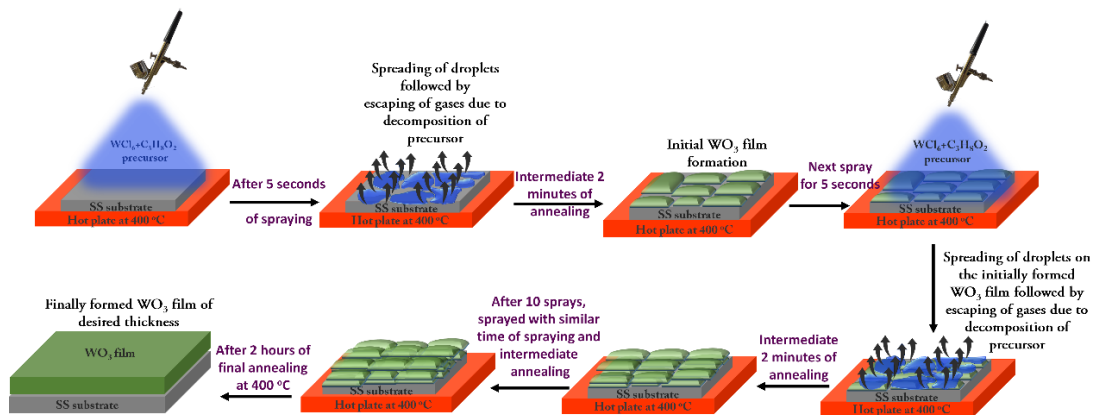

Fig. 3.3: Schematic presentation of the plausible WO₃ film formation mechanism on SS substrate through spray pyrolysis.
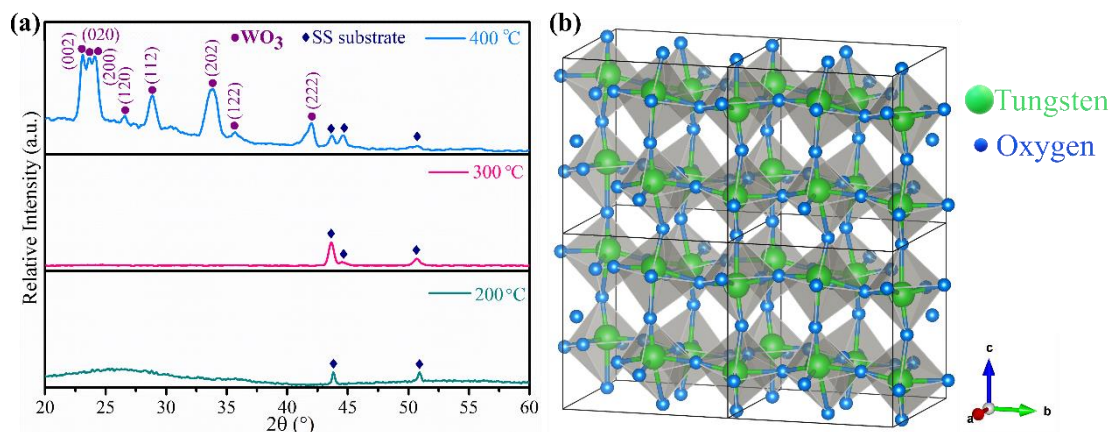
Fig. 3.4: (a) GIXRD patterns of the films fabricated at 200 °C, 300 °C and 400 °C, (b) schematic representation of the monoclinic crystal structure of WO_3. (The crystal structure is drawn using the VESTA visualization interface software and the crystallographic information file is taken from the Materials Project database (mp-19033)).

The GIXRD pattern of the fabricated film at 400 °C is presented in Fig. 3.4 (a). It is perceived from the diffraction pattern that the film fabricated at 400 °C is predominantly crystalline in nature. The obtained diffraction planes, namely, (002), (020), (200), (120), (112), (202), (122) and (222), are coinciding well with the monoclinic structured WO_3 (ICDD: 00-043-1035). The diffraction pattern also exhibited a high intensity along the (002) plane, which can be considered as the preferred growth direction. An alike diffraction pattern with a pre-dominant triplet of (002), (020) and (200) planes of monoclinic WO_3 is also stated in the previous report (Sivakumar et al. 2004). The XRD pattern also showed certain diffraction planes at 2θ values 43.6°, 44.6° and 50.6°, and they belong to the diffraction planes of beneath SS substrate. The non-appearance of diffraction planes from the secondary phases supports the establishment of a pure WO_3 phase. In the current study, the annealing temperature of 400 °C is above the thermal decomposition and crystallization temperatures (~230 °C and 255 °C, respectively) of the precursor (in bulk form) (depicted from the TGA/DTG and DSC analysis, Fig. 3.2). At this annealing temperature, the spray-deposited precursor on the substrate have received necessary thermal energy for the decomposition and crystallization, sequentially. In this work, the films fabricated with the same procedure at 200 °C and 300 °C displayed a complete amorphousness (shown

in Fig. 3.4), and it is ascribed to the deficiency of sufficient thermal energy for crystallization. The attained results are appropriately coinciding with the formerly reported studies, which recommend that the required fabrication temperature for achieving the crystalline WO_3 phase in the films is ~ 400 °C. Ozkan et al. have stated in their report that at the temperature of 390 °C, monoclinic structured WO_3 has started to crystallize from the amorphous phase (Ozkan et al. 2003). Similarly, Rougier et al. have specified that WO_3 crystallization is generally reported in the temperature range between 350 to 400 °C (Rougier et al. 1999). In addition, Zheng et al. have stated in their study that amorphous WO_3 forms at a temperature of less than 300 °C, whereas the monoclinic WO_3 phase dominates when the temperature is raised above 300 °C (Zheng et al. 2011). A pictorial representation of the monoclinic crystal structure of WO_3 is presented in Fig. 3.4 (b).

The WO_3 film fabricated at 400 °C (henceforward called as WO_3 film) is examined under SEM, and it displayed a dense, continuous, uniform, and granular morphology (as displayed in Fig. 3.5 (a)), evidencing that the film is deposited well on the SS substrate at the temperature of 400 °C. The fractional area of the surface porosity of fabricated WO_3 film is found to be only 4.7 % (shown in Appendix I), demonstrating the superior degree of densification of the film. Also, the non-appearance of cracks on the surface of the film supports the good deposition of WO_3 film on SS. The average grain size of the film is found to be 360 ± 70 nm from the histogram of grain size distribution, shown in Fig. 3.5 (b).

The films fabricated at 200 °C and 300 °C exhibited a thickness of ~26.5 μm and ~17.9 μm, respectively (presented in Appendix I). The supplied thermal energy is also insufficient for proper decomposition and densification in the films at 200 °C and 300 °C, resulting in higher thickness with pores. It is observed that the thickness has reduced with increasing the substrate temperature due to the commencement of densification with the temperature. A well-densified WO_3 film is accomplished at 400 °C and its cross-sectional view (shown in Fig. 3.5 (c)) revealed that the thickness is ~3.6 μm. Fig. 3.5 (d) displays the pie chart of the atomic percentage of elements that exists on the surface of the WO_3 film, obtained from EDAX analysis. It is observed that elements W and O are nearly in the atomic ratio of 1:3, which corresponds to

stoichiometric WO_3. Other than W and O, the element C is also traced. The presence of carbon in the film can be devoted to the inadvertent surface adsorption from the atmosphere in the form of CO, CO_2, and hydrocarbons, etc. (Regragui et al. 2000). It is noticed from Fig. 3.5 (e-h) that the WO_3 film comprises a uniform distribution of W, O and C elements on the surface. The topographical feature of the film obtained from AFM (3D micrograph, area 2 μm × 2 μm) is displayed in Fig. 3.5 (i). It is noticed that the surface of the film is rough, with the presence of sharp grains all over the surface. The average surface roughness of the film is 15.9 nm.
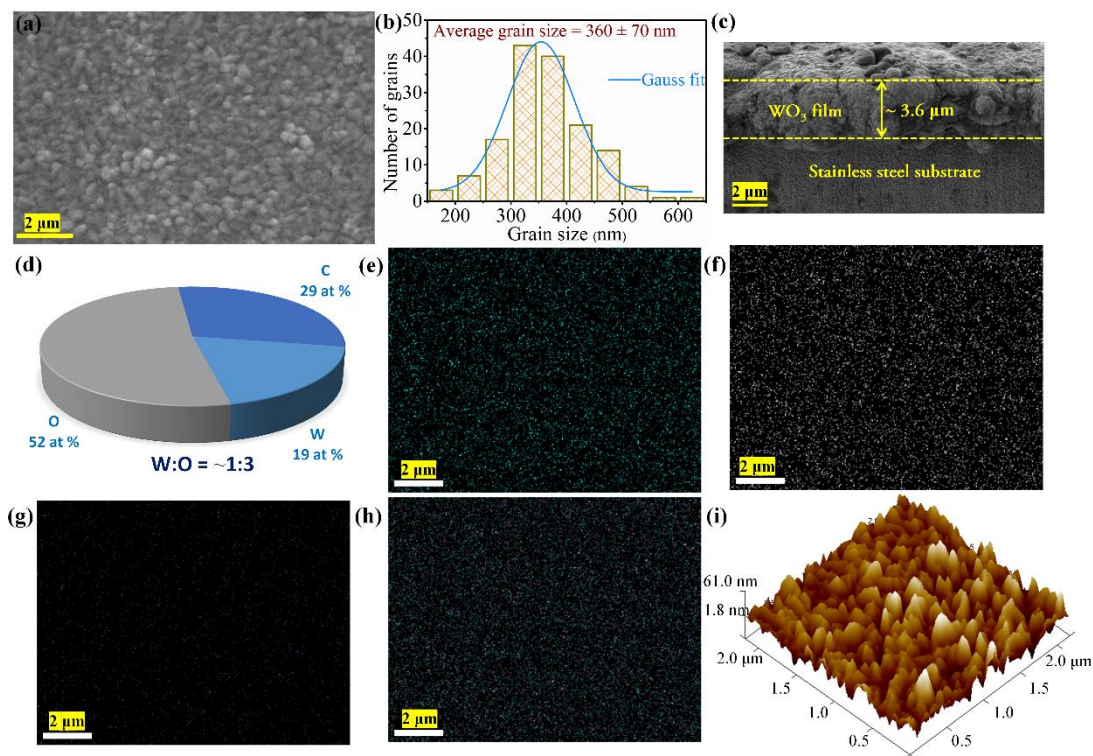
Fig. 3.5: (a) SEM image displaying dense, continuous and uniform WO_3 film on SS substrate, (b) its histogram showing grain size distribution, (c) cross-sectional view showing thickness of WO_3 film on SS substrate, (d) pie chart showing the atomic percentage of elements present in WO_3 film derived from EDAX analysis, EDAX elemental mapping presenting the distribution of (e) W, (f) O, (g) C, respectively, on the surface of WO_3 film, (h) image showing the combination of all the three maps and (i) AFM image of WO_3 film.

To examine the chemical state of the elements present on the surface of the fabricated WO$_3$ film, X-ray photoelectron spectroscopy (XPS) is performed in the current study. The elemental existence of W, O and C are also traced in the wide scan XPS spectrum of WO$_3$ film (shown in Fig. 3.6 (a)). The peaks of W 4f, W 4d, W 4p, O 1s and W 4s are spotted at their particular positions in the spectrum, and it is in decent agreement with the earlier reports (Barreca et al. 2003) (Liu et al. 2014). The Cl 2p high-resolution XPS spectrum is represented in Appendix I and it is assured that there are no peaks belonging to Cl 2p. The non-appearance of chlorine traces from both EDS and XPS analysis recommends that WCl$_6$ in the precursor is wholly transformed into WO$_3$ with chlorine as evaporated by-product gas during the fabrication of the film at 400 °C.
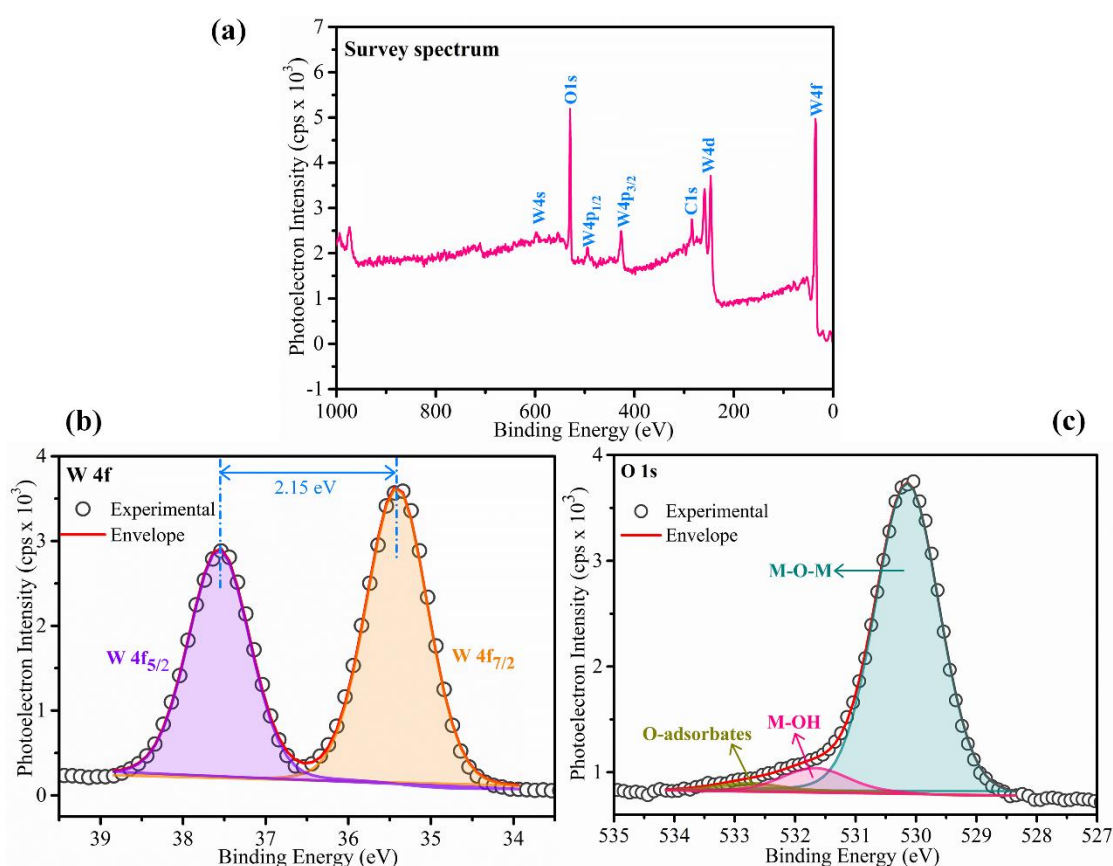

Fig. 3.6: (a) Wide scan XPS spectrum of WO$_3$ film, deconvoluted high-resolution XPS spectra of WO$_3$ film in regions of (b) W 4f and (c) O 1s.

Table 3.1: Details of the deconvoluted W 4f peaks.

Deconvoluted peak	Binding energy (eV)	Area (cps × eV)
W 4f$_{7/2}$	35.4	3520.0
W 4f$_{5/2}$	37.5	2707.2
	(Spin-orbit splitting = 2.1)	(Peak ratio = 4:3)

The W 4f high-resolution XPS spectrum is deconvoluted to inspect the chemical state of the tungsten element in the film and it is presented in Fig. 3.6 (b). After deconvolution, W 4f exhibited two symmetric peaks, W 4f$_{7/2}$ and W 4f$_{5/2}$, which are positioned at the binding energy of 35.4 ± 0.4 eV and 37.5 ± 0.4 eV, respectively. They correspond to the presence of W atoms with the oxidation state of +6 (stoichiometric WO$_3$) (Tesler et al. 2015) (Liu et al. 2014) (Weinhardt et al. 2008). The details of the deconvoluted W 4f peaks are given in Table 3.1. The spin-orbit splitting between the categorized deconvoluted peaks is obtained as 2.1 eV and also the peak ratio is found as 4:3, which also proposes that tungsten is in the valence state of +6, and it is in accordance with the former reports (Vasilopoulou et al. 2014) (Hui et al. 2015).

Moreover, the high-resolution XPS spectrum of the O 1s peak is also deconvoluted and resulted in three significant peaks (shown in Fig. 3.6 (c)). The dominant peak situated at the binding energy of 530.1 ± 0.2 eV belongs to the lattice oxygen, M-O-M (in this case, WO$_3$) (Liu et al. 2014) (Hennek et al. 2013) The deconvoluted peak situated at 531.6 ± 0.5 eV binding energy is credited to the surface metal hydroxide species (M-OH), whereas the deconvoluted peak positioned at the binding energy of 532.7 ± 0.5 eV is dedicated to the weakly bonded O-adsorbates (M-OR) like H$_2$O (Tesler et al. 2015)(Hennek et al. 2013). The relative area fraction of the M-O-M peak is calculated, i.e., (area of M-O-M) / (area of M-O-M + area of M-OH + area of M-OR), and it has a relative area fraction of 91 %. Similarly, the relative area fraction is calculated for M-OH and M-OR peaks also. The information associated with the deconvoluted O 1s peaks is presented in Table 3.2. Based on the discussions mentioned above on survey spectrum and deconvoluted W 4f and O 1s spectra, it is confirmed that pure and stochiometric WO$_3$ film is well deposited on the SS substrate supporting GIXRD and EDAX analysis.

Table 3.2: Details of the deconvoluted O 1s peaks.

Deconvoluted peak	Binding energy (eV)	Area (cps × eV)	Relative area fraction (%)
M-O-M	530.1	4085.8	91
M-OH	531.6	302.3	6.7
O-adsorbates	532.7	100.3	2.2

Scratch hardness is the resistance provided by the surface of the coating to the dynamic surface deformation by moving a hard scratching element called indenter of a given tip radius under a constant load and speed. Scratch test produces a scratch on the surface by the indenter along a specified path; the scratch width is measured, and the value is used to determine the scratch hardness of the coatings. In the present study, the scratch hardness of the WO_3 coated on SS is compared with the uncoated SS under the same testing parameters to determine the increment in the scratch hardness. Also, on every scratch track, at four different positions, the width of the scratch is measured, and the corresponding average value of the scratch width 'b' is considered. Fig. 3.7 (a-f) presents the respective SEM images of the scratches caused on the uncoated and coated SS substrates when different normal loads (5, 10 and 15 N) are applied. The considered average value of scratch width 'b' is also presented in Fig. 3.7.
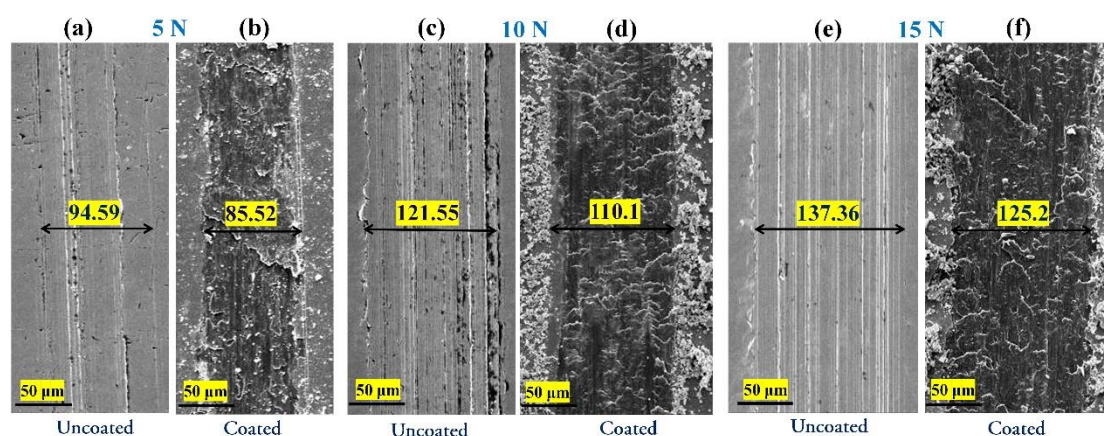

Fig. 3.7: SEM images displaying the scratches obtained on (a) uncoated SS, (b) coated SS when 5 N normal load is applied; (c) uncoated SS, (d) coated SS when 10 N normal load is applied; and (e) uncoated SS, (f) coated SS when 15 N normal load is applied.

From Fig. 3.7, it is apparent that at every normal load, the coated SS exhibited a decrement in the scratch width compared to the uncoated SS under the same testing conditions. For example, at a normal load of 15 N, the obtained scratch width in the uncoated SS is 137.36 μm, whereas the corresponding value is 125.2 μm in the coated SS. The decrement in the scratch width of the coated SS is attributed to the presence of WO_3 film on the surface, which offers a hindrance to the deformation by the surface of the indenter, eventually resulting in lesser indenter penetration and lesser scratch width. However, the absence of such WO_3 film on the uncoated SS substrate produced a comparatively low resistance to the scratch by the indenter, which in turn gave rise to a relatively high scratch width at every particular normal load. The existence of noticeable sharp cuts on the uncoated SS surface is also reflected in Fig. 3.7 (a, c and e), caused by indenter scratching with different normal loads. Nevertheless, the presence of such cuts is not found on the coated SS (noticed in Fig. 3.7 (b, d and f)), ascribed to the presence of the WO_3 film and its resistance to indenter penetration. Fig. 3.8 presents the schematic of the decrement in the scratch width because of resistance offered by the WO_3 film on the SS compared to the uncoated SS when a normal load of 15 N is applied.
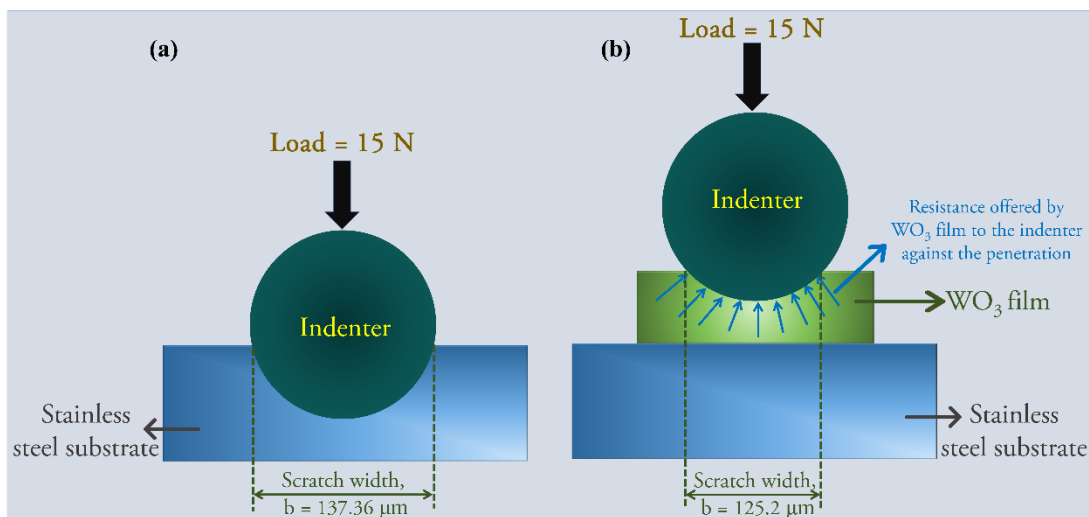

Fig. 3.8: A schematic representation showing a high scratch width in the (a) uncoated SS substrate compared to the (b) coated SS substrate when a normal load of 15 N is applied.

Table 3.3: Values of the scratch hardness 'H_S' (in GPa) of uncoated and WO$_3$ coated SS at different normal loads 'F_N'.

Normal load, 'F_N' (N)	Scratch hardness, 'H_S' (GPa)	
	Uncoated SS	Coated SS
5	1.42	1.74
10	1.72	2.1
15	2.02	2.43

Additionally, from the obtained scratch width values, the scratch hardness value is calculated through equation 2.6, and it is listed in Table 3.3. From equation 2.6, it is inferred that the value of scratch hardness is directly proportional to the normal load applied and is also inversely proportional to the width of the scratch. At a particular normal load, when the load-bearing area decreases, the width of the scratch decreases, subsequently resulting in a high scratch hardness value. It is also observed from Table 3.3 that at every specific normal load, the coated SS displays a relatively high value of scratch hardness apparently than the uncoated SS, as the scratch width decreases (shown in Fig. 3.7).

Table 3.4: The details of crystallinity, morphology, thickness, and oxide formation of the fabricated WO$_3$ film.

Name	Feature of the film	Derived from
Nature	Highly crystalline with pure WO$_3$	GIXRD
Morphology	Extremely dense with density > 95 %, uniform and crack-free	SEM
Thickness	> 3 μm	FESEM
WO$_3$ (M-O-M) content	More than 91 %	XPS

It is reported in the previous study that resistance to scratch is comparatively better in crystalline WO$_3$ film than in the amorphous film (Hasan et al. 2012); similarly, from the current study, it can be inferred that the obtained crystallinity rather than

amorphousness supports in better scratch resistance. Also, it is previously reported that the dense film assists in achieving better scratch hardness (Sarraf et al. 2014). The micrometre rage thickness (~3.6 μm) of WO$_3$ film might have also aided in ensuing a better scratch hardness by retarding the indenter penetration. The overall enhancement in the scratch hardness of the coated SS compared to the uncoated SS is due to the relevant features and quality of the film, which are consolidated in Table 3.4. It can be concluded that due to these features of the WO$_3$ film (presented in Table 3.4) on SS, the failure of the film caused by surface deformation through the indenter is comparatively less, and the resistance provided by the film to the indenter penetration is high. Therefore, these features prompted relatively low scratch width and high scratch hardness in the WO$_3$-coated SS than the uncoated SS.

In the current study, the surface wettability is analyzed by finding the WCA of the fabricated WO$_3$ film. Fig. 3.9 (a) displays the photograph of the surface of the film after dropping the droplet of water on it. It is noticed that the WCA of the film is ~ 31°, and the water droplet seemed to have spread after dropping on the surface, and it shows that the surface of the film is in a hydrophilic state. On the other hand, the WCA of the uncoated SS substrate is found to be ~79° (shown in Appendix I). It is noticed that the value of WCA reduced after depositing WO$_3$ film on the substrate. This hydrophilic wetting state of WO$_3$ film is dedicated to the inherent hydrophilicity of WO$_3$ (Tesler et al. 2015) and the existence of –OH functional group and adsorbed water on the surface of the film, recognized in XPS analysis. It is also mentioned in the previous report that the presence of –OH functional groups and the adsorbed water on the surface help in attaining hydrophilicity (Kwak et al. 2010).

Later, the WO$_3$ film is subjected to chemical treatment with OTS to generate a covalently bound self-assembled monolayer (SAM) on the surface to convert the hydrophilic nature to hydrophobic nature. The film is re-investigated to measure the change in the WCA after the chemisorption with OTS. Remarkably, the post-modified film revealed a WCA of 136° (~105° more than unmodified WO$_3$ film) (shown in Fig. 3.9 (b)), which substantiated the formation of the hydrophobic natured surface. The attained hydrophobic nature is dedicated to the effective serviceability of OTS as a SAM on the surface of the film. To examine the stability in the hydrophobicity of OTS-

treated WO$_3$ film, the WCA is measured again after a period of 100 days. Impressively, the film continued to be non-wetting and displayed a WCA of ~136° (as shown in Fig. 3.9 (c)), which is alike to the value obtained initially, demonstrating the remarkable stability of chemisorbed OTS on the WO$_3$ film. A schematic illustrating the hydrophilicity of WO$_3$ film with spread water droplet and modification by treating with OTS into a hydrophobic surface inhibiting the spread of water droplet is shown in Fig. 3.9 (d). The variation in the WCA of uncoated SS, WO$_3$ film before and post-OTS treatment, and the OTS-treated WO$_3$ film after 100 days duration is pictorially represented in Fig. 3.10. It is directed that rough topographical surface is an important factor for hydrophobicity and hydrophobic surfaces are generally achieved by combining surface roughness and surface hydrophobization step through chemical modification (Ke et al. 2010). The achieved hydrophobicity in the WO$_3$ film in the current study can be attributed to both the high surface roughness of the film (obtained from AFM analysis) as well as chemisorption of OTS as a covalent bonded SAM on the surface of the film.
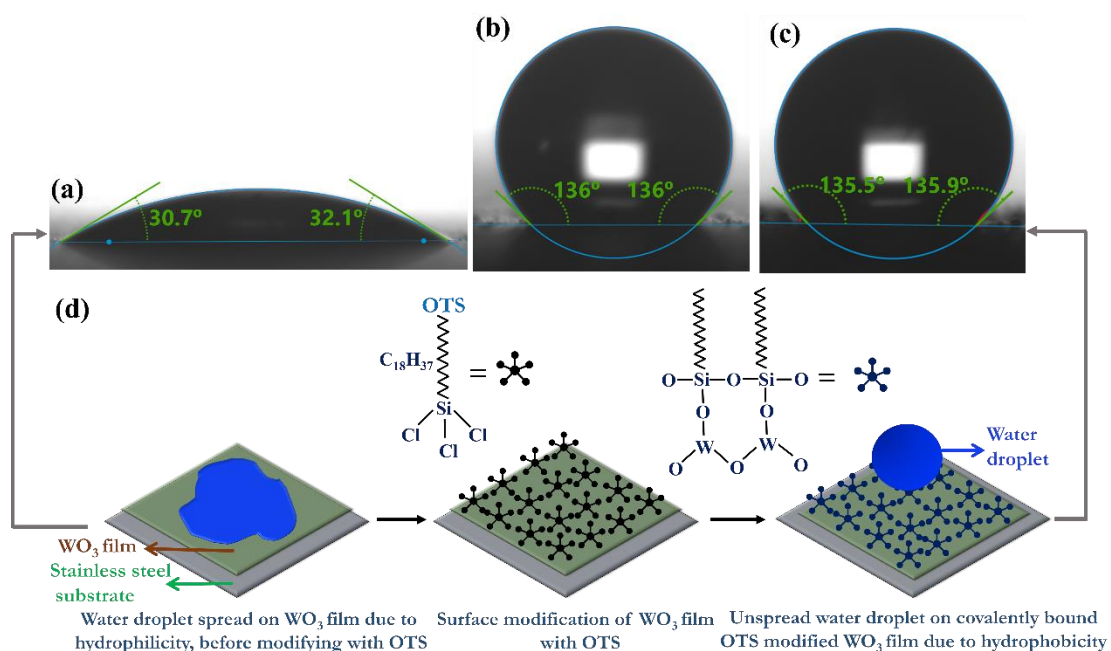

Fig. 3.9: Water droplet of 1 µl on WO$_3$ film (a) before, (b) after surface modification with OTS, (c) OTS-treated WO$_3$ film after 100 days and (d) a pictorial representation displaying the change in surface wettability of WO$_3$ film after modifying with OTS.
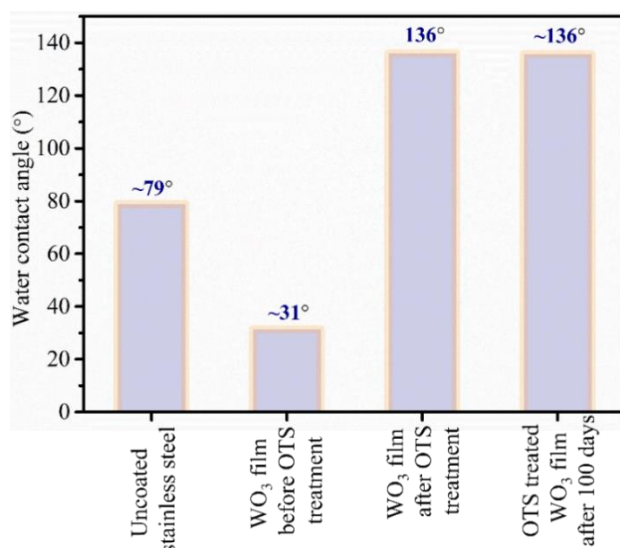
Fig. 3.10: Variation of the WCA (°) on uncoated SS substrate, WO₃ film before and after OTS treatment, and OTS-treated WO₃ film after 100 days.

The formation of covalently bonded OTS SAM on the surface of the WO$_3$ film is presumed to happen in three stages: (i) The development of silanetriol, which is a hydroxyl group of the OTS, formed due to the hydrolysis of chloromoieties of the OTS, (ii) The physisorption of developed silanetriol with the surface hydroxyl groups of the WO$_3$ film through a hydrogen bond and (iii) The establishment of immobilized Si$_{silane}$–O–Si$_{silane}$ and Si$_{silane}$–O–W cross-linking covalent bonds through the condensation reaction on the surface of the film, which develops as a SAM with the alkyl chain (C$_{18}$H$_{37}$–) standing outward from the surface of the film (Ke et al. 2010) (Hui et al. 2015) (Sagiv 1980). The schematic representation of OTS SAM formation on WO$_3$ films is represented in Fig. 3.11. In the present study, the development of such covalently bound OTS SAM on the surface of the WO$_3$ film might be helped in the generation of hydrophobicity and also assisted in the stability.
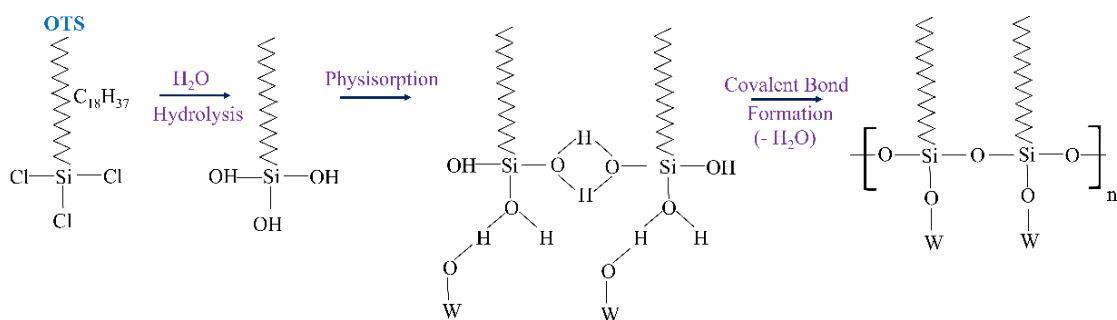
Fig. 3.11: OTS SAM formation mechanism on WO₃ film.

78

3.3.3 Analysis of the WO₃ films on glass substrates

The XRD patterns of the uncoated glass, 5, 10 and 15 sprays films are shown in Fig. 3.12 (a). It is noticed that all the films exhibited crystallinity with the diffraction planes exactly coinciding with the diffraction planes of the monoclinic structured phase of WO_3 (ICDD: 00-043-1035), whereas the uncoated glass is amorphous in nature. The non-appearance of secondary phases confirmed the formation of the pure WO_3 phase with a preferred orientation of the (002) plane. It is noticed that the 5 sprays film revealed a low crystallinity compared to the 10 and 15 sprays films. It is attributed to the fewer number of sprays and consequently less deposition of the precursor, and less transformation into the desired oxide (WO_3). As the number of sprays increased from 5 to 15, the crystallinity of the films has improved, and it is because of the more deposition of the precursor and its conversion into WO_3. Therefore, as the volume of the metal oxide formation increases with the number of sprays, the films get more densified, which in turn improves the crystallinity of the films.

Fig. 3.12: (a) XRD patterns of uncoated glass, 5 sprays, 10 sprays and 15 sprays films, SEM images of (b) 5 sprays, (c) 10 sprays, and (d) 15 sprays films.

The surface morphological features of all the films are presented in Fig. 3.12 (b, c, and d). It is noticed that the 5 sprays film is non-uniform due to the lack of more

79

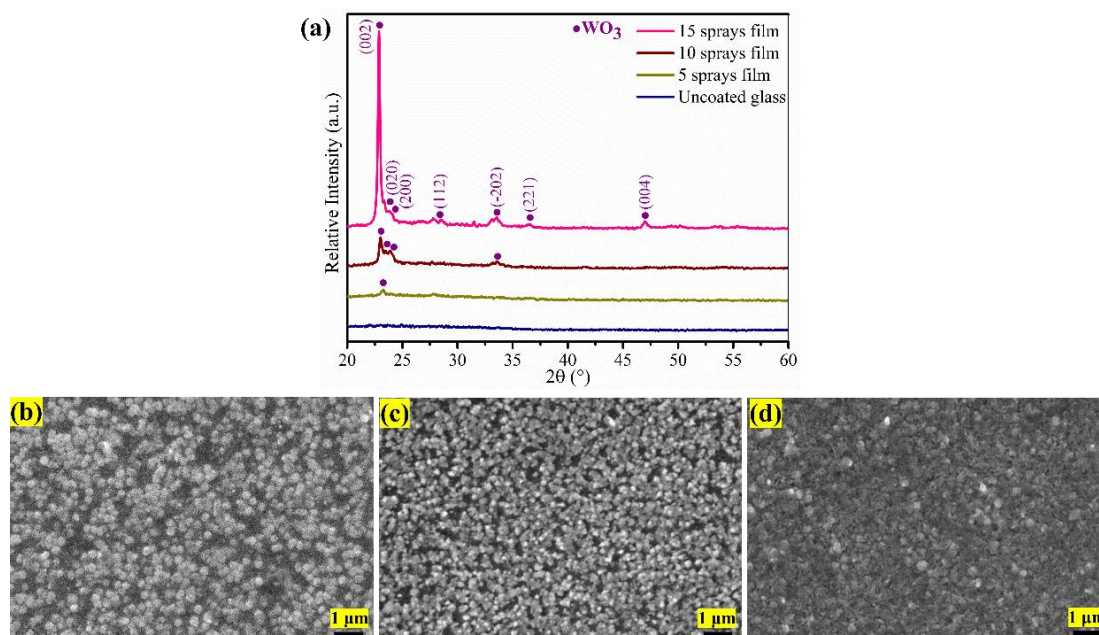sprays, but with an increment in the number of sprays from 5 to 15, the films have achieved more uniformity and densification. The coverage with a regular distribution of submicron-sized grains all over the substrate with the increment in the spray number is ascribed to more precursor solution deposition and its transformation to WO_3. It is also observed that films are entirely free from cracks. Due to low crystallinity and non-uniformity in the 5 sprays film compared to the 10 and 15 sprays films, further characterization studies are conducted for the 10 and 15 sprays films only.

The topographical features of the 10 and 15 sprays films through AFM images (3D micrographs of 5 μm × 5 μm) are shown in Fig. 3.13. It is noticed that the size of individual surface grains has enlarged slightly from the 10 to 15 sprays films. The average grain size of the 10 and 15 sprays film is found to be 320 ± 20 nm and 418 ± 40 nm, respectively. The average surface roughness of the 10 and 15 sprays films is 12.5 and 17.1 nm, respectively, and this increase in surface roughness from the 10 to 15 sprays film is due to an enhancement in the crystallinity of the films (Pujar et al. 2018). The thickness of the 10 and 15 sprays films is found to be 380 and 550 nm, respectively.
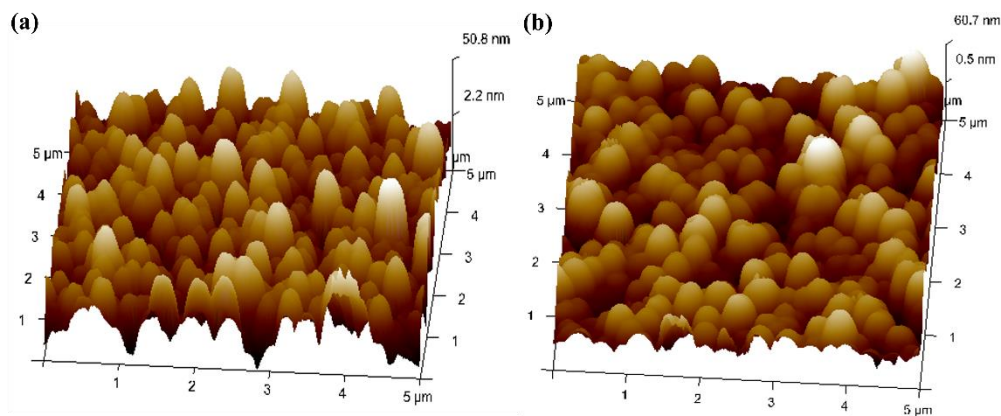
Fig. 3.13: AFM images of (a) 10 sprays and (b) 15 sprays films.

To analyse the surface elemental composition and chemical state of the elements present on the films, XPS is engaged. Fig. 3.14 (a) displays the wide scan XPS spectra of the 10 and 15 sprays films, and it revealed the presence of W, O and C elements. The presence of carbon in the films is due to unintentional surface adsorption in the form of CO, CO_2, and hydrocarbons, etc., from the atmosphere (Regragui et al. 2000). In both

the films, binding energy levels of W 4f, W 4d, W 4p, O 1s and W 1s have attained at the exact binding energy locations, as revealed in previous reports (Barreca et al. 2003) (Liu et al. 2014). No traces of chlorine are spotted in the survey spectra of both films. It proves the complete transformation of WCl_6 to WO_3 with the evaporation of chlorine gas during the fabrication of the films at 400 ℃. The high-resolution XPS spectra of Cl 2p of both films are given in Appendix II.
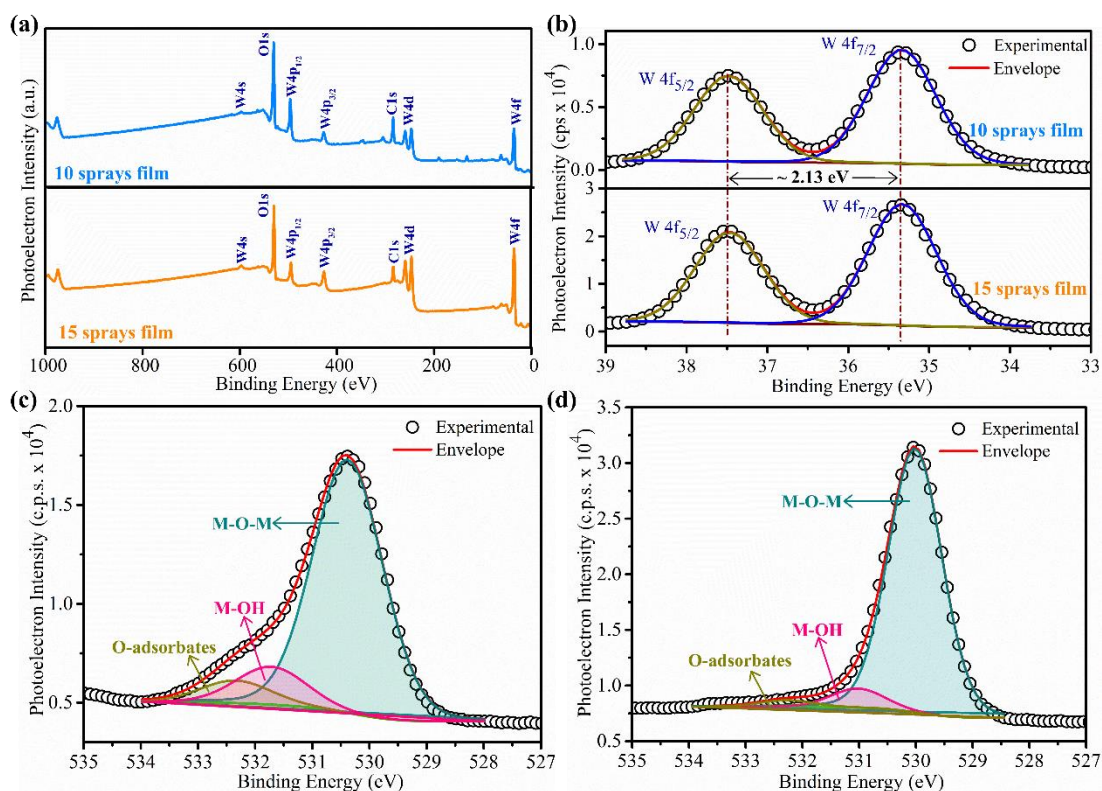
Fig. 3.14: (a) Wide scan XPS spectra, (b) deconvoluted high-resolution XPS spectra of W 4f of 10 sprays and 15 sprays films, respectively, and deconvoluted high-resolution XPS spectra of O 1s of (c) 10 sprays and (d) 15 sprays films.

Also, the high-resolution XPS spectra of W 4f of the 10 and 15 sprays films are deconvoluted, and they are presented in Fig. 3.14 (b). The deconvolution of the W 4f peak displayed two symmetric peaks, W $4f_{7/2}$ at 35.3 ± 0.5 and W $4f_{5/2}$ at 37.4 ± 0.5, which signifies that the W atoms are in an oxidation state of +6 (as expected for stoichiometric WO_3) (Tesler et al. 2015). The splitting of spin-orbital between W $4f_{7/2}$ and W $4f_{5/2}$ is 2.1 eV with a peak ratio of 4:3, which exactly matches the earlier report

(Vasilopoulou et al. 2014). The details of deconvoluted W 4f peaks of both films are given in Table 3.5.

Table 3.5: Details of deconvoluted W 4f peaks of 10 and 15 sprays films.

Film	Deconvoluted peaks	Binding energy (eV)	Area (cps × eV)
10 sprays	W 4f$_{7/2}$	35.3	10006.3
	W 4f$_{5/2}$	37.4	7534.5
		(Spin-orbit splitting = 2.1)	(Peak ratio = ~ 4:3)
15 sprays	W 4f$_{7/2}$	35.3	28201.8
	W 4f$_{5/2}$	37.4	20993.3
		(Spin-orbit splitting = 2.1)	(Peak ratio = ~ 4:3)

Table 3.6: Details of deconvoluted O 1s peaks of 10 and 15 sprays films.

Film	Deconvoluted peaks	Binding energy (eV)	Area (cps × eV)	Relative area fraction (%)
10 sprays	M-O-M	530.3	20731.7	80.7
	M-OH	531.7	3094.1	12.0
	O- adsorbates	532.3	1841.4	7.1
15 sprays	M-O-M	530.0	29378.4	91.1
	M-OH	531.0	2121.0	6.5
	O- adsorbates	532.2	748.8	2.3

Furthermore, the O 1s peak in the XPS spectrum of the 10 and 15 sprays films is deconvoluted, and it resulted in three significant components situated at approximate binding energies of 530.3 ± 0.5 eV, 531.3 ± 0.5 eV and 532.3 ± 0.5 eV attributed to lattice oxygen (M-O-M, here WO$_3$), surface metal hydroxide groups (M-OH) and weakly bound O-adsorbates (H$_2$O), respectively (Tesler et al. 2015) (Liu et al. 2014) (Hennek et al. 2013). The deconvoluted respective high-resolution XPS spectra of O 1s peaks of the 10 and 15 sprays films are displayed in Fig. 3.14 (c) and (d), and the information such as binding energies, peak areas and relative area fractions are presented in Table 3.6. It is apparent that the lattice oxygen percentage has improved

with the increase in the number of sprays from 10 to 15. The enhancement in the lattice oxygen is accredited to the densification and crystallisation of the 15 sprays film. Also, the relative areas of W 4f peaks (given in Table 3.5) displayed an enhancement with the number of sprays, which further confirmed the densification of the film with the number of sprays, and it supports the analysis depicted from SEM images of the films.
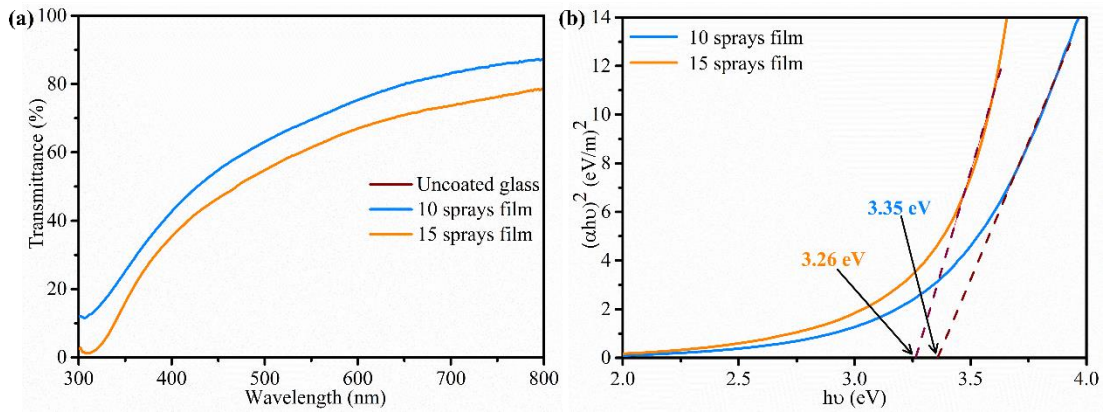
Fig. 3.15: Transmittance plot of uncoated glass, 10 and 15 sprays films, (b) Tauc's plot of 10 and 15 sprays films.

Also, the films are inspected under UV-Vis spectrometry to examine the transparency in the visible region. The normalized optical transmittance spectra of the 10 and 15 sprays films, along with the uncoated glass, are displayed in Fig. 3.15 (a). It is noticed that there is a slight decrement in the transparency of the 15 sprays film compared to the 10 sprays film, and it is ascribed to the increase in the number of sprays, which in turn enhanced the density of the film. The other factor for the reduction in the transparency of the 15 sprays film is due to the increment in the surface roughness. The high surface roughness scatters the incoming light and causes a decrement in the transparency (Wannes et al. 2018). The optical energy band gap of the films is estimated using Tauc's relation, as shown in equation 3.2.

$$(\alpha h\upsilon) = \alpha_o (h\upsilon - E_g)^n \tag{3.2}$$

Where α is the optical absorption coefficient, $h\upsilon$ is the photon energy, α_o is the proportionality constant, E_g is the optical energy band gap and n is an index which has a value of ½ for direct band gap semiconductors and has a value of 2 for indirect band gap semiconductors (Narendrudu et al. 2016). Here, the value of index 'n' is taken as

½, by considering WO$_3$ as a direct band gap semiconductor (Regragui et al. 2000). The E$_g$ from Tauc's plot represented in Fig. 3.15 (b) is estimated to be 3.35 and 3.26 eV for the 10 and 15 sprays film, respectively. The obtained values fit well with the formerly reported values (Regragui et al. 2000, 2001).

Fig. 3.16 (a-i) displays the SEM images of the top view of the uncoated glass, 10 and 15 sprays films on which scratches are performed by different normal loads, 5, 10 and 15 N, respectively. In the present study, the scratch hardness of the 10 and 15 sprays films are compared with the uncoated glass by maintaining the same scratch testing parameters. Also, the scratch width is measured at four different positions on the scratch track, and the average scratch width value is taken into consideration. From Fig. 3.16, it is observed that at every normal load, the scratch width has decreased with increasing the number of sprays from the uncoated glass. With the enhancement in the number of sprays, more amount of WO$_3$ is deposited on the glass substrate resulting in an increment of thickness, densification of the film and establishing a hindrance to the scratch penetration by the indenter, and therefore the scratch width is decreased. As there is no WO$_3$ film over the uncoated glass, the resistance to the scratch penetration by the uncoated glass is minimum and subsequently, it presented high values of scratch width compared to both the films, irrespective of the normal load applied. In Fig. 3.16 (a, d, and g), some sharp cuts are observed on the surface of the uncoated glass, which are formed due to scratching by the indenter with different normal loads, and the intensity of cuts increased with the normal load. However, the formation of such sharp cuts is absent on both films, irrespective of the normal load, due to the presence of WO$_3$ and its resistance to the scratching indenter. Fig. 3.17 displays the pictorial presentation of scratch width variation on uncoated glass, 10 and 15 sprays films, respectively, when a normal load of 10 N is applied.
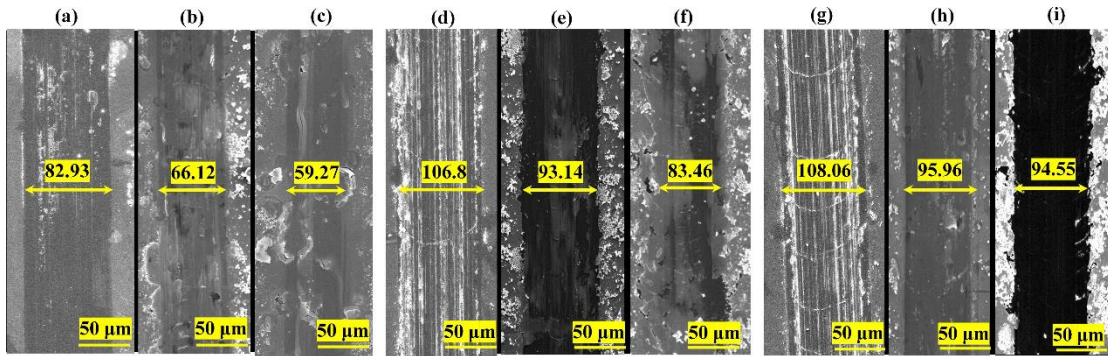
Fig. 3.16: SEM images of scratches obtained on (a) uncoated glass, (b) 10, (c) 15 sprays films when 5 N normal load is applied; (d) uncoated glass, (e) 10, (f) 15 sprays films when 10 N normal load is applied and (g) uncoated glass, (h) 10, (i) 15 sprays films when 15 N normal load is applied.

The calculated scratch hardness (GPa) values obtained from scratch width using equation 2.6 at different normal loads on uncoated glass, 10, and 15 sprays films are given in Table 3.7. It is noticed that, in all the cases, the uncoated glass presented low values of scratch hardness, whereas the scratch hardness has increased with the number of sprays. For example, at applied 10 N normal load, the calculated scratch hardness of uncoated glass is 2.23 GPa, whereas, for 15 sprays film, it improved to 3.65 GPa. Due to the enhancement in the number of sprays, at a constant load, material failure due to dynamic surface deformation is less, resulting in the decrement of scratch width, i.e., an increment in scratch hardness. Within the experimental range, the increment noticed in scratch hardness for both films followed a similar trend at every normal load. Thus, it can be inferred that scratch resistance has improved at a higher number of sprays. In addition, Hasan et al. reported in their study that the resistance to wear has enhanced with the crystallinity of the films (Hasan et al. 2012). In the current study, a similar trend can be collated as the crystallinity of the films enhanced with the number of sprays, assuring an improvement in scratch resistance. So, in the present investigation, the overall increment in scratch hardness for the 15 sprays film is dedicated to the combined benefaction of improvement in crystallinity, densification and thickness of the films compared to the 10 sprays film, determined by XRD, SEM and XPS analysis. The summarized details of high scratch resistant 15 sprays film is shown in Table 3.8.
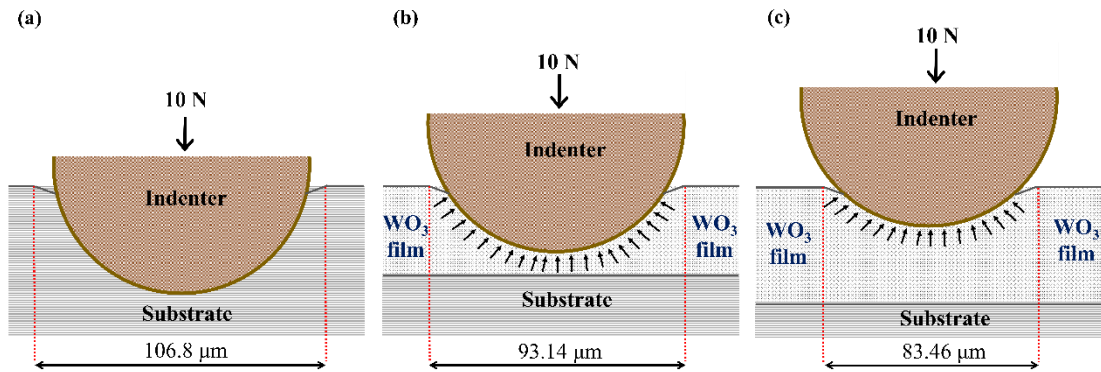
Fig. 3.17: Pictorial presentation of scratch width variation on (a) uncoated glass, (b) 10 and (c)15 sprays films when a normal force of 10 N is applied.

The scratch hardness values obtained in other metal oxide coatings reported in the previous studies are shown in Table 2.2. It is noticed from Table 2.2 that most of the metal oxide coatings on which the scratch hardness property is examined are deposited through conventional techniques such as sputtering, plasma spraying and chemical vapor deposition. A few reports also performed the scratch hardness study of the coatings deposited through electrochemical anodization. It can be mentioned here that the current study is the first one to the best of our knowledge that examines the scratch hardness of WO_3 film deposited on metallic and glass substrates, respectively, through a low-cost, facile solution-processed spray pyrolysis technique. Though the present WO_3 film is deposited through the inexpensive solution-processed method, the obtained scratch hardness values can be nearly comparable to the scratch hardness values of the earlier metal oxide coatings deposited through conventional and high-cost techniques.

Table 3.7: Values of the scratch hardness 'H_S' (in GPa) of uncoated glass, 10 and 15 sprays films at different normal loads 'F_N'.

Normal load, 'F_N' (N)	Scratch hardness, 'H_S' (GPa)		
	Uncoated	10 sprays	15 sprays
5	1.85	2.91	3.62
10	2.23	2.93	3.65
15	3.27	4.14	4.27

Table 3.8: The details of crystallinity, morphology, thickness, and oxide formation of the fabricated high scratch resistant 15 sprays film.

Name	Feature of the film	Derived from
Nature	Highly crystalline with pure WO_3	XRD
Morphology	Highly dense, uniform and crack-free	SEM
Thickness	550 nm	NNSR
WO_3 (M-O-M) content	More than 91 %	XPS
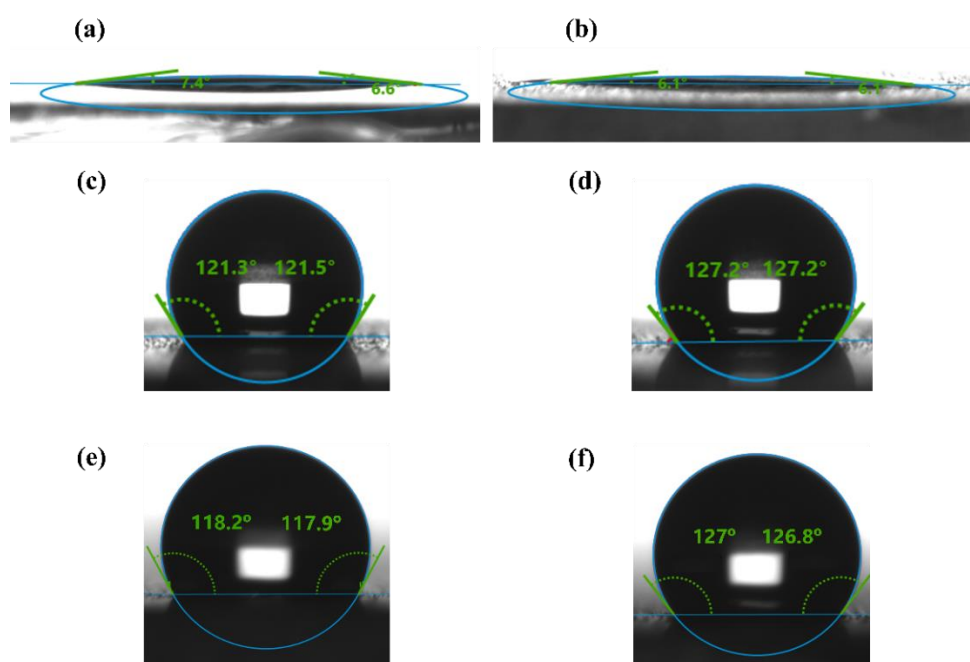
Fig. 3.18: Photographs of 1 μl water droplet on (a) 10 and (b) 15 sprays films before OTS treatment, (c) 10 and (d) 15 sprays films after OTS treatment, (e) and (f) OTS-treated 10 and 15 sprays films respectively after a year.

The WCA measurements are conducted for the 10 and 15 sprays films to inspect the surface wetting properties. Fig. 3.18 (a and b) display the photographs of the 10 and 15 sprays films, respectively, after dropping a water droplet on the surface. It is observed that the water droplet instantaneously spread on the surface of the films with

a WCA < 8°, confirming the hydrophilic nature of the films. Moreover, the WCA of the uncoated glass substrate is revealed to be ~51° (given in Appendix II). It is observed that the value of WCA decreased after depositing the WO_3 film on the glass substrate. The hydrophilic wetting state before the surface treatment is attributed to the presence of hydroxide groups and adsorbed water on the WO_3 films, which are noticed through the XPS analysis (Kwak et al. 2010). Later, the films are chemically treated with OTS to create a covalent bonded SAM which is applied for the modification of hydrophilic to hydrophobic surfaces (Ke et al. 2010). After the chemisorption of the films with OTS, the films are re-inspected to measure the WCA. It is revealed that 10 and 15 sprays films are hydrophobic with a WCA > 120°, as shown in Fig. 3.18 (c and d), respectively, which showed the functionality of OTS as a SAM on top of the films. The pictorial representation of water droplet before and after OTS treatment of the WO_3 films are shown in Fig 3.19 (a).

Fig. 3.19: (a) The schematic illustration of water droplet before and after OTS treatment, (b) The variation of the WCA (°) on uncoated glass substrate, 10 and 15 sprays films before and after OTS treatment, and the OTS-treated 10 and 15 sprays films after a year.
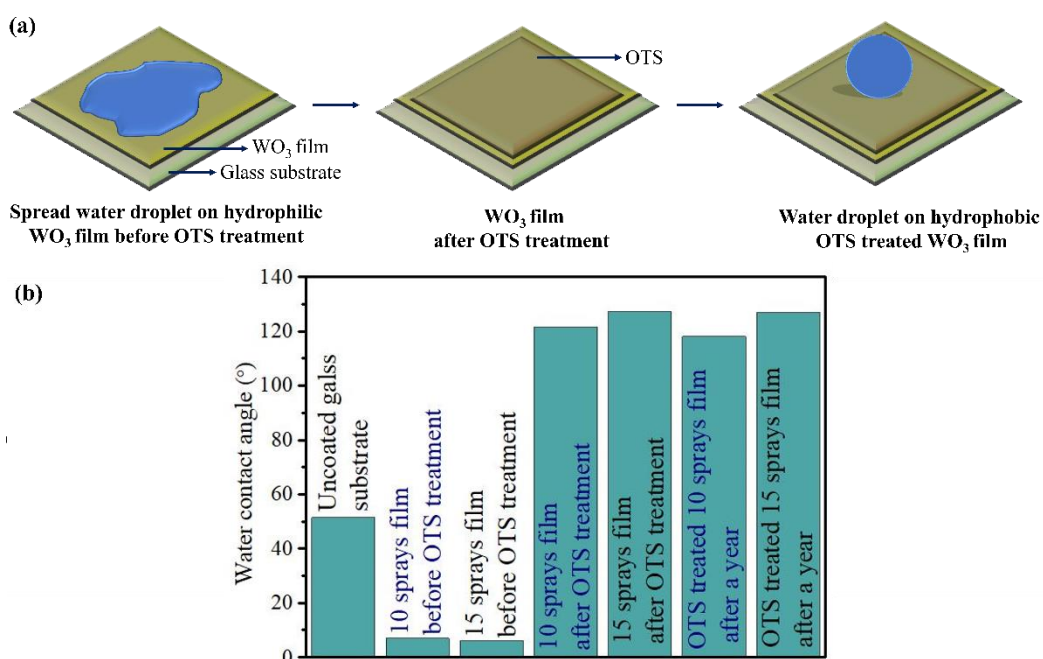
To examine the stability of both OTS-treated 10 and 15 sprays films, the WCA is measured after a year. From Fig. 3.18 (e and f), it is observed that both films remained non-wetting and displayed almost the same WCA of ~120° as previous measurements (WCA > 120°), proving that OTS has no sign of deterioration on the films even after a year. The established OTS SAM on the surface assisted in the hydrophobic behaviour of WO_3 films. Also, due to the covalent bond formation, not much degradation happened in the hydrophobicity even after a year. The variation in the WCA of the uncoated glass substrate, the 10 and 15 sprays films before and after OTS treatment, and the OTS- treated 10 and 15 sprays films after a year is pictorially represented in Fig. 3.19 (b).

3.4 Conclusions

Pure and robust WO_3 films were accomplished on SS and glass substrates, respectively, at 400 °C via a simplistic, minimal capital-intensive spray pyrolysis technique. Thermal analysis revealed the thermal decomposition and crystallization of the precursor at ~230 °C & 255 °C, respectively. The fabricated monoclinic crystal structured WO_3 film on SS was uniform, dense, and exhibited better scratch hardness than the uncoated SS substrate, irrespective of applied normal load of 5 to 15 N. Hydrophilic natured WO_3 film (WCA, ~31°) was efficaciously transmuted into hydrophobic (WCA, 136°) by chemical treatment with OTS to generate a SAM on the film's surface. The hydrophobicity of OTS-treated film was preserved even after 100 days. The 10 and 15 times sprayed WO_3 films on glass substrates were polycrystalline with a monoclinic crystal structure. An augmentation in the scratch hardness of the films with the number of sprays in contrast to the uncoated glass was recognized at every applied normal load (5, 10 and 15 N). The deposited films were found to be hydrophilic (WCA < 8°), transformed to hydrophobic (WCA > 120°) by chemically treating with OTS to form a SAM on the surface, and the hydrophobicity persisted the same (WCA, ~ 120°) even after a year.

The page was left intentionally blank

CHAPTER 4

FABRICATION OF SOLUTION COMBUSTION PROCESSED SPIN-COATED ZINC OXIDE-BASED, TITANIUM OXIDE-BASED, INDIUM OXIDE-BASED THIN FILMS AND THEIR CHARACTERIZATIONS

4.1 Introduction

This chapter deals with the semiconducting zinc oxide (ZnO) based, titanium oxide (TiO_2) based and indium oxide (In_2O_3) based thin films that are developed through the solution combustion method. All the respective combustible precursors are deposited on the glass substrates by using the spin coating method, and followed by annealing at appropriate temperatures to fabricate the respective films. In this chapter, the development and characterization of the zinc oxide-based precursors and their thin films are discussed initially. Later, the development and characterization of the titanium oxide-based precursors and their thin films, followed by the indium oxide-based precursors and their thin films, are discussed.

4.2 Zinc oxide-based thin films

In this section, the preparation and characterization of pristine zinc oxide (ZnO) and titanium doped ZnO (1, 2 and 3 wt.% of Ti) based combustible precursors and thin films are discussed. The thermal behaviour of all the combustible precursors (pristine and doped) was examined initially through TGA. The fabricated spin-coated pristine and doped thin films were studied through various thin film characterization techniques such as GIXRD, FESEM, EDAX, AFM, UV-Vis and XPS. The gas sensing characteristics of the fabricated thin films were studied under various gases such as ammonia, formaldehyde etc.
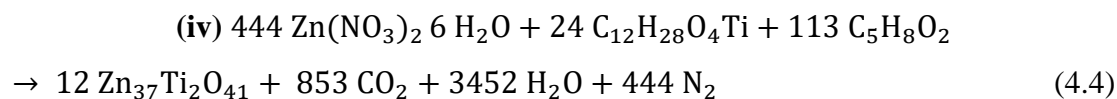
4.2.1 Experimental procedure

4.2.1.1 Materials

All the reagents were of analytical grade and utilized without additional purification. Here, Zinc nitrate hexahydrate ($Zn(NO_3)_2$ $6H_2O$) (SRL Chemicals), titanium (IV) isopropoxide ($C_{12}H_{28}O_4Ti$) (Sigma-Aldrich), acetylacetone ($C_5H_8O_2$) (Merk), 2-methoxyethanol ($C_3H_8O_2$) (Molychem) were used in this study. For silver electrodes, silver conductive adhesive paste (Alfa Aesar) was used.

4.2.1.2 Preparation of precursors and their characterization

1 M of precursors comprising 2 g of $Zn(NO_3)_2$ $6H_2O$ (as Zn source and oxidizer) and stoichiometric amounts of $C_{12}H_{28}O_4Ti$ (as Ti source) with varying Ti weight percentages (0, 1, 2 and 3 wt.%, respectively) were prepared by dissolving them in $C_3H_8O_2$ which was used as a solvent. Here, $C_5H_8O_2$ was used as a fuel. According to the balanced equations, i.e., equation 4.1 (0 wt.% Ti), equation 4.2 (1 wt.% Ti), equation 4.3 (2 wt.% Ti), equation 4.4 (3 wt. % Ti), the stoichiometric quantities of $C_{12}H_{28}O_4Ti$ and $C_5H_8O_2$ were added in the respective precursors.

(i) $12\ Zn(NO_3)_2\ 6\ H_2O + 5\ C_5H_8O_2\ \rightarrow\ 12\ ZnO + 25\ CO_2 + 92\ H_2O + 12\ N_2$ (4.1)

$$\textbf{(ii)}\ 348\ Zn(NO_3)_2\ 6\ H_2O + 6\ C_{12}H_{28}O_4Ti + 127\ C_5H_8O_2$$
$$\rightarrow\ 6\ Zn_{58}TiO_{60} + 707\ CO_2 + 2680\ H_2O + 348\ N_2 \tag{4.2}$$

$$\textbf{(iii)}\ 84\ Zn(NO_3)_2\ 6\ H_2O + 3\ C_{12}H_{28}O_4Ti + 26\ C_5H_8O_2$$
$$\rightarrow\ 3\ Zn_{28}TiO_{30} + 166\ CO_2 + 650\ H_2O + 84\ N_2 \tag{4.3}$$

$$\textbf{(iv)}\ 444\ Zn(NO_3)_2\ 6\ H_2O + 24\ C_{12}H_{28}O_4Ti + 113\ C_5H_8O_2$$
$$\rightarrow\ 12\ Zn_{37}Ti_2O_{41} + 853\ CO_2 + 3452\ H_2O + 444\ N_2 \tag{4.4}$$
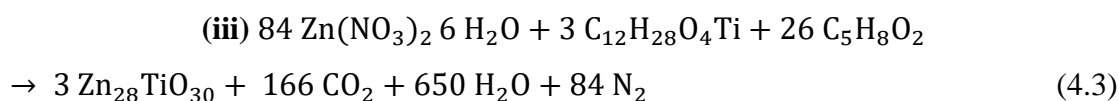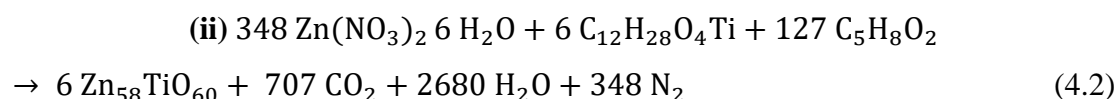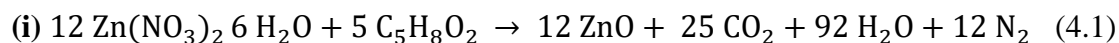
Later, the precursors were stirred (at 250 rpm) for 3 h at room temperature to attain compositional homogenous and optical clearness. The precursors were then aged for 12 h. The dried precursors were studied under thermogravimetric analysis (TGA, PerkinElmer, Thermo-Gravimetric Analyzer TGA 4000) for thermal analysis with a scanning rate of 10 °C/min from 35 °C to 600 °C in the nitrogen atmosphere.

4.2.1.3 Fabrication of films and their characterization

In this study, corning glasses (Corning Incorporated; thickness 0.96 to 1.06 mm) were utilized as the substrates, and the substrates were initially cleaned with tap water and soap solution thoroughly. Later, the substrates were cleaned ultrasonically for 10 min in distilled water, acetone and again in distilled water, respectively. Further, the substrates were exposed to UV-Ozone for the elimination of organics and sterilizing the surface. Later, the prepared individual stable precursor was spin coated on different substrates by spin coating method. The maintained time and spinning speed were 30 s and 3000 rpm, respectively. After spinning, the samples were immediately heated for 20 min on a hot plate held at 400 °C to avoid entrapment of by-product gases (generated during combustion) and rectify the morphological defects, if any. Likewise, the samples were spin coated for 15 times with intermediate heating for 20 min as denoted above. Lastly, the samples were annealed at 400 °C for 4 h. The schematic representation of the fabrication of thin films in the current study is shown in Fig. 4.1.
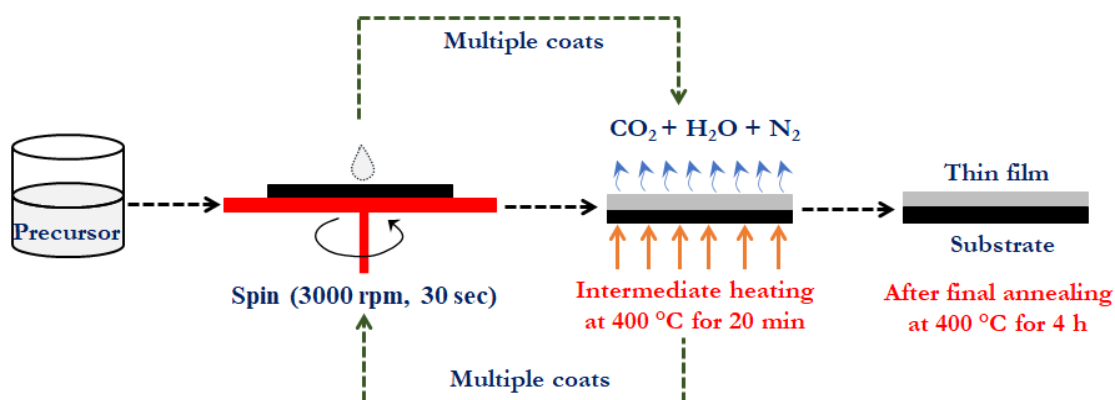
Fig. 4.1: Schematic representation of the fabrication of thin films in the current study.

The 0, 1, 2 and 3 wt.% Ti doped ZnO thin films hereafter are named as ZT0, ZT1, ZT2 and ZT3 films, respectively, from this section. The films were studied under PANalytical multi-purpose high-resolution X-Ray diffractometer (GIXRD) (Empyrean) (source of copper Kα radiation) with a grazing angle of 0.7° and a step size of 0.07° to inspect the crystal structure of the films. The average crystallite size of all the films is estimated using the Scherrer formula (shown in equation 4.5) (Holzwarth and Gibson 2011).

$$D = \frac{K\lambda}{\beta\cos\theta} \tag{4.5}$$

Here D is the crystallite size (nm), λ is the wavelength of Cu Kα radiation (λ = 0.154 nm), θ is the Bragg diffraction angle (°), and K is the Scherrer constant (it is assumed here as 0.9), and β is the full width at half maximum of diffraction peak (radians). Generally, for estimating the crystallite size, β is considered by subtracting the instrumental peak broadening from the actual/total broadening that is given by the XRD measurement unit. To examine the microstructure of the surface of the fabricated films and analyse the elemental composition, field emission scanning electron microscopy (FESEM) (Carl Zeiss Sigma) provided with energy-dispersive X-ray analysis (EDAX) (Oxford instruments) were utilized, respectively. The topography and surface roughness of the films were assessed from atomic force microscopy (AFM) (Innova SPM). The mode used was tapping and the scanning area was 5×5 μm^2. The films were studied under UV–Visible spectrometer (UV-Vis) (Lambda 950, Perkin Elmer) to estimate the degree of transparency and the optical energy band gap was estimated from absorption spectra through Tauc's plot. The average thickness of the fabricated films was measured by using near normal spectroscopic reflectometer (HO-NNSR-01, Holmarc). The thickness of ZT0, ZT1, ZT2 and ZT3 was 138 ± 3 nm, 137 ± 1 nm, 138 ± 4 nm, and 136 ± 1 nm, respectively. To check the chemical state of the elements existing in the films, X-ray photoelectron spectroscopic study (XPS, Kratos Axis Ultra DLD) was conducted. The C-H peak of adsorbed carbon positioned at a binding energy of 284.6 eV was used for the calibration of the resulted spectra. Furthermore, XPS curve fitting software package (XPSPEAK41) was utilized to perform the fitting of the spectra. Full-width half maximum (FWHM) and Gaussian/Lorentzian (G/L) ratio were maintained constant to evade the discrepancy during the peak fitting. For the best peak fitting, a minimum chi-square was selected. Shirley was used as the background type in the fitting. The fitted XPS spectra of C 1s of all the films and the details of the fitting parameters are given in Appendix III.
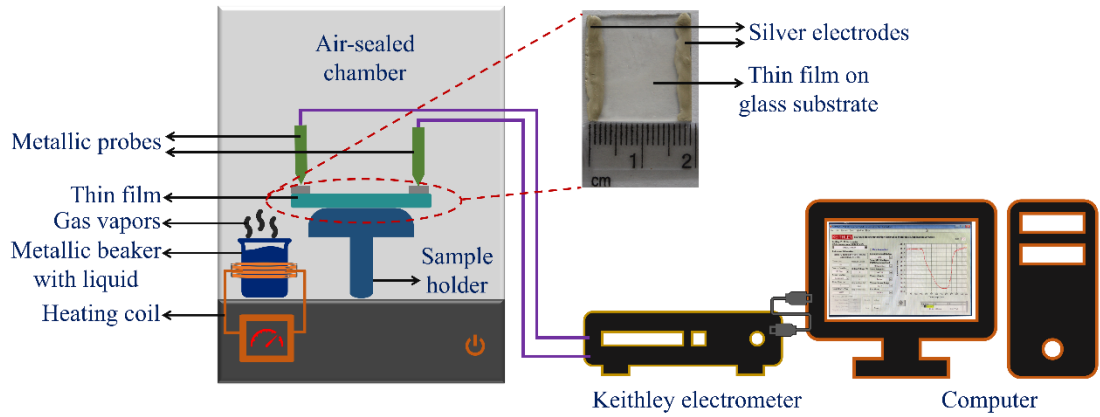
Fig. 4.2: Schematic representation of custom-made gas sensing measurement equipment.

The gas sensing characterization of all the films was performed towards ammonia (NH_3) gas in the present study. It was executed in a custom-made set-up, which contains air-sealed chamber, metallic probes, metallic beaker, sample holder and heating coil. The schematic representation of the custom-made gas sensing measurement equipment is shown in Fig. 4.2. The static liquid gas method was utilized in this study to estimate the appropriate concentration of the target gas (C) in ppm and the estimation was performed by using equation 4.6.

$$C = \frac{22.4 \times \varphi \times \rho \times V_1}{M \times V_2} \times 1000 \qquad (4.6)$$

Here C is concentration of the gas in ppm, φ is volume fraction of the gas, ρ is density of the liquid (g/ml), V_1 is volume of the liquid in μL, M is molecular weight of the liquid (g/mol), and V_2 is volume of the chamber in L (Poloju et al. 2018). The volume of the chamber used in the present study is 10 L. For the gas sensing measurements in this study, silver electrodes were deposited on two opposite edges of all the films as the electrical contacts. To make the silver electrodes, the silver paste was applied longitudinally on two opposite edges of the films (as shown in Fig. 4.2) with the help of a tiny nail brush. Later, the films with silver paste were dried on a hot plate maintained at 110 °C for 15 min to evaporate the solvent in the paste. After drying, the silver electrodes were formed on the film. Later, the respective film with silver electrode was placed on the sample holder in the air-sealed chamber through a front

door adjustment. The film was connected with a metallic probe on each silver electrode present on its edge. Later, the NH_3 solution in appropriate quantity (measured through Eq. 4.6) was injected through a syringe in the metallic beaker connected to a heating coil, which was present at the bottom of the chamber. The gas vapors were ejected when the solution in the beaker achieved the required temperature and the gas vapors were then sensed by the film. The variation in the electrical resistance of the film upon exposing to the gas vapors was measured through a Keithley electrometer (model no. 6517 B), which was connected to a computer. The applied DC voltage was -3 V during the measurement. After reaching the resistance to a saturation level, the chamber door was opened to pass the gas vapors outside and to simultaneously allow the atmospheric air inside the chamber. The gas response or gas sensitivity (S) was calculated in the present study by using equation 4.7.

$$S = \frac{R_a - R_g}{R_g} \tag{4.7}$$

where R_a is resistance of the film in air and R_g is resistance of the film in the target gas (Manjunath et al. 2021a). In this manner, the gas response of the films to different concentrations of NH_3 gas (25 to 100 ppm) was studied in the current study. The selectivity test of ZT0 film was performed towards 100 ppm concentration of gases such as formaldehyde, ethanol, xylene, methanol, and toluene, respectively. All the gas sensing measurements were conducted at room temperature. The time taken by the film to attain a 90 % change in the total resistance was considered as response time during the adsorption and as recovery time during the desorption of the target gas in this study.

4.2.2 Results and discussion

The TGA plots of the pristine, 1, 2 and 3 wt.% Ti doped combustible precursors are presented in Fig. 4.3 (a, b, c and d, respectively). The TGA curve of all the precursors is categorized into five regions with respect to temperature, namely, region I (35 °C to ~150 °C), region II (~150 °C to ~205 °C), region III (~205 °C to ~235 °C), region IV (~235 °C to ~360 °C) and region V (~360 °C to 600 °C); and the respective weight loss in each region is given in Fig 4.3. It is noticed that the weight loss has occurred in four steps in all the precursors. The first major weight loss (~50 to 59 %)

in region I can be attributed to the evaporation of the solvent. A minor weight loss is observed in region II in all the precursors and it can be dedicated to the loss of bound water, i.e., evaporation of water molecules from zinc nitrate hexahydrate (Manjunath et al. 2021a). In region III, a sudden weight loss of 10 to 12 % is traced in all the TGA curves of the precursors and it can be credited to the combustion reaction that occurred in the precursor. Generally, a combustion reaction takes place between the oxidizer and fuel with the liberation of enormous heat and by-product gases. This leads to weight loss due to the sudden release of the by-product gases. The generated heat helps in the formation of desired metal oxide. The attained combustion temperature range to produce pristine and doped ZnO in this study is in line with the previous report (Manjunath et al. 2020). Commenting on region IV, a gradual weight loss (~3 to 8 %) is noticed in all the precursors and it can be dedicated to the further removal of carbonaceous impurities left out after the combustion reaction. Further, in region V, no change in the TGA curve or no noticeable weight loss is detected; it can be due to the formation of stable ZnO or Ti-doped ZnO at higher temperatures.
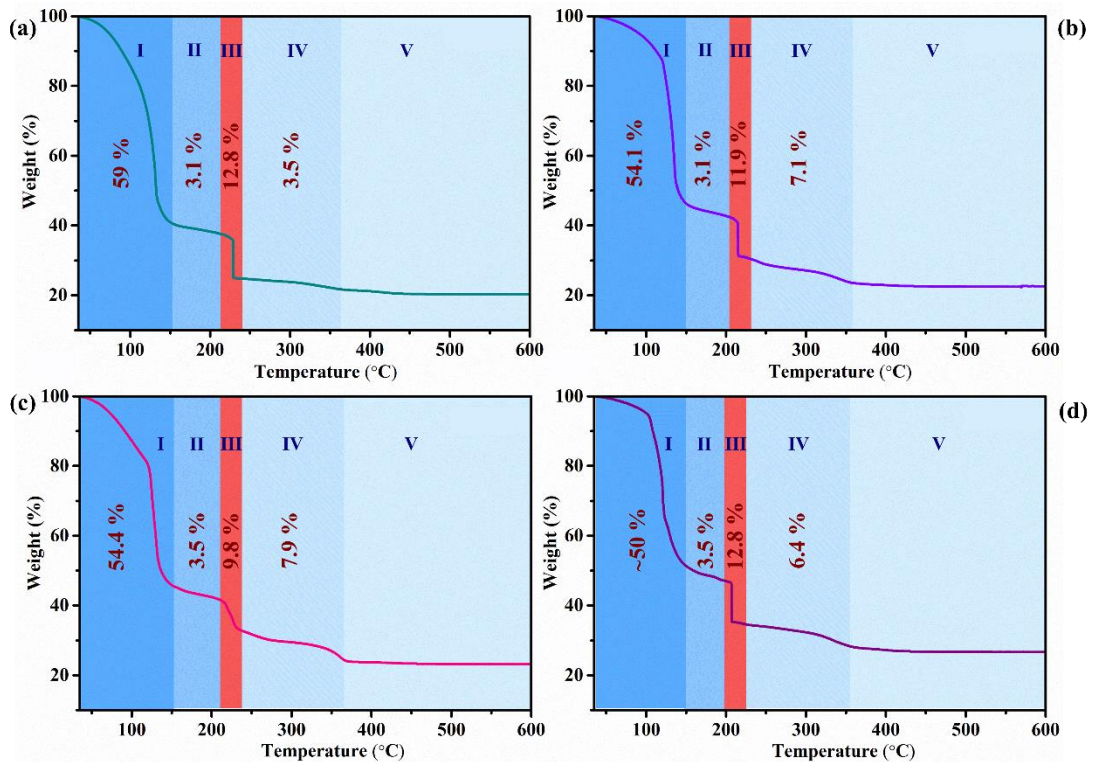
Fig. 4.3: TGA plots of (a) pristine, (b) 1 wt.% Ti, (c) 2 wt.% Ti and (d) 3 wt.% Ti doped combustible precursors, respectively.

The GIXRD patterns of the ZT0 (0 wt.% Ti), ZT1 (1 wt.% Ti), ZT2 (2 wt.% Ti) and ZT3 (3 wt.% Ti) films are presented in Fig. 4.4 (a). It is observed that the films are predominantly crystalline in nature. The obtained diffraction planes, namely, (100), (002), (101), (102), (110), (103) and (112), are well coinciding with the hexagonal wurtzite crystal structure of ZnO (ICDD: 00-036-1451). A schematic representing the mentioned crystal structure of ZnO is shown in Fig. 4.4 (b). In the case of doped films, the absence of diffraction planes from the secondary phases of TiO_2 or Zn_2TiO_4 is noticed and it affirms that the Ti atoms are successfully substituted the Zn atoms in the present study.
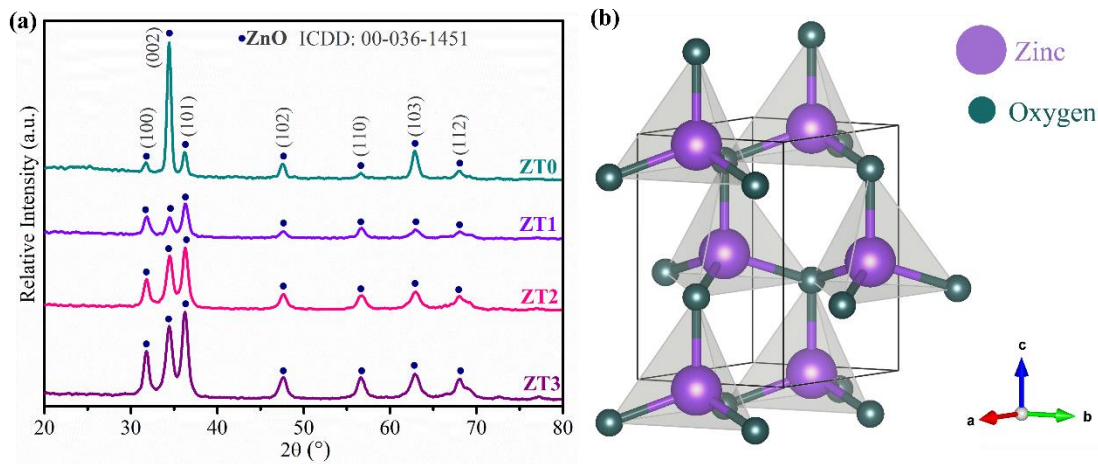
Fig. 4.4: (a) GIXRD patterns of ZT0, ZT1, ZT2 and ZT3 films, (b) schematic representing the hexagonal wurtzite crystal structure of ZnO. (The crystal structure is drawn using the VESTA visualization interface software and the crystallographic information file is taken from the Materials Project database (mp-2133)).

The diffraction pattern of ZT0 film showed a high intensity along the (002) plane, which can be considered as the preferred growth direction in the film. The (002) direction, i.e., the c-axis, is the preferential orientation which is generally detected in ZnO films (Lu 2007) (Bergum et al. 2014) (Kumar et al. 2020). The preferred growth direction along the (002) plane in ZT0 film of the present study is well coordinated with the previous reports. However, the preferred growth direction has changed towards the (101) plane in ZT1, ZT2 and ZT3 films. The change in the growth orientation upon doping with Ti is also observed in the earlier report(Bergum et al. 2014). A previous study reported that the substitution of Zn atoms by Ti atoms originates a distortion of the polycrystalline structure of ZnO (Chung et al. 2008). It is observed that ZT1 film

showed the minimum crystallinity among all the films and ZT0 film achieved the maximum crystallinity. The obtained trend of the crystallinity is ZT0 > ZT3 > ZT2 > ZT1. The average crystallite size of ZT0 film is found to be 14 nm, and it is ~10 nm for ZT1, ZT2 and ZT3 films, respectively (from equation 4.5). The average crystallite size has decreased after doping Ti (ZT1, ZT2 and ZT3 films) and it can be concluded that the dopant Ti has a suppressive effect on the ZnO crystal growth. The decrement in the crystallite size of pristine ZnO after doping with Ti is also noticed in the previous reports (Eshaghi et al. 2015) (Sridhar et al. 2014).

From the FESEM images (Fig. 4.5 (a, b)), it is observed that ZT0 film has equipped with high porosity and with larger, spherical-shaped grains. It is also noticed from the images (Fig. 4.5 (c to h)) that the microstructure of films such as ZT1, ZT2 and ZT3 is completely changed after Ti doping. The microstructure of these doped films is dense with much smaller, uniformly distributed grains, and the microstructure resembles almost similar in all doped films. A reduction in the grain size from pristine ZnO film to Ti doped ZnO film is also noticed in previous studies (Eshaghi et al. 2015) (Liu et al. 2012) (Sridhar et al. 2014). It can be concluded from the microstructural features that the dopant Ti has a substantial influence on the morphology of the doped films compared to pristine film. These results coincide well with GIXRD analysis, where the average crystallite size of ZnO decreases after doping with Ti. The films are quite uniform, and the existence of cracks and peeling are not detected, which confirms the effective fabrication of the films. It is observed from Fig. 4.6 (a) that ZT0 film has revealed the presence of Zn, O elements along with C element. The carbon in the film can be attributed to the surface adsorption from the atmosphere in the form of CO and CO_2 etc. (Regragui et al. 2000). The Zn, O, and C elements along with Ti element are observed in the spectra of ZT1, ZT2 and ZT3 films (Fig. 4.6 (b, c and d, respectively)). Interestingly, it is also discerned that the resulted weight percentage of Ti obtained from the spectra is almost the same as the doping level maintained in the respective precursors that are used for depositing the respective films, which confirms the effective doping of Ti in the host ZnO crystal. The elemental mapping of all the films is given in appendix III. It is noticed that the Zn, O, Ti and C elements are uniformly distributed on the surface of the respective films.
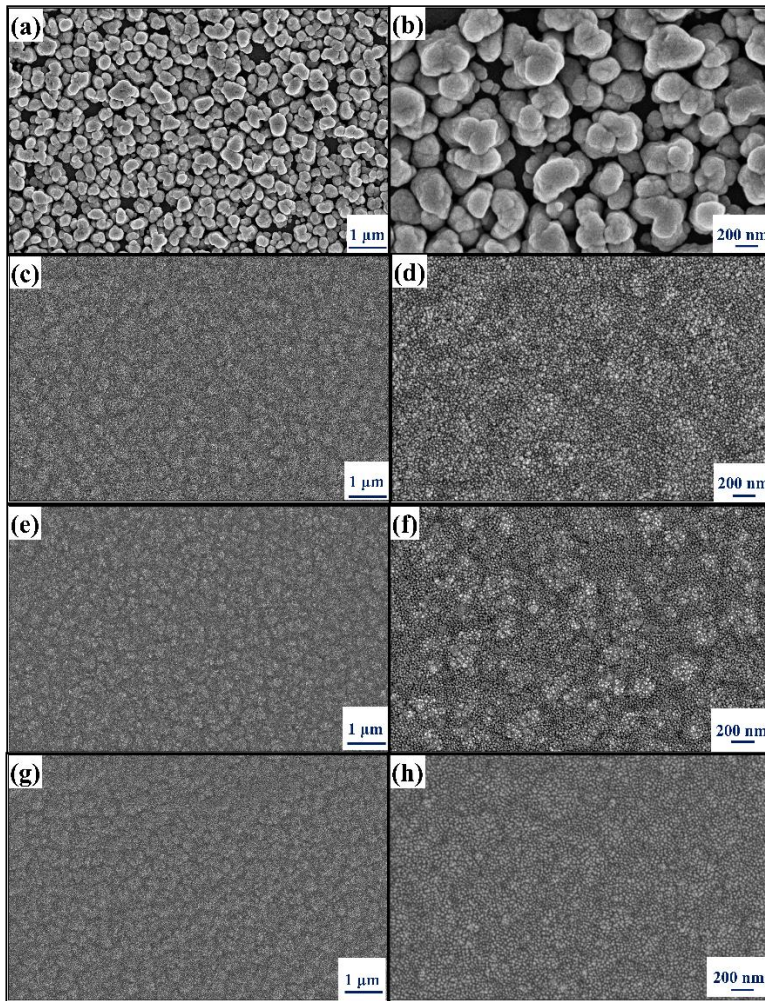
Fig. 4.5: FESEM images showing morphology of (a, b) ZT0, (c, d) ZT1, (e, f) ZT2 and (g, h) ZT3 films, respectively.
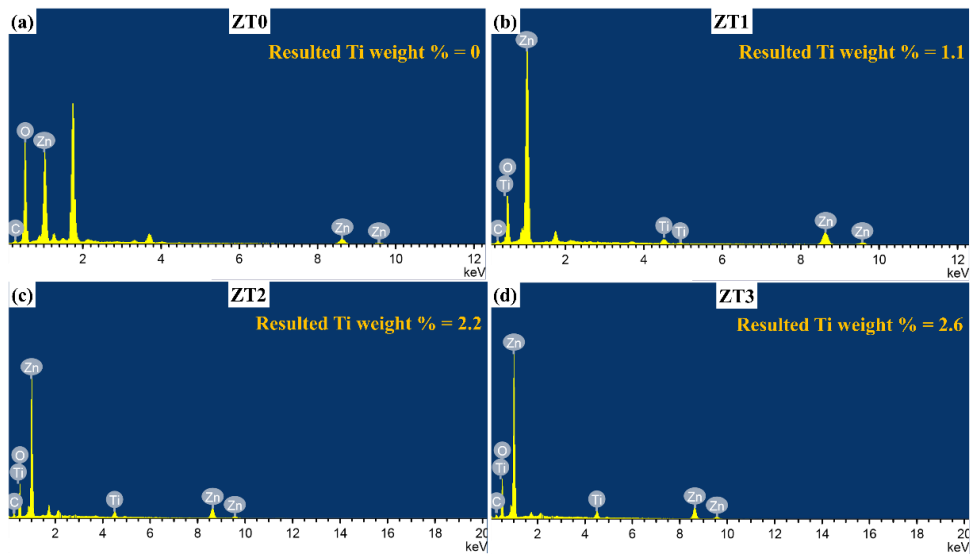
Fig. 4.6: EDAX spectra of (a) ZT0, (b) ZT1, (c) ZT2 and (d) ZT3 films, respectively.
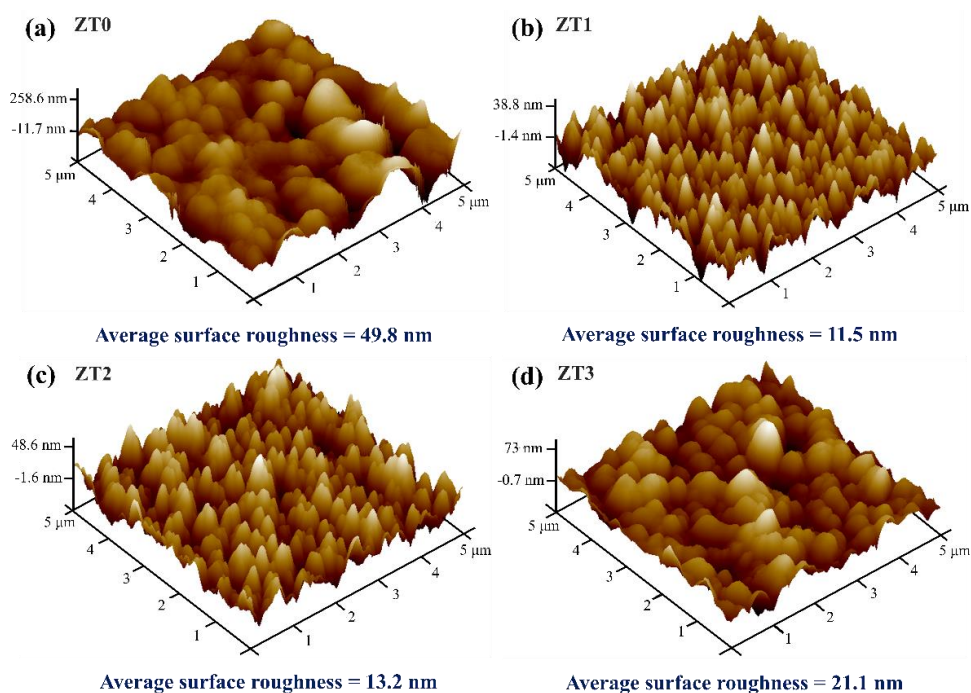
Fig. 4.7: AFM images with average surface roughness values of (a) ZT0, (b) ZT1, (c) ZT2 and (d) ZT3 films, respectively.

The morphological features of all the films are derived from AFM and the resulted 3D surface topographical images are shown in Fig. 4.6. It is noticed from Fig. 4.7 (a) that ZT0 film is comprised of bigger-sized grains contributing an average surface roughness of 49.8 nm. The morphology of ZT0 film with bigger-sized grains and intermediate pores, which is determined from AFM analysis, is in decent agreement with the FESEM images (Fig. 4.5 (a, b)). The morphology is varied and the grain size is significantly reduced after Ti doping in ZT1, ZT2, and ZT3 films compared to ZT0 film (Fig. 4.7 (b, c and d, respectively)) and it is similar to the FESEM analysis. ZT1 film has a minimum average surface roughness of 11.5 nm compared to other films with a dense morphology. The average surface roughness of ZT2 and ZT3 films is 13.2 nm and 21.1 nm, respectively. The trend of average surface roughness of the films is derived as ZT0 > ZT3 > ZT2 > ZT1. The decrement of the surface roughness in Ti doped films compared to pristine film was also noticed in the previous reports (Eshaghi et al. 2015) (Sridhar et al. 2014). It is known that the surface roughness of the film is influenced by the crystallinity; the higher the crystallinity, the higher is the surface

101

roughness of the film (Pujar et al. 2018). It is observed that the crystallinity (traced from GIAXRD analysis) and surface roughness (derived from AFM analysis)) of the films are well interconnected and has followed the same trend, i.e., ZT0 > ZT3 > ZT2 > ZT1. Since ZT0 film has high crystallinity, it exhibited high surface roughness, whereas the low crystallinity in ZT1 film led to low surface roughness (Sridhar et al. 2014).
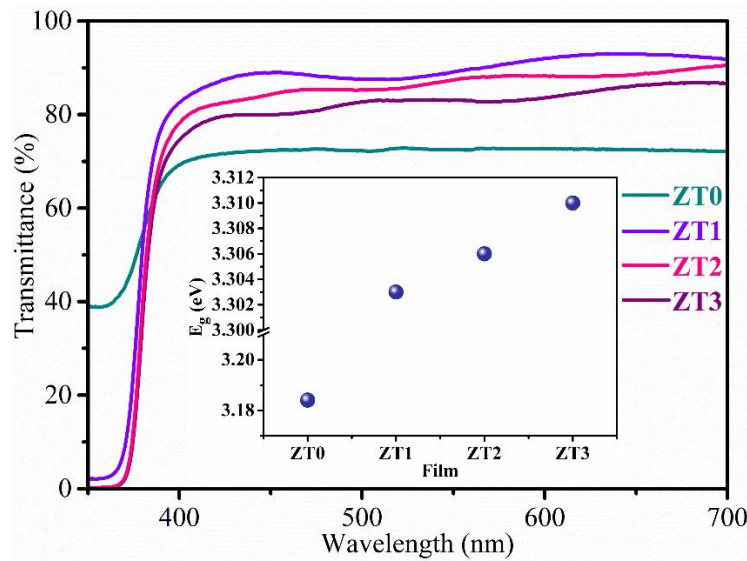
Fig. 4.8: Transmittance plots of ZT0, ZT1, ZT2 and ZT3 films. Inset showing the variation in the optical energy bandgap (E_g) of the films.

Fig. 4.8. displays the normalized transmission curves of all the films and it indicates that the value of the average transmittance of all the films varies in the range of ~70 to 90% in the visible region. All the fabricated films in the present study hold good optical transparency in the visible region. It is observed that ZT0 film exhibited the minimum transparency (~70%) compared to the other films, whereas maximum transparency (~90%) resulted in ZT1 film. The noticed trend in the transparency of the films is ZT1 > ZT2 > ZT3 > ZT0. The surface roughness plays a vital role in the optical properties of the thin film. It is reported that if the surface roughness is high, the incoming light scatters and the transparency decreases (Eshaghi et al. 2015). It can be deduced that the transparency is inversely related to the surface roughness. The transmittance of the films exhibited an exact inverse relation with the surface roughness in the present investigation; i.e., the higher the surface roughness, the lower is the transparency. A similar correlation between transparency and surface roughness was detected in the previous reports as well (Eshaghi et al. 2015) (Kumar et al. 2020). As

ZT0 film comprised a higher surface roughness, the scattering of the incoming light is higher; so, it results in minimum transparency. ZT2 and ZT3 films with comparatively less surface roughness than ZT0 showed better transmittance than ZT0 film. Compared to all the films, ZT1 film owned a lower surface roughness; therefore, it exhibited maximum transparency in the current study.

The optical energy band gap (E_g) of the fabricated films is estimated through Tauc's relation (presented in equation 3.2). Here, the value of index 'n' in equation 3.2 is considered as ½, since ZnO is a direct band gap semiconductor (Chen et al. 2010). The variation of the E_g values of all the films obtained from Tauc's plot is presented in the inset of Fig. 4.8; the respective Tauc's plot of the films are in Appendix III. It is found that the value of E_g of ZT0 film is 3.184 eV. The E_g value has gradually increased with increasing the Ti doping content. In this study, ZT3 film has derived the highest E_g value of 3.31 eV. The increment in the E_g value with increasing the Ti doping content from pristine ZnO film was also observed in the literature (Eshaghi et al. 2015) (Sridhar et al. 2014) (Naderi et al. 2017) (Liu et al. 2012) (Lin et al. 2005). The gradual enhancement of E_g value with Ti addition can be dedicated to Burstein–Moss effect and it is given in the following equation 4.8.

$$\Delta E^{BM} = \left(\frac{h^2}{8m^*}\right)\left(\frac{3N}{\pi}\right)^{2/3} \tag{4.8}$$

Here ΔE^{BM} is denoted as the broadening of E_g, h is denoted as the Plank constant, m* is denoted as the effective mass of electron and N is denoted as the carrier concentration (Shelke et al. 2013). From equation 4.8, it is inferred that the broadening of E_g has a direct relation with the N and there will be an increase in E_g if the N increases. The N enhances due to substitutional doping of Ti^{4+} in the Zn^{2+} sites, which donates two extra electrons as per equation 4.9.

$$Ti \underset{Zn}{\rightarrow} Ti^{\bullet\bullet}_{Zn} + 2e' \tag{4.9}$$

Therefore, in the present study, it can be presumed that the enhancement in the E_g value with the Ti dopant content is due to an increment in carrier concentration (Liu et al. 2012). Basically, the electrons from the dopant atoms fill the states near the conduction band minimum (CBM), which causes the displacement of the fermi level towards the

CBM. This effectively lifts the band gap upwards. This phenomenon prompts an enhancement in E_g with the doping concentration (Er et al. 2021; Eshaghi et al. 2015).

The band gap generally signifies the energy difference between the top of valence band and the bottom of conduction band. In a direct band gap, the top of valence band and the bottom of conduction band have the same momentum value. Whereas, in the case of an indirect band gap, the top of valence band occurs at a different momentum value than the bottom of conduction band. The fundamental band gap between the valence band and conduction band obtained using an incident photon source characterized by UV-Vis spectroscopy is called an apparent optical band gap.

It is also observed that ZT2 and ZT3 films exhibit less transparency compared to ZT1 film though their E_g values are higher. It can be assumed that the relatively high surface roughness values of ZT2 and ZT3 films than ZT1 film played a dominating part in the decrement of the transparency by scattering the incoming light, although they possess high E_g values.

The fabricated films are evaluated under XPS characterization to study the oxidation states of Zn, Ti and O. The wide spectra of all the films are given in Fig. 4.9 (a). The wide spectrum of ZT0 film reveals the presence of peaks of Zn and O elements at their respective binding energy positions. A peak at ~284 eV represents the binding energy of C 1s. The presence of C can be ascribed to adventitious carbon contamination (Joshi et al. 2019). In the case of ZT1, ZT2 and ZT3 films, the element Ti is detected in the wide scan along with Zn, O and C elements, and it confirms the coexistence of Zn, Ti and O elements in Ti doped ZnO films. The results of elemental presence derived from the XPS wide spectra are in decent agreement with the data obtained from the EDAX analysis.

Furthermore, the Zn 2p high-resolution spectra of all the films are displayed in Fig. 4.9 (b). It is noticed that the Zn 2p exhibited two distinct peaks at binding energies located at 1021.4 ± 0.6 eV and 1044.5 ± 0.6 eV in all the films. They can be assigned to the spin-orbit transitions of Zn $2p_{3/2}$ and Zn $2p_{1/2}$ peaks of Zn-O bonding with a spin-orbit splitting of ~23.1 eV; it approves that the Zn is in the oxidation state of +2. The obtained results are in good coordination with the reference value of ZnO that is

reported in the literature (Joshi et al. 2019) (Cao et al. 2019) (Li et al. 2018). The details of deconvoluted Zn 2p peaks of all the films are given in Table 4.1.
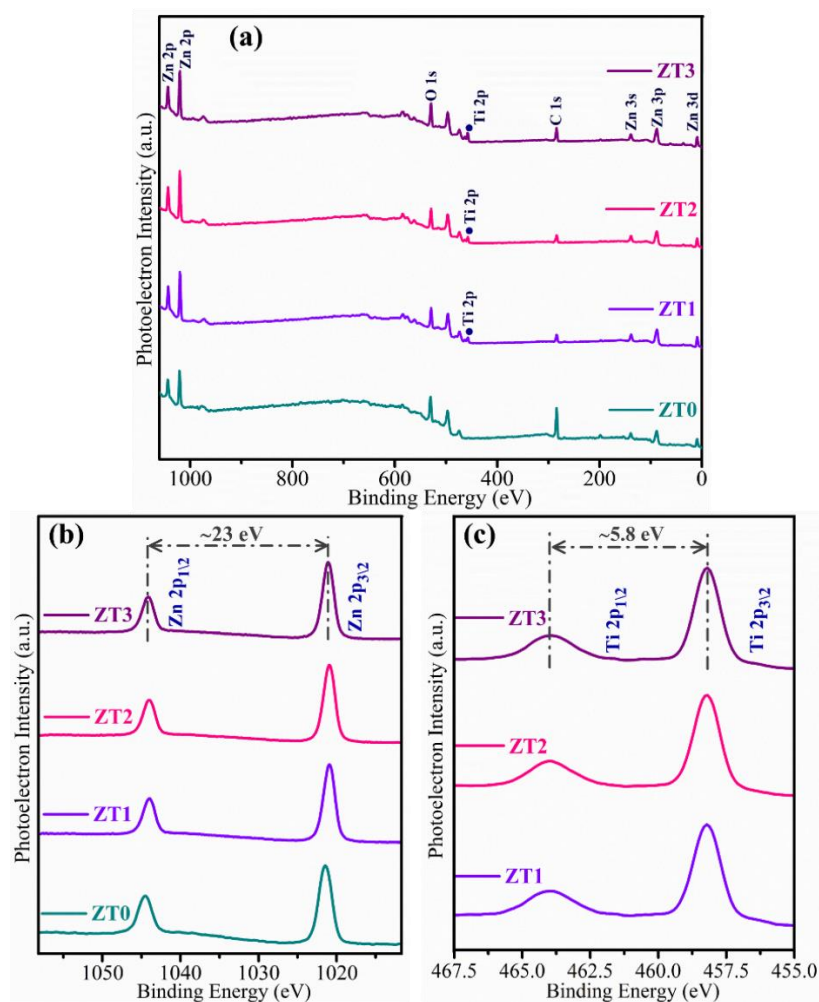
Fig. 4.9: (a) Wide scan XPS spectra of all the films, (b) Zn 2p high-resolution XPS spectra of ZT0, ZT1, ZT2 and ZT3 films, and (c) Ti 2p high-resolution XPS spectra of ZT1, ZT2 and ZT3 films.

The Ti 2p high-resolution spectra of ZT1, ZT2 and ZT3 films are presented in Fig. 4.9 (c). It is observed that the Ti 2p has also displayed a doublet situated at the binding energies of 458.2 ± 0.1 eV and 463.9 eV. They correspond to the spin-orbit transitions of Ti $2p_{3/2}$ and Ti $2p_{1/2}$, respectively, of Ti-O bonding. The spin-orbit splitting between the peaks is found to be ~5.8 eV. The obtained results convey that the element Ti is in the oxidation state of +4 and it is in decent correlation with the literature (Cao et al. 2019) (Wang et al. 2000) (Wiatrowski et al. 2018). The details of

deconvoluted Ti 2p peaks of all the films are given in Table 4.2. It can be concluded from XPS analysis that the films are composed with the required elemental states of Zn and Ti, respectively.

Table 4.1: Details of deconvoluted Zn 2p peaks of all the films.

Film	Deconvoluted peaks	Binding energy (eV)
ZT0	Zn $2p_{3/2}$	1021.4
	Zn $2p_{1/2}$	1044.5
		(Spin-orbit splitting = 23.1)
ZT1	Zn $2p_{3/2}$	1020.9
	Zn $2p_{1/2}$	1044.0
		(Spin-orbit splitting = 23.1)
ZT2	Zn $2p_{3/2}$	1020.8
	Zn $2p_{1/2}$	1043.9
		(Spin-orbit splitting = 23.1)
ZT3	Zn $2p_{3/2}$	1021.0
	Zn $2p_{1/2}$	1044.0
		(Spin-orbit splitting = 23)

Table 4.2: Details of deconvoluted Ti 2p peaks of all the films.

Film	Deconvoluted peaks	Binding energy (eV)
ZT1	Ti $2p_{3/2}$	458.2
	Ti $2p_{1/2}$	463.9
		(Spin-orbit splitting = 5.7)
ZT2	Ti $2p_{3/2}$	458.1
	Ti $2p_{1/2}$	463.9
		(Spin-orbit splitting = 5.8)
ZT3	Ti $2p_{3/2}$	458.1
	Ti $2p_{1/2}$	463.9
		(Spin-orbit splitting = 5.8)
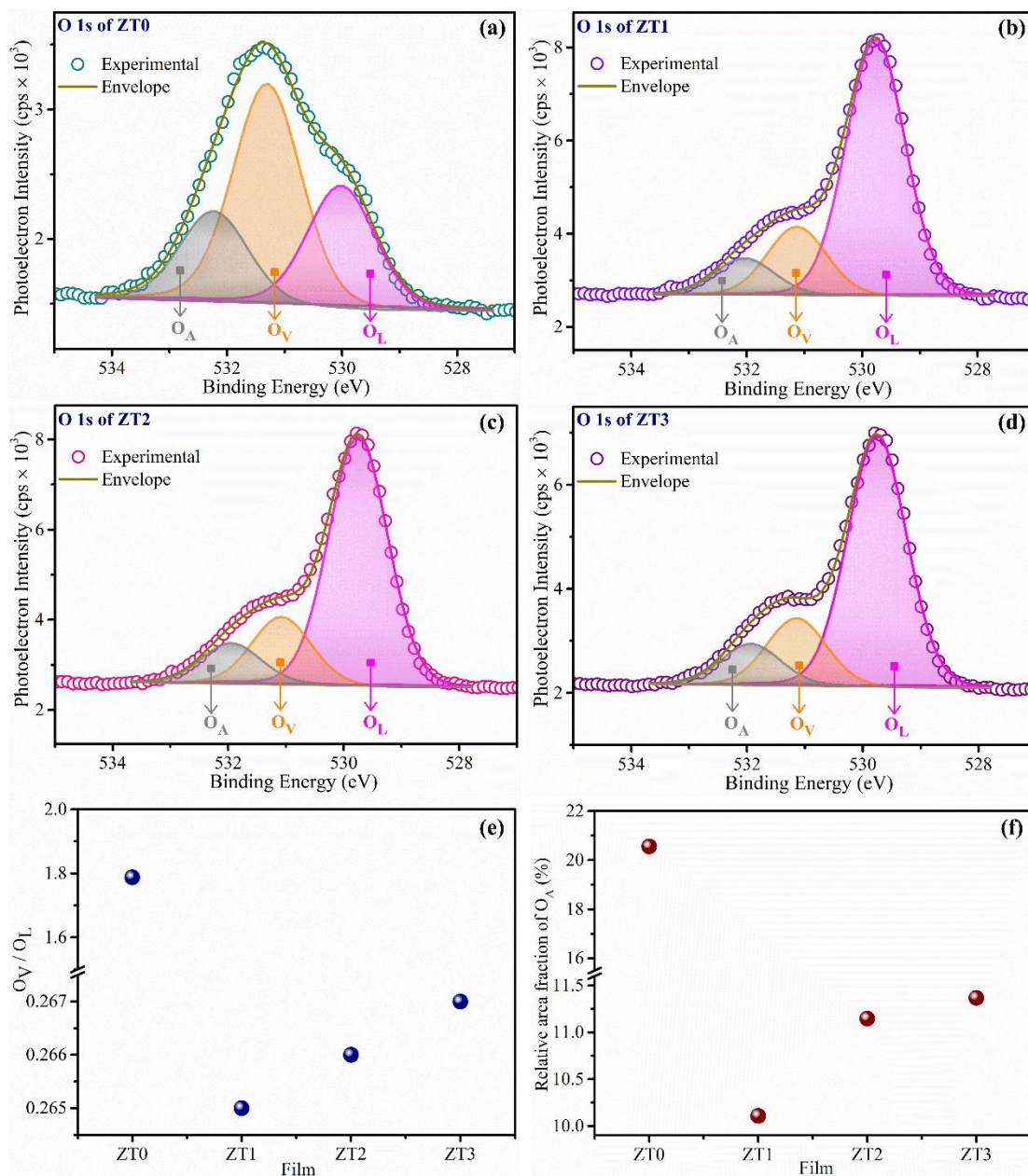
Fig. 4.10: Deconvoluted O 1s high-resolution XPS spectrum of (a) ZT0, (b) ZT1, (c) ZT2 and (d) ZT3 films, respectively, (e) Variation of O_V/O_L and (f) Variation of O_A relative area fraction in ZT0, ZT1, ZT2 and ZT3 films, respectively.

The respective deconvoluted O 1s high-resolution spectrum of ZT0, ZT1, ZT2, and ZT3 films are shown in Fig. 4.10 (a to d). The O 1s spectrum of every film is deconvoluted into three peaks that are centred at binding energies of ~530 ± 0.3 eV (Peak 1), 531 ± 0.3 eV (Peak 2) and 532 ± 0.3 eV (Peak 3). Peak 1 is dedicated to the O^{2-} ions in the Zn-O bonding of the wurtzite crystal structure of Zn^{2+} (lattice oxygen

(O_L)). Peak 2 is attributed to the O^{2-} state of oxygen vacancies or defects in the oxygen-deficient regions, which supports the non-stoichiometric ZnO formation (oxygen vacancies (O_V)). Lastly, Peak 3 is assigned to loose oxygen bonds on the surface (surface adsorbed oxygen species (O_A)) (Chen et al. 2010) (Claros et al. 2020) (Li et al. 2018). It is observed from Fig. 4.10 (a) that Peak 2 (O_V) appeared to be much stronger than the other two peaks in ZT0 film, which demonstrates that the majority of O^{2-} is in the state of oxygen vacancies. In the case of doped films, i.e., ZT1, ZT2 and ZT3, Peak 1 (O_L) seems to be dominating (Fig. 4.10 (b, c and d, respectively)). It can be confirmed that a high amount of oxygen vacancies is developed in ZT0 film compared to the other films.

Table 4.3: The respective position and area of O 1s deconvoluted peaks of all the films.

Film	Peak	Peak position (eV)	Area (cps × eV)
ZT0	O_L	530.0	1506.2
	O_V	531.3	2693.7
	O_A	532.2	1086.9
ZT1	O_L	529.7	7263.8
	O_V	531.1	1929.9
	O_A	532.0	1033.9
ZT2	O_L	529.7	7300.1
	O_V	531.0	1945.6
	O_A	531.9	1159.8
ZT3	O_L	529.7	6357.1
	O_V	531.1	1694.9
	O_A	531.9	1032.7

For further validation, the oxygen vacancy concentration, i.e., the ratio of the area of oxygen vacancies to the area of lattice oxygen (O_V/O_L) (Manjunath et al. 2021b), is calculated for all the films. The variation of O_V/O_L of all the films is represented in Fig. 4.10 (e) and it is found that ZT0 film has attained the highest oxygen vacancy concentration in contrast to other films. Whereas the minimum O_V/O_L is found in ZT1

film, and it follows the ZT0 > ZT3 > ZT2 > ZT1 trend. Additionally, the relative area fraction of adsorbed oxygen species (% of O_A), i.e., (area of O_A/(areas of O_L+O_V+O_A)), is calculated and the variation of it is projected in Fig. 4.10 (f). Remarkably, ZT0 film also showed the maximum relative area fraction of O_A, followed by ZT3, ZT2 and ZT1 films. The trend of the relative area fraction of O_A can be represented as ZT0 > ZT3 > ZT2 > ZT1. The respective position and area of O 1s deconvoluted peaks of all the deposited films are detailed in Table 4.3.
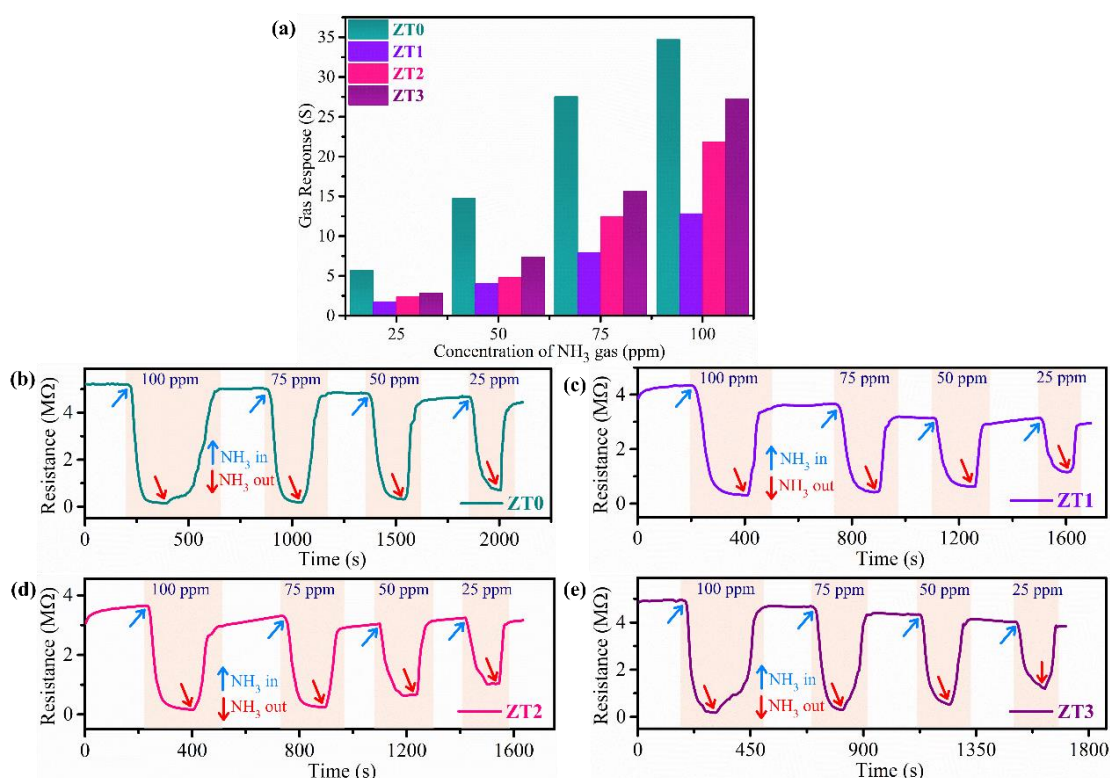
Fig. 4.11: (a) Gas response of all the films towards different concentrations of NH_3 gas at room temperature; the electrical resistance variation of (b) ZT0, (c) ZT1, (d) ZT2 and (e) ZT3 films, respectively, at various concentrations of NH_3 gas.

The gas response (S) of all the films towards different concentrations of NH_3 gas (25 to 100 ppm) at room temperature is presented in Fig. 4.11 (a). With the enhancement in NH_3 gas concentration from 25 to 100 ppm, the magnitude of the gas response of all the films has increased significantly, which reveals the dependency of the gas response on the NH_3 gas concentration. The key reason for such kind of linear dependency is due to strong relation of gas response on the removal of chemisorbed

oxygen species which occurs during the reaction with the target gas molecules. It causes the return of the electrons to the conduction band, which results in the decrement of electrical resistance and increment of gas response. Thus, when the films are exposed to low NH_3 concentration, the NH_3 molecules coverage on the films' surface is less, which causes lower reactions with chemisorbed oxygen species and, consequently, minimal gas response. When NH_3 concentration is enhanced, the coverage of gas molecules of NH_3 on the surface of the films is more and the reactions of gas molecules with chemisorbed oxygen species also enhance, which leads to an increment in the gas response (Shingange et al. 2016). The gas response is maximum in pristine ZT0 film compared to Ti doped films irrespective of NH_3 gas concentration. The trend of the gas response of the films at every concentration of NH_3 gas is noticed to be ZT0 > ZT3 > ZT2 > ZT1. A reduction in the gas response in Ti doped ZnO sample compared to pristine ZnO sample was also observed in the previous study (Han et al. 2010). In the current study, the highest gas response value of 34.7 has achieved in the case of ZT0 film at 100 ppm of NH_3 gas concentration. The probable reasons behind the high gas response in ZT0 film compared to other films are explained in further sections.

The variation in the electrical resistance of all the films is recorded when they are exposed to different concentrations of NH_3 gas and the resistance variation in ZT0, ZT1, ZT2 and ZT3 films is displayed in Fig. 4.11 (b, c, d and e, respectively). The resistance of all the films has gradually reduced when the NH_3 gas is introduced, and it is due to the adsorption of NH_3 molecules on the films and the reaction with chemisorbed oxygen species. A progressive increment in the resistance value is noticed when the NH_3 gas is allowed to leave the chamber, indicating the simultaneous desorption of NH_3 molecules and adsorption of oxygen molecules due to inward airflow in the chamber (Manjunath et al. 2020). The decrement (during NH_3 gas exposure) and increment (during NH_3 gas evacuation) in the resistance of all the films have occurred at all the concentrations of NH_3 gas. A comparatively large variation in the resistance of all the films is noticed at higher NH_3 concentrations and vice versa. The resistance variation confirms that all the fabricated films in the present study have exhibited the gas sensing behavior towards the NH_3 gas at room temperature.

The measured response and recovery times of all the films as a function of NH_3 concentration are shown in Fig. 4.12 (a) and (b), respectively. The range of the response time is found to be 100 to 114 s, 83 to 112 s, 82 to 105 s, and 81 to 91 s, respectively, for ZT0, ZT1, ZT2, and ZT3 films when NH_3 gas concentration varied from 25 to 100 ppm (Fig. 4.12 (a)). ZT0 film has exhibited a high response time compared to the doped films at all concentrations of NH_3 gas. Generally, the output of metal oxide-based sensors is the electrical resistance modulation. The relation between the electrical resistance (ρ), mobility (μ) and carrier concentration (N) is given by '$\rho = 1/Ne\mu$'. The electrical resistance relies on N when μ is constant. And the N is a function of oxygen vacancy concentration. The gas sensor kinetics depends on the following diffusions and reactions of oxygen vacancies: (i) the surface reaction, $O_O^x \rightarrow (V_O^{\bullet\bullet})_s + 2e' + \frac{1}{2} O_2$ (g), (ii) the surface diffusion of oxygen vacancies $(V_O^{\bullet\bullet})_s$, (iii) the reaction between the surface oxygen vacancies $(V_O^{\bullet\bullet})_s$ and the grain boundary vacancies $(V_O^{\bullet\bullet})_{gb}$, (iv) the grain boundary diffusion of vacancies $(V_O^{\bullet\bullet})_{gb}$, (v) the reaction between the grain boundary vacancies $(V_O^{\bullet\bullet})_{gb}$ and the volume vacancies $(V_O^{\bullet\bullet})_v$ and lastly (vi) volume diffusion of vacancies $(V_O^{\bullet\bullet})_v$ (Izu et al. 2003). When the kinetics of sensing are governed by the diffusion, then the smaller crystallite size helps in faster diffusion, as the diffusion of oxygen vacancies is directly proportional to the size of the crystal. The distance for the diffusion of oxygen vacancies reduces by reducing the crystallite size. Hence the response time reduces with the reduction in the crystallite size. When the kinetics of sensing are governed by the surface reactions, it is stated that the reaction between surface vacancies and grain boundary vacancies, and the reaction between grain boundary vacancies and volume vacancies are dependent on the crystallite size. It is due to the increment in the area for these reactions when the crystallite size reduces (Izu et al. 2003) (Manjunath et al. 2020). From the discussion, it is derived that the smaller crystallite size can aid in a lower response time. In the present study, it can be concluded from the description that the high response time in ZT0 film can be due to its high crystallite size (derived from GIAXRD analysis). A comparatively lower response time in ZT1, ZT2 and ZT3 films can be dedicated to their reduced crystallite size.
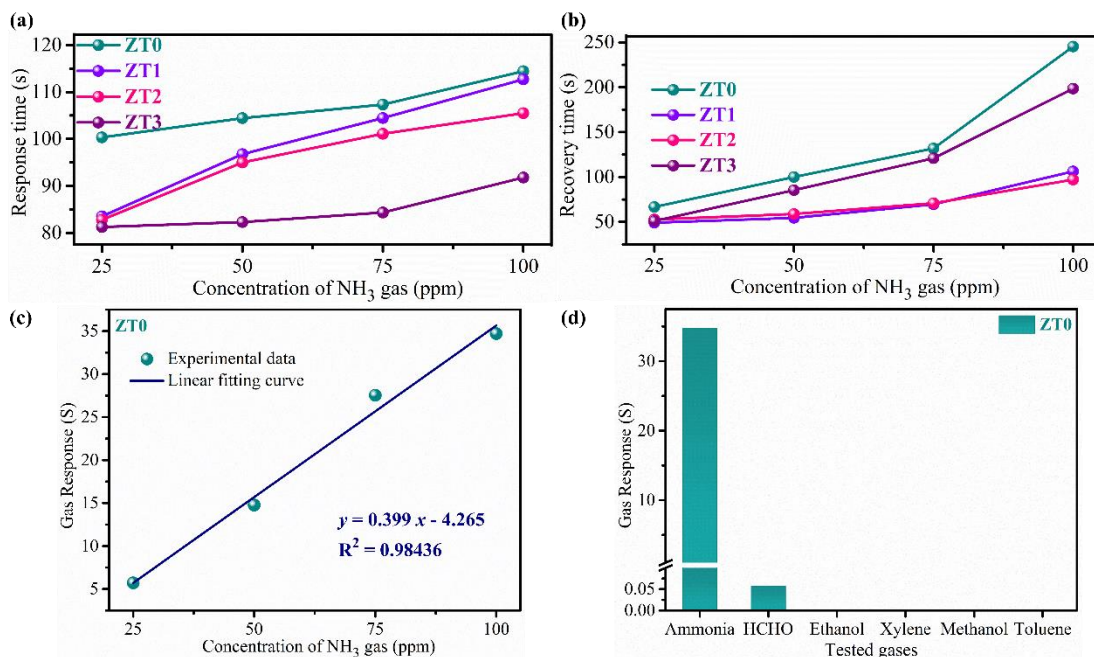
Fig. 4.12: (a) Response time, (b) recovery time of all the films towards different concentrations of NH_3 gas, (c) fitted curve of gas response of ZT0 film as a function of NH_3 gas concentration and (d) the response of ZT0 film when tested against different gases of 100 ppm at room temperature.

From Fig. 4.12 (b), the range of the recovery time is noticed to be 66 to 245 s, 49 to 106 s, 52 to 97, and 51 to 198 s, respectively, for ZT0, ZT1, ZT2, and ZT3 films when NH_3 gas concentration varied from 25 to 100 ppm. ZT0 film has exhibited a high recovery time and the recovery time is comparatively lower in ZT1, ZT2 and ZT3 films at all concentrations of NH_3 gas. The reason for the high recovery time in ZT0 film can be attributed to the high porosity (noticed in Fig. 4.5 (a and b)). Due to high porosity, the NH_3 gas molecules might have penetrated deeper layers of the film when it was exposed to the target gas. When the target gas was allowed to leave the chamber, the penetrated NH_3 gas molecules in porous ZT0 film might have taken more time to desorb from the deeper layers. Simultaneously, due to its porous nature, it might have allowed more atmospheric oxygen to penetrate, adsorb and generate the chemisorbed species; this process might have also taken a relatively higher time to recover its initial resistance. The cause for comparatively low recovery time in ZT1, ZT2, and ZT3 films can be dedicated to their dense/non-porous morphology, which might not have

permitted more NH$_3$ gas molecules to penetrate beneath the film. Due to this, these gas molecules have desorbed quickly and helped in faster recovery time.

Furthermore, the limit of detection of high gas-responded ZT0 film is estimated using the equation, which is obtained through linear curve fitting as shown in Fig. 4.12 (c). The relation between the obtained gas response at different concentrations of NH$_3$ gas is fitted with a linear fitting function, $y = 0.399\,x - 4.265$. Here y is the gas response and x is the concentration of NH$_3$ gas. The limit of detection of the ZT0 film is found to be ~10.7 ppm.

Table 4.4. The values of kinetic diameter, ionization energy of the different target gases.

Gas	Kinetic diameter (nm)	Ionization energy (eV)	Reference
Ammonia	0.36	10.18	(Ganesh et al. 2017)
Formaldehyde	0.4	10.87	(Kulandaisamy et al. 2016)
Ethanol	0.45	10.47	(Kulandaisamy et al. 2016)
Xylene	0.58 to 0.68	8.52	(Alomair and Alqaheem 2019) (Aluri et al. 2011)
Methanol	0.38 to 0.41	10.85	(Elshof et al. 2003) (Dojahn et al. 2001)
Toluene	0.58	8.82	(Ganesh et al. 2017)

Gas selectivity is the response given by the gas sensor against a particular target gas in a group of various gases. This test is hence performed with various target gases. It is a vital feature for assessing the efficiency of the gas sensors and it is also considered the main measure for the practical usage of them (Ganesh et al. 2017) (Manjunath et al. 2021b). In this study, the gas selectivity test is performed on the high gas-responded ZT0 film against various target gases such as formaldehyde (HCHO), ethanol, xylene, methanol, and toluene of 100 ppm concentration at room temperature and these gas response values are related with the value obtained towards NH$_3$ gas of 100 ppm concentration. The plot displaying the gas response of ZT0 film towards various gases is shown in Fig. 4.12 (d). ZT0 film revealed a high gas selectivity towards the NH$_3$ gas

and a very minute detection to HCHO gas. ZT0 film also exhibited a negligible response towards other gases like ethanol, xylene, methanol, and toluene. It is confirmed that ZT0 film is highly selective and can be used as an NH_3 gas sensor at room temperature due to its significant detection compared to other target gases. The deterministic reasons for the high response of the film to only NH_3 gas can be due to the existence of lone pair of electrons in NH_3 with prominent electron donating ability. The electron pair can be easily transported to the sensing area of the material when it comes into contact and produces significant resistance change. In addition, the kinetic diameter of the NH_3 molecule is comparatively lower than the kinetic diameters of other target gas molecules. The gas molecules with lower kinetic diameter have the capability to diffuse rapidly into the sensing zone, which results in a good gas response (Ganesh et al. 2017) (Manjunath et al. 2020). The low ionization energy of the gas molecules also assists in achieving high selectivity. The kinetic diameter as well as the ionization energy of the different target gases are detailed in Table 4.4. It is noted from Table 4.4 that even though xylene and toluene gas molecules have low ionization energy than NH_3 gas molecule, their bigger kinetic diameter will decrease their selectivity (Ganesh et al. 2017).

Commenting on the gas sensing mechanism, it commences with the adsorption of the atmospheric oxygen molecules on SMOs (here, ZnO (n-type)). It is well known that when SMOs are exposed to air, numerous oxygen molecules get adsorbed on the surface of the SMOs. The adsorbed oxygen molecules dissociate and each oxygen atom extracts the electrons from the SMO's conduction band and turns into chemisorbed oxygen species such as O_2^-, O^- and O^{2-}, and they depend on the operating temperature of the SMO sensor (Ganesh et al. 2017). It is reported that the adsorbed oxygen molecules turn in the form of O_2^- (at < 100 °C), O^- (at 100 to 300 °C) and O^{2-} (at > 300 °C) by reacting with the electrons of the SMO. Therefore, as mentioned, the adsorbed oxygen molecules convert to O_2^- at room temperature conditions (Shingange et al. 2016) (Hsu et al. 2014) (Kumar et al. 2020) and the kinetics of reactions are shown in equations 4.10 and 4.11.

$$O_{2 \text{ (gas)}} \leftrightarrow O_{2 \text{ (ads)}} \qquad\qquad (4.10)$$

$$O_{2\,(ads)} + e^- \rightarrow O_2^-$$ (4.11)

The adsorbed oxygen molecules are capable of extracting the electrons up to a specific depth (called Debye length) from the surface. The layer/region up to the Debye length is called the electron depletion layer due to the depletion of its charge carriers. The area of the electron depletion layer relies on morphology of the surface, grain size, concentration of oxygen vacancies, amount of adsorbed oxygen and the operating temperature (Miller et al. 2014) (Manjunath et al. 2021b). As stated above, when the adsorbed oxygen molecules pick the electrons from the conduction band of SMO, the density of electrons in SMO decreases. It results in the enhancement of the resistance of SMO till an equilibrium attains with the ambient atmosphere (called baseline resistance). When NH_3 gas is introduced, it reacts with the chemisorbed oxygen species that are present on the surface of SMO and it oxidizes to N_2, H_2O, and releases the electrons. Consequently, the released electrons from the oxidation reaction arrive at the SMO's conduction band. Thus, the area of the electron depletion layer declines, and it causes an increment in the density of electrons (carrier concentration) and a simultaneous decrement in the electrical resistance of SMO. The possible reaction when NH_3 gas molecules interact with chemisorbed oxygen species is shown in equation 4.12 (Ganesh et al. 2017).

$$4NH_3 + 3O_2^- \rightarrow 2N_2 + 6H_2O + 3e^-$$ (4.12)
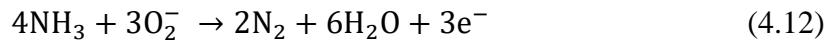
Table 4.5. The results obtained from various characterization studies of all the films.

Film	Crystallinity	ACS (nm)	Morphology	ASR (nm)	O_V/O_L	O_A (%)	S
ZT0	High	14	Highly porous	49.8	1.788	20.55	34.7
ZT1	Very low	~10	Dense	11.5	0.265	10.11	12.8
ZT2	Low	~10	Dense	13.2	0.266	11.14	21.8
ZT3	Moderate	~10	Dense	21.1	0.267	11.36	27.2

ACS = Average crystallite size, ASR = Average surface roughness, S = Gas response at 100 ppm

The results derived from various characterization studies of all the films that can be related to their attained gas response values in the present study are summarized in Table 4.5. As stated earlier, the pristine ZT0 film has the maximum gas response at all concentrations of NH_3 gas in comparison with Ti doped films in the current study. It is known that the grain size of SMO significantly influences the sensor's response. The reduction in the grain size assists in the enhancement of gas sensitivity. The gas response can exponentially enhance when the grain size is smaller or closer than the Debye length. When the grain size is way larger than twice the Debye length, the contact potential barrier governs the gas response instead of the grain size. Many reports have concentrated on the reduction of the grain size to increase the gas sensing properties. It is noted that the grain size has an inverse relation with the van der Waals force, which encourages agglomeration. Henceforth, the size of the grain should not be blindly decreased. In this scenario, it not only reduces the surface area but also inhibits the gas diffusion in between the grains (Zhu and Zeng 2017) (Seeley et al. 2009). Many reports in the literature showed that the films with low crystallite size showed a better gas response (Zhu and Zeng 2017). Based on this, in this study, one would expect that ZT1, ZT2 and ZT3 films exhibit a high gas response because of their smaller crystallite size. Remarkably, ZT0 film with a large crystallite size displays a major gas response, which is not intuitive. With a closer look at diffraction data, it inevitably directs that not only the crystallite size but also the other crucial property of the film, like crystallinity, can play a vital factor in influencing the gas response (Seeley et al. 2009). It is stated in the literature that better crystallinity increases the ability to detect the gas/chemical species (Katoch et al. 2013) (Choi et al. 2011). In their study, Choi et al. claimed that ZnO-based sensors with better crystallinity exhibited a superior gas response by eradicating the grain size effect (Choi et al. 2011). In another report, Katoch et al. also proved that higher crystallinity helped in achieving a good response in ZnO-based sensor (Katoch et al. 2013). Similarly, Manjunath et al., in their study, observed that ZnO-based film with high crystallinity and crystallite size exhibited a larger gas response towards NH_3 gas than the film with low crystallinity and crystallite size (Manjunath et al. 2021a). From this description, it can be correlated that in the present study, better crystallinity in ZT0 film is a factor in achieving comparatively high gas

116

response by abolishing the crystallite size effect. The order of crystallinity and average crystallite size of all the films are detailed in Table 4.5.

It is reported that the morphological features take part a crucial role in the gas sensing behaviour of the film. The fabricated film should comprise high porosity and roughness to promote the gas sensing performance (Kumar et al. 2020) (Zhu and Zeng 2017) (Gan et al. 2014). Due to its porous nature, the target gas can diffuse more into the film and react with chemisorbed oxygen species, and the gas sensing performance can be improved. Kumar et al., in their study, observed that the film containing high surface roughness exhibited a high gas response to NH_3 gas (Kumar et al. 2020). In the present case, ZT0 film has possessed those features of porous morphology with high surface roughness in contrast to other films (shown in Table 4.5). The NH_3 gas molecules might be penetrated more in the ZT0 film due to its porous nature, reacted with chemisorbed oxygen species and aided in large variation in electrical resistance. This can also be one of the reasons for achieving a high gas response in ZT0 film than the other films.

It is also found in the literature that enhancing the proportion of surface defects such as oxygen vacancies is beneficial in enhancing the gas sensing performance of SMOs like ZnO (Zhu and Zeng 2017) (Hsu et al. 2014). The presence of oxygen vacancies offers the adsorbed oxygen molecules to generate excess active sites (chemisorbed oxygen species) by transferring the electrons from the surface of films. These active sites will further promote the reaction with target gas molecules (Zeng et al. 2020). In the current study, ZT0 film has a high O_V/O_L compared to other films, as presented in Table 4.5. The high O_V/O_L in ZT0 film might have encouraged a greater number of electrons in the chemisorption process and directed to generate abundant active sites on surface of ZT0 film. In this scenario, ZT0 film might have depleted the electrons in a larger number and led to the formation of a thick depletion layer on surface. After the interaction of NH_3 gas molecules with active sites, the electrons might be released back to the ZT0's conduction band and caused a great shrink in the depletion layer, which aided in large electrical resistance variation and high gas response.
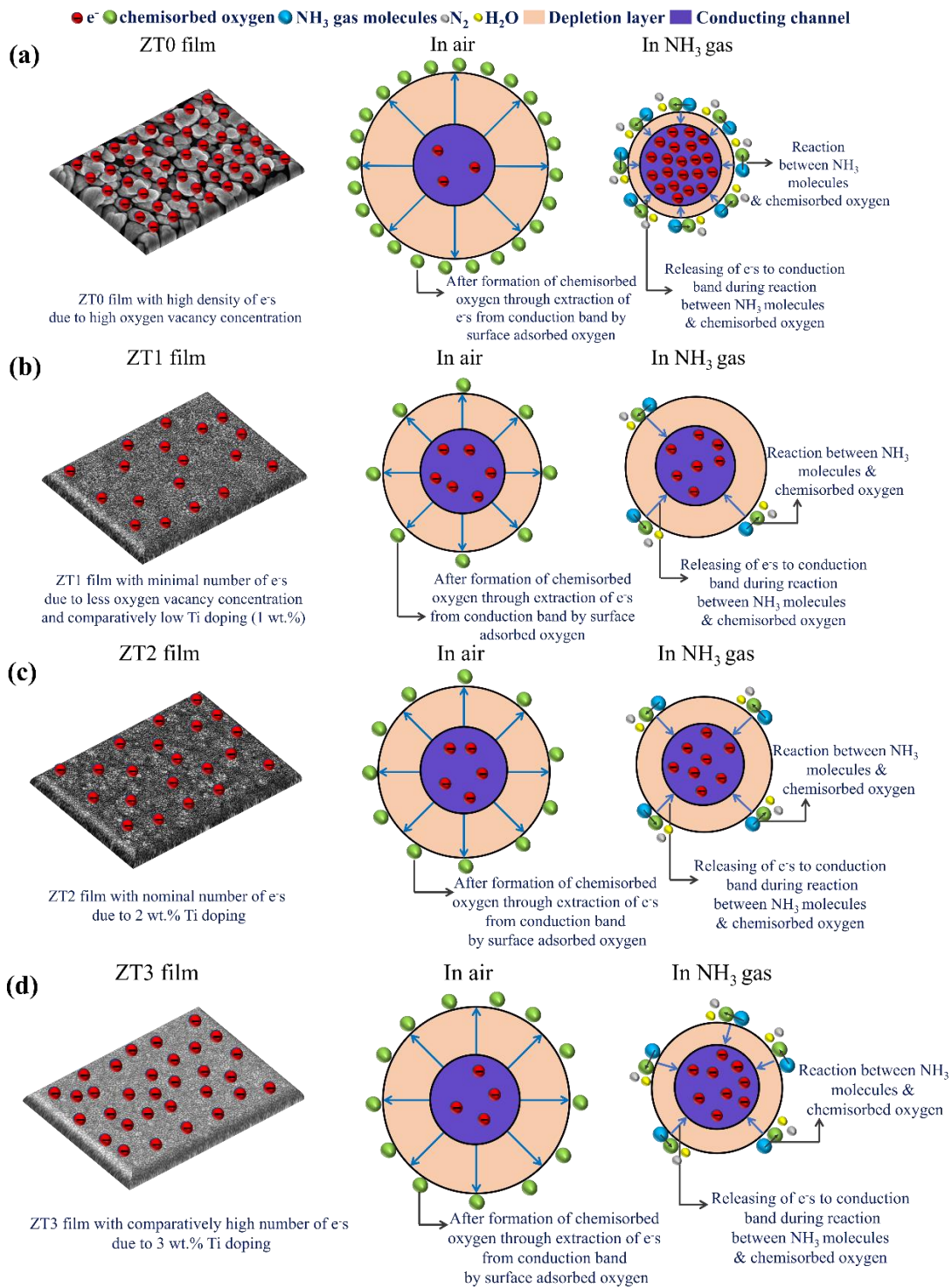
Fig. 4.13: Schematic representing the plausible gas sensing mechanism that occurred in (a) ZT0, (b) ZT1, (c) ZT2 and (d) ZT3 films.

Moreover, it is aforementioned that the electron depletion layer is dependent on the amount of adsorbed oxygen. If the amount of adsorbed oxygen is high, it extracts more electrons from the surface of the sensing layer, which causes a thick depletion layer and originates more active sites to take part in the gas sensing phenomenon. It is noticed from Table 4.5 that ZT0 film has a high % of O_A compared to other films. It means the high fraction of O_A in ZT0 film might have aided in the creation of more active sites to contribute in high gas response. The overall probabilistic reasons for attaining high gas sensing in ZT0 film than the other films can be high crystallinity, porous nature with high surface roughness, more O_V/O_L, and more % of O_A, as given in Table 4.5. The plausible gas sensing mechanism that occurred in ZT0 film is schematically represented in Fig. 4.13 (a).

Commenting on doped films, it is observed that ZT3 film exhibited relatively better gas response, followed by ZT2 and ZT1 films. It is categorized that the crystallinity of the film, O_V/O_L, and % of O_A contribute to the high gas response. It is observed from Table 4.5 that ZT3 film possessed comparatively better crystallinity than ZT1 and ZT2 films. The trend of crystallinity can be derived as ZT3 > ZT2 > ZT1. Also, the values of O_V/O_L and % of O_A of these films are in the trend, ZT3 > ZT2 > ZT1. It can be assumed that relatively high amounts of O_V/O_L and % of O_A might have promoted to generate comparatively higher active sites and aided to achieve better gas response in ZT3 film. A minor reduction in crystallinity and mentioned values (O_V/O_L and % of O_A) might have reduced the gas response in ZT2 film compared to ZT3 film. As ZT1 film possessed low crystallinity, slightly low values of O_V/O_L and % of O_A among all the films (given in Table 4.5), it can be presumed that these might be the factors for its inferior gas sensing properties. Furthermore, an increment in the doping % of Ti can enhance the donation of electrons, according to equation 4.9. During doping, the Ti^{4+} ions replace the Zn^{2+} ions and induce positive valence charges. These positive valence charges that emerged from the substitution need to be compensated by the generation of extra electrons to maintain the charge neutrality (Eshaghi et al. 2015) (Ganesh et al. 2017). The generated electrons are driven to the ZnO's conduction band of and cause enhancement in the concentration of electrons. It can also be assumed that ZT3 film might have possessed relatively more electron concentration due to

comparatively high doping of Ti (3 wt.%). This electron concentration might have contributed to generate relatively high active sites for NH_3 gas sensing. In the case of ZT1 film, due to the low doping of Ti (1 wt.%) in comparison with ZT2 and ZT3 films, it might have comprised less concentration of electrons and lower active sites, which resulted in poorer gas sensing properties. Therefore, low Ti doping can also be a reason for inferior gas response in ZT1 film. The plausible gas sensing mechanism that happened in the case of ZT1, ZT2, and ZT3 films is schematically represented in Fig. 4.13 (b), (c), and (d), respectively.

4.3 Titanium oxide-based thin films

In this current section, preparation and characterization of pristine titanium oxide (TiO_2) and niobium doped TiO_2 (6 at. % of Nb) based combustible precursors and thin films are discussed. The thermal behaviour of the combustible precursors (pristine and doped) is inspected initially through TGA and DTA. The fabricated spin coated pristine and doped thin films are analyzed under several thin film characterization techniques such as GIAXRD, FESEM, EDAX, UV-Vis and XPS. The gas sensing characteristics of the fabricated thin films are examined under various target gases such as ammonia, formaldehyde etc.

4.3.1 Experimental procedure

4.3.1.1 Materials

All the reagents were of analytical grade and utilized without additional purification. Titanium (IV) isopropoxide ($C_{12}H_{28}O_4Ti$) (Sigma-Aldrich, India), niobium (V) chloride ($NbCl_5$) (Sigma-Aldrich), nitric acid (HNO_3) (Molychem), 2-methoxyethanol ($C_3H_8O_2$) (Molychem) and hydrochloric acid (HCl) (Molychem) were utilized in this study. For silver electrodes, silver conductive adhesive paste (Alfa Aesar) was used.

4.3.1.2 Preparation of precursors and their characterization

In this work, two precursors (of 2 M) were prepared; one is for pristine condition, and another is for doped condition (6 at. % Nb). According to the balanced equation, i.e., equation 4.13 (pristine), stoichiometric amounts of $C_{12}H_{28}O_4Ti$ (as Ti

source and fuel) and HNO_3 (as an oxidizer) were taken, and they were dissolved in $C_3H_8O_2$ (solvent). This mixture is called solution A.

In the preparation of the doped precursor, stoichiometric quantities of $C_{12}H_{28}O_4Ti$ and HNO_3 were taken according to equation 4.14 and dissolved in $C_3H_8O_2$. This mixture is termed solution B. Later, 0.05 g of $NbCl_5$ (as Nb source) was taken and dissolved in diluted HCl (1 ml) (solution C). Later, solution C was added dropwise to solution B to form solution D. Finally, solution A was used for the pristine condition, and solution D was used for the doped condition.

$$\text{(i) } 72\, HNO_3 + 5\, C_{12}H_{28}O_4Ti \rightarrow 5\, TiO_2 + 60\, CO_2 + 106\, H_2O + 36\, N_2 \qquad (4.13)$$

$$\text{(ii) } 6798\, HNO_3 + 470\, C_{12}H_{28}O_4Ti + 30\, NbCl_5$$
$$\rightarrow 5\, Ti_{94}Nb_6O_{203} + 5640\, CO_2 + 9979\, H_2O + 3399\, N_2 + 75\, Cl_2 \qquad (4.14)$$
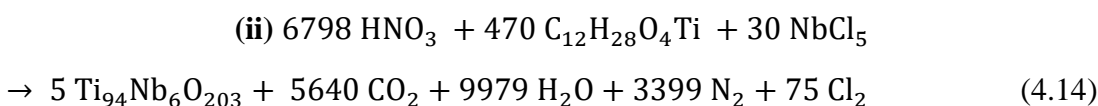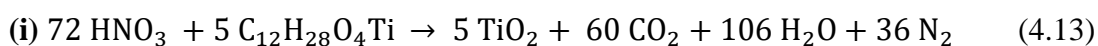
Later, the precursors (Solution A and D) were stirred (at 250 rpm) on a magnetic stirrer for 3 h at ambient temperature to achieve optical clearness and compositional homogenous. The precursors were then aged for 24 h. The dried precursors were examined under thermogravimetric analysis and differential thermal analysis (TGA, Seiko Instruments TGA, DTA Exstar 6300) from ambient temperature to 600 °C with 10 °C/min scanning rate in a nitrogen atmosphere.

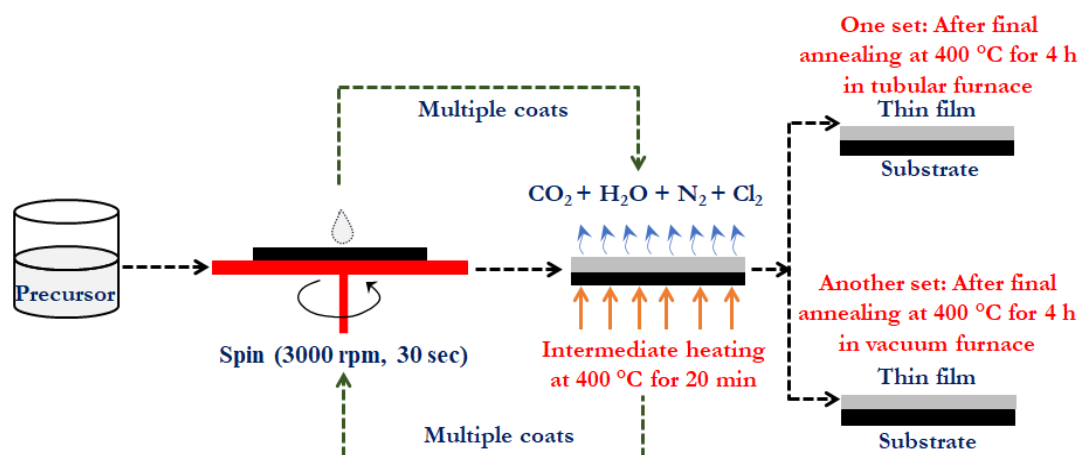### 4.3.1.3 Fabrication of films and their characterization

Fig. 4.14: Schematic representation of the fabrication of thin films in the current work.

In the current study, corning glasses (Corning Incorporated; thickness 0.96 to 1.06 mm) were used as the substrates and the substrates were thoroughly cleaned. The same procedure was followed for cleaning the glass substrates, as mentioned in section 4.2.1.3. Later, the individual, stable precursor was deposited on different glass substrates through the spin coating method. The maintained time and spinning speed were 30 s and 3000 rpm, respectively. After spinning, the samples were immediately heated for 20 min on a hot plate maintained at 400 °C. Similarly, the samples were spin coated for 15 times with intermediate heating for 20 min as denoted above. Likewise, two sets of samples were fabricated. One set of samples were annealed at 400 °C in a tubular furnace for 4 h at atmospheric pressure. Another set of samples were annealed at 400 °C in a vacuum furnace for 4 h and the maintained vacuum during annealing was $\sim 4 \times 10^{-5}$ mbar. Hereafter, in this section, the pristine and 6 at. % Nb films annealed in the tubular furnace are called TO and NTO, respectively. Whereas the pristine and 6 at. % Nb films annealed in the vacuum furnace are denoted as TO-V and NTO-V, respectively. The schematic representation of the fabrication of thin films in the current work is shown in Fig. 4.14.

The films were studied under PANalytical multi-purpose high-resolution X-Ray diffractometer (GIXRD) (Empyrean) (source of copper Kα radiation) with a grazing angle of 1° and a step size of 0.07° to inspect the structural properties of the films. To examine the morphological features of the fabricated films and to check the elemental composition, field emission scanning electron microscopy (FESEM) (Carl Zeiss Sigma) comprised with energy-dispersive X-ray analysis (EDAX) (Oxford instruments) were applied, respectively. The films were analysed under UV–Visible spectrometer (Shimadzu UV-3600 UV–Vis–NIR Spectrophotometer) to evaluate the transparency levels and the optical energy band gap was estimated from absorption spectra using Tauc's plot. The thickness of all the fabricated films was measured by near normal spectroscopic reflectometer (HO-NNSR-01, Holmarc). The thickness of TO, NTO, TO-V, and NTO-V was 174 ± 2 nm, 171 ± 3 nm, 176 ± 5 nm, and 177 ± 4 nm, respectively. To inspect the chemical state of the elements present in the films, X-ray photoelectron spectroscopic study (XPS, Kratos Axis Ultra DLD) was engaged. For the XPS spectra calibration, the C-H peak of adsorbed carbon, situated at the binding energy of 284.6 eV, was utilized. XPS curve fitting software package (XPSPEAK41)

was used to conduct the fitting of the spectra. Full-width half maximum (FWHM) and Gaussian/Lorentzian (G/L) ratio were maintained constant to avoid the discrepancy during the peak fitting. A minimum chi-square was selected for best fitting and Shirley was used as the background type. The fitted XPS spectra of C 1s of all the films and the details of the fitting parameters are given in Appendix IV.

The gas sensing characterization of all the films was performed towards NH_3 gas in the present study and executed in a custom-made setup. In this study, the same experimental setup and procedure were followed for gas sensing characterization of all the fabricated films, as mentioned in section 4.2.1.3 (zinc oxide-based films). The silver electrodes were placed on two opposite edges of all the films to prepare the electrical contacts for gas sensing characterization. The gas sensing characteristics of the films to different concentrations of NH_3 gas (25 to 100 ppm) were inspected in the current study. The selectivity test of TO-V film was conducted towards gases such as formaldehyde, ethanol, methanol, xylene, and toluene of 100 ppm concentration. In this study also, all the gas sensing measurements were conducted at room temperature. The time taken by the film to attain a 90 % change in the total resistance was considered as the response time during the adsorption process and as the recovery time during the desorption of the target gas in this current study as well.

4.3.2 Results and discussion

The DTA, TGA and its derivate DTG curves of undoped and doped precursors utilized to fabricate the films in the current study are displayed in Fig. 4.15 (a) and (b), respectively. The respective plots of the precursors are categorized into five regions with respect to temperature and they are denoted as region I (26 °C to ~120 °C), region II (~120 °C to ~150 °C), region III (~150 °C to ~250 °C), region IV (250 °C to ~330 °C) and region V (~330 °C to 600 °C). It is noticed that the weight loss in both the precursors has happened in four steps. A gradual weight loss has appeared in region I, with a peak in the DTG curve in both the precursors. Correspondingly, an endothermic peak is detected in the DTA curve. Considering this, region I can be attributed to the evaporation of the solvent in the precursors.
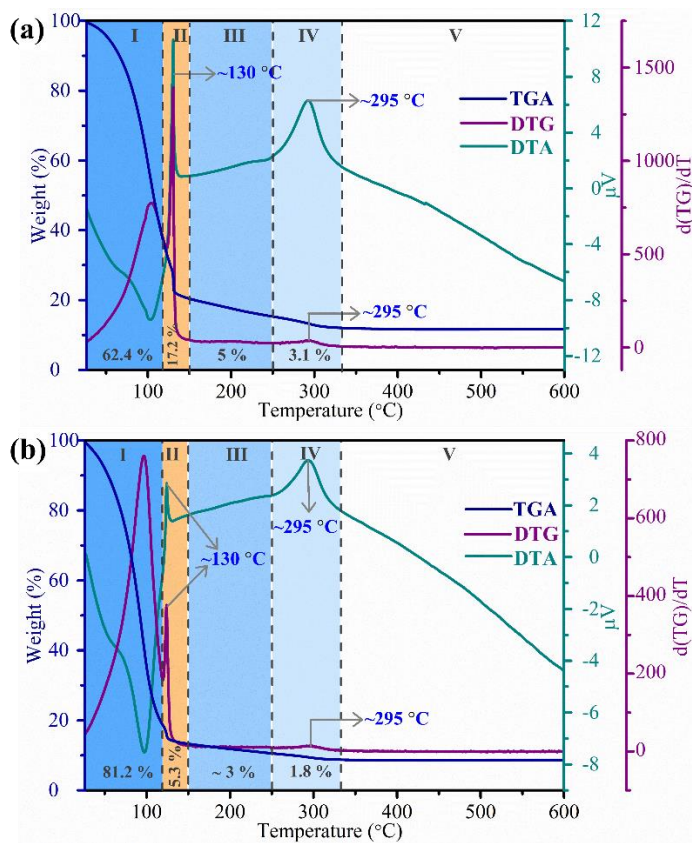
Fig. 4.15: TGA, DTG and DTA thermograms of (a) undoped and (b) doped combustible precursors, respectively.

In region II of both the precursors, a sudden weight loss is traced in the TGA curve with a peak in the DTG curve at ~130 °C. Also, an exothermic peak is emerged in the DTA curve at the same temperature of ~130 °C. The features of sudden weight loss and exothermicity can be dedicated to the combustion reaction in the precursors. As mentioned earlier, combustion is the reaction that occurs between oxidizer (here HNO_3) and fuel (here $C_{12}H_{28}O_4Ti$) at a particular temperature and it generates a high amount of heat energy (exothermicity) with some by-product gases. The liberation of heat energy aids in the formation of respective metal oxides (here TiO_2/Nb doped TiO_2). The escaping of the by-product gases causes sudden weight loss. Furthermore, in region III, a gradual weight loss is noticed and it can be credited to the further escaping of by-product gases with temperature. In region IV, the weight loss has continued gradually and a very small peak is spotted in the DTG curve, which can be dedicated to the removal of carbonaceous impurities that are remained after the combustion reaction. In the DTA curve, another exothermic peak is observed in region IV at a temperature of

~295 °C. The exothermic peak can be ascribed to the crystallization of the derived metal oxide from the combustion reaction. Commenting on region V, there is no loss of weight traced and this can be attributed to the formation of stable respective metal oxide at higher temperatures.
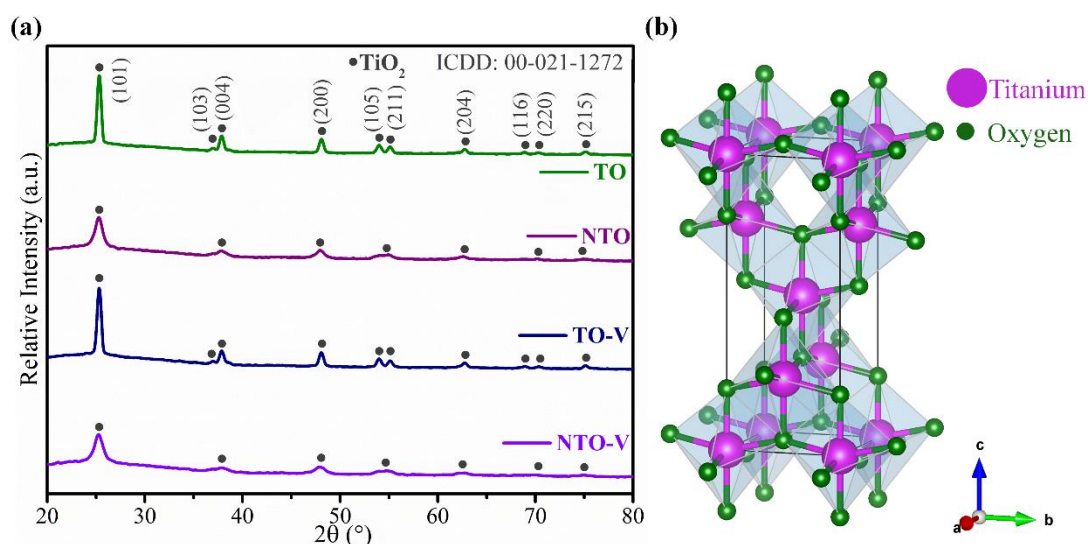

Fig. 4.16: (a) GIXRD patterns of TO, NTO, TO-V and NTO-V films, (b) Schematic representing the tetragonal anatase crystal structure of TiO_2. (The crystal structure is drawn using VESTA visualization interface software and crystallographic information file is taken from the American Mineralogist Crystal Structure Database (amcsd 0011765)).

The GIXRD patterns of TO, NTO, TO-V, and NTO-V films are presented in Fig. 4.16 (a). It is noticed that all the films are polycrystalline and the obtained diffraction planes are precisely agreeing with the tetragonal anatase crystal structure of TiO_2 (ICDD: 00-021-1272). A schematic presentation of the tetragonal anatase crystal structure of TiO_2 is displayed in Fig. 4.16 (b). It is observed from Fig. 4.16 (a) that the traces of rutile or brookite structure of TiO_2 and secondary phases due to dopant Nb such as Nb_2O_5, Nb_2O_3, $TiNb_2O_7$ are not detected in the diffraction patterns. The non-existence of dopant phases infers the effective substitution of Nb atoms in the sites of Ti of TiO_2 crystal structure and it is in decent agreement with the previous reports (Zhao et al. 2010) (Wang et al. 2010a) (Liu et al. 2011). The pristine films (TO and TO-V) are highly crystalline in nature with sharper diffraction planes, whereas the crystallinity has decreased after doping Nb (NTO and NTO-V films), irrespective of annealing

atmospheres. Thus, the dopant Nb acted as a suppressor to the crystallization of host TiO_2. A similar decrement in the crystallinity after doping Nb in TiO_2 films is also observed in the literature (Ok et al. 2012). It indicates that the dopant Nb has significantly affected the crystallinity, and it also restricted the crystal growth of host TiO_2 in NTO and NTO-V films (Fallah et al. 2014). To further confirm it, the average crystallite size of all the films is estimated from the Scherrer formula, as shown in equation 4.5. It is revealed that the average crystallite size of both pristine films (TO and TO-V) is ~17 nm. In the case of both Nb doped TiO_2 films (NTO and NTO-V), the average crystallite size is reduced to ~9 nm. The decrement in the crystallite size further confirms the inhibition of crystal growth by dopant Nb and it coincides with the earlier studies as well (Wang et al. 2010a) (Kaleji et al. 2012) (Lee et al. 2007).
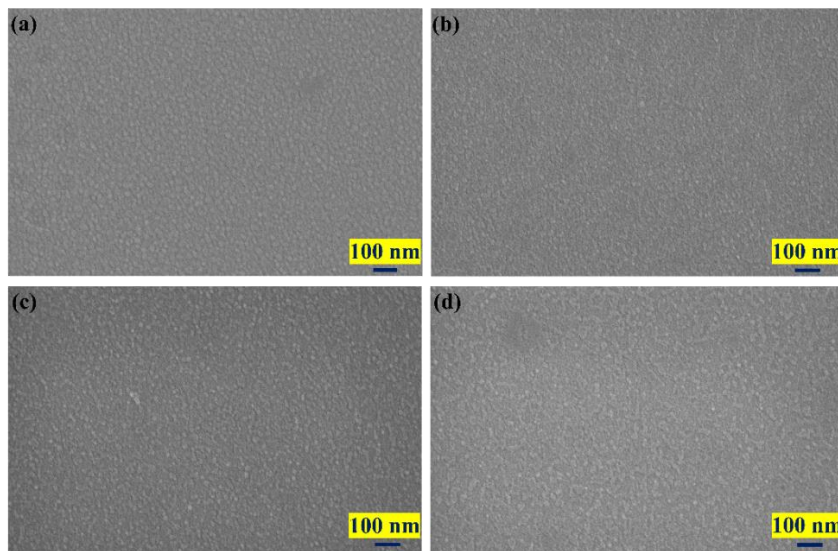
Fig. 4.17: FESEM images of (a) TO, (b) NTO, (c) TO-V and (d) NTO-V films.

From the FESEM images (Fig. 4.17), it is noticed that all the films exhibit almost similar morphology and the morphology is found to be dense. There are no noteworthy differences observed between the pristine and doped films. A similar observation with no significant morphological changes in pure and 6 at. % Nb doped TiO_2 is also traced in the literature (Wang et al. 2010a). It is detected that the air and vacuum annealing also does not impact much on the morphological properties of the films. It is also proved that all the films are uniform in nature and the presence of cracks and peeling of the film are not perceived, which approves the effective fabrication of the films in this study. The EDAX spectra of all the films are revealed in Fig. 4.18.

From Fig. 4.18 (a and c), it is observed that TO and TO-V films have revealed the presence of Ti and O elements along with carbon. The presence of the C element in the films is because of the surface adsorption of CO, and CO_2 etc., from the atmosphere (Regragui et al. 2000). The presence of Ti, O, C elements with Nb element are observed in the EDAX spectra of NTO and NTO-V films (Fig. 4.18 (b and d, respectively)). Remarkably, the resulted at. % of dopant Nb from the EDAX spectra of NTO and NTO-V films is almost the same as the doping concentration considered in the precursor (6 at. %). The result approves the effective doping of Nb in host TiO_2 crystal. The elemental mapping of all the fabricated films is presented in appendix IV. The uniform distribution of the elements Ti, O, Nb, and C is observed on the entire surface of the respective films.
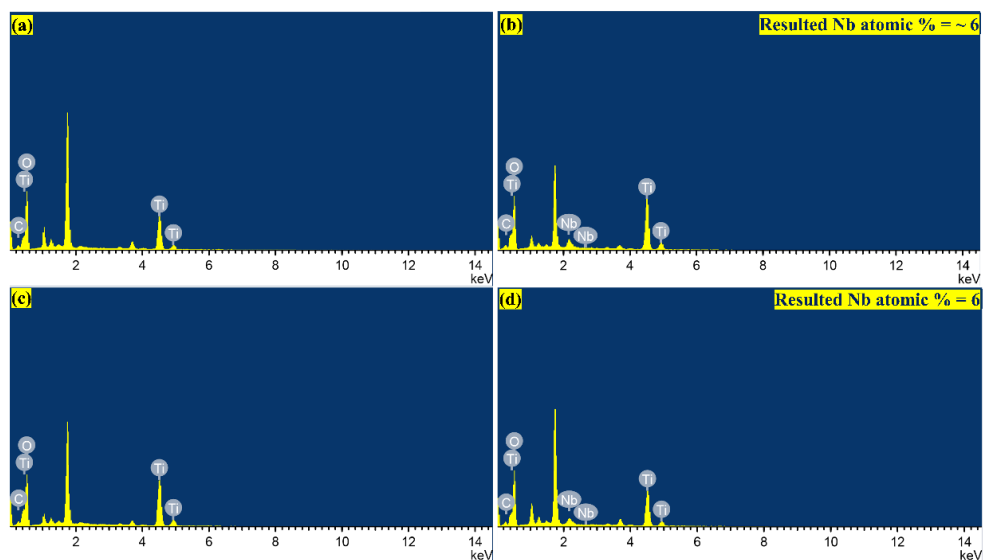
Fig. 4.18: EDAX spectra of (a) TO, (b) NTO, (c) TO-V and (d) NTO-V films.

The wide scans of all the fabricated films are displayed in Fig. 4.19 (a). The wide scans of pristine TO and TO-V films reveal the existence of peaks from the elements Ti and O at their respective binding energy positions (Wu et al. 2018) (Diebold and Madey 1996). As stated earlier, the presence of the peak at ~284 eV belongs to C 1s. The presence of carbon can be dedicated to adventitious carbon contamination (Joshi et al. 2019). Commenting on the wide scans of NTO and NTO-V films, the presence of peaks from the dopant Nb such as Nb 3d and Nb 3p at their respective binding energies is noticed along with Ti, O, and C peaks. The obtained wide scans of

NTO and NTO-V films are in good relation with the previous reports (Lee et al. 2007) (Kwoka et al. 2017). The analysis confirms the coexistence of Ti, Nb, and O elements in doped (NTO and NTO-V) films. Also, the resulted elemental presence from the wide scan XPS spectra is in decent connection with the data derived from the EDAX analysis of the present study.
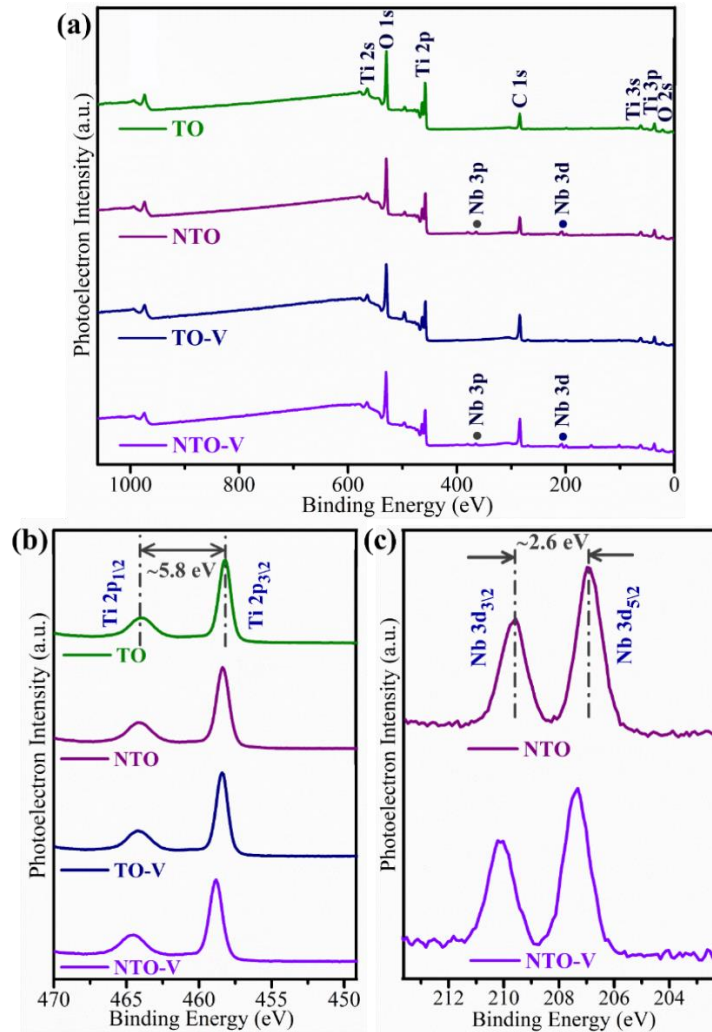
Fig. 4.19: (a) Wide scan XPS spectra of all the films, (b) Ti 2p high-resolution XPS spectra of all the films, and (c) Nb 3d high-resolution XPS spectra of NTO and NTO-V films.

The high-resolution XPS spectra of Ti 2p of all the films are shown in Fig. 4.19 (b). It is noticed that Ti 2p has revealed a doublet positioned at the binding energies of 458.4 ± 0.4 eV and 464.2 ± 0.3 eV, that belong to the spin-orbit transitions of Ti $2p_{3/2}$ and Ti $2p_{1/2}$. The separation between the two peaks is found to be ~5.8 eV. The derived

results confirm that the valency of the element Ti is +4 and the valence bond structure between Ti-O corresponds to TiO_2. The obtained results in this study are matching well with the literature (Manole et al. 2013) (Wu et al. 2018). The details of deconvoluted Ti 2p peaks of all the films are given in Table 4.6.

Table 4.6: Details of deconvoluted Ti 2p peaks of all the films.

Film	Deconvoluted peaks	Binding energy (eV)
TO	Ti $2p_{3/2}$	458.1
	Ti $2p_{1/2}$	463.9
		(Spin-orbit splitting = 5.8)
NTO	Ti $2p_{3/2}$	458.3
	Ti $2p_{1/2}$	464.1
		(Spin-orbit splitting = 5.8)
TO-V	Ti $2p_{3/2}$	458.4
	Ti $2p_{1/2}$	464.2
		(Spin-orbit splitting = 5.8)
NTO-V	Ti $2p_{3/2}$	458.8
	Ti $2p_{1/2}$	464.5
		(Spin-orbit splitting = 5.7)

Table 4.7: Details of deconvoluted Nb 3d peaks of NTO and NTO-V films.

Film	Deconvoluted peaks	Binding energy (eV)
NTO	Nb $3d_{5/2}$	206.9
	Nb $3d_{3/2}$	209.5
		(Spin-orbit splitting = 2.6)
NTO-V	Nb $3d_{5/2}$	207.3
	Nb $3d_{3/2}$	210.0
		(Spin-orbit splitting = 2.7)

The high-resolution XPS spectra of Nb 3d of the doped films (NTO and NTO-V) are presented in Fig. 4.19 (c). The Nb 3d exhibited two distinct peaks situated at the

binding energies of 206.9 ± 0.4 eV and 209.5 ± 0.5 eV. The obtained peaks correspond to the spin-orbit transitions of Nb $3d_{5/2}$ and Nb $3d_{3/2}$; the spin-orbit splitting is found to be ~2.7 eV. It confirms that the valence state of dopant Nb is +5 (Manole et al. 2013) (Lee et al. 2007) (Kwoka et al. 2017). The details of deconvoluted Nb 3d peaks of the NTO and NTO-V films are presented in Table 4.7. From the derived XPS analysis, it is indicated that the respective films are equipped with the required elemental states of Ti and Nb.

Table 4.8: The respective position, areas of O 1s deconvoluted peaks of all the films

Film	Peak	Peak position (eV)	Area (cps × eV)
TO	O_L	529.4	16656.0
	O_V	530.5	1969.8
	O_A	531.6	1688.4
NTO	O_L	529.6	15318.4
	O_V	530.8	2026.9
	O_A	531.8	1297.3
TO-V	O_L	529.6	11716.5
	O_V	531.0	2233.8
	O_A	532.0	1576.1
NTO-V	O_L	530.0	10897.2
	O_V	531.5	2549.3
	O_A	532.4	1421.3

The deconvoluted O 1s high-resolution spectrum of all the films is displayed in Fig. 4.20 (a to d, respectively). The O 1s spectrum of all the films is deconvoluted into three significant peaks, which are positioned at binding energies of ~529.6 ± 0.4 eV (Peak 1), 531 ± 0.5 eV (Peak 2) and 532 ± 0.4 eV (Peak 3). The major peak, i.e., Peak 1 is dedicated to the O^{2-} ions of lattice oxygen (O_L). The middle peak, i.e., Peak 2 is attributed to the O^{2-} state of oxygen vacancies or defects in the oxygen-deficient regions (oxygen vacancies (O_V)). Lastly, the high binding energy peak, i.e., Peak 3 is assigned to weak oxygen bonds on the surface (surface adsorbed oxygen species (O_A)) (Chen et

al. 2010) (Li et al. 2018) (Manjunath et al. 2021b). The respective position and area of deconvoluted O 1s peaks of all the films are given in Table 4.8.
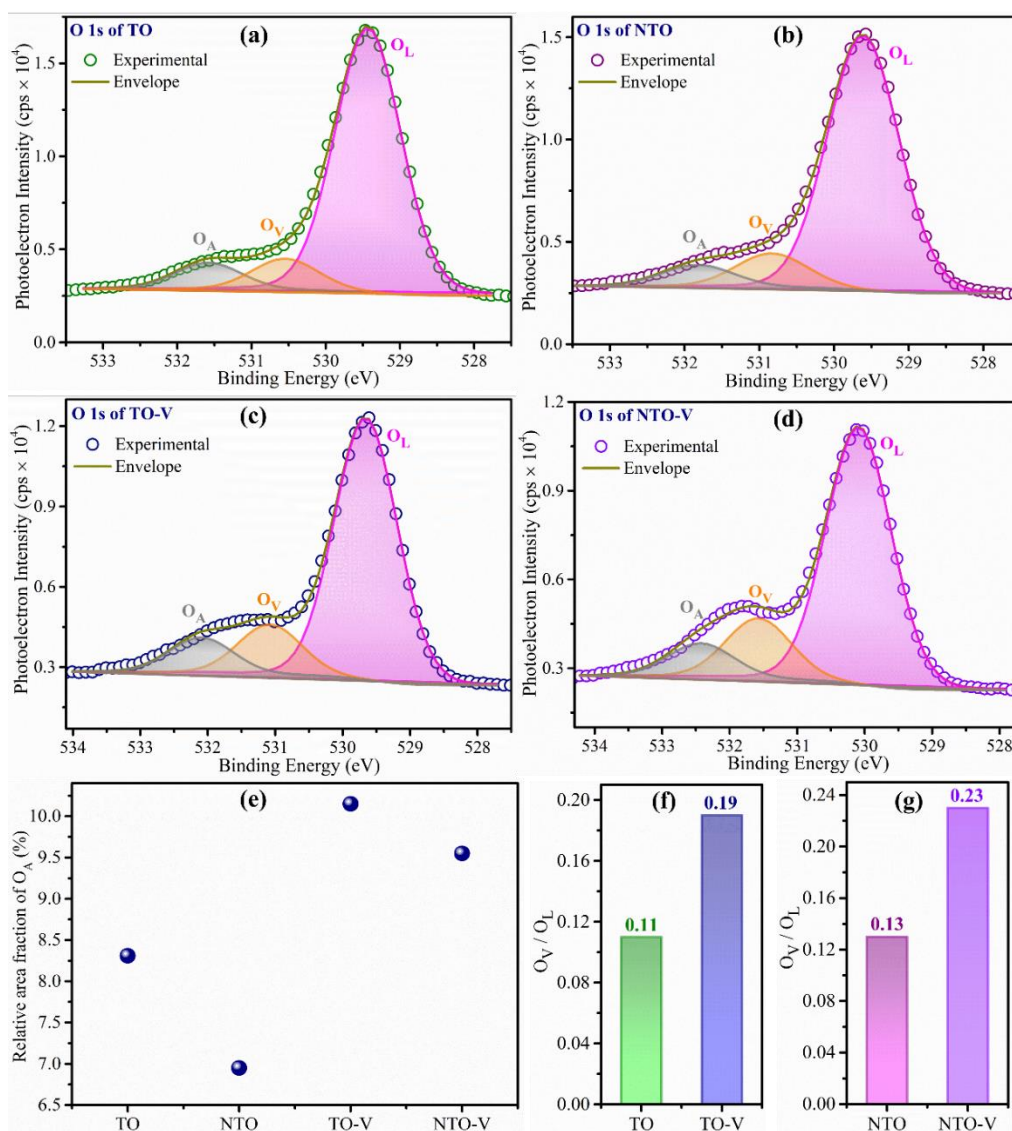
Fig. 4.20: Deconvoluted O 1s high-resolution XPS spectrum of (a) TO, (b) NTO, (c) TO-V and (d) NTO-V films, respectively, (e) Variation of relative area fraction of O_A in TO, NTO, TO-V and NTO-V films, Variation of O_V/O_L in (f) TO, TO-V films and (g) NTO, NTO-V films, respectively.

The relative area fraction of adsorbed oxygen species (% of O_A), i.e., (the area of O_A/(areas of $O_L+O_V+O_A$)) of all the films is calculated and the variation of it is displayed in Fig. 4.20 (e). It is noticed that TO-V film has exhibited the maximum % of O_A of 10.15. NTO-V film has revealed a % of O_A of 9.55, which is lower than TO-

V film. And it is followed by TO (8.31 %) and NTO films (6.95 %). The obtained trend of the % of O_A in the films is TO-V > NTO-V > TO > NTO. It is known that annealing the film in a vacuum atmosphere enhances the formation of oxygen vacancies in the film. To validate this point, O_V/O_L, called the oxygen vacancy concentration, is calculated for all the films (Manjunath et al. 2021b). Fig. 4.20 (f) shows the variation of O_V/O_L in TO and TO-V films, whereas, Fig. 4.20 (g) displays its variation in NTO and NTO-V films, respectively. The O_V/O_L has enhanced in the vacuum-annealed film (TO-V) compared to the air-annealed film (TO) (Fig. 4.20 (f)). Similarly, O_V/O_L is high in NTO-V film in contrast to NTO film (Fig. 4.20 (g)). It is also observed from Fig. 4.20 (f and g) that there is no considerable improvement in the oxygen vacancy concentration in NTO film compared to TO film. A similar observation is traced in NTO-V film compared to TO-V film. From these results, it can be inferred that doping has not generated more oxygen vacancies. Instead, the vacuum treatment has produced more oxygen vacancies in the present study.
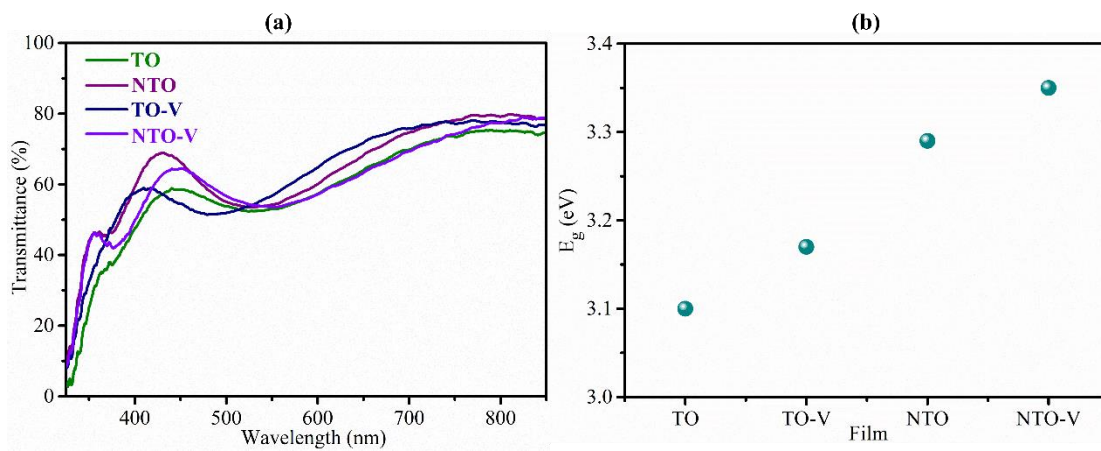
Fig. 4.21: (a) Transmittance plots of all the films, (b) the representation of variation in the optical energy bandgap (E_g) of the films.

Furthermore, the transparency level of all the films is inspected in this study and their normalized transmittance plots are shown in Fig. 4.21 (a). It is noticed that all the films exhibit a similar range of transparency and the average transparency of all the films is more than 50 % in the visible region. A significant absorption peak is noticed in the spectrum of all the films at the wavelength range of around 485 to 540 nm and it can be dedicated to the anatase titanium oxide, which has a high refractive index of value ~2.4 at the wavelength of 500 nm (Zhao et al. 2010). It is observed that the dopant

Nb does not substantially affect the transparency of the films in the current study. It is in line with the previous report where the undoped and Nb doped TiO_2 films have shown a similar range of transparency (Manole et al. 2013).

The E_g of all the fabricated films is estimated by Tauc's relation (equation 3.2). Here in this equation, the value of index 'n' has considered as 2 because anatase TiO_2 is known as an indirect band gap semiconductor (Zhao et al. 2010). The variation of the E_g values estimated from Tauc's plot of all the films is represented in Fig. 4.21 (b). The Tauc's plots of all the films are shown in Appendix IV. From Tauc's plots, it is found that the pristine films (TO and TO-V) have attained the E_g value of 3.1 and 3.17 eV, respectively. In the case of doped films (NTO and NTO-V), E_g has enhanced to the values of 3.29 and 3.35 eV, respectively. The increment in the E_g value of Nb doped films compared to pure TiO_2 films is also noticed in the earlier reports, and the enhancement is dedicated to the Burstein–Moss effect in the literature (Fallah et al. 2014) (Zhao et al. 2010). According to equation 4.8, it is noted that the widening of E_g is directly related to the N. The E_g enhances if the N rises because of the filling of the conduction band edge by the additional carriers (Eshaghi et al. 2015; Zhao et al. 2010). Here, in this case, the substitutional doping of Nb^{5+} in the Ti^{4+} sites donate extra carriers as per equation 4.15.

$$Nb \underset{Ti}{\rightarrow} Nb^{\bullet}_{Ti} + e' \qquad (4.15)$$

Hence, in the current report, it can be assumed that the increment in the E_g value of Nb doped films than pristine films is because of the augmentation in the N upon doping. It is noticed from Fig. 4.20 (f) that the O_V/O_L is high in TO-V film than in TO film. It is also observed from Fig. 4.21 (b) that there is a slight enhancement of E_g in TO-V film compared to TO film. The comparative enhancement of E_g can be dedicated to the increment of the N in TO-V film by the oxygen vacancies, which generates charge carriers according to equation 4.16. And the increment in N probably might cause the slight widening of E_g in TO-V film, as discussed previously. Commenting on doped films, a similar enhancement in E_g is also observed in NTO-V film in contrast to NTO film (Fig. 4.21 (b)). It can also be dedicated to the increment in the N due to the increased oxygen vacancies in NTO-V film than the NTO film (Fig. 4.20 (g)).
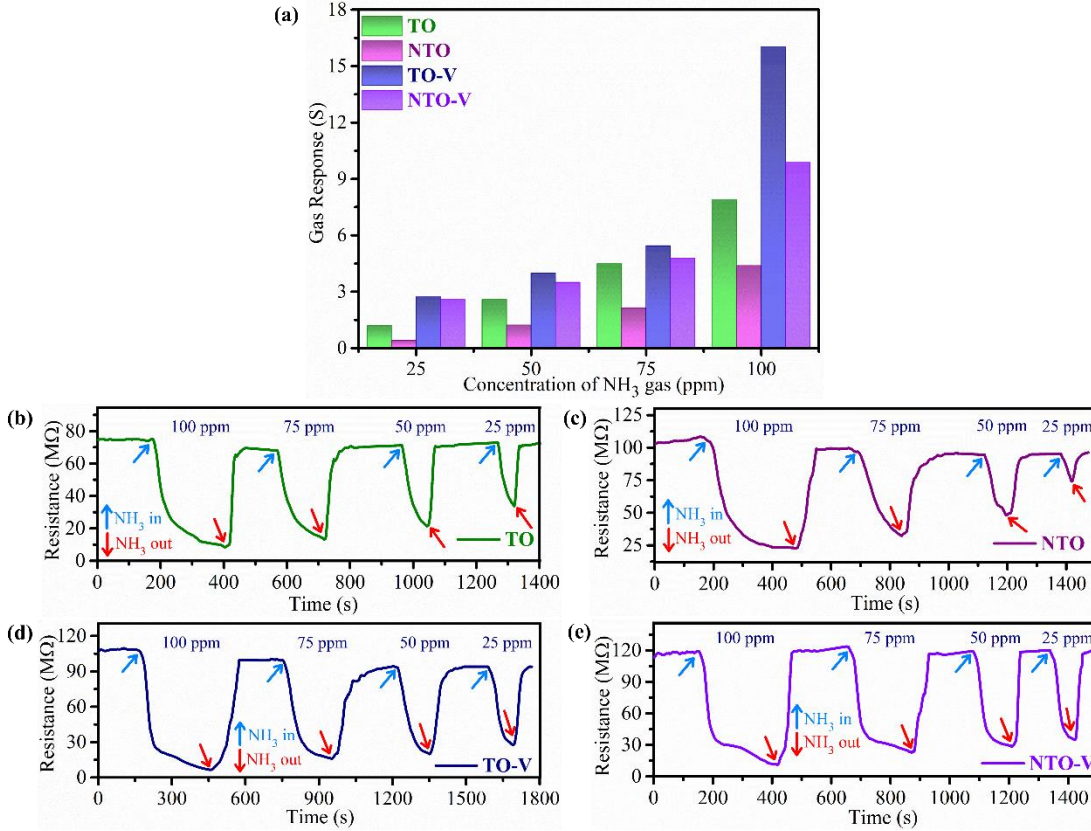
$$O_O^x \rightarrow V_O^{\bullet\bullet} + 2e' + \frac{1}{2} O_2 \ (g) \qquad\qquad (4.16)$$

Fig. 4.22: (a) Gas response of all the films towards different concentrations of NH$_3$ gas at room temperature, the electrical resistance variation of (b) TO, (c) NTO, (d) TO-V, and (e) NTO-V films, respectively, at various concentrations of NH$_3$ gas.

The gas response (S) of all the films towards different concentrations of NH$_3$ gas (25 to 100 ppm) at room temperature is shown in Fig. 4.22 (a). The gas response of all the films in the present study is calculated according to equation 4.7. It is perceived that the gas response values of all the films have augmented with the increment in NH$_3$ gas concentration from 25 to 100 ppm. It reveals the dependence of the gas response of the films on the target gas concentration. As explained previously, the main cause for such linear connection is due to the strong relation of gas response on the chemisorbed oxygen species removal that happens because of the reaction between target gas and chemisorbed oxygen. It aids in returning electrons to the conduction band and causes a variation in the electrical resistance that leads to the increment of gas response. Accordingly, when the films with a fixed surface area are exposed to low NH$_3$ gas

concentration, there is a low coverage of NH_3 molecules on the surface of the films. It causes lower surface reactions with chemisorbed oxygen species which further leads to minimal gas response. With the increase of gas concentration, the NH_3 molecules coverage widens on the surface of the film and the reactions with the chemisorbed oxygen species also increase, which causes an increment in the gas response (Shinde et al. 2007) (Shingange et al. 2016).

Also, from Fig. 4.22 (a), it is noticed that the gas response is highest in the case of TO-V film in contrast to the other fabricated films at all concentrations of NH_3 gas. The next maximum gas response is found in NTO-V film, followed by TO and NTO films, irrespective of NH_3 gas concentration. The resulted trend in the gas response of the films at every NH_3 gas concentration is TO-V > NTO-V > TO > NTO. In the present study, the maximum gas response of value ~16 has attained in TO-V film at an NH_3 gas concentration of 100 ppm. The plausible factors behind the comparatively high gas response in TO-V film than the other films are explained below sections.

The transient variation in the electrical resistance of all the films is recorded when the films are exposed to different concentrations of NH_3 gas and the resistance change in TO, NTO, TO-V and NTO-V films is projected in Fig. 4.22 (b, c, d and e, respectively). Generally, the variation in the resistance relies on the concentration of the target gas and it also depends on the simultaneous adsorption and desorption of the oxygen and gas molecules on the surface of the film (Manjunath et al. 2020). It is observed that the resistance of all the films is gradually decreased when the NH_3 gas is projected into the testing chamber. The gradual decrement in the resistance is attributed to the adsorption of the NH_3 molecules on the surface of the films and their reaction with chemisorbed oxygen species. After a certain time, when the NH_3 gas is allowed to leave the chamber, the resistance of the films is progressively enhanced. It is due to the simultaneous desorption of NH_3 molecules from the surface of the films and the adsorption of oxygen molecules from the atmosphere when air replaces the target gas in the chamber. The resistance of all the films is dipped and raised when NH_3 gas is exposed and evacuated, respectively; this variation occurred at all the concentrations of NH_3 gas. Thus, the variation in the resistance approves that all the films have evidenced the gas sensing behavior towards the NH_3 gas at room temperature in the present study.
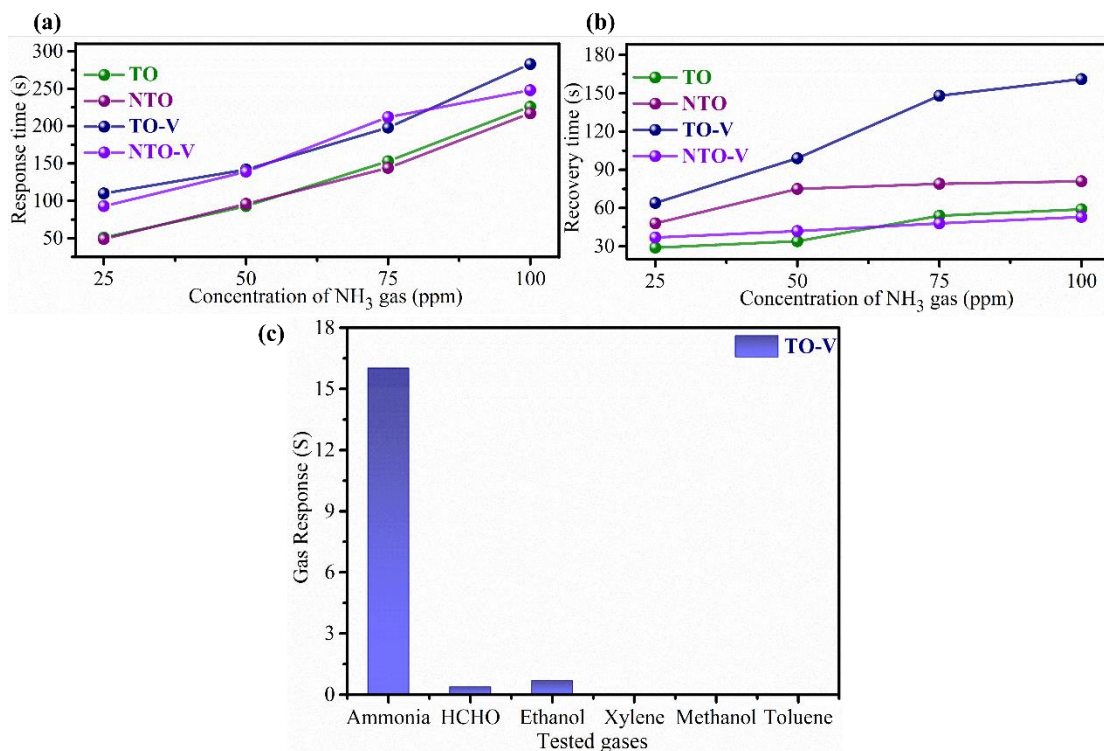
Fig. 4.23: (a) Response time, (b) recovery time of all the fabricated films towards different concentrations of NH_3 gas, and (c) the gas response of TO-V film when tested against different gases of 100 ppm at room temperature.

The response and recovery times of all the films are measured from the variation in resistance during adsorption and desorption at every concentration of NH_3 gas in the current study. The response and recovery times are plotted as a function of NH_3 concentration and projected as Fig. 4.23 (a) and (b), respectively. It is observed that the response time is increased with the increase in NH_3 gas concentration in all the films. The range of the response time is 51 to 226 s, 49 to 217 s, 110 to 283 s, and 93 to 248 s, respectively, for TO, NTO, TO-V, and NTO-V films when NH_3 gas concentration varied from 25 to 100 ppm (Fig. 4.23 (a)). The plausible reason for increasing response time with the concentration of gas can be as follows: at lower concentrations, the adsorption of the number of NH_3 molecules on the surface of the film will be less; therefore, the reactions between NH_3 and chemisorbed oxygen molecules will be minimal, which results in a low gas response and fast response time. In the case of a high concentration of NH_3 gas, the number of adsorbed NH_3 molecules on the film's

surface will be high. The reactions between NH_3 and chemisorbed oxygen molecules can possibly be more, which results in a high gas response and slow response time.

Fig. 4.23 (b) shows that the recovery time of all the fabricated films is also enhanced with increasing NH_3 gas concentration. The range of the recovery time is 29 to 59 s, 48 to 81 s, 64 to 161 s, and 37 to 53 s, respectively, for TO, NTO, TO-V, and NTO-V films when NH_3 gas concentration is varied from 25 to 100 ppm. The fast recovery time at low NH_3 gas concentrations can probably be due to the low number of adsorbed NH_3 molecules on the surface of the film and they can be desorbed in a shorter time when the gas is allowed to escape from the chamber. On the other hand, at higher NH_3 gas concentrations, the adsorbed NH_3 molecules on the surface of the film can be higher in number and they may take a longer time to desorb when the target gas is released from the testing chamber, which causes an increment in the recovery time.

In the present study, the gas selectivity experiment is executed to the high gas-responded TO-V film against various target gases such as formaldehyde (HCHO), ethanol, xylene, methanol and toluene of 100 ppm concentration and these gas response values are related to the value obtained towards NH_3 gas of 100 ppm concentration. The graph showing the response of TO-V film against the mentioned gases is projected as Fig. 4.23 (c). It is noticed that TO-V film revealed a high gas response towards the NH_3 gas and the film exhibits a very minimal response to HCHO and ethanol gases. Notably, TO-V film revealed negligible detection against the other target gases such as ethanol, xylene, methanol and toluene. Thus, it is assured that the TO-V film is highly selective towards the NH_3 gas at room temperature due to its substantial detection compared to other target gases. Three reasons can be predicted for selectivity to only NH_3 gas; firstly, because of electron-donating capability due to the existence of lone pair of electrons in NH_3 (Pandeeswari and Jeyaprakash 2014). The second reason can be the comparatively lower kinetic diameter of the NH_3 molecule than the other target gas molecules (shown in Table 4.4) (Ganesh et al. 2017) (Manjunath et al. 2021b). The final factor can be the low ionization energy of the NH_3 molecule (Ganesh et al. 2017).

Discussing the gas sensing mechanism of the present study, it is familiar that the gas sensing process of SMO (here, anatase TiO_2 (n-type)) belongs to the surface-controlled type in which the resistance change of SMO is governed by the target gas molecules and quantity of chemisorbed oxygen species on the surface (Shinde et al. 2007). This mechanism primarily comprises three processes which are adsorption, transfer of the charges, and desorption (Poloju et al. 2018). As mentioned in the earlier section, when SMO is exposed to air, the oxygen molecules adsorb on the surface of SMO. After adsorption, they dissociate, and each oxygen atom picks the electrons from the conduction band of SMO. They turn as chemisorbed oxygen species, O_2^- (at room temperature), by reacting with the electrons of the SMO (Ganesh et al. 2017) (Shingange et al. 2016), and the kinetics of these reactions are given in equations 4.10 and 4.11.

According to the electron depletion region theory, the electrons from the conduction band of SMO get extracted by the absorbed oxygen molecules. This leads to the increment of the electrical resistivity of the film till an equilibrium with the ambient oxygen atmosphere (Poloju et al. 2018) (Ganesh et al. 2017). The adsorbed oxygen molecules can extract the electrons up to a specific depth from the surface of SMO (termed as Debye length). The amount of adsorbed oxygen is one of the crucial parameters upon which the Debye length highly relies (Miller et al. 2014) (Manjunath et al. 2021b). When the NH_3 gas is introduced, the gas molecules react with the chemisorbed oxygen species present on the surface of SMO. During the reaction, the NH_3 gas molecules pull the chemisorbed oxygen species from the surface, oxidize to N_2, H_2O and release the electrons. Subsequently, the electrons released from the reaction reach the conduction band of SMO. During this phenomenon, the area of the electron depletion layer decays and leads to a decrement in the electrical resistance of SMO. The reaction that occurs when NH_3 gas molecules interact with chemisorbed oxygen species is given in equation 4.12 (Ganesh et al. 2017) (Miller et al. 2014).

Table 4.9: The obtained crystallinity, average crystallite size, relative area fraction of adsorbed oxygen, oxygen vacancy concentration and gas response at NH_3 gas concentration (100 ppm) of all the fabricated films.

Film	Crystallinity	Average crystallite size (nm)	O_A (%)	O_V/O_L	S (100 ppm)
TO	High	~17	8.31	0.11	7.89
NTO	Comparatively low	~9	6.95	0.13	4.39
TO-V	High	~17	10.15	0.19	16.02
NTO-V	Comparatively low	~9	9.55	0.23	9.88

The results derived from various characterization tools of all the films that can be correlated to their achieved gas response values in the current study are tabulated in Table 4.9. As specified formerly, TO-V film has accomplished the maximum gas response in the current study at all concentrations of NH_3 gas in contrast to other films. The probabilistic factor that assisted in reaching a relatively high gas response in TO-V film can be discussed as follows. It is familiar that the gas mechanism initiates with the adsorption of oxygen molecules on the surface of the film and their transformation into chemisorbed oxygen species by extracting the electrons from conduction band and creating a thick depletion layer. The change in resistance of the film during the gas sensing process is highly influenced by the quantity of chemisorbed oxygen exists on the surface of the film (Shinde et al. 2007). In the present study, TO-V film attained more % of O_A (given in Table 4.9), which indicates that the quantity of chemisorbed oxygen on surface of TO-V film is higher than the other films. Therefore, the high quantity of chemisorbed oxygen on the surface of TO-V film might have formed by extracting more electrons from the conduction band and might have generated a thick depletion layer. The high quantity of chemisorbed oxygen is nothing but the greater number of active sites that can react with NH_3 gas molecules. When NH_3 gas comes in contact with the surface of the film, more reactions between the gas molecules and the active sites might have occurred due to the superior number of active sites on the surface of TO-V film. As shown in equation 4.12, these reactions might have released more

electrons back to the conduction band and the density of electrons might have increased in TO-V film. At this instant, the depletion layer significantly shrinks and supports in large resistance variation, which leads to a comparatively high gas response in TO-V film. It is also observed from Table 4.9 that the % of O_A follows the trend as TO-V > NTO-V > TO > NTO. From Fig. 4.20 (a), the derived trend in the gas response of the films at every NH_3 gas concentration is TO-V > NTO-V > TO > NTO. It can be concluded that the gas response of all the films at all concentrations of NH_3 gas is highly dependent on % of O_A, i.e., chemisorbed oxygen species. The amount of chemisorbed oxygen species on the surface of the respective film played a dominant role in its gas response value at every concentration of NH_3 gas in this study. The probable gas mechanism that occurred in all the films is schematically shown in Fig. 4.24.

Now addressing the comparison between vacuum-annealed TO-V and NTO-V films, it is likely to receive a high gas response in NTO-V film due to its low crystallite size (given in Table 4.9). But, interestingly, TO-V film with bigger crystallite size has achieved comparatively high gas response at all concentrations of NH_3. It is stated in the former section that the small crystallite size cannot be the sole factor for achieving high gas response. The blind reduction of the crystallite sizes can inhibit the diffusion of the gases, which in turn causes inferior gas response (Zhu and Zeng 2017). It infers that another significant film property should be associated with gas sensing; hence, here, it is assumed as the crystallinity. It is also categorized earlier that the crystallinity of the film plays a vital part in determining the gas response. The better crystallinity supports increasing the abilities in the detection of the gas/chemical species (Seeley et al. 2009) (Choi et al. 2011) (Katoch et al. 2013). It is previously described that the gas sensing mechanism of TiO_2 is controlled by surface reactions. The content of amorphous phase and crystalline anatase phase in TiO_2 will exhibit a crucial part in the gas response of the film. It is proposed that the amorphous phase in TiO_2 comprises lower surface energy than the crystalline anatase phase. The lower surface energy comprised amorphous phase causes a lower gas response in TiO_2 films (Seeley et al. 2009). In the study conducted by Seeley et al., it is proved that the amorphous phase degraded the gas sensing properties of the TiO_2 film and it is stated that the degree of crystallinity is required to attain a better gas response. Also, the film with high crystallinity showed a major gas response though it has a grain growth (Seeley et al.

2009). From this portrayal, it can be concluded that higher crystallinity in TO-V film is also a prominent reason for attaining high gas response than NTO-V film by restraining the adverse effects of crystal growth in the present study. It is also observed from Table 4.9 that there is a slight change in O_V/O_L value in TO-V and NTO-V films. Among these films, it can be presumed that O_V/O_L has not influenced much the variation of gas response. Therefore, it can be collectively concluded that a comparatively high % of O_A and crystallinity in TO-V film majorly influenced in achieving high gas response than in NTO-V film.

Discussing the air-annealed TO and NTO films, the TO film possessed a comparatively higher gas response than NTO film, though TO film has a larger crystallite size (shown in Table 4.9). The above analysis can be implied here and can be deduced that the better crystallinity in TO film has assisted in comparatively better gas response than NTO film with low crystallinity. TO film also possessed more % of O_A than NTO film. It indicates that the surface of TO film comprises more chemisorbed oxygen species, in other words, a greater number of active sites. These active sites of TO film might have supported better resistance modulation during the contact with NH_3 gas molecules, which resulted in a relatively high gas response than NTO film. Here too, there is a minute change in O_V/O_L in TO and NTO films and it can be presumed that O_V/O_L has not influenced much in the variation of gas response among these films. On that account, it can be collectively assumed that a relatively high % of O_A and crystallinity in TO film immensely influenced in attaining high gas response than NTO film. Overall, it can be concluded that the respective pristine TO-V (TO) film exhibited a better gas response at all concentrations of NH_3 gas than the doped NTO-V (NTO) film in the current study.
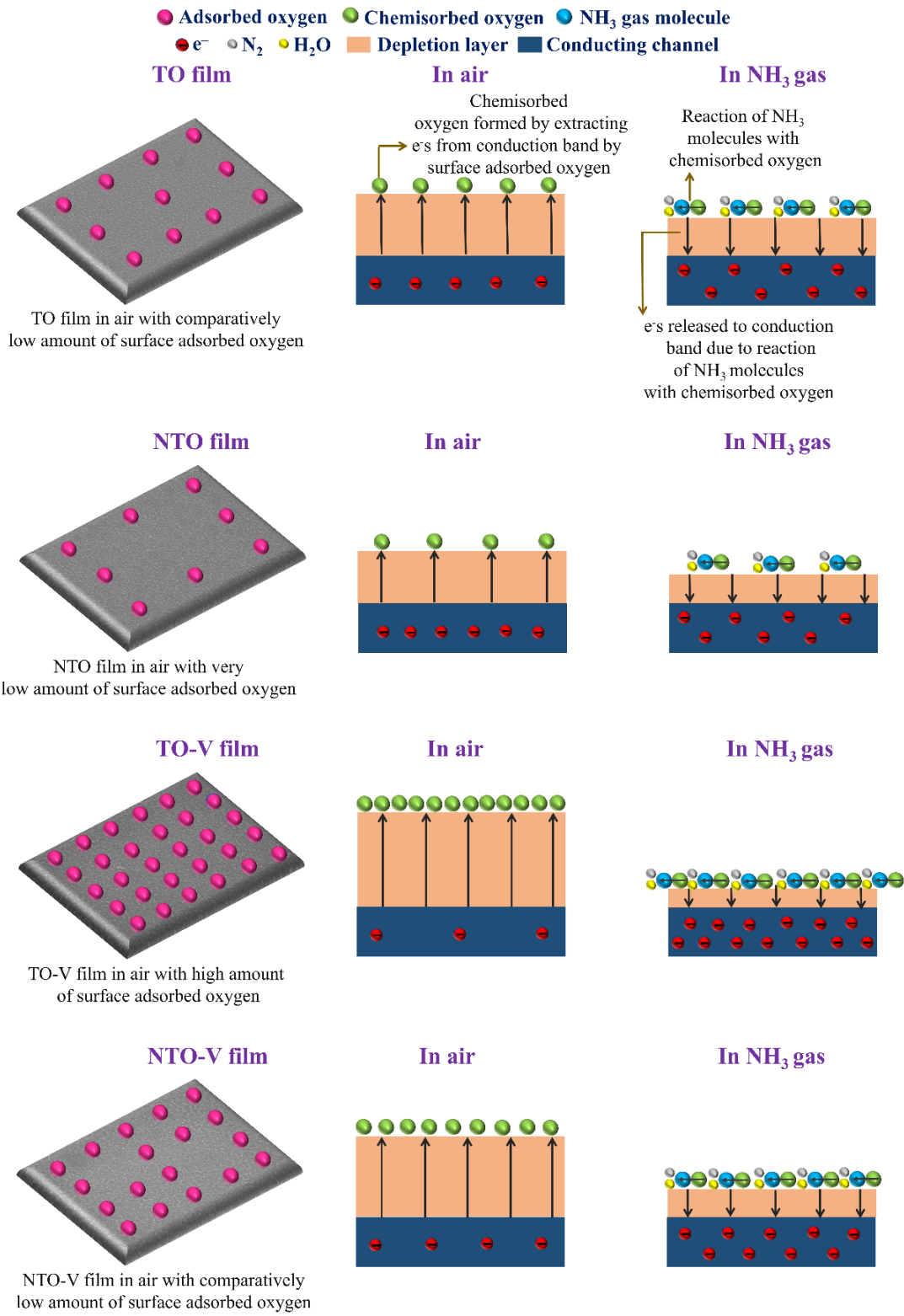
Fig. 4.24: Schematic representation of the probable gas sensing mechanism that occurred in all the films.

4.4 Ti and Zn co-doped indium oxide thin films

In this section, the preparation and characterization of Ti and Zn co-doped indium oxide, In_2O_3 (ITiZO) based combustible precursor and thin films are discussed. Initially, the thermal behaviour of the combustible precursor was inspected through TGA. The fabricated spin-coated thin films were inspected through various thin film characterization techniques such as GIXRD, SEM, EDAX, AFM and UV-Vis.
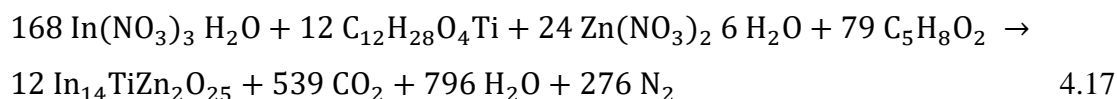
4.4.1 Experimental procedure

4.4.1.1 Materials

All the reagents were of analytical grade and utilized without any additional purification. Indium nitrate ($In(NO)_3$ H_2O) (Alfa Aesar), titanium (IV) isopropoxide ($C_{12}H_{28}O_4Ti$) (Sigma-Aldrich), zinc nitrate hexahydrate ($Zn(NO_3)_2$ $6H_2O$) (SRL Chemicals), acetylacetone ($C_5H_8O_2$) (SRL Chemicals) and 2-methoxyethanol ($C_3H_8O_2$) (Molychem) were used in this study.

4.4.1.2 Preparation of precursor and its characterization

In this work, stoichiometric amounts of $In(NO)_3$ H_2O, $C_{12}H_{28}O_4Ti$, $Zn(NO_3)_2$ $6H_2O$, $C_5H_8O_2$ were taken according to the balanced equation 4.17, and they were dissolved in $C_3H_8O_2$ (5.6 ml). The molarity of the precursor was 0.3 M. The precursor was stirred (at 250 rpm) for 2 h at ambient temperature to attain a clear and homogenous solution. The thermal behaviour of the precursor was examined under TGA and DTA (TGA, Seiko Instruments TGA, DTA Exstar 6300) in the nitrogen atmosphere from room temperature to 600 °C with 10 °C/min heating rate.

$$168\ In(NO_3)_3\ H_2O + 12\ C_{12}H_{28}O_4Ti + 24\ Zn(NO_3)_2\ 6\ H_2O + 79\ C_5H_8O_2\ \rightarrow$$
$$12\ In_{14}TiZn_2O_{25} + 539\ CO_2 + 796\ H_2O + 276\ N_2 \qquad\qquad 4.17$$

4.4.1.3 Preparation of ITiZO films and their characterization

The corning glass substrates (Corning Incorporated; thickness 0.96 to 1.06 mm) were ultrasonically cleaned for 5 min using distilled water, followed by acetone, isopropyl alcohol, and again distilled water. The glass substrates were finally dried with N_2 gas. Later, the substrates were subjected to UV ozonization for 15 min for surface activation. The precursor was spin coated at 3000 rpm on the substrates for 30 s. After

spinning, the respective samples were heated at 300 °C/350 °C for 20 min. Likewise, two samples were spin coated three times. Finally, the two samples were annealed at two variable annealing temperatures, 300 °C and 350 °C, respectively, for 4 h. The schematic representation of the fabrication of thin films in the present work is shown in Fig. 4.14. After annealing, the ITiZO films were analyzed under thin film X-Ray diffraction (PANalytical X'Pert) for the structural properties with a grazing angle of 0.5° and a scanning rate of 2°/min with Cu K_α X-ray source (λ = 1.54 Å). Microstructural analysis of the films was examined through scanning electron microscopy (SEM, JSM 6380, JEOL). Elemental presence in the films was inspected by energy dispersive X-Ray analysis (EDAX, AMETEK). The transparency of the films in the visible region was derived by a UV-Visible spectrometer (Shimadzu UV-3600 Spectrophotometer). The surface roughness of films was derived from atomic force microscopy (AFM, Innova SPM). The thickness of the films was measured through near normal spectroscopic reflectometer (HO-NNSR-01, Holmarc). The thickness was 80 ± 1 nm and 78 ± 1 nm for 300 °C and 350 °C annealed films.
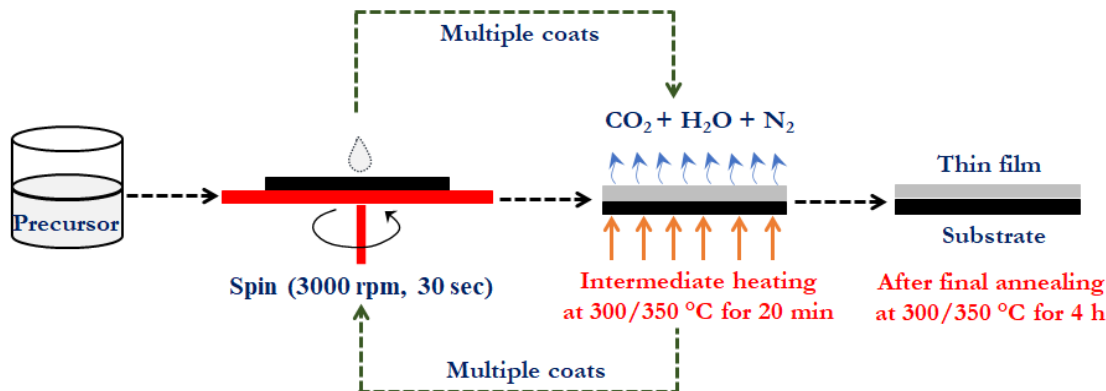
Fig. 4.25: Schematic representation of the fabrication of thin films in the present work.

4.4.2 Results and discussion

The TGA, DTG and DTA thermograms of the combustible precursor are shown in Fig. 4.26. The thermograms are subdivided into four regions, namely, region I (room temperature to 110 °C), region II (110 °C to 136 °C), region III (136 °C to 400 °C) and region IV (400 °C to 600 °C). A gradual weight loss of 86 % in TGA curve with a peak in DTG curve and an endothermic peak in DTA curve is noticed in region I and it is attributed to the evaporation of the solvent. In region II, a sudden weight loss of 6 % is

observed with another peak in DTG curve at 123 °C. An exothermic peak at 123 °C is also noticed in the DTA curve. The sudden weight loss with exothermic response in region II is dedicated to the occurrence of combustion of the precursor associated with the escape of by-product gases. In region III, another gradual, minor weight loss of 2 % is observed in TGA curve with no changes in DTG and DTA curves, and it is due to the further escape of carbonaceous impurities that emerged during the combustion reaction. In region IV, no weight loss and no changes are detected in the thermal curves and it confirms the formation of the desired stable oxide.
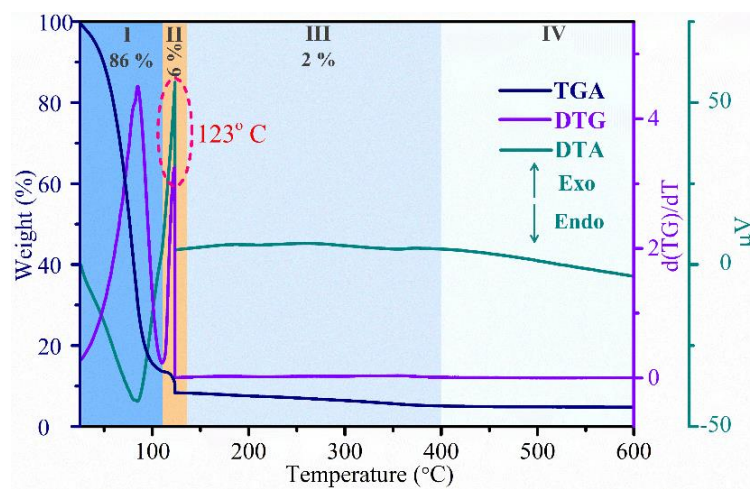

Fig. 4.26: TGA, DTG and DTA thermograms of the combustible precursor.

GIXRD patterns of 300 and 350 °C annealed films along with uncoated glass are shown in Fig. 4.27 (a). It is observed that both films exhibited crystallinity without forming any secondary phases of dopants Ti and Zn, whereas uncoated glass is completely amorphous. It is noticed that 300 °C annealed film is less crystalline compared to 350 °C annealed film. The crystallinity of films showed an increment with annealing temperature. The diffraction planes (222), (400), (440) and (622) in 350 °C annealed film match well with the cubic bixbyite structure of indium oxide (ICDD: 00–006-0416). The schematic representation of the cubic bixbyite crystal structure of In_2O_3 is shown in Fig. 4.27 (b) (Marezio 1966). The average crystallite size is calculated from the Scherrer formula (shown in equation 4.5) and it is found to be 9.2 and 11.5 nm, respectively, for 300 and 350 °C annealed films; as annealing at high temperatures promotes the grain growth (Pujar et al. 2018). Fig. 4.27 (c) and (d) show the AFM images of 300 and 350 °C annealed films, and it is noticed that both the films are smooth

with a surface roughness of 0.4 and 0.5 nm, respectively. The reason for the slight reduction in the surface roughness for 300 °C annealed film is due to less crystallinity compared to 350 °C annealed film (Pujar et al. 2018).
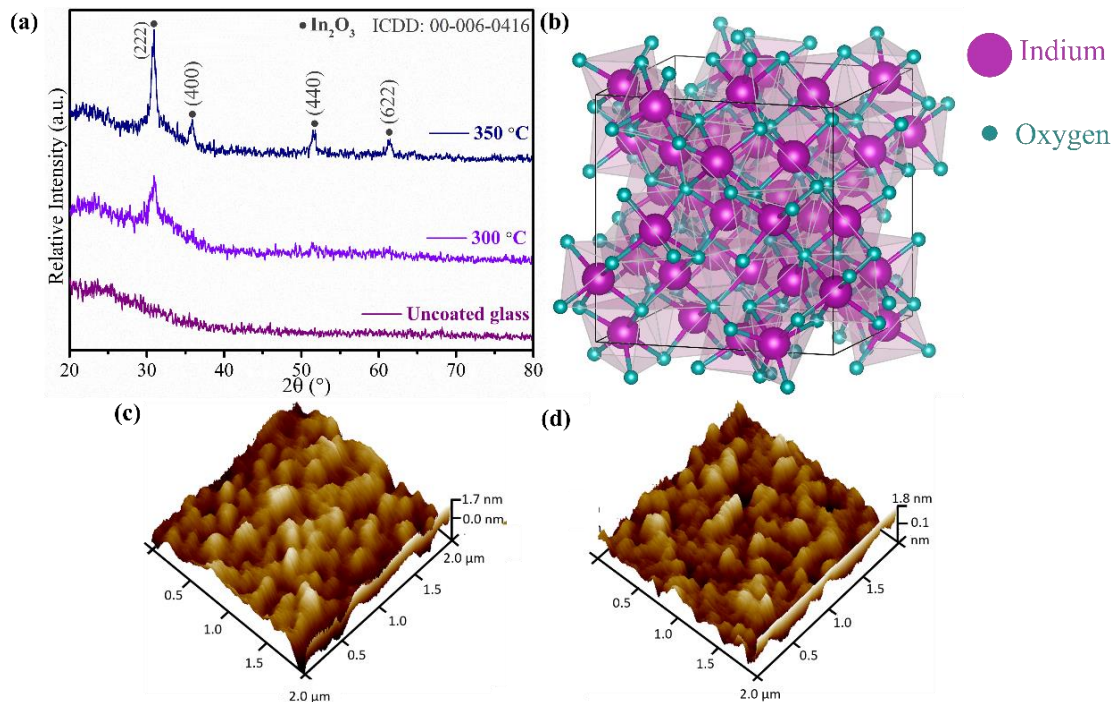
Fig. 4.27: (a) GIXRD patterns of uncoated glass, 300 and 350 °C annealed ITiZO films, (b) cubic bixbyite crystal structure of In_2O_3. (The crystal structure is drawn using the VESTA visualization interface software and the crystallographic information file is taken from the Crystallography open database (2310009)); AFM images of (c) 300 and (d) 350 °C annealed ITiZO films, respectively.

Fig. 4.28 (a and b) displays the SEM images of 300 °C and 350 °C annealed films. It is observed that the surfaces of both films are uniform, free from pinholes, cracks, and pores, and microscopically showing featureless morphology. Fig. 4.28 (c and d) shows the EDAX spectra of 300 °C and 350 °C annealed films and from the spectra, the presence of In, Ti, Zn and O elements is noticed in both the films, which proves the successful deposition of ITiZO films at both the temperatures.
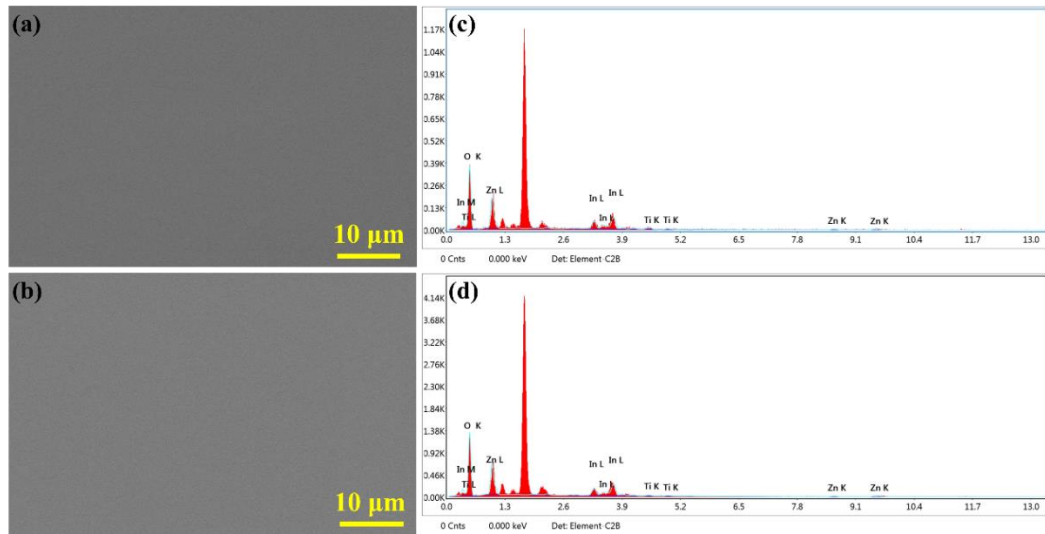
Fig. 4.28: SEM images of (a) 300 °C and (b) 350 °C annealed ITiZO films and respective EDAX spectra of (c) 300 and (d) 350 °C annealed ITiZO films.
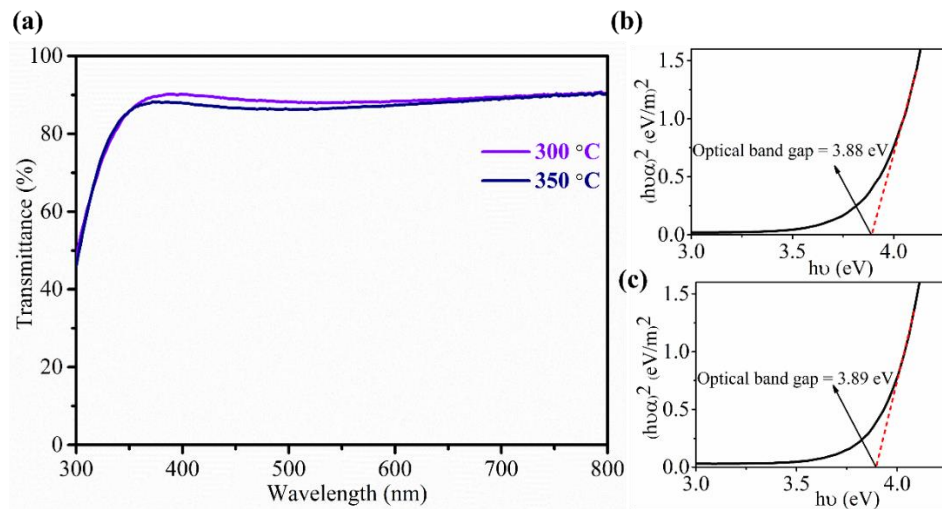
Fig. 4.29: (a) Transmittance plot of 300, 350 °C annealed ITiZO films, Tauc's plot of (b) 300 (c) 350 °C annealed ITiZO films, respectively.

Fig. 4.29 (a) shows the normalized transparency plot of 300 °C and 350 °C annealed films. It is observed that the 300 and 350 °C annealed films are highly transparent, with transparency of ~90 % and 85 %, respectively, in the visible range. It is noticed that as the annealing temperature increased to 350 °C, the transparency of the film decreased. It is known that carrier concentration (N) increases with annealing temperature due to the formation of oxygen vacancies and results in the generation of free charge carriers, as shown in equation 4.16. It is also known that the carrier

concentration has an inverse relation with the plasma wavelength (λ_p) (λ_p α $1/\sqrt{N}$). According to the relation, the plasma wavelength decreases with an increase in the temperature (as 'N' increases with temperature). The incoming light with a wavelength more than the plasma wavelength cannot propagate and results in reflection. So, in turn, the transparency decreases at higher annealing temperatures. The other reason for the transparency reduction in the 350 °C annealed film is due to the increase in surface roughness; the light scatters at higher surface regions on the film, which in turn reduces the transparency (ben Wannes et al. 2018). The optical energy band gap (E_g) of the films is estimated through Tauc's relation (as shown in equation (3.2)). Here, the value of index 'n' is taken as ½ by considering In_2O_3 as a direct band gap semiconductor (Ge et al. 2022). The estimated E_g is ~3.8 eV for the 300 and 350 °C annealed films (represented in Fig. 4.29 (b and c)).

4.5 Conclusions

The thermal analysis confirmed the combustion temperature of the precursors utilized for pristine and Ti doped ZnO films was in the range of ~205 to 235 °C. Polycrystalline films were fabricated on glass substrates with a hexagonal wurtzite crystal structure of ZnO without any secondary phases of dopant oxides. ZT0 film was porous and rough, whereas ZT1, ZT2, and ZT3 films were dense and comparatively smooth. The transparency of the films was in the range of ~70 to 90%, and the E_g of the films was enhanced with Ti doping. A high crystallinity, O_V/O_L and % of O_A were found in ZT0 film. All the films responded to NH_3 gas (25 to 100 ppm) at room temperature during the gas sensing test. ZT0 film exhibited high gas response compared to doped films at all concentrations of NH_3 gas, and the gas response in doped films followed the trend of ZT3 > ZT2 > ZT1. The highest gas response in the present study was found in ZT0 film with a value of 34.7 at 100 ppm of NH_3 gas.

The combustion temperature of the precursors used for fabricating undoped and Nb doped TiO_2 films was between ~120 to 150 °C. All the films were deposited on glass substrates and were found to be polycrystalline with a tetragonal anatase crystal structure of TiO_2 without any dopant oxide phases. Pristine (TO and TO-V) films exhibited high crystallinity than doped (NTO and NTO-V) films. All the films exhibited

similar morphological features. The transparency of the films was more than ~50 % and the E_g was found to be relatively higher in doped films than in undoped films. All the films detected NH_3 gas (25 to 100 ppm) at room temperature. Gas response of all the films towards all concentrations of NH_3 gas was found to be extremely dependent on the % of O_A; the higher % of O_A, the higher the gas response of the film. High crystallinity and more % of O_A were found in TO-V film than in NTO-V film, due to which it exhibited high gas response than NTO-V film. The same factors helped in attaining a relatively gas response in TO film compared to NTO film. The highest gas response in the current work was attained in TO-V film with a value of ~16 at 100 ppm of NH_3 gas.

The combustion temperature of the precursor utilized to fabricate Ti and Zn co-doped indium oxide (ITiZO) thin films was found to be 123 °C. The ITiZO films deposited on the glass substrates were crystalline with a cubic bixbyite crystal structure of In_2O_3. No formation of any secondary phases of dopant oxides was found. The films were crack and pore-free, smooth with low roughness ranging from 0.4 to 0.5 nm. The films achieved more than 85% transparency in the visible range with an optical band gap of ~3.8 eV.

The gas sensors fabricated in the current chapter are transparent (> 50 %) in the visible range and they can be operated at room temperature conditions. Therefore, these gas sensors can be potentially applied in optoelectronic devices and miniaturized transparent devices where the combination of transparency and gas sensing is desired.

The page was left intentionally blank

CHAPTER 5

DEVELOPMENT OF SCREEN-PRINTABLE PARTICLE-FREE AQUEOUS SOLUTION COMBUSTIBLE INDIUM OXIDE-BASED INKS, FILMS & THEIR CHARACTERIZATIONS

5.1 Introduction

This chapter deals with the indium oxide (In_2O_3) based screen-printed films that are developed through particle-free aqueous solution combustible inks. In Chapter 4, indium oxide-based films are developed by the spin coating method. In this current study, to explore the fabrication of the indium oxide-based films by screen-printing method, this method is chosen because it is known that screen-printing comprises certain advantages such as mass production of films in less time. It is also known that indium oxide-based thin films are effective in electronic applications; therefore, the indium oxide system is considered in this study instead of other oxide systems. The work in Chapter 5 aims to develop particle-free solution combustible inks that are aqueous-based. The metal precursors used in Chapter 4, such as indium nitrate and zinc nitrate, are soluble in water. But titanium isopropoxide (source of Ti) is insoluble in water and forms agglomerated particles, which is highly undesirable for the motive. Commonly, the other favorable dopant in the indium oxide system is tin (Sn). Also, the metal source, tin chloride, is soluble in water, and it is also commonly utilized tin source in the solution combustion process to synthesize indium tin oxide (ITO). Thus, to prepare aqueous-based inks which are combustible, the dopant Sn is chosen over Ti in the present work.

The experimental advantages of this work are as follows. Primarily, the developed approach is 'particle-free' where the functional material is molecular-precursor based, which avoids the extra processing step of synthesizing nano or microparticles (generally performed in a particle-based approach). The developed method completely eradicates the disadvantages like agglomeration of particles in ink and clogging of mesh pores (because the nano/microparticles stick to screen mesh), which results in improper printing. Secondly, here water is used as the solvent, which

is abundantly available, cost-effective, non-toxic, and helps in reducing hazardous organic content in ink. Lastly, screen printing helps in the mass production of films, as mentioned earlier.

In this chapter, the development and characterization of the indium oxide-based particle-free aqueous solution combustible inks are discussed first. All the respective combustible inks are screen-printed on the glass substrates, followed by annealing at appropriate temperatures to fabricate the respective films. Later, the characterization of the indium oxide-based screen-printed thin films is discussed.
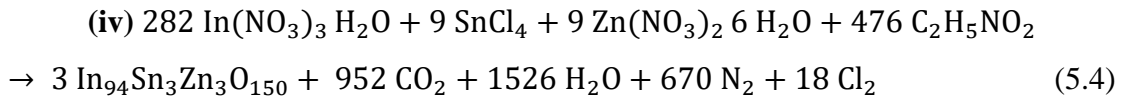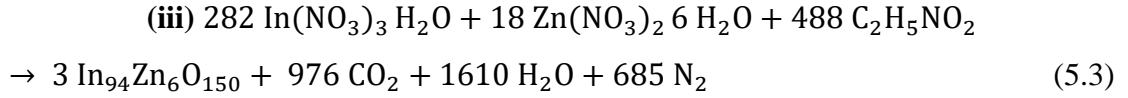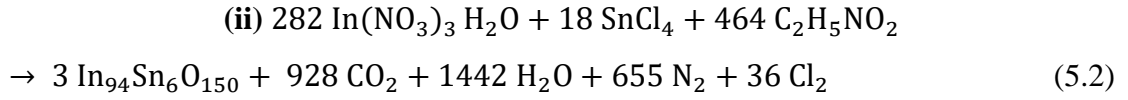
5.2 Experimental procedure

5.2.1 Materials

All the reagents were of analytical grade and utilized without additional purification. Indium nitrate ($In(NO)_3$ H_2O) (Alfa Aesar), zinc nitrate hexahydrate ($Zn(NO_3)_2$ $6H_2O$) (SRL Chemicals), tin (IV) chloride ($SnCl_4$) (Sigma-Aldrich), glycine ($C_2H_5NO_2$) (Molychem) and hydroxyethyl cellulose (Sigma-Aldrich) were used in this study. For silver electrodes, silver conductive adhesive paste (Alfa Aesar) was used.

5.2.2 Preparation of inks and their characterization

In this study, to prepare pure In_2O_3, 6 at. % Sn doped In_2O_3, 6 at. % Zn doped In_2O_3, and 3 at. % Sn, 3 at. % Zn co-doped In_2O_3 films, particle-free aqueous solution combustible precursors with molarity 0.3 M are developed. Stoichiometric quantities of $In(NO)_3$ H_2O, $SnCl_4$, $Zn(NO_3)_2$ $6H_2O$ and $C_2H_5NO_2$ were taken according to the equations 5.1, 5.2, 5.3 and 5.4, respectively, to develop the inks. All the stoichiometric amounts of the mentioned chemicals were dissolved in distilled water, and they were stirred rigorously (at 250 rpm) for 2 h. Later 1 g of hydroxyethyl cellulose (as a binder) was added in smaller amounts to mix properly in every precursor, and finally, all the precursors were stirred at low rpm (50 rpm) for 16 h at room temperature. The low rpm was chosen for the proper rotation of magnetic bead, as the high rpm would not allow the bead to rotate appropriately due to conversion of precursors into viscous inks after addition of the binder. After stirring, all the inks were further used for the screen-printing.

(i) $6 \, In(NO_3)_3 \, H_2O + 10 \, C_2H_5NO_2 \rightarrow 3 \, In_2O_3 + 20 \, CO_2 + 31 \, H_2O + 14 \, N_2$ (5.1)

(ii) $282 \, In(NO_3)_3 \, H_2O + 18 \, SnCl_4 + 464 \, C_2H_5NO_2$

$\rightarrow 3 \, In_{94}Sn_6O_{150} + 928 \, CO_2 + 1442 \, H_2O + 655 \, N_2 + 36 \, Cl_2$ (5.2)

(iii) $282 \, In(NO_3)_3 \, H_2O + 18 \, Zn(NO_3)_2 \, 6 \, H_2O + 488 \, C_2H_5NO_2$

$\rightarrow 3 \, In_{94}Zn_6O_{150} + 976 \, CO_2 + 1610 \, H_2O + 685 \, N_2$ (5.3)

(iv) $282 \, In(NO_3)_3 \, H_2O + 9 \, SnCl_4 + 9 \, Zn(NO_3)_2 \, 6 \, H_2O + 476 \, C_2H_5NO_2$

$\rightarrow 3 \, In_{94}Sn_3Zn_3O_{150} + 952 \, CO_2 + 1526 \, H_2O + 670 \, N_2 + 18 \, Cl_2$ (5.4)
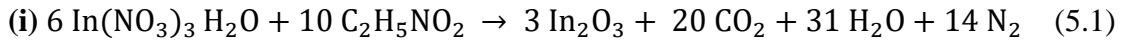
The thermal behaviour of all the inks was inspected under thermogravimetric analysis (TGA, Seiko Instruments TGA) in a nitrogen atmosphere from room temperature to 700 °C with a scanning rate of 10 °C/min. Fourier-transform infrared (FTIR) spectra of all the inks were obtained through the FTIR spectrometer (MAGNA 550, Nico-142 let Instrument Co.).

5.2.3 Fabrication of the films and their characterization

In the present work, corning glasses (Corning Incorporated; thickness 0.96 to 1.06 mm) were utilized as the substrates and the substrates were properly cleaned. The exact method was followed for cleaning the glass substrates, as stated in section 4.2.1.3. Initially, the screen mesh was prepared with a stretched tension of 20 N/m. Later, the formulated individual, stable particle-free aqueous combustible inks were screen-printed on different glass substrates. Patterns of area 2×2 cm^2 were printed using the polymer squeegee blade, which was positioned at an angle of 45° to the screen mesh. During the operation of screen-printing, the printing speed was held at 50 mm/s, the printing force was preserved at ~30 N and the snap-off distance was maintained at ~1.5 mm. After printing, the samples were annealed at 400 °C for 2 h in a muffle furnace. The schematic representation of the fabrication of screen-printed films in the present work is displayed in Fig. 5.1. Hereafter in this chapter, pure In_2O_3 screen-printed film is called IO film, 6 at. % Sn doped In_2O_3 screen-printed film is called ITO film, 6 at. % Zn doped In_2O_3 screen-printed film is called IZO film and 3 at. % Sn, 3 at. % Zn co-doped In_2O_3 screen-printed film is called ITZO film.
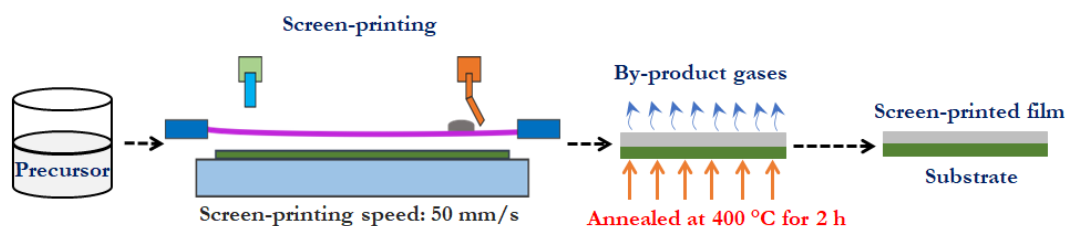
Fig. 5.1: Schematic representation of the fabrication of screen-printed films in the present work.

To examine the structural properties of the screen-printed films, they were analysed under PANalytical multi-purpose high-resolution X-Ray diffractometer (GIXRD) (Empyrean) (source of copper Kα radiation) with a grazing angle of 0.5° and a step size of 0.07°. To inspect the microstructural features of the screen-printed films and to check the elemental presence, field emission scanning electron microscopy (FESEM) (Carl Zeiss Sigma) included with energy-dispersive X-ray analysis (EDAX) (Oxford instruments) were respectively used. The topography and surface roughness of the screen-printed films were derived from atomic force microscopy (AFM) (Innova SPM). Here, tapping mode was utilized and the area of scanning was 2×2 μm^2. The screen-printed films were analysed under UV–Visible spectrometer (Shimadzu UV-3600 UV–Vis–NIR Spectrophotometer) to assess the transparency in the visible region and the optical energy band gap was estimated through Tauc's plot from the absorption spectra. To examine the chemical state of the elements that are present in the screen-printed films, X-ray photoelectron spectroscopic study (XPS, Kratos Axis Ultra DLD) was conducted. The C-H peak of adsorbed carbon, located at the binding energy of 284.6 eV, was used for the calibration of the received spectra. XPS curve fitting software package (XPSPEAK41) was utilized to conduct the fitting. Full-width half maximum (FWHM) and Gaussian/Lorentzian (G/L) ratio were held constant to evade the discrepancy in fitting the peak. For best fitting, a minimum chi-square was selected, and Shirley background was utilized during the peak fitting. The fitted XPS spectra of C 1s of all the screen-printed films and the details of the fitting parameters are given in Appendix V. The thickness of all the screen-printed films was measured through a digital thickness gauge (Mitutoyo: model no. 547-401), and the average thickness was around 5 μm for all the screen-printed films.

In the present study, the gas sensing characterization of the screen-printed films was performed towards ethanol (C_2H_5OH) gas and it was conducted in a custom-made air-sealed chamber. In this study also, the same experimental setup and procedure were used for the gas sensing characterization of all the screen-printed films, as mentioned in section 4.2.1.3. Here too, the silver electrodes were deposited on two opposite edges of all the screen-printed films to prepare the electrical contacts for gas sensing characterization. The gas sensing properties of the screen-printed films towards different concentrations of ethanol gas (50 to 100 ppm) were examined in the current study. The selectivity test of IO film was conducted towards gases such as methanol, xylene, and toluene of 100 ppm concentration. In this study, all the gas sensing measurements were conducted at room temperature only. The time taken by the film to attain a 90 % change in the total resistance was measured as the response time during the adsorption process and as the recovery time during the desorption of the ethanol gas in this current study as well.

5.3 Results and discussion

The TGA and DTG curves of formulated screen-printable particle-free aqueous solution combustible inks to prepare pure In_2O_3, 6 at. % Sn doped In_2O_3, 6 at. % Zn doped In_2O_3 and 3 at. % Sn, 3 at. % Zn co-doped films are shown in Fig. 5.2 (a to d), respectively. The TGA and DTG curves in this study are categorized into five regions as a function of temperature. They are represented as region I (room temperature to 100 °C), region II (100 °C to 250 °C), region III (250 °C to 320 °C), region IV (320 °C to 600 °C) and region V (600 °C to 700 °C), respectively. It is traced that the weight loss in all the inks happened in four steps. The first weight loss of ~80 % is noticed in region I, and it can be due to evaporation of the solvent (water) in the inks. A slight weight loss (~3 to 4 %) is detected in region II of all inks and it can be credited to the loss of bound water molecules from metal nitrate hydrate precursors. Approximately a sudden weight loss of 6 % is found in all the thermograms in region III, and it can be dedicated to the combustion reaction, which generates weight loss with simultaneous evaporation of the by-product gases. The temperature of ~280 °C can be considered as the combustion temperature for all the inks, and it is detected from the peak that appeared in the respective DTG curves. In region IV, a gradual weight loss of ~4 to 6 % is traced

and it can be devoted to the removal of carbonaceous impurities generated during the combustion reaction and to the decomposition of the binder. It is observed that there is no weight loss above 600 °C (region V), and it specifies the formation of the stable desired oxide at high temperatures (Manjunath et al. 2021a).

Fig. 5.2: TGA and DTG curves of particle-free aqueous solution combustible inks to prepare (a) pure In_2O_3, (b) 6 at. % Sn doped In_2O_3, (c) 6 at. % Zn doped In_2O_3 and (d) 3 at. % Sn, 3 at. % Zn co-doped In_2O_3 films, respectively.

The obtained FTIR spectra of all the screen-printable particle-free aqueous solution combustible inks are shown in Fig. 5.3. It is observed that five bands exist in all the spectra. The band located at the low wave number of ~1064 cm^{-1} can be assigned to the CH–O–CH$_2$ stretch of the binder (Pushpamalar et al. 2006). The band positioned at the wave number of ~1365 cm^{-1} can be credited to the asymmetrical stretching of the nitrate ions (NO$_3^-$) present in the inks (MacHado et al. 2010). The band situated at wave number ~1640 cm^{-1} can be allotted to the angular vibration of the interlayer molecules of water (MacHado et al. 2010). A minute band detected at the wave number of ~2920 cm^{-1} can be dedicated to the C–H stretching vibration (Pushpamalar et al. 2006). The broad band traced at the wave number of ~3367 cm^{-1} can be ascribed to the symmetric

stretching of the O–H group that is linked with the nitrates present in the inks (MacHado et al. 2010).
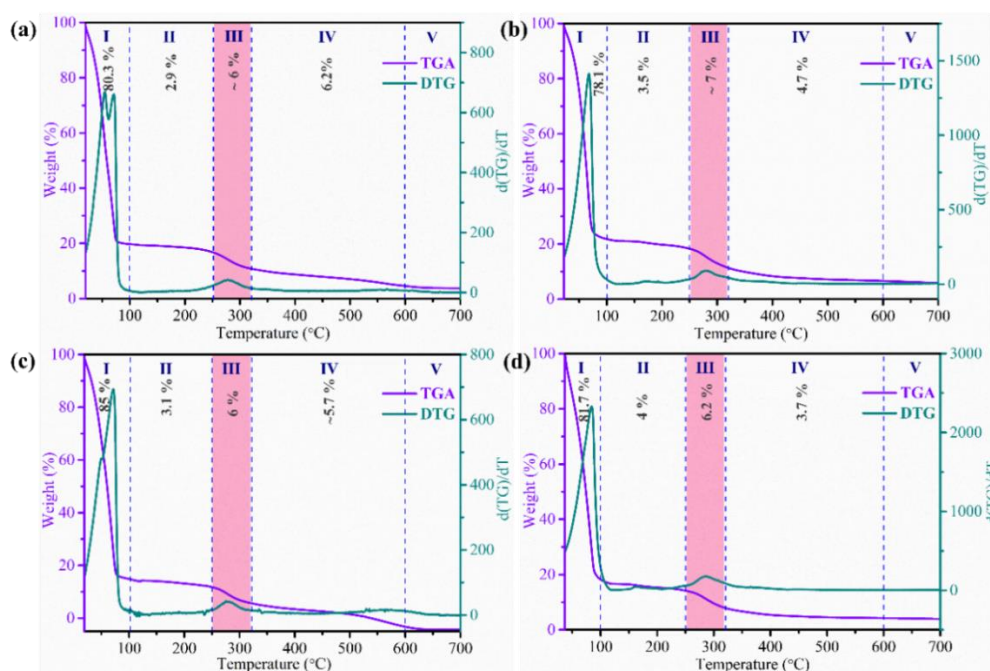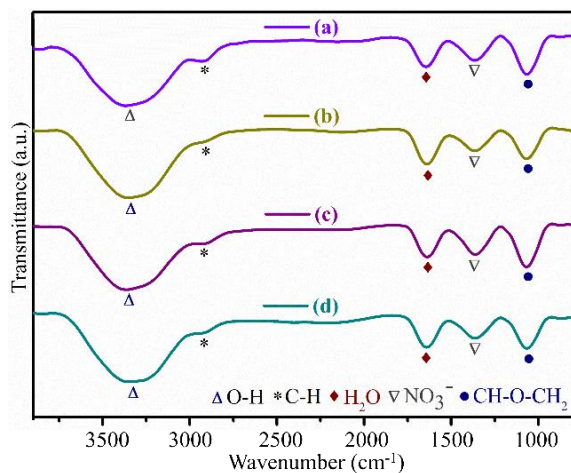

Fig. 5.3: FTIR spectra of particle-free aqueous solution combustible inks to prepare (a) pure In_2O_3, (b) 6 at. % Sn doped In_2O_3, (c) 6 at. % Zn doped In_2O_3 and (d) 3 at. % Sn, 3 at. % Zn co-doped In_2O_3 films, respectively.
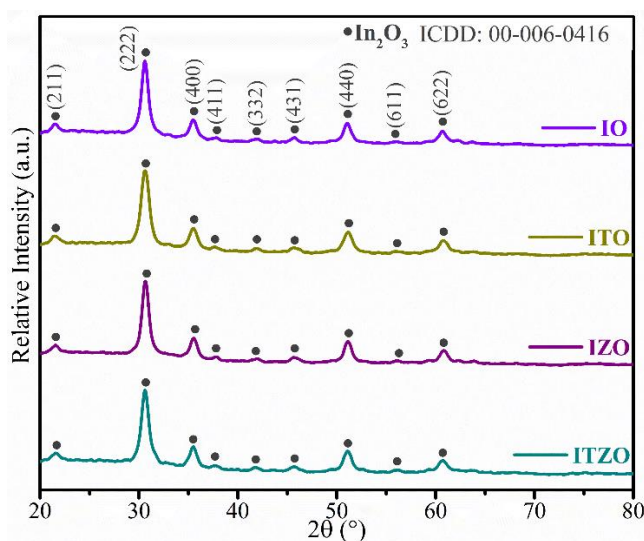
Fig. 5.4: GIXRD patterns of all the screen-printed films.

The GIXRD patterns of all the screen-printed films that are fabricated at 400 °C are shown in Fig. 5.4. It is perceived that all the screen-printed films are polycrystalline in nature. The obtained diffraction planes, namely, (211), (222), (400), (411), (332), (431), (440), (611) and (622), are well coordinated with the cubic bixbyite crystal structure of In_2O_3 (ICDD: 00–006-0416). It is also observed that there are no secondary oxide phases of dopants Sn and Zn in ITO, IZO and ITZO films. The absence of

secondary oxide phases confirmed the substitutional doping/co-doping of Sn and Zn into the host In_2O_3 (Pujar et al. 2017). The average crystallite size of all the screen-printed films is estimated from the Scherrer formula, as shown in equation 4.5. The average crystallite size of IO film is found to be 10.6 nm, whereas it has slightly reduced to 8.9 nm, 9.7 nm, and 9.6 nm in the case of doped films (ITO, IZO and ITZO, respectively). The present study concludes that inhibition of the crystal growth has occurred after doping in the indium oxide host structure.
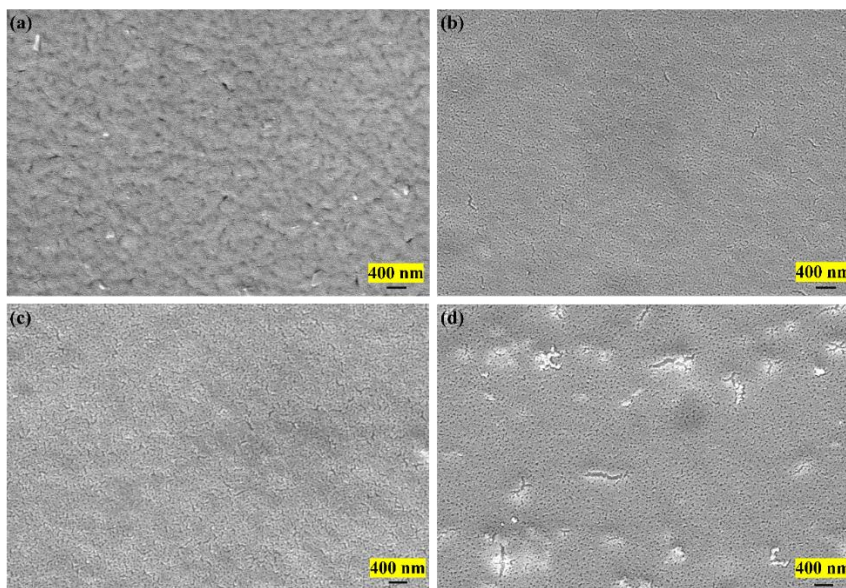
Fig. 5.5: SEM images of (a) IO, (b) ITO, (c) IZO, and (d) ITZO screen-printed films.

The SEM images of all the screen-printed films are shown in Fig 5.4. It is observed from Fig. 5.5 (a) that IO film has equipped with comparatively larger grains and with small nano-sized pores. The presence of the pores can be dedicated to the escape of the gases during the combustion reaction. In the case of doped ITO, IZO, and ITZO films (Fig. 5.5 (b to d)), a reduction in the grain size is noticed. The reduction in the grain size observed in doped films is in line with the results obtained from the GIXRD analysis in this study. The existence of tiny pores is also detected in the surface of ITO, IZO, and ITZO films which is due to the escape of the by-product gases generated in the combustion reaction. In the case of ITZO film, it is also observed that some clusters with cracks have protruded from the surface of the film. It is also found that in all the screen-printed films, the grains are well-interconnected. The EDAX spectra of the screen-printed films are shown in Fig. 5.6. The presence of the elements

like In, O and C is detected in IO film (Fig. 5.6 (a)). The existence of In, O and C, along with the dopant Sn element, is traced in ITO film (Fig. 5.6 (b)). Similarly, the elements In, O and C, together with the dopant Zn element, are detected in IZO film (Fig. 5.6 (c)). In the case of ITZO film, the elements In, O and C, along with dopants Sn, Zn elements, are traced in ITZO film (Fig. 5.6 (d)). The presence of host elements in pristine film and the existence of host elements with respective dopant elements in the case of ITO, IZO, and ITZO confirms the successful fabrication of the screen-printed films in the present study. The presence of the C element in all the screen-printed films can be because of the surface adsorption from the atmosphere in the form of CO and CO_2 etc. (Regragui et al. 2000).
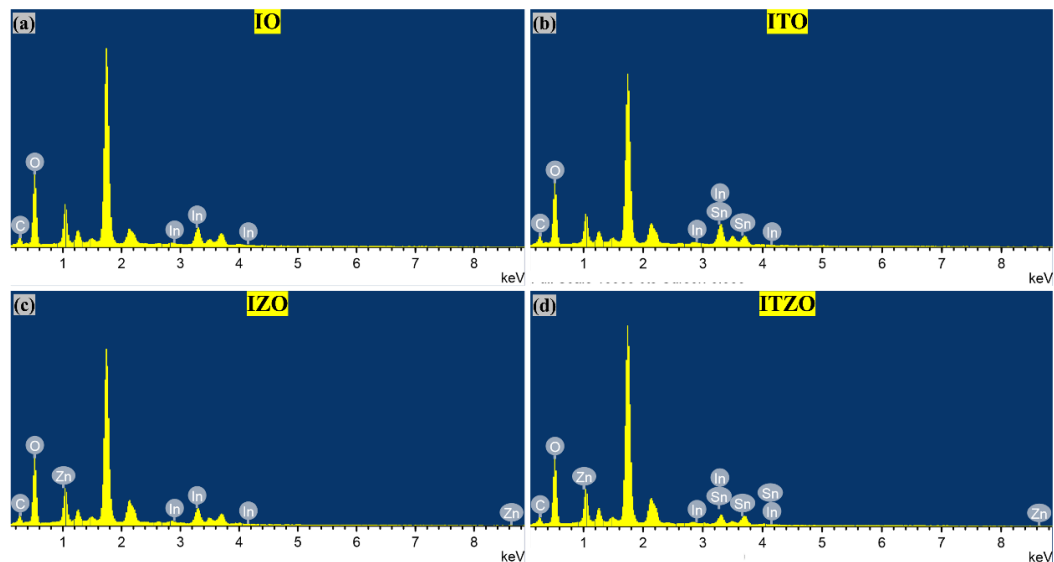
Fig. 5.6: EDAX spectra of (a) IO, (b) ITO, (c) IZO and (d) ITZO screen-printed films.

The AFM images with their average surface roughness of all the screen-printed films are shown in Fig. 5.7. It is observed that IO film showed a morphology with slightly bigger grains which is different from the doped films (Fig. 5.7 (a)) and it is in line to the SEM images. In fact, all the doped films exhibited a similar morphology with relatively less grain size. Alike from the SEM image, ITZO film exhibited a morphology of few clusters emerging out from the surface. IO film is comparatively rougher than the other films, with an average surface roughness of 10.2 nm, followed by ITZO and IZO films (average surface roughness of 8.2 and 7.2 nm, respectively). In contrast to other films, ITO film has the lowest surface roughness of 3.3 nm.
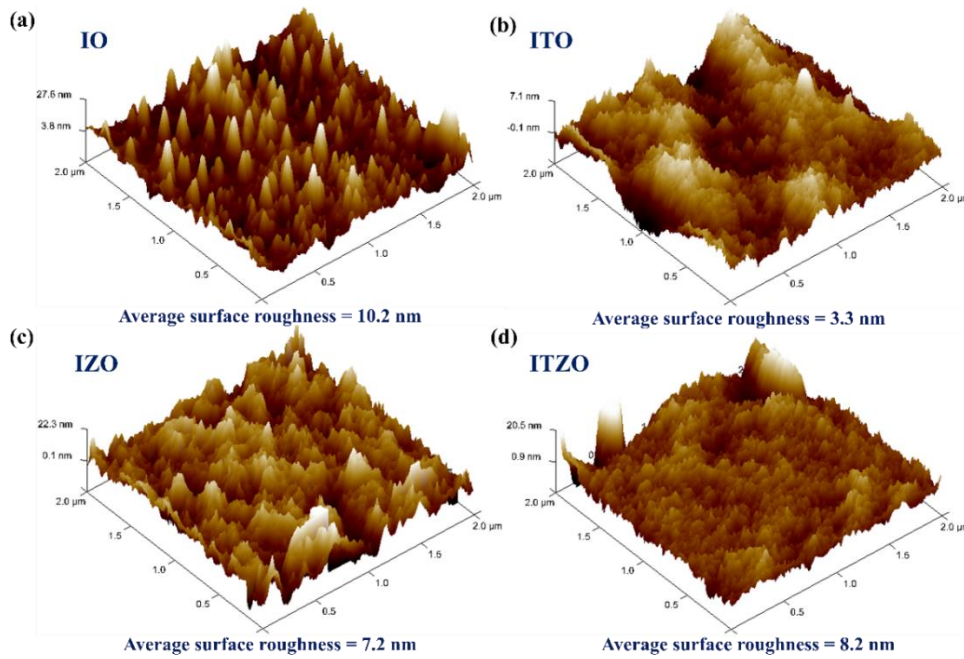
Fig. 5.7: AFM images with average surface roughness values of (a) IO, (b) ITO, (c) IZO, and (d) ITZO screen-printed films, respectively.
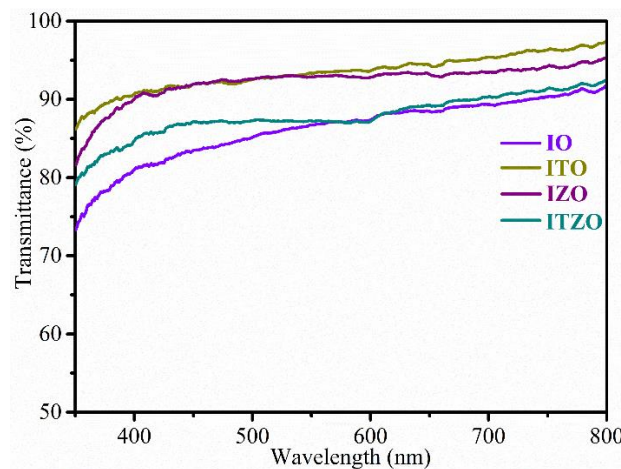
Fig. 5.8: Transmittance plots of IO, ITO, IZO and ITZO screen-printed films.

The normalized transmittance curves of all the screen-printed films in the visible range are shown in Fig. 5.8, and the transparency of all the films is in the range of 75 to 95 %. The IO film has exhibited relatively lower transparency compared to the other films. The reason for it can be dedicated to its higher surface roughness, which is derived from AFM analysis. It is stated earlier that the surface roughness of the films plays a vital role in their optical properties. It is reported in the literature that the incoming light scatters when the surface roughness is high, and it causes a decrement

160

in the transparency (Eshaghi et al. 2015). It can be inferred that the transparency has an inverse relation with the surface roughness (Kumar et al. 2020). The IO film with a high average surface roughness of 10.2 nm exhibited a lower transparency. The IZO and ITZO films embraced with comparatively lower average surface roughness than IO film displayed a better transparency than IO film. The high transparency is detected in ITO film that comprised relatively low surface roughness than the other films. The E_g of the screen-printed films is assessed via Tauc's relation (equation (3.2)) and In_2O_3 is considered as a direct band gap semiconductor. The respective Tauc's plot of the screen-printed films is placed in Appendix V. It is observed that the estimated E_g value of all the screen-printed films is ~ 3.6 eV. The obtained E_g value of the screen-printed films in the present study is in good correlation with the previous reports, where the direct E_g value of the In_2O_3 is mentioned as ~ 3.6 eV (Reddy et al. 2017) (Shankar et al. 2016).
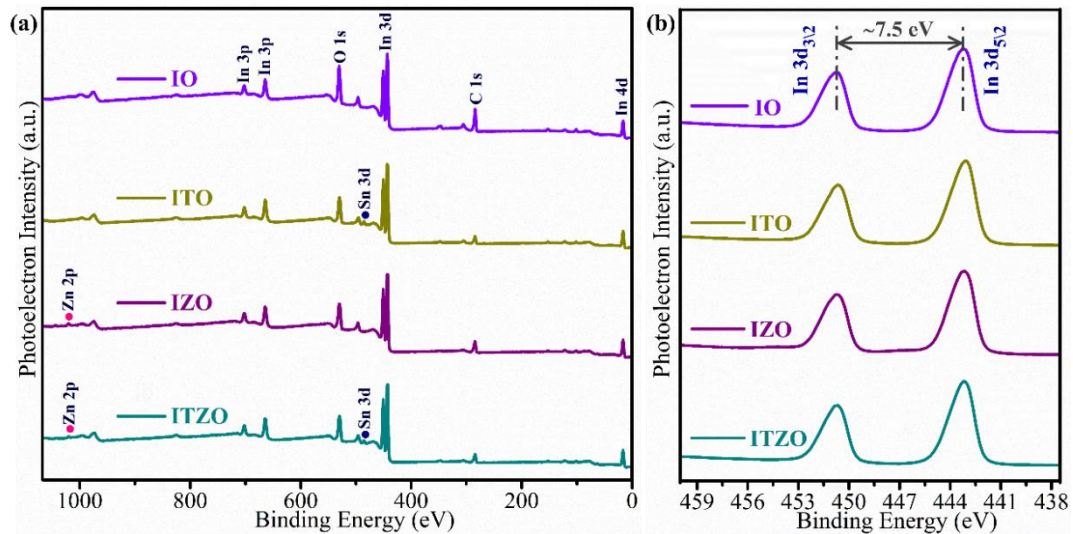
Fig. 5.9: (a) Wide scan XPS spectra and (b) In 3d high-resolution XPS spectra of the screen-printed films, respectively.

The wide scan survey XPS spectra of the screen-printed films are shown in Fig. 5.9 (a). The existence of the peaks related to In and O elements is detected at their respective binding energy locations in IO film (Sundaresh et al. 2021) (Pujar et al. 2018). A peak situated at the binding energy of ~284 eV is observed in all the screen-printed films, and it belongs to the element C. The presence of element C can be credited

to adventitious carbon contamination (Joshi et al. 2019). In the case of ITO film, dopant Sn peak is traced along with the peaks belonging to host In and O elements. In IZO film, the presence of peak belong to dopant Zn is observed along with the host elements. The presence of peaks which belongs to the dopant elements, i.e., Sn and Zn are spotted along with host elements' peaks in ITZO film. The presence of respective elements in the corresponding films is well-matched with the EDAX analysis.

Table 5.1: Details of deconvoluted In 3d peaks of all the screen-printed films.

Film	Deconvoluted peaks	Binding energy (eV)
IO	In $3d_{5/2}$	443.2
	In $3d_{3/2}$	450.6
		(Spin-orbit splitting = 7.4)
ITO	In $3d_{5/2}$	443.0
	In $3d_{3/2}$	450.6
		(Spin-orbit splitting = 7.6)
IZO	In $3d_{5/2}$	443.1
	In $3d_{3/2}$	450.7
		(Spin-orbit splitting = 7.6)
ITZO	In $3d_{5/2}$	443.1
	In $3d_{3/2}$	450.6
		(Spin-orbit splitting = 7.5)

The high-resolution XPS spectra of In 3d and the details of deconvoluted In 3d peaks of all the screen-printed films are shown in Fig. 5.9 (b) and Table 5.1, respectively. It is perceived that the In 3d high-resolution spectrum of all the screen-printed films is resolved into two distinct peaks with the binding energies situated at ~443 and 450.6 eV, respectively. These peaks can be allocated to spin-orbit transitions of In $3d_{5/2}$ and In $3d_{3/2}$ with a peak-to-peak parting of ~7.5 eV. It validates that the element In is in the oxidation state of +3 and substantiates the materialization of In_2O_3. The attained results are in decent correlation with the studies in the literature (Reddy et al. 2017) (Das and Soni 2017) (Yang et al. 2014).
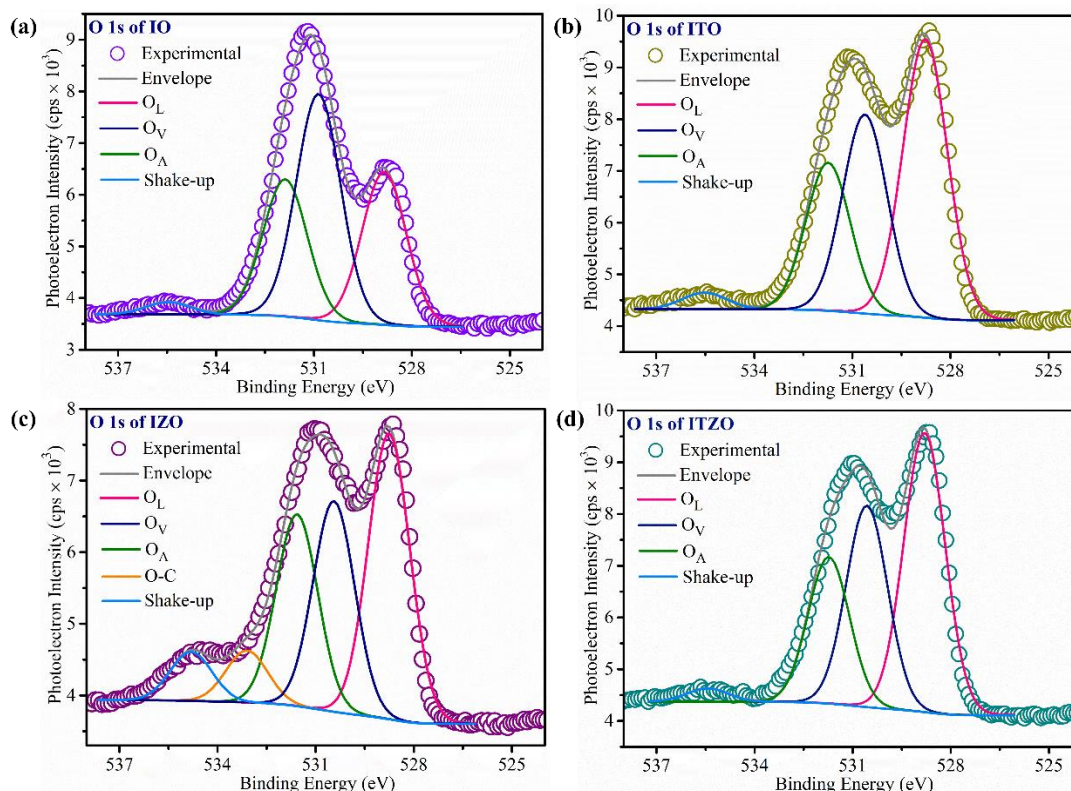
Fig. 5.10: Deconvoluted O 1s high-resolution XPS spectrum of (a) IO, (b) ITO, (c) IZO and (d) ITZO films, respectively.

The deconvoluted O 1s high-resolution XPS spectra of all IO, ITO, IZO and ITZO films are shown in Fig. 5.10 (a to d). The O 1s spectrum of every screen-printed film is deconvoluted into certain peaks that are located at the binding energies of ~529 ± 0.3 eV (Peak 1), 531 ± 0.6 eV (Peak 2) and 532 ± 0.5 eV (Peak 3). The Peak 1 can be devoted to the Metal-Oxygen-Metal lattice feature, i.e., lattice oxygen (O_L), the Peak 2 can be accredited to the oxygen ions of oxygen vacancies (O_V), and the Peak 3 can be allotted to surface adsorbed oxygen (O_A) (Shingange et al. 2016) (Han et al. 2022). The deconvoluted peak that appeared at the binding energy of 533.1 eV can be associated with the O-C that belongs to hydroxy ethyl cellulose, which is utilized as a binder in the current report (Burrell et al. 1986). Lastly, the peak that emerged at the binding energy of 535.4 ± 0.6 eV can be assigned to the O 1s satellite (shake-up) (Beamson et al. 1994). The respective position and area of O 1s deconvoluted peaks of all the deposited films are detailed in Table 5.2.

Table 5.2: The respective position, areas of O 1s deconvoluted peaks of all the screen-printed films

Film	Peak	Peak position (eV)	Area (cps × eV)
IO	O_L	528.8	5138.2
	O_V	530.8	7598.8
	O_A	531.8	4614.3
	Shake-up	535.4	412.9
ITO	O_L	528.7	9262.0
	O_V	530.6	6621.5
	O_A	531.7	4929.2
	Shake-up	535.5	548.2
IZO	O_L	528.7	6429.8
	O_V	530.4	4745.2
	O_A	531.5	4323.4
	O-C	533.1	1169.7
	Shake-up	534.8	1106.1
ITZO	O_L	528.8	8652.4
	O_V	530.5	6237.7
	O_A	531.7	4541.3
	Shake-up	535.4	410.9

The oxygen vacancy concentration (O_V/O_L) is calculated from the O 1s high-resolution spectra of all the screen-printed films, and the variation of O_V/O_L is represented in Fig. 5.11 (a). It is observed that IO film has achieved the highest O_V/O_L compared to the other films. Whereas the minimum O_V/O_L has found in ITO film. The trend of O_V/O_L is found to be IO > IZO > ITZO > ITO. Furthermore, the relative area fraction of surface adsorbed oxygen (% of O_A) is calculated from O 1s high-resolution spectra of all the screen-printed films, and the variation of it is displayed in Fig. 5.11 (b). Here too, it is noticed that IO film has exhibited the maximum % of O_A, and it is followed by IZO film. The % of O_A is similar in ITO and ITZO films.
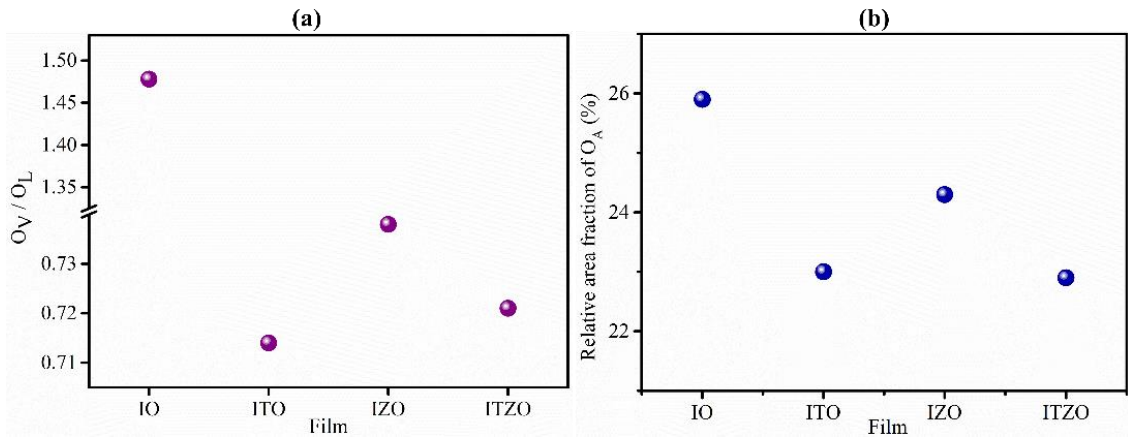
Fig. 5.11: Variation of (a) O_V/O_L and (b) % of O_A in IO, ITO, IZO, and ITZO films, respectively.

Fig. 5.12 (a, b and c) shows the room temperature gas response (S) of all the screen-printed films with different concentrations of ethanol gas (50, 75 and 100 ppm, respectively). The gas response of all the screen-printed films in the current report is calculated according to equation 4.7. It is noticed that the gas response of all the screen-printed films has enhanced with the augmentation in ethanol gas concentration from 50 to 100 ppm. It proves the dependency of the gas response of the films on the concentration of the ethanol gas. The gas response has a strong relation to the chemisorbed oxygen removal that happens during the surface reactions with the target gas molecules. The occurrence of these surface reactions causes the return of the charge carriers to the conduction band, which in turn reduces the electrical resistance and enhances the gas response of the screen-printed films. Henceforth, when the surface of the films is exposed to low ethanol gas concentration, the distribution of ethanol gas molecules on the surface will be less, that leads to minimal surface reactions with chemisorbed oxygen and subsequently causes a low gas response. When the ethanol gas concentration is enhanced from low to high, the surface reactions of gas molecules with chemisorbed oxygen also boost, that causes a betterment in the response of the screen-printed films (Shingange et al. 2016) (Shinde et al. 2007).

It is observed from Fig. 5.12 that IO film has attained maximum gas response compared to other screen-printed films at all tested concentrations of ethanol gas at room temperature. The succeeding high gas response is noticed in IZO film, and it is followed by ITZO film. The minimum gas response is observed in ITO film irrespective

of ethanol gas concentration. The observed trend in the gas response of the screen-printed films at every concentration of ethanol gas is expressed as IO > IZO > ITZO > ITO. In the current report, the highest gas response of ~17.3 has accomplished in the IO film at an ethanol gas concentration of 100 ppm at room temperature. The probable factors for attaining the comparatively high gas response in IO film in contrast to other screen-printed films are described in the following sections.
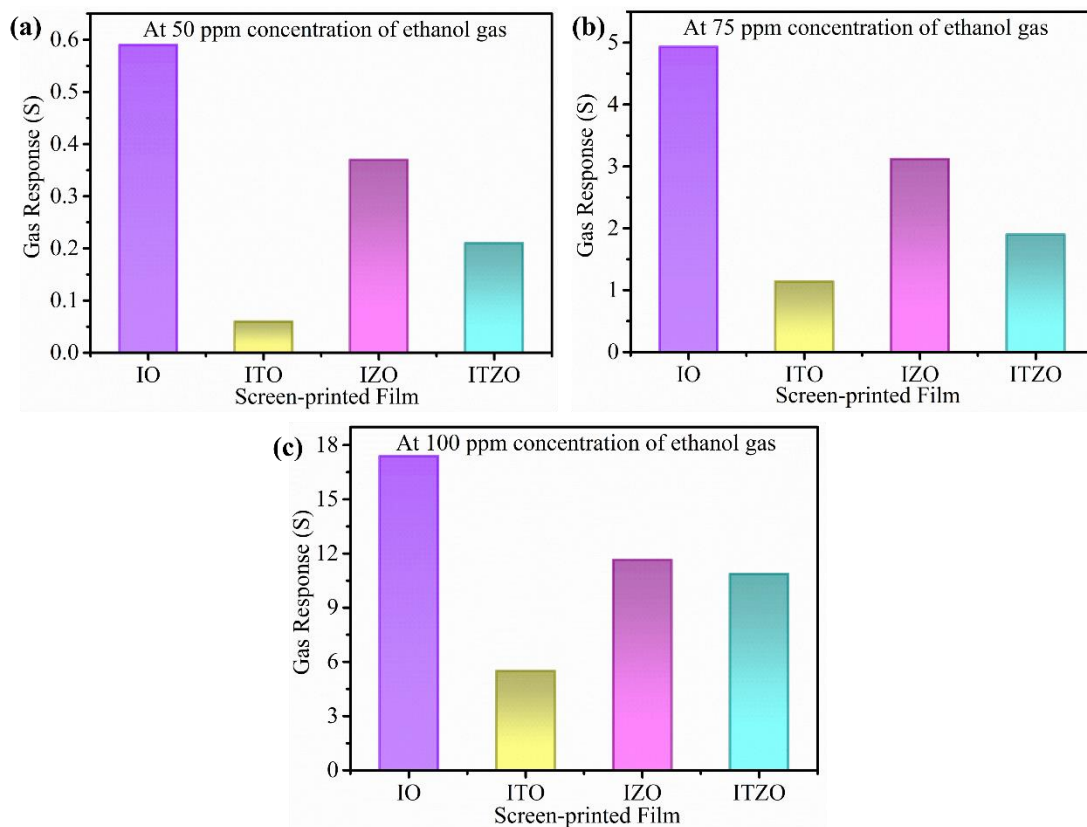
Fig. 5.12: Room-temperature gas response of all the screen-printed films when they are exposed to ethanol gas concentrations of (a) 50 ppm, (b) 75 ppm and (c) 100 ppm, respectively.

It is well known that the SMO-based films basically work on the theory of variation in the electrical resistance on exposure to the target gases (Shankar et al. 2016). In this study too, when the screen-printed films are exposed to the ethanol gas of different concentrations, the variation in the electrical resistance is noticed. The transient variation in the electrical resistance of all the IO, ITO, IZO and ITZO films is

recorded during the exposure and removal of ethanol gas from the testing chamber, and it is projected in Fig. 5.13 (a, b, c and d, respectively).
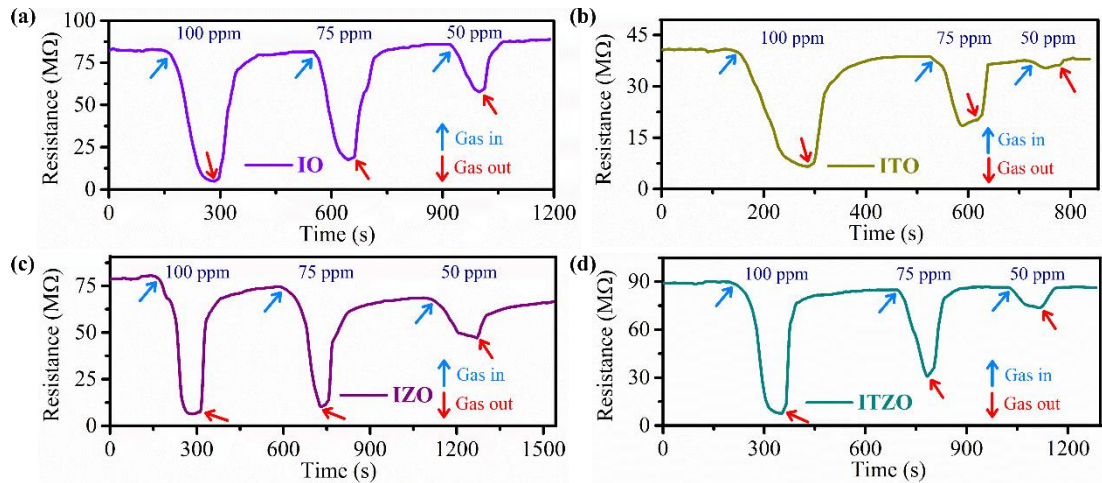
Fig. 5.13: The electrical resistance variation of (a) IO, (b) ITO, (c) IZO and (d) ITZO films, respectively, at 50, 75 and 100 ppm concentrations of ethanol gas.

Usually, the variation in the electrical resistance of the thin film gas sensors depends on the concentration of exposed target gas. The simultaneous adsorption and desorption of respective target gas and oxygen molecules on surface of the film is also another crucial factor for the electrical resistance variation (Manjunath et al. 2020) (Ganesh et al. 2017). It is noticed from Fig. 5.13 that, after the introduction of the ethanol gas into the testing chamber, the electrical resistance of all the screen-printed films has progressively lessened. This is due to the adsorption of the ethanol gas molecules on surface of the screen-printed films, followed by the surface reactions with chemisorbed oxygen. When the ethanol gas is permitted to vacate the testing chamber, the electrical resistance of the screen-printed films has gradually improved. It is because of the concurrent desorption of ethanol gas molecules and adsorption of oxygen molecules on surface of the films from the atmosphere when the target gas is replaced by the air in the testing chamber. The gradual decrement and increment in the electrical resistance during ethanol gas introduction and evacuation, respectively, are noticed in all the screen-printed films and this phenomenon is detected at every concentration of ethanol gas.
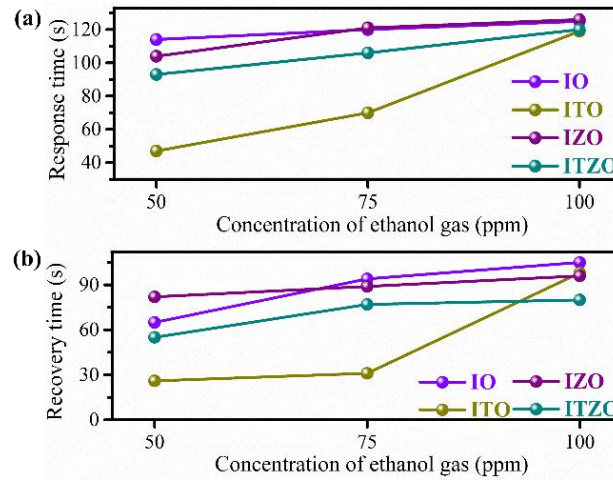
Fig. 5.14: (a) Response time, (b) recovery time of all the screen-printed films towards different concentrations of ethanol gas.

The calculated response and recovery times of all the screen-printed films as a function of ethanol gas concentration are displayed in Fig. 5.14 (a) and (b), respectively. The range of the response time is observed to be 114 to 125 s, 47 to 119 s, 104 to 125 s, and 93 to 120 s, respectively, for IO, ITO, IZO, and ITZO films when the ethanol gas concentration varied from 50 to 100 ppm (Fig. 5.14 (a)). The gas response time has augmented with the upsurge in the ethanol gas concentration in all the screen-printed films. The probable cause for enhancing response time with the increment of ethanol gas concentration can be expressed as follows: at lower concentrations of ethanol gas, the adsorption of the number of ethanol gas molecules on the surface of the screen-printed film can be fewer; consequently, the surface reactions between ethanol gas and chemisorbed oxygen molecules can be less, which results in a low gas response and fast response time. When the high concentration of the ethanol gas is enhanced, the number of adsorbed ethanol gas molecules on the surface of the screen-printed film can be more, and the subsequent surface reactions among ethanol gas and chemisorbed oxygen molecules can be probably excessive, which results in a high gas response and slow response time.

It is mentioned in the previous chapter (section 4.2.2) that the smaller crystallite size can support in achieving the lower response time. From Fig. 5.14 (a), it is observed that IO film exhibited a slightly higher response time than the other films, and it is followed by IZO and ITZO films. Whereas ITO film has revealed a faster response time

in contrast to other films. It can be correlated that the high response time in IO film can be due to its relatively large crystallite size, followed by IZO and ITZO films (derived from GIXRD analysis). A comparatively lower response time in ITO film can be dedicated to its low crystallite size.

It is observed from Fig. 5.14 (b) that in all the screen-printed films, the recovery time has also increased with increasing the ethanol gas concentration, i.e., faster recovery time at low ethanol gas concentration and slower recovery time at high ethanol gas concentration. The range of the recovery time is 65 to 105 s, 26 to 98 s, 82 to 96 s and 55 to 80 s, respectively, for IO, ITO, IZO and ITZO films when the ethanol gas concentration varied from 50 to 100 ppm. The probable factor for the faster recovery time at low ethanol gas concentrations can be due to a smaller number of adsorbed ethanol gas molecules on the surface of the screen-printed films. These gas molecules can be desorbed in a shorter time when the gas is allowed to vacate from the chamber. Besides, the adsorbed ethanol gas molecules on surface of the screen-printed films can be more in number at high ethanol gas concentrations. These excess gas molecules take extra time to desorb when the target gas evacuates from the chamber, which leads to an enhancement in the recovery time.
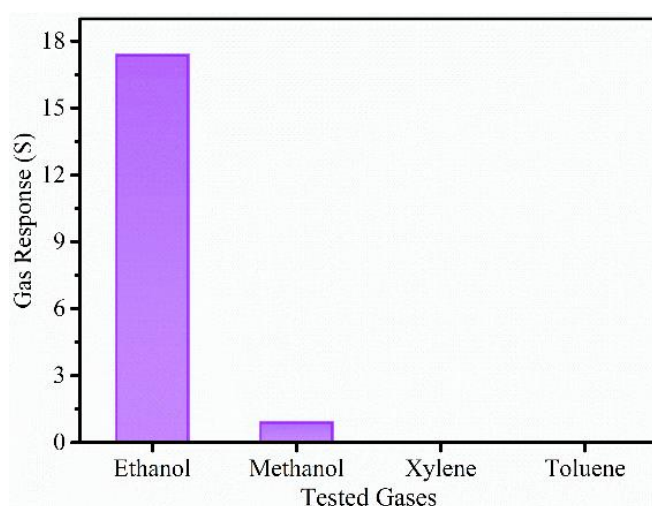

Fig. 5.15: The gas response of IO film when tested against ethanol, methanol, xylene, and toluene gases of 100 ppm concentration at room temperature.

In this report, to check the gas selectivity, the test is performed on the high gas-responded IO film towards target gases such as xylene, methanol and toluene of 100

ppm concentration at room temperature and these gas response values are compared with the value obtained towards ethanol gas of 100 ppm concentration. The graph showing the gas response values of IO film towards various target gases is displayed in Fig. 5.15. IO film exhibited a high detection towards ethanol gas and a minimal detection against methanol gas. The gas response value obtained against ethanol gas is ~20 times more than the response value resulted towards methanol gas. IO film revealed no detection towards xylene and toluene gases. It is assured that IO film is highly selective towards ethanol gas, and it can be utilized as an ethanol gas sensor at room temperature due to its substantial detection in contrast to mentioned other target gases. The probabilistic reasons for the high detection towards only ethanol gas can be due to the low kinetic diameter of ethanol gas (0.45 nm) compared to the kinetic diameters of xylene (0.58 to 0.68 nm) and toluene (0.58 nm) molecules (Ganesh et al. 2017) (Manjunath et al. 2020). The other reason is the low ionization energy of the gas molecules (Ganesh et al. 2017). Although the kinetic diameter of methanol gas (0.38 to 0.41 nm) is lower than ethanol gas, the ionization energy of methanol gas (10.85 eV) is higher than the ethanol gas (10.47 eV). Therefore, the gas response is comparatively lower towards methanol gas than ethanol gas.

It is familiar that the gas sensing mechanism of SMO film (here, In_2O_3 (n-type)) is based on the variation in the electrical resistance because of adsorption or desorption of the target gas molecules on surface of SMO film and also due to the amount of chemisorbed oxygen species present on the surface (Shinde et al. 2007) (Sankarasubramanian et al. 2015). Furthermore, as explained in the earlier chapter, the adsorbed oxygen molecules capture the electrons up to a certain depth from surface of SMO film and turn into chemisorbed oxygen. Due to this, the density of electrons in SMO film decreases (Miller et al. 2014) (Manjunath et al. 2021b). It leads to the increment of electrical resistance of SMO film till an equilibrium reaches with ambient atmosphere (Ganesh et al. 2017). When the SMO film is exposed to ethanol gas, the gas molecules react with the chemisorbed oxygens present on surface of SMO film. Upon interaction, the ethanol gas readily oxidizes to CO_2 and H_2O by re-injecting the electrons to conduction band of SMO film. Consequently, the decrement of the electron depletion layer occurs, which causes a decrement in electrical resistance of SMO film.

The plausible reaction that occurs between ethanol gas molecules and chemisorbed oxygen can be expressed through equation 5.5 (Hsu et al. 2014).

$$C_2H_5OH + 3O_2^- \rightarrow 2CO_2 + 3H_2O + 3e^- \qquad (5.5)$$
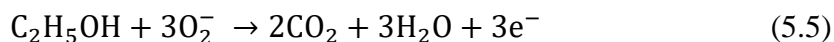
As stated previously, the pristine IO film has achieved a relatively high gas response towards all concentrations of ethanol gas in contrast to other films. The probabilistic reasons for attaining a comparatively high gas response in IO film can be described as follows. The presence of oxygen vacancies promotes the adsorbed oxygen to generate excess active sites (chemisorbed oxygen species) by transporting the electrons from the surface of SMO films. These active sites will further participate in the reaction with the target gas molecules (Zeng et al. 2020) (Hsu et al. 2014). In the present study, it is detected that IO film possesses high O_V/O_L in contrast to other films, as shown in Fig 5.11 (a). The relatively high O_V/O_L might have pronounced the chemisorption process and helped to create plentiful active sites on surface of IO film. During the chemisorption process, the electrons might be depleted in more numbers and a thick depletion layer might be generated on surface of IO film. After the interaction of active sites with ethanol gas molecules, the electrons might be injected back into the conduction band of IO film and resulted in significant shrinkage in the depletion layer. This phenomenon might be encouraged in large modulation in the electrical resistance, causing a comparatively high gas response in IO film (Manjunath et al. 2021b).

As aforementioned, the modulation in electrical resistance of SMO film during the gas sensing process is also guided by the proportion of adsorbed oxygen present on the surface of SMO film (Shinde et al. 2007). It is also stated that the electron depletion layer relies on the quantity of adsorbed oxygen. If the amount of adsorbed oxygen is more, it captures more electrons, leads to the creation of a thick depletion layer, and facilitates a higher number of active sites to participate in the oxidation of ethanol gas. It is observed from Fig. 5.11 (b) that IO film achieves a comparatively high % of O_A, indicating the quantity of chemisorbed oxygen on IO film's surface is greater than the other screen-printed films. Hence, the high % of O_A in IO film might have assisted in

the generation of more active sites, which contributed to the reactions with ethanol gas molecules and resulted in a relatively high gas response.

It is mentioned in the literature that the morphological features of the film also play a crucial role in the gas sensing performance. Gan et al., in their report, stated that roughness and porosity are favourable for a good gas response in a film (Gan et al. 2014). Kumar et al., in their analysis, noticed that the film comprising high surface roughness displayed a better gas response (Kumar et al. 2020). In the current study, it is observed that IO film possesses comparatively high surface roughness with porous morphology than the other screen-printed films, which can be one of the factors in attaining a relatively high gas response in IO film. The overall plausible reasons for achieving a better gas response in IO film than the other films can be due to more O_V/O_L, % of O_A, and high surface roughness with porosity.

Discussing doped films, it is observed that IZO film reveals a relatively better response at all concentrations of ethanol gas and is followed by ITZO and ITO films. It is mentioned earlier that O_V/O_L and % of O_A contribute to a high gas response. In Fig. 5.11, the values of O_V/O_L and % of O_A of IZO film are higher than those of ITO and ITZO films. It can be presumed that comparatively high quantities of O_V/O_L and % of O_A encourage the creation of relatively higher active sites, which resulted in a better gas response in IZO film than in ITO and ITZO films. Comparing ITO and ITZO films, it is noticed that ITZO film possesses a relatively high gas response than ITO film. One of the reasons can be dedicated high O_V/O_L in ITZO film than in ITO film (shown in Fig. 5.11 (a)). It is observed that both ITO and ITZO films exhibit a similar % of O_A (shown in Fig. 5.11 (b)). It can be expected that the % of O_A does not contribute much to better gas sensing behaviour in ITZO film than in ITO film. The other reasons for attaining better gas response can be due to the relatively high surface roughness in ITZO film than ITO film. It is also observed that some relatively bigger cracks are detected in ITZO film. The gas molecules might have diffused more into ITZO film and reacted with active sites, which improved gas sensing performance more than ITO film. As ITO film possesses low values of O_V/O_L, % of O_A and low surface roughness than the other films, it can be assumed that these can be the aspects for its inferior gas sensing

properties. The feasible gas sensing mechanism in all the screen-printed films is shown in Fig. 5.16.
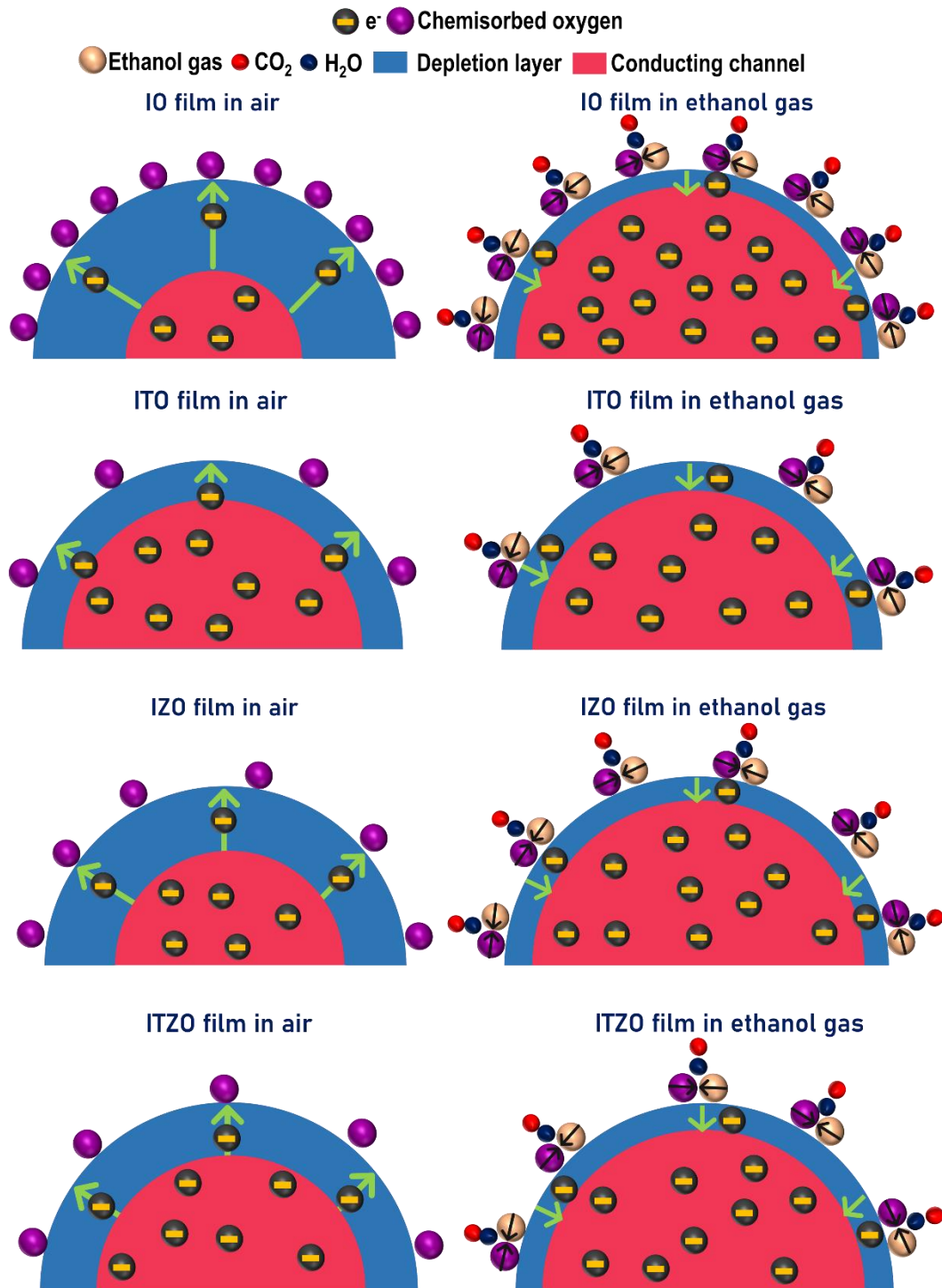
Fig. 5.16: Schematic representation of the feasible gas sensing mechanism in all the screen-printed films.

5.4 Conclusion

In this study, pristine In_2O_3, Ti doped In_2O_3, Zn doped In_2O_3 and Ti, Zn coped-In_2O_3 based screen-printed films were fabricated through particle-free aqueous solution combustible inks, respectively. The combustion temperature of all the inks was detected at ~280 °C. All the prepared inks were deposited on glass substrates through the screen-printing method. In this study, all the screen-printed films were polycrystalline with a cubic bixbyite crystal structure of In_2O_3. No secondary phases of dopant oxides were traced. IO film comprised relatively bigger grains, whereas smaller grains were found in other screen-printed films. The average surface roughness was revealed to be high in IO film (10.2 nm) and it was low in ITO film (3.3 nm). The transparency of all the screen-printed films ranged from ~75 to 95 %, and the E_g of the screen-printed films was found to be ~ 3.6 eV. The O_V/O_L and % of O_A were found to be higher in IO film than in other films. All the screen-printed films at room temperature detected the ethanol gas (50 to 100 ppm concentration). Among them, IO film revealed better gas response than doped films at all measured concentrations of ethanol gas, and the gas response in doped films followed the trend of IZO > ITZO > ITO. In the current study, the highest gas response was observed in IO film with a value of 17.3 towards 100 ppm concentration of ethanol gas at room temperature. The developed gas sensors are transparent (> 75 %), can be performed at room temperature conditions and can be mass-produced. These gas sensors can be potentially applied in optoelectronic devices, which require transparency and gas sensing.

CHAPTER 6

DEVELOPMENT OF BARIUM STANNATE-BASED METAL OXIDES THROUGH THE POLYMERIZED COMPLEX METHOD & THEIR CHARACTERIZATIONS

6.1 Introduction

This chapter deals with the pristine perovskite structured barium stannate ($BaSnO_3$) (BSO) and lanthanum doped barium stannate (La-BaSnO$_3$) (LBSO) powders and pellets that are synthesized through polymerized complex method (PCM). In this chapter, the preparation of $La_xBa_{1-x}SnO_{3-\delta}$ (x = 0, 0.05, 0.1 and 0.15) (x = atomic percentage) powders and pellets through the mentioned method is discussed initially. The synthesized powders are studied for the temperature-dependent phase evolution of the BSO phase with structural, microstructural, and compositional properties and the effect on these properties by substituting Ba with La is investigated in detail. A comprehensive correlation is conducted between electrical conductivity and La dopant concentration in the developed pellets.

6.2 Experimental procedure

6.2.1 Materials

All the reagents were of analytical grade and utilized without additional purification. Barium nitrate ($Ba(NO_3)_2$) (Molychem), tin chloride ($SnCl_2$) (Sigma - Aldrich), lanthanum nitrate hydrate ($La(NO_3)_3.6H_2O$) (Molychem), citric acid ($C_6H_8O_7$) (Sigma- Aldrich), ethylene glycol ($C_2H_6O_2$) (Molychem) and ethanol (CSS) were used in this study.

6.2.2 Preparation of precursors, powders, and pellets

The precursor solution comprising $Ba(NO_3)_2$, $SnCl_2$, and $La(NO_3)_3.6H_2O$ were stoichiometrically weighed with varying La doping percentages, x = 0, 0.05, 0.1 and 0.15, respectively. In the next step, they were dissolved in ethylene glycol of quantity 20 ml with a fixed concentration of Sn as 0.1 mol L^{-1}. Later, the solution was mixed

with 1 mol L^{-1} solution of citric acid in ethanol of quantity 20 ml and then stirred for 1 h at 80 °C to obtain a homogeneous solution. It was then stirred again for 28 h at 135 °C to get a brown color solution to generate polymerized citrate complexes. Later, the solution was heated at 100 °C for 8 h in a vacuum oven to eliminate the residual amount of ethylene glycol. The prolonged heating helps in formation of complexation, elimination of metal segregation, and compositional homogeneity in the solution. The final solution was divided into six parts and heated at 400 °C, 500 °C, 600 °C, 700 °C, 800 °C and 900 °C respectively, for 3 h in a muffle furnace. The obtained powders of variable La doping percentage ($x = 0, 0.05, 0.1$ and 0.15) that were synthesized at 500 °C were compressed under a load of 12.5 kN to obtain the green compacts by using a uniaxial hydraulic press (40 TON, UTM). These green compacts were sintered at 1000 °C for 4 h in a high-temperature furnace. The applied high load, high temperature, and prolonged heating help in reducing the porosity of the pellets. The process flow diagram is schematically presented in Fig. 6.1.
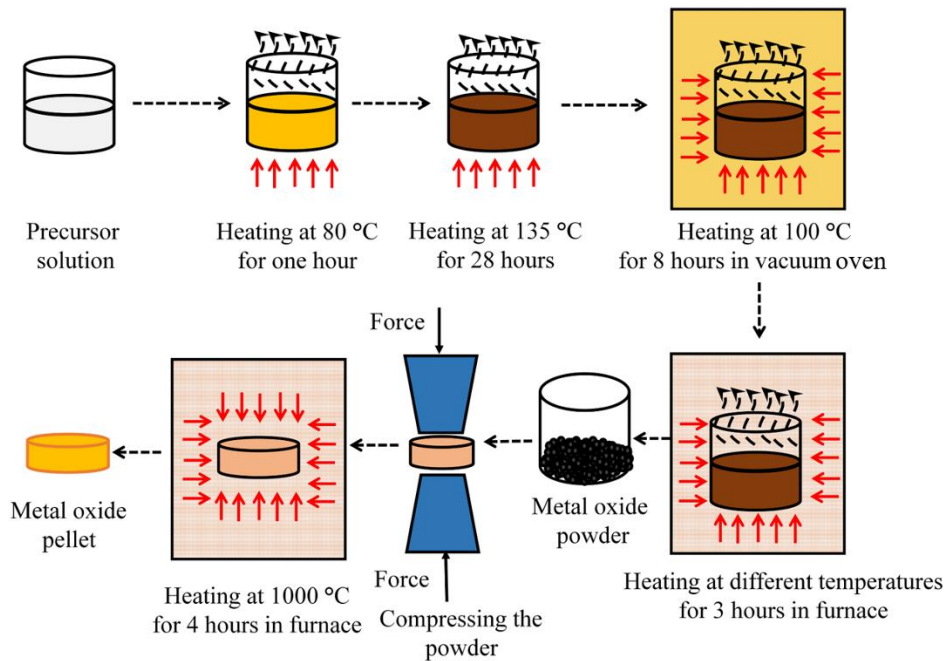

Fig. 6.1: Schematic representation of the experimental process flow chart.

6.2.3 Characterization of BSO and LBSO powders and their pellets

To examine the structural properties and resultant phases in all the powders of variable La doping percentage ($x = 0, 0.05, 0.1$ and 0.15) synthesized at different

temperatures, X-ray diffraction technique (XRD, JEOL-JPX 8) was executed by using the Cu Kα radiation source (1.54 Å) with a scanning rate of 2 °/min and a step size of 0.02°. The infrared spectra for undoped powders ($x = 0$) that were synthesized at different temperatures ranging from 400 to 800 °C and also the powders ($x = 0, 0.05,$ 0.1 and 0.15) that were synthesized at 900 °C were recorded by Fourier transform infrared spectroscopy (FTIR, JASCO FTIR-4200, JAPAN) in the range of 400 to 4000 cm^{-1} by using KBr pellet method. Elemental analysis was carried out using X-ray photoelectron spectroscopy (XPS, Kratos Axis Ultra DLD) for the powders ($x = 0$ and 0.05) synthesized at 900 °C. The spectra were calibrated using the C-H peak of C 1s centred at 284.6 eV (details of fitting parameters are presented in Appendix VI). The fitting was performed by fixing the Gaussian-Lorentzian (GL) ratio and the full-width half maximum (FWHM) of the peaks. The electrical conductivity of the sintered pellets was measured through a two-point probe instrument (SES Instruments Pvt. Ltd.) at ambient temperature. Scanning electron microscopy (SEM, JSM 6380, JEOL), energy-dispersive X-ray analysis (EDAX, AMETEK) were performed, respectively, to examine the surface morphology and elemental composition of all the sintered pellets.

6.3 Results and discussion

The XRD patterns of all the La$_x$Ba$_{1-x}$SnO$_{3-\delta}$ ($x = 0, 0.05, 0.1$ and 0.15) powders that are synthesized from 400 °C to 900 °C are shown in Fig. 6.2 (a to d), respectively. In all the powders of variable La doping percentage, the existence of cubic perovskite phase (ICDD: 15-0780) with diffraction planes, namely (110), (111), (200), (211), (220), (310), (222) and (321) is observed at 600 °C and above (Shan et al. 2014). The traces of intermediate phases such as barium carbonate (BaCO$_3$) (ICDD: 45-1471) and tin oxide (SnO$_2$) (ICDD: 41-1445) are identified up to 700 °C, and they are disappeared above 700 °C. Pure BSO and LBSO phases emerged and intensified at 800 °C and 900 °C without any secondary phases in $x = 0$ and $x = 0.05, 0.1, 0.15$ La doping concentrations, respectively. The cubic perovskite structure of BSO is represented in Fig. 6.2 (e). In Fig. 6.2 (a), it is noticed that at low temperatures, 400 and 500 °C, the powders are almost amorphous with small traces of intermediate phases BaCO$_3$ and SnO$_2$. While, at 600 °C, a trace of BSO phase is identified along with the intermediate phases. In Fig. 6.2 (b, c, and d), it is observed that the powders synthesized at 400 and

500 °C are completely amorphous, whereas they are crystallized at 600 °C; and LBSO phase with intermediate phases are identified at 600 °C. It is confirmed that in between 500 °C to 600 °C, the BSO and LBSO phases have evolved in the respective powders.
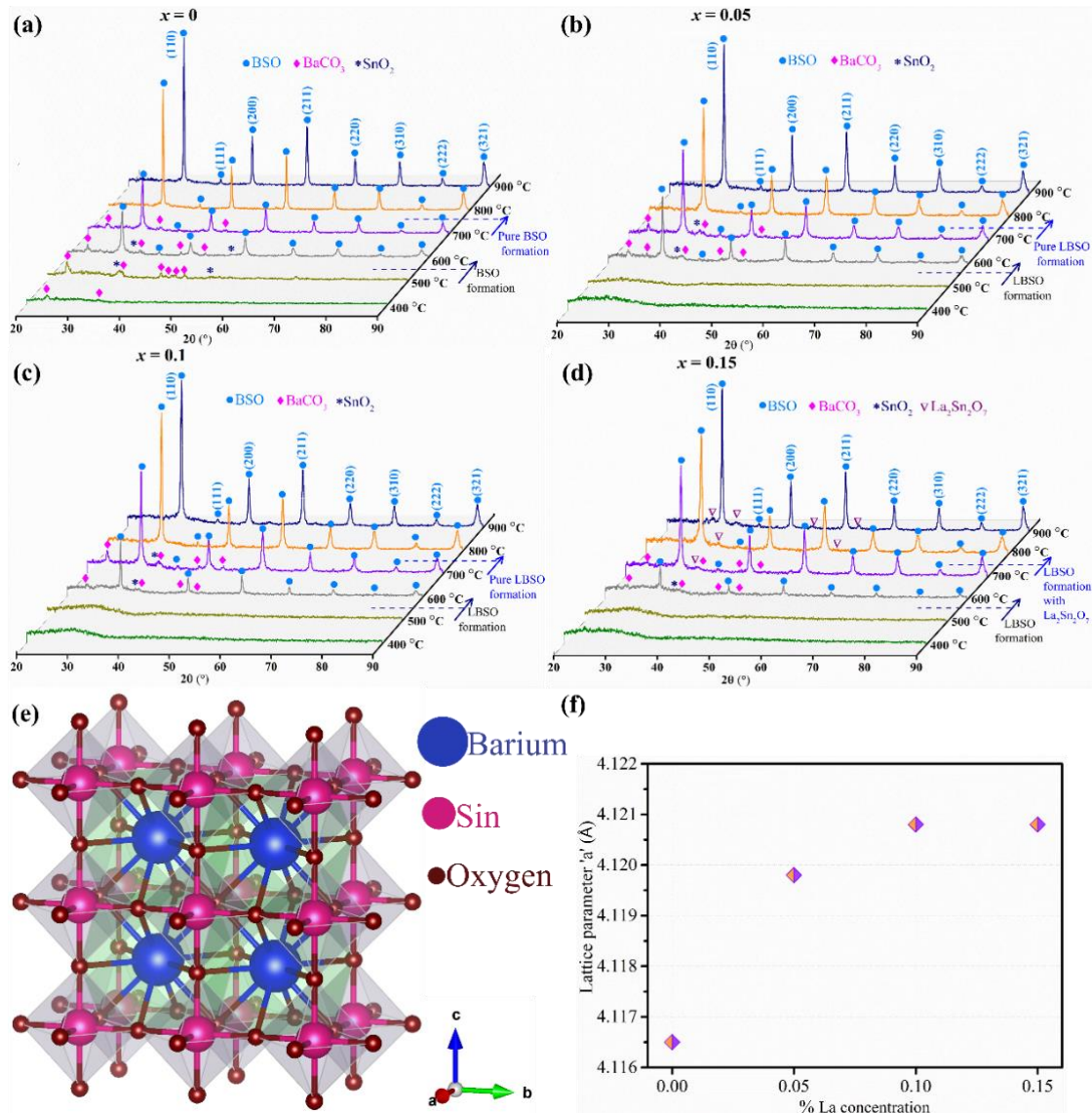
Fig. 6.2: XRD patterns of $La_xBa_{1-x}SnO_{3-\delta}$ powders (a) $x = 0$, (b) $x = 0.05$, (c) $x = 0.1$, (d) $x = 0.15$ that are synthesized at different temperatures from 400 °C to 900 °C; (e) cubic perovskite structure of BSO and (f) Variation of lattice parameter with enhancing the % of La doping concentration in BSO. (The crystal structure is drawn using the VESTA visualization interface software and the crystallographic information file is taken from the Materials Project database (mp-3163)).

It is also identified that there is no formation of the secondary phases of La, up to $x = 0.1$, but beyond $x > 0.1$, i.e., at $x = 0.15$, additional minuscule X-ray reflections due to an impurity pyrochlore phase $La_2Sn_2O_7$ (ICDD: 13-0082) are detected in the diffraction patterns (shown in Fig. 6.2 (d)), which confirm the solubility limit of La in $BaSnO_3$ is up to $x = 0.1$ in the current study (Luo et al. 2015).

The average crystallite size for the powders synthesized at 900 °C is estimated by using the Scherrer formula (given in equation 4.5). The obtained crystallite size of the undoped powder ($x = 0$) is 47.6 nm, whereas it is 26.4 nm, 24.3 nm, and 27.9 nm for $x = 0.05, 0.1$ and 0.15 powders, respectively. The lattice parameter 'a' is calculated for all the powders synthesized at 900 °C and it is noticed that the lattice parameter of undoped powder ($x = 0$) is 4.116 Å, which is in decent relation with the previous reports (Hadjarab et al. 2008; Zidi et al. 2010). The lattice parameter has increased up to $x = 0.1$ and remained constant at $x \geq 0.1$ with the value of 4.1208 Å. The lattice parameter variation with increasing % of La doping concentration is shown in Fig. 6.2 (f). This information, along with the non-appearance of La secondary phases up to $x = 0.1$, confirmed the solubility limit of La in BSO in the current study. The increment in the lattice parameter though the ionic radius of La^{3+} (1.36 Å) is less than the ionic radius of Ba^{2+} (1.61 Å), is attributed to the occupation of the additional electron donated by La^{3+} in the conduction band having Sn5s-O2p σ* anti-bonding orbitals. This additional electron probably induced the partial reduction of Sn^{4+} (ionic radius = 0.71 Å) to Sn^{2+} (ionic radius = 1.12 Å), enlarging the Sn-O bond length (Yasukawa et al. 2010) (Trari et al. 1994).

The FTIR spectra of undoped powders ($x = 0$) that are synthesized at different temperatures and $La_xBa_{1-x}SnO_3$ powders ($x = 0, 0.05, 0.1$ and 0.15) that are synthesized at 900 °C are shown in Fig. 6.3 (a) and (b), respectively. The band located at the wave number of ~550 cm^{-1} corresponds to the hydroxyl metal vibration (Sn-OH). The band situated at the wave number of ~640 cm^{-1} corresponds to $(SnO_3)^{2-}$, which marks the development of the cubic perovskite BSO phase (Ansaree and Upadhyay 2015). The small trace of band at the wave number of ~856 cm^{-1} either assigns to the vibration associated with the carbonate bond $(CO_3)^{2-}$ of $BaCO_3$ (Deepa et al. 2011) or to the adsorption of CO_2 from the atmosphere (Lu and Schmidt 2008). And the intense band

denoted at the wavenumber of ~1455 cm^{-1} belongs either to the carbonate bond (BaCO$_3$) and/or to the M-OH group vibration (Ansaree and Upadhyay 2015).
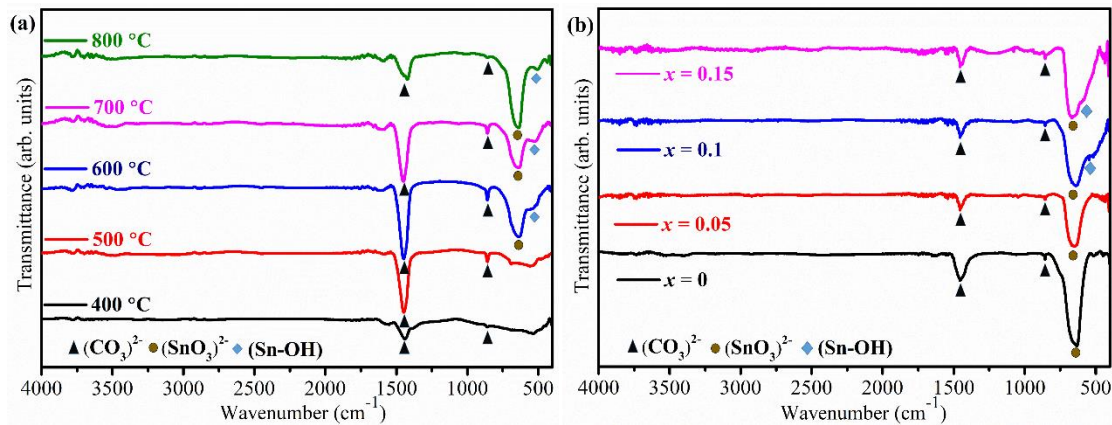
Fig. 6.3: FTIR spectra of (a) Undoped powders ($x = 0$) which are synthesized at different temperatures and (b) La$_x$Ba$_{1-x}$SnO$_{3-\delta}$ powders (x = 0, 0.05, 0.1, 0.15) which are synthesized at 900 °C.

In Fig. 6.3 (a), the presence of only bands of carbonate bond (CO$_3$)$^{2-}$ is noticed with no trace of (SnO$_3$)$^{2-}$ bands in the FTIR spectra of powders synthesized at 400 and 500 °C. Whereas in the FTIR spectrum of powder synthesized at 600 °C, (SnO$_3$)$^{2-}$ vibration is detected at the wave number of ~640 cm^{-1} along with the bands of (CO$_3$)$^{2-}$. It confirms the evolution of BSO phase between the temperature range of 500 to 600 °C and it matches well with the evidence from the XRD patterns (Fig. 6.2). It is also noticed that with the increase in temperature above 600 °C, there is an increment in the intensity of (SnO$_3$)$^{2-}$ band, whereas there is a decrement in the intensity of (CO$_3$)$^{2-}$ bands, which represent the enhancement in BSO phase at the expense of BaCO$_3$ phase.

In Fig. 6.3 (b), in all the FTIR spectra irrespective of doping, high intense (SnO$_3$)$^{2-}$ bands are noticed at the wave number of ~640 cm^{-1}, and it confirms the presence of BSO/LBSO phase in the respective powders. Also, the small traces of (CO$_3$)$^{2-}$ are noticed in the FTIR spectra, though they are not detected in diffraction patterns at 900 °C. One of the reasons for it might be the existence of very small traces of BaCO$_3$ ranging below the critical size of Bragg reflection, and the other reason might be the atmospheric CO$_2$ adsorption (Ansaree and Upadhyay 2015) (Lu and Schmidt 2008). As mentioned earlier, vibration at the wave number ~1455 cm^{-1} might be due to

the combined effect of the M-OH group and $(CO_3)^{2-}$ vibration (Ansaree and Upadhyay 2015).

A mechanism for the formation of BSO phase from $BaCO_3$ and SnO_2 is proposed by Huang et al. with a core-shell structure where SnO_2 is the core and $BaCO_3$ is the shell (Huang et al. 2016). During heating, $BaCO_3$ rapidly diffuses over the SnO_2 core, where it reacts with SnO_2 to form a BSO interlayer between them. The reaction between the intermediate phases $BaCO_3$ and SnO_2 to form BSO phase is shown in equation 6.1. The formed BSO interlayer inhibits the direct contact between $BaCO_3$ and SnO_2, and it retards the further formation of BSO. With increasing the temperature, the reaction between $BaCO_3$ and SnO_2 again accelerates due to the cracking of BSO interlayer. This cracking occurs due to the generation of local stresses at the interface of BSO and SnO_2 as a result of the difference in the molar volumes (the molar volume ratio of BSO to SnO_2 is ~ 2) (Huang et al. 2016). These cracks allow $BaCO_3$ to diffuse further and to react with SnO_2 at the core to form the complete BSO phase. The same mechanism can also be applied to LBSO phase formation as well. A pictorial representation of the mechanism for the formation of BSO/LBSO phases with temperature is shown in Fig. 6.4.

$$BaCO_3 \text{ (s)} + SnO_2 \text{ (s)} \longrightarrow BaSnO_3 \text{ (s)} + CO_2 \text{ (g)} \qquad (6.1)$$
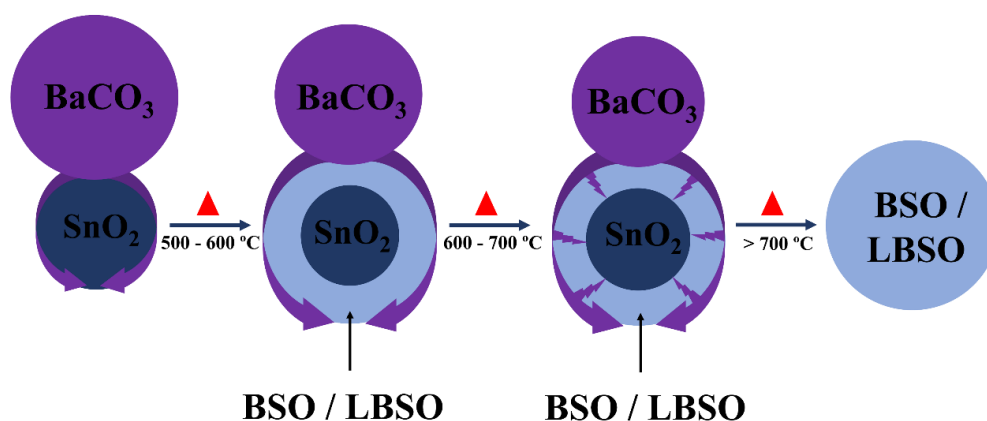
Fig. 6.4: Mechanism of BSO/LBSO formation from the intermediate phases $BaCO_3$ and SnO_2.

XPS analysis is carried out for powders ($x = 0$ and 0.05) which are synthesized at 900 °C to investigate the valence states of the elements present and the effects caused

by the same. The elements such as Ba, Sn, C and O are noticed in the wide scan spectra of the $x = 0$ powder, shown in Fig. 6.5 (a). In the case of $x = 0.05$ powder, La element is detected along with the host elements, shown in Fig. 6.5 (b). The deconvoluted high-resolution spectrum of La of $x = 0.05$ powder revealed two peaks, namely, La $3d_{5/2}$ and La $3d_{3/2}$ spin-orbitals. Each peak comprises a doublet positioned at 834.4 eV (Main Peak) and 838.1 eV (Satellite Peak) of La $3d_{5/2}$, and 851.3 eV (Main Peak) and 854.8 eV (Satellite Peak) of La $3d_{3/2}$, as shown in Fig. 6.5 (b) (Sethulakshmi et al. 2015). The splitting of spin-orbital between respective main and satellite peaks of La $3d_{5/2}$ and La $3d_{3/2}$ level is ~16.8 eV, which confirms that La is in a +3 state (Luo et al. 2015).
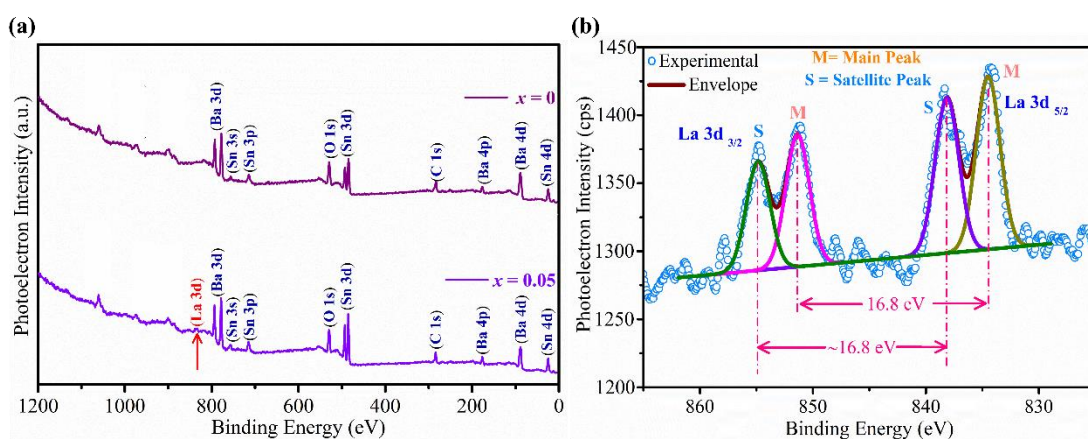
Fig. 6.5: (a) Wide scan XPS spectra of $x = 0$ and 0.05 powders synthesized at 900 °C and (b) high-resolution XPS spectrum of La 3d core levels of $x = 0.05$ powder.

Fig. 6.6: The deconvoluted Sn 3d high-resolution XPS spectra of (a) $x = 0$ and $x = 0.05$ powders synthesized at 900 °C.

The deconvoluted Sn 3d high-resolution XPS spectra of $x = 0$ and 0.05 powders are shown in Fig. 6.6 (a) and (b), respectively. It is observed that the spectra of Sn revealed two peaks of Sn $3d_{5/2}$ and Sn $3d_{3/2}$ that are positioned at 485.5 ± 0.5 eV and 494.3 ± 0.5 eV, respectively. To recognize the Sn element's valence states, the Sn $3d_{5/2}$ peak is deconvoluted and it showed the presence of two peaks positioned at 485.6 eV ± 0.7 eV and 486.5 eV, which are attributed to Sn^{2+} and Sn^{4+} valence states, respectively. Also, the Sn $3d_{3/2}$ peak is deconvoluted; after deconvolution, two peaks are detected at 493.2 ± 0.8 eV and 494.8 ± 0.1 eV, and they are dedicated to Sn^{2+} and Sn^{4+} valence states, respectively (Xia et al. 2014). The details of deconvoluted Sn 3d peaks of $x = 0$ and $x = 0.05$ powder are shown in Table 6.1 and 6.2, respectively. The area ratio of Sn^{4+} and Sn^{2+} (Sn^{4+} / Sn^{2+}) is found to be ~ 1 in Sn $3d_{5/2}$ and Sn $3d_{3/2}$ peaks in $x = 0$ powder, whereas the ratio is reduced to ~ 0.3 in Sn $3d_{5/2}$ and Sn $3d_{3/2}$ peaks in $x = 0.05$ powder. The reason can be dedicated to the deduction in Sn^{4+} state in $x = 0.05$ powder. This deduction in Sn^{4+} state is due to the partial reduction of Sn^{4+} to Sn^{2+} because of the donation of an extra electron by La^{3+}, as mentioned in the structural analysis section. The presence of a comparatively high amount of Sn^{2+} in doped powder causes an increment in the lattice parameter, and this increment is shown in Fig. 6.2 (f).

Table 6.1: Details of deconvoluted Sn 3d peaks of $x = 0$ powder.

Peak	Oxidation state	Binding energy (eV)	Area (cps. eV)	Sn^{4+} / Sn^{2+}
Sn $3d_{5/2}$	Sn^{2+}	484.9	2789.5	
	Sn^{4+}	486.5	2669.3	~ 1
Sn $3d_{3/2}$	Sn^{2+}	493.2	1746.6	
	Sn^{4+}	494.8	1876.1	~ 1

Table 6.2: Details of deconvoluted Sn 3d synthetic peaks of $x = 0.05$ powder.

Core level	Oxidation state	Binding energy (eV)	Area (cps. eV)	Sn^{4+} / Sn^{2+}
Sn $3d_{5/2}$	Sn^{2+}	485.6	5159.3	
	Sn^{4+}	486.5	1497.4	~ 0.3
Sn $3d_{3/2}$	Sn^{2+}	494.0	3148.4	
	Sn^{4+}	494.7	1223.7	~ 0.3

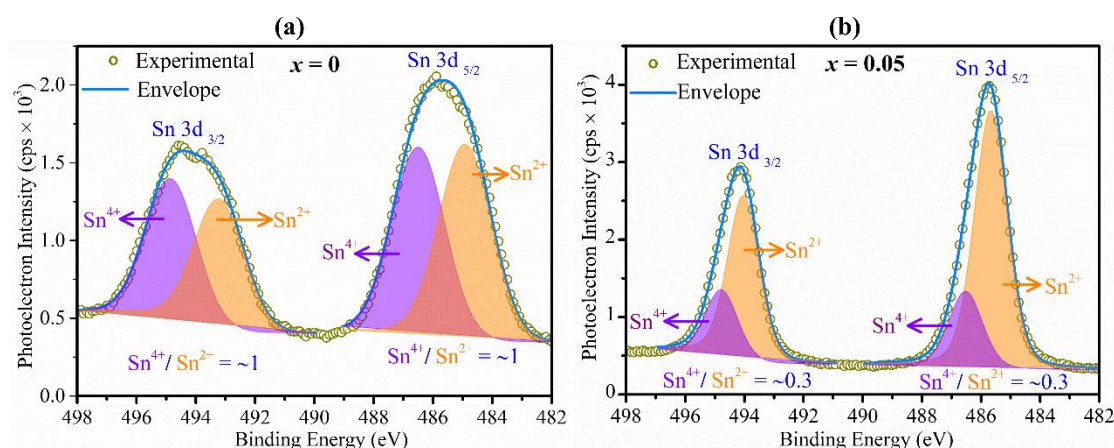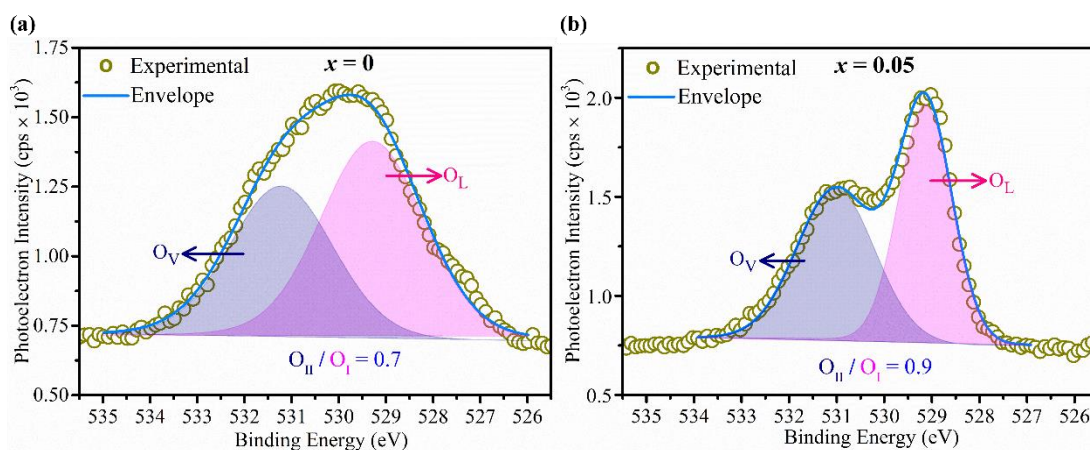Fig. 6.7: The deconvoluted O 1s high-resolution XPS spectra of (a) $x = 0$ and $x = 0.05$ powders synthesized at 900 °C.

The deconvoluted O 1s high-resolution XPS spectra of $x = 0$ and 0.05 powders are shown in Fig. 6.7 (a) and (b), respectively. It is observed that the deconvoluted O 1s spectrum revealed two peaks at 529.2 ± 0.1 eV and 531.2 ± 0.2 eV, where the former peak refers to the lattice oxygen (O_L), and the latter peak refers to the oxygen vacancies (O_V). The details of O 1s deconvoluted peaks of $x = 0$ and $x = 0.05$ powders are shown in Table 6.3. The calculated ratio of the area of oxygen vacancies to the area of lattice oxygen, O_V/O_L (it represents the oxygen vacancy concentration) (Jaim et al. 2017) is 0.7 for $x = 0$, and it is 0.9 for $x = 0.05$, which shows the increase in the oxygen vacancy concentration with La doping. The difference in the electronegativity values of Ba^{2+} (0.89) and O^{2-} (3.44) is higher as compared to La^{+3} (1.1) and O^{2-} (3.44), so the attractive force between La^{3+} and O^{2-} is less, which can be a reason for the increment in the oxygen vacancies (Luo et al. 2015).

Table 6.3: Details of O 1s deconvoluted peaks of $x = 0$ and 0.05 powders.

Sample	O 1s deconvoluted peaks	Binding energy (eV)	Area (cps. eV)	O_V / O_L
$x = 0$	O_L	529.2	2112.9	0.7
	O_V	531.2	1612.5	
$x = 0.05$	O_L	529.1	1728.6	0.9
	O_V	531.0	1587	
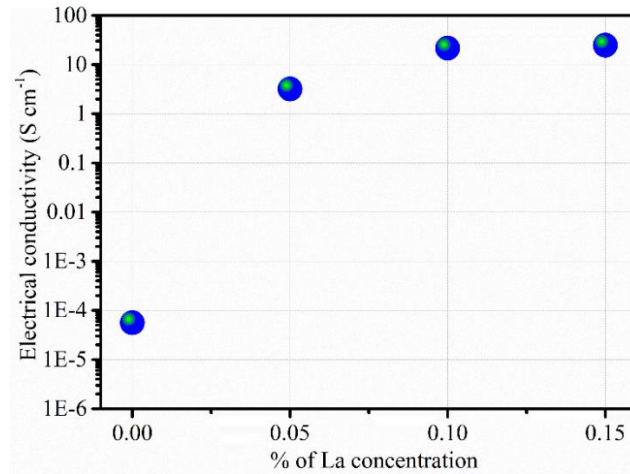
Fig. 6.8: Electrical conductivity of the pellets as a function of % of La concentration.

Table 6.4: Electrical conductivity values of $La_xBa_{1-x}SnO_{3-\delta}$ (x = 0, 0.05, 0.1, 0.15) pellets.

Pellet	σ (S cm^{-1})
$x = 0$	5.6×10^{-5}
$x = 0.05$	3
$x = 0.1$	22
$x = 0.15$	25

The variation of electrical conductivity (σ) of the pellets (sintered at 1000 °C) with respect to La doping concentration is shown in Fig. 6.8. It is identified from Fig. 6.8 that σ is enhanced with La doping in BSO, and the value of σ of all the pellets is

shown in Table 6.4. The enhancement in σ due to La doping in BSO can be accredited to the substitution of La^{3+} in the Ba^{2+} site, where La^{3+} acts as an electron donor, as shown in equation 6.2.

$$La \underset{Ba}{\rightarrow} La^{\bullet}_{Ba} + e'$$ (6.2)

Along with the above substitution reaction, oxygen vacancies may also be generated due to the high-temperature processing of pellets. The loss of oxygen from the lattice also contributes to the generation of sufficient charge carriers, which results in the enhancement of σ of the pellets (as shown in equation 4.16).

It is derived that the σ value of undoped BSO is low owing to its semi-conducting nature. But, the magnitude of it has improved with 0.05 % La doping, which shows the degenerative semiconducting nature of BSO. The σ value augmented ahead as the doping concentration of La increased to 0.1 % and it became nearly constant with further increment in doping. The variation in σ with respect to doping concentration (dσ/dC) from 0.05 to 0.1 % La is found to be ~380, whereas from 0.1 to 0.15 % is ~60. It shows that increment in σ is not that high in the case of doping La from 0.1 to 0.15% when compared to 0.05 to 0.1%, though the doping level is augmented by a constant percent of 0.05. From XPS analysis, it is assured that the percentage of the Sn^{2+} state enhanced from the Sn^{4+} state with increasing La doping from 0 to 0.05 %. With a further increase in La doping percentage, the percentage of the Sn^{2+} state can be enhanced. This ionic reduction of Sn^{4+} to Sn^{2+} necessitates two extra electrons, which may cause the localization of the charge carriers generated through equations 6.2 and 4.16. The proposed reduction reaction from Sn^{4+} to Sn^{2+} is shown in equation 6.3.

$$Sn^{4+} + 2e' \rightarrow Sn^{2+}$$ (6.3)

These electrons will not participate in electrical conduction, but they participate in the reduction reaction (equation 6.4). This might be the reason for the decrease in the rate of σ with the increase in the doping concentration. Also, doping beyond 0.1 % exceeds the solubility limit of La in BSO in the present study, where $La_2Sn_2O_7$ secondary phases are formed (as observed in XRD patterns). These secondary phases

might have also hindered the further enhancement in the σ and held the σ value almost the same as 0.1 % doping of La.

The SEM images of all the pellets are displayed in Fig. 6.9. It is noticed that all the pellets have nano-sized granular morphology. An interconnection between the grains is identified in all the pellets, which helps as the probable percolation path for the movement of charge carriers, and it is represented in Fig. 6.9 (a to d). The presence of elements like barium, tin, lanthanum, and oxygen are identified on the pellets through EDAX spectra, as shown in Fig. 6.10. It is also observed that the position of some of the peaks of Ba and La are almost coinciding with each other since they have nearly the same energy value, which is in accordance to the former report (Ansaree and Upadhyay 2015). Also, the pie charts displayed in the inset, along with each EDAX pattern, showed the atomic percentage of the elements present in the respective pellets. The respective atomic ratio of La and Ba depicted from EDAX spectra is in decent agreement with the theoretical atomic ratio in $La_xBa_{1-x}SnO_{3-\delta}$ ($x = 0, 0.05, 0.1$ and 0.15), which confirms the precise doping of La at Ba site.
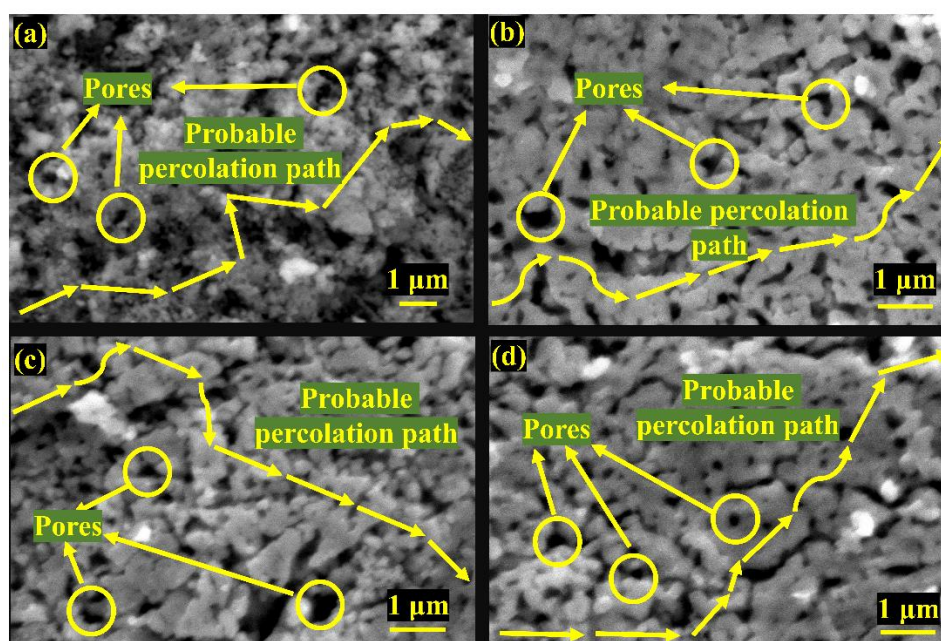
Fig. 6.9: SEM images of $La_xBa_{1-x}SnO_3$ (a) $x = 0$, (b) $x = 0.05$, (c) $x = 0.1$ and (d) $x = 0.15$ pellets.
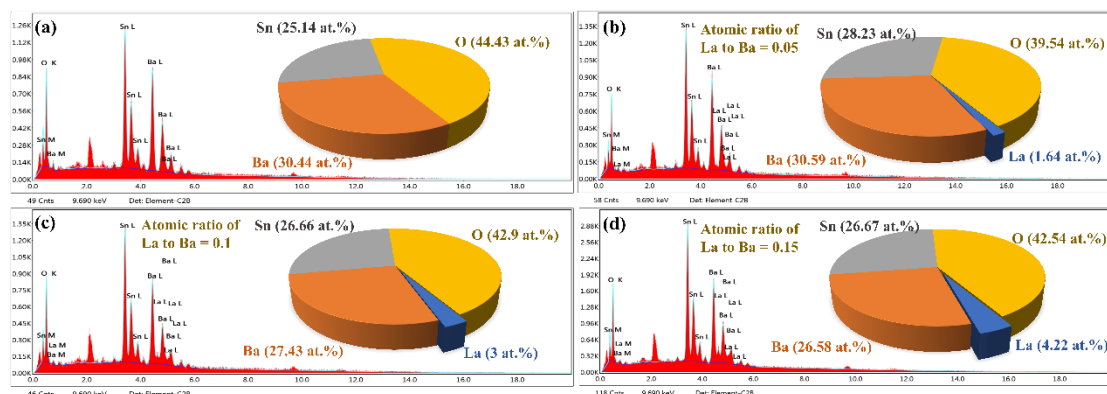
Fig. 6.10: EDAX spectra of La$_x$Ba$_{1-x}$SnO$_3$ (a) $x = 0$, (b) $x = 0.05$, (c) $x = 0.1$, and (d) $x = 0.15$ pellets; Inset pie charts represent the atomic percentage of Ba, Sn, O, and La elements in the respective pellets.

6.4 Conclusions

In this study, La$_x$Ba$_{1-x}$ SnO$_{3-\delta}$ ($x = 0$, 0.05, 0.1, and 0.15) ceramics were synthesized through the polymerized complex method. The XRD patterns showed the presence of cubic perovskite BSO and LBSO phases along with small traces of intermediate phases BaCO$_3$ and SnO$_2$ at 600 °C in undoped and doped conditions, respectively, which confirmed the evolution of these phases from the intermediate phases between 500 to 600 °C. The formation of pure BSO and LBSO phases was recognized at 800 °C and above. The presence of pyrochlore phase La$_2$Sn$_2$O$_7$ was identified at $x = 0.15$, which assured the solubility limit of doping La in BSO up to 0.1 %. Lattice parameter increment (from 4.1165 to 4.1208 Å) with La doping concentration up to $x = 0.1$ further assured the limit of solubility. FTIR investigations also confirmed the evolution of BSO phase between 500 to 600 °C. A reduction in the concentration of Sn^{4+} with La doping was detected in XPS analysis, attributed to the change in the ionic state of Sn^{4+} to Sn^{2+}. An enhancement in the concentration of oxygen vacancies by doping La was also recognized. A progressive increment in σ with La doping was noticed. SEM images of the pellets showed interconnected nano-granular morphology, which might act as a percolation path for the charge carrier movement. The efficient doping of La at the Ba site was confirmed through the atomic ratio of La and Ba in all the doped pellets.

CHAPTER 7

CONCLUSIONS

In the present dissertation, facile and minimal-cost spray-pyrolyzed WO_3 films are fabricated through thermal decomposition, and their properties are analysed. The fabrication of spin-coated metal oxide films such as ZnO-based, TiO_2-based and In_2O_3-based films is performed via solution-combustion synthesis, and their properties are discussed. The screen-printable particle-free aqueous solution combustible In_2O_3-based inks and screen-printed films are developed and their properties are addressed. The fabricated ZnO-based, TiO_2-based and In_2O_3-based films are applied as gas sensors. Barium stannate-based powders and pellets are prepared through the polymerized complex method and their properties are also examined. Based on these experimental results and analysis, the following conclusions are extracted:

✦ The annealing temperature of 400 °C was discerned to be appropriate for the thermal decomposition of precursor and crystallization, which occurred at ~230 and 255 °C. The substrates with pure and monoclinic crystal structured WO_3 coating have exhibited an enhancement in scratch hardness compared to uncoated substrates, irrespective of the applied normal load. Post-treating with OTS, the inherent hydrophilic WO_3 films (WCA < 31°) turned as hydrophobic (WCA > 120°). These films can be potentially applied as antifouling coatings.

✦ Precursors to develop pristine, 1, 2, and 3 wt.% Ti doped ZnO films displayed their combustion temperature at < 235 °C. The fabricated films are pure with hexagonal wurtzite ZnO crystal structure. Pristine ZnO film revealed a superior gas sensing behavior towards NH_3 gas compared to doped films at room temperature and the film is extremely selective to NH_3 gas in contrast to other tested gases. The film presented a maximum gas response of 34.7 at 100 ppm of NH_3 gas, and the attributed probabilistic reasons are relatively high crystallinity, porosity, more oxygen vacancy concentration, and high fraction of adsorbed oxygen.

✦ The combustion temperature of the precursors to fabricate respective air and vacuum-annealed pristine and 6 at. % Nb doped TiO_2 films is detected at < 150 °C. The films are polycrystalline with tetragonal anatase TiO_2 crystal structure. The pristine vacuum-annealed film showed better gas sensing properties towards NH_3 gas in contrast to other films and it revealed a high selectiveness to the same gas. It exhibited a maximum gas response of ~16 at 100 ppm NH_3 gas at room temperature, possibly due to its comparatively high crystallinity and more fraction of adsorbed oxygen.

✦ The combustion temperature is traced at 123 °C for the precursor utilized for the fabrication of Ti and Zn co-doped In_2O_3 films. The films exhibited crystallinity with cubic bixbyite In_2O_3 crystal structure without forming any secondary phases of dopants. The attained optical transparency of the films is $>$ 85% in the visible range.

✦ The screen-printable particle-free aqueous solution combustible inks to develop pristine In_2O_3, doped and co-doped In_2O_3 films showed their combustion temperature at ~280 °C. The polycrystalline screen-printed films with cubic bixbyite In_2O_3 crystal structure revealed no secondary phases of dopant oxides. Pristine In_2O_3 film attained superior room temperature gas sensing performance upon exposure to ethanol gas compared to other films and displayed selectivity to ethanol gas only. It showed a maximum gas response of 17.3 towards 100 ppm concentration of ethanol gas and the plausible factors are relatively high porosity, more oxygen vacancy concentration, and fraction of adsorbed oxygen.

✦ BSO/LBSO phase has emerged between 500 to 600 °C comprising small traces of intermediate phases such as $BaCO_3$ and SnO_2 in $La_xBa_{1-x}SnO_{3-\delta}$ ($x = 0$, 0.05, 0.1 and 0.15) metal oxides. The pure BSO/LBSO phase has formed without intermediate phases at 800 °C and above. The solubility limit of dopant La in BSO is found to be up to $x = 0.1$. An incremental response in the electrical conductivity of BSO pellets (sintered at 1000 °C) has been accomplished by doping La with a maximum electrical conductivity of 25 S cm^{-1}.

7.1 Scope for future work

The present work has directed the facile, low-cost spray coating and spin coating methods for depositing metal oxide films. The current work has also aimed to formulate screen-printable particle-free inks for fabricating metal oxide films. The present work also explored the evolution of the barium stannate phase as a function of temperature. The present study provides the following scope for future work:

1. Due to the facileness in the process of depositing WO_3 films presented in this study, they can be extended on different grades of steels like ferritic steels, austenitic steels, surgical-grade steels, and duplex alloys (mixing of ferrite and austenite), which are commonly utilized in maritime and chemical industries, transport, and underwater pipelines, etc. The antifouling properties of these films can be explored by immersing them in the various fouling culture (algae etc.)

2. Other metal oxides, such as zirconia (ZrO_2) which has tremendous usage as hard coatings on SS, can be deposited through the developed low-cost spray-pyrolysis method. Similar studies (as demonstrated above) can also be performed on these films and their properties can be investigated as an approach for the antifouling coatings.

3. Using the particle-free approach, several other novel and complex metal oxide-based films can be fabricated by the screen-printing method. They can be studied for their sensing properties towards various harmful gases.

4. Room temperature gas detection capabilities of the metal oxide-based gas sensors developed in this study can be further investigated and modified to trace the toxic gases at very low concentrations (in ppb), which can be potentially utilized as breath markers in clinical diagnostics for medical appliances.

5. A similar work which deals with the effect of dopant antimony 'Sb' on BSO (SBSO) can be conducted, and their properties can be compared with LBSO. Also, similar work can be performed on other stannate systems like strontium stannate (SrSnO3) (SSO) and La-doped SSO (LSSO) developed through the polymerized complex method.

The page was left intentionally blank

APPENDIX

APPENDIX I
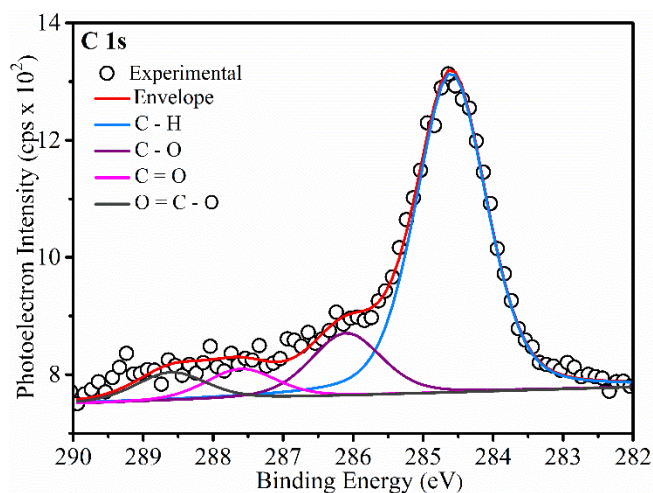
Fig. I: High-resolution XPS spectrum of C 1s of WO$_3$ film on SS substrate.

Table I: C 1s XPS peak fitting parameters of C 1s of WO$_3$ film on SS substrate.

Deconvoluted peaks	Position constraints	Position (eV)	G/L ratio	FWHM constraints	FWHM
C-H (peak I)	--	284.6	30	--	1.19
C-O (peak II)	Peak I + 1.5 eV	286.1	30	(Peak I) × 1	1.19
C=O (peak III)	Peak I + 3.0 eV	287.6	30	(Peak I) × 1	1.19
O=C-O (peak IV)	Peak I + 4.0 eV	288.6	30	(Peak I) × 1	1.19

Carbon 1s (C 1s) peak presented at 284.6 eV is utilized for the XPS spectrum's calibration. The peak fitting of the C 1s peak is executed to discover the position of the C-H peak for the charge correction. C 1s spectrum is fit with the four peaks presented at 284.6 eV (C-H, Peak I), Peak I + 1.5 eV (C-O, Peak II), Peak I + 3.0 eV (C=O, Peak III) and Peak I + 4.0 eV (O=C-O, Peak IV). The Gaussian/Lorentz (G/L) ratio and FWHM of all the peaks in the C 1s spectrum are fit by the XPS curve fitting software and their values are constrained to be the same. Fig. I presents the C 1s XPS peak fitting of WO$_3$ film on SS substrate. Table I provides the details of peak position constraints and the parameters of C 1s deconvoluted peaks of WO$_3$ film on SS substrate.
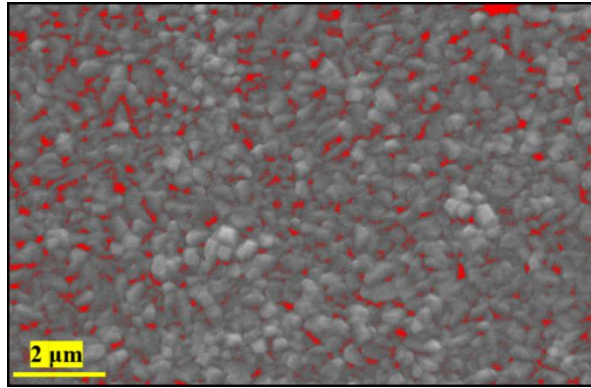
Fig. II: SEM image of WO$_3$ film showing the area of the pores (in red colour). The area of the pores is found to be 4.7 %.
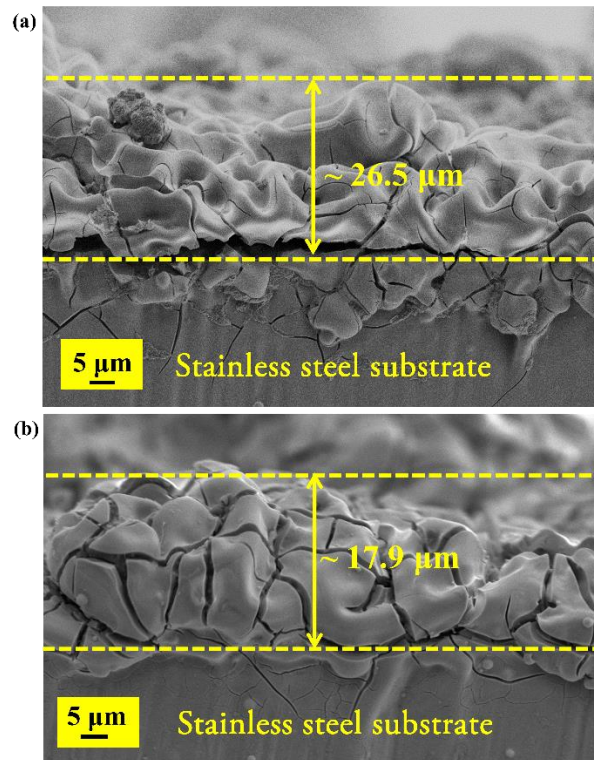
Fig. III: The cross-sectional view (obtained from FESEM) showing the thickness of the films fabricated at (a) 200 °C and (b) 300 °C on SS substrate.
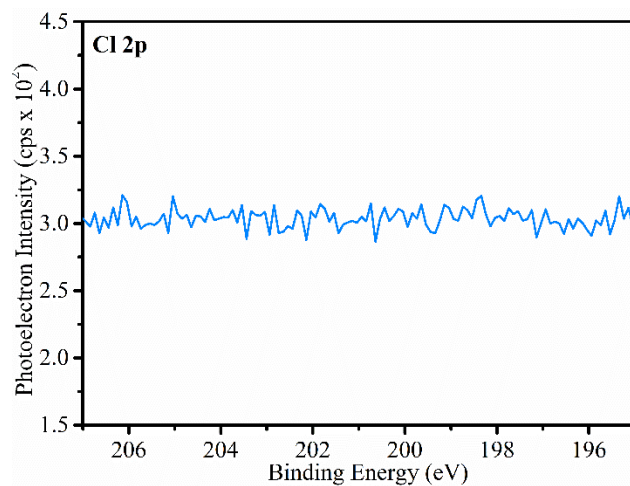
Fig. IV: High-resolution XPS spectrum of Cl 2p of WO$_3$ film on SS substrate.
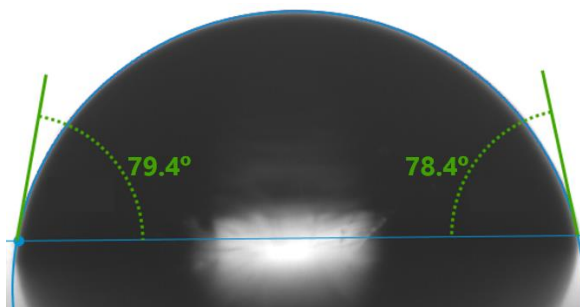
Fig. V: The WCA of the uncoated SS substrate.

APPENDIX II

      Carbon 1s (C 1s) peak presented at 284.6 eV is utilized for the calibration of the XPS spectra. The peak fitting of the C 1s peak is conducted in order to determine the position of the C-H peak for accounting the charge correction. The fitting of the XPS is performed as mentioned in Appendix I. Fig. VI (a and b) show the C 1s XPS peak fitting of 10 and 15 sprays, respectively. Table II and III provide the peak position constraints and parameters of C1s deconvoluted peaks of 10 and 15 sprays films, respectively.
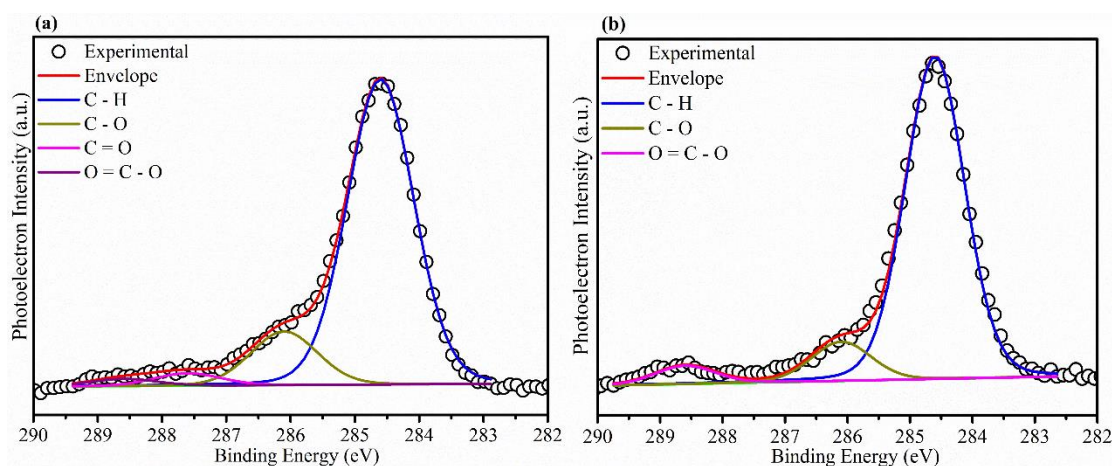
Fig. VI: C 1s high-resolution XPS spectrum of the (a) 10 sprays and (b) 15 sprays films, respectively.

Table II: C 1s XPS peak fitting parameters of the 10 sprays film.

Deconvoluted peaks	Position constraints	Position (eV)	G/L ratio	FWHM constraints	FWHM
C-H (peak I)	--	284.6	10	--	1.22
C-O (peak II)	Peak I + 1.5 eV	286.1	10	(Peak I) $\times$ 1	1.22
C=O (peak III)	Peak I + 3.0 eV	287.6	10	(Peak I) $\times$ 1	1.22
O=C-O (peak IV)	Peak I + 4.0 eV	288.6	10	(Peak I) $\times$ 1	1.22

Table III: C 1s XPS peak fitting parameters of the 15 sprays film.

Deconvoluted peaks	Position constraints	Position (eV)	G/L ratio	FWHM constraints	FWHM
C-H (peak I)	--	284.6	12	--	1.12
C-O (peak II)	Peak I + 1.5 eV	286.1	12	(Peak I) × 1	1.12
O=C-O (peak IV)	Peak I + 4.0 eV	288.6	12	(Peak I) × 1	1.12
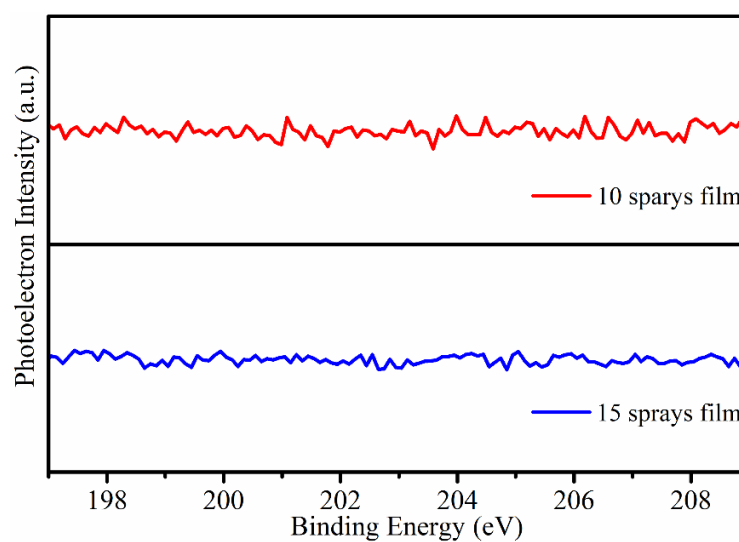
Fig. VII: High-resolution XPS spectra of Cl 2p of 10 and 15 sprays films.

Fig. VIII: The WCA of the uncoated glass substrate.

APPENDIX III

The peak of Carbon 1s (C 1s) that is located at 284.6 eV is utilized for the calibration of the XPS spectra. The peak fitting of the C 1s peak is executed to determine the position of the C-H peak for the charge correction. The fitting of the XPS was performed as mentioned in Appendix I. Fig. IX (a to d) show the C 1s XPS peak fitting of ZT0, ZT1, ZT2 and ZT3 films, respectively. Table IV, V, VI and VIII provide the peak position constraints and parameters of C1s deconvoluted peaks of ZT0, ZT1, ZT2 and ZT3 films, respectively.

Fig. IX: C 1s high-resolution XPS peak fitting of (a) ZT0, (b) ZT1, (c) ZT2 and (d) ZT3 films, respectively.

Table IV: C 1s XPS peak fitting parameters of the ZT0 film.

Deconvoluted peaks	Position constraints	Position (eV)	G/L ratio	FWHM constraints	FWHM
C-H (peak I)	--	284.6	25	--	1.103
C-O (peak II)	Peak I + 1.5 eV	286.1	25	(Peak I) × 1	1.103
C=O (peak III)	Peak I + 3.0 eV	287.6	25	(Peak I) × 1	1.103
O=C-O (peak IV)	Peak I + 4.0 eV	288.6	25	(Peak I) × 1	1.103

Table V: C 1s XPS peak fitting parameters of the ZT1 film.

Deconvoluted peaks	Position constraints	Position (eV)	G/L ratio	FWHM constraints	FWHM
C-H (peak I)	--	284.6	15	--	1.16
C-O (peak II)	Peak I + 1.5 eV	286.1	15	(Peak I) × 1	1.16
C=O (peak III)	Peak I + 3.0 eV	287.6	15	(Peak I) × 1	1.16
O=C-O (peak IV)	Peak I + 4.0 eV	288.6	15	(Peak I) × 1	1.16

Table VI: C 1s XPS peak fitting parameters of the ZT2 film.

Deconvoluted peaks	Position constraints	Position (eV)	G/L ratio	FWHM constraints	FWHM
C-H (peak I)	--	284.6	11	--	1.18
C-O (peak II)	Peak I + 1.5 eV	286.1	11	(Peak I) × 1	1.18
C=O (peak III)	Peak I + 3.0 eV	287.6	11	(Peak I) × 1	1.18
O=C-O (peak IV)	Peak I + 4.0 eV	288.6	11	(Peak I) × 1	1.18

Table VII: C 1s XPS peak fitting parameters of the ZT3 film.

Deconvoluted peaks	Position constraints	Position (eV)	G/L ratio	FWHM constraints	FWHM
C-H (peak I)	--	284.6	10	--	1.1
C-O (peak II)	Peak I + 1.5 eV	286.1	10	(Peak I) × 1	1.1
C=O (peak III)	Peak I + 3.0 eV	287.6	10	(Peak I) × 1	1.1
O=C-O (peak IV)	Peak I + 4.0 eV	288.6	10	(Peak I) × 1	1.1
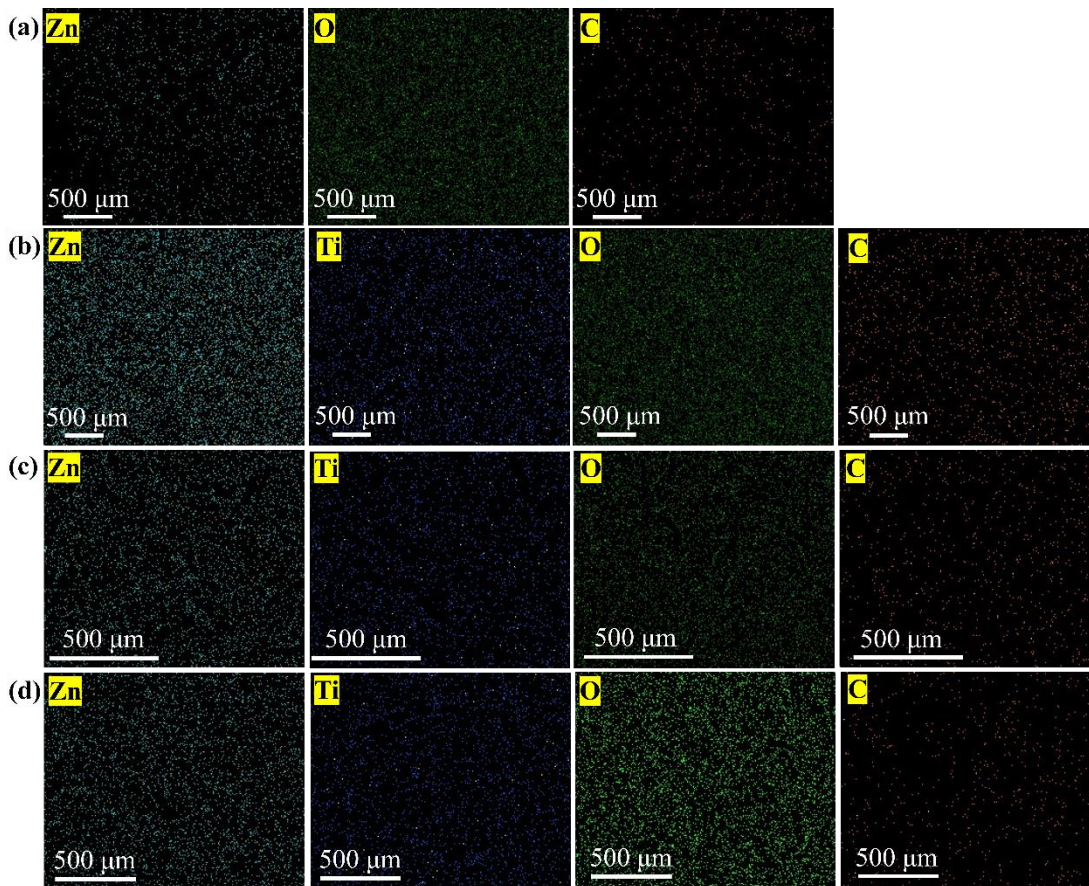
Fig. X: EDAX elemental mapping displaying the distribution of respective elements present in (a) ZT0, (b) ZT1, (c) ZT2 and (d) ZT3 films.
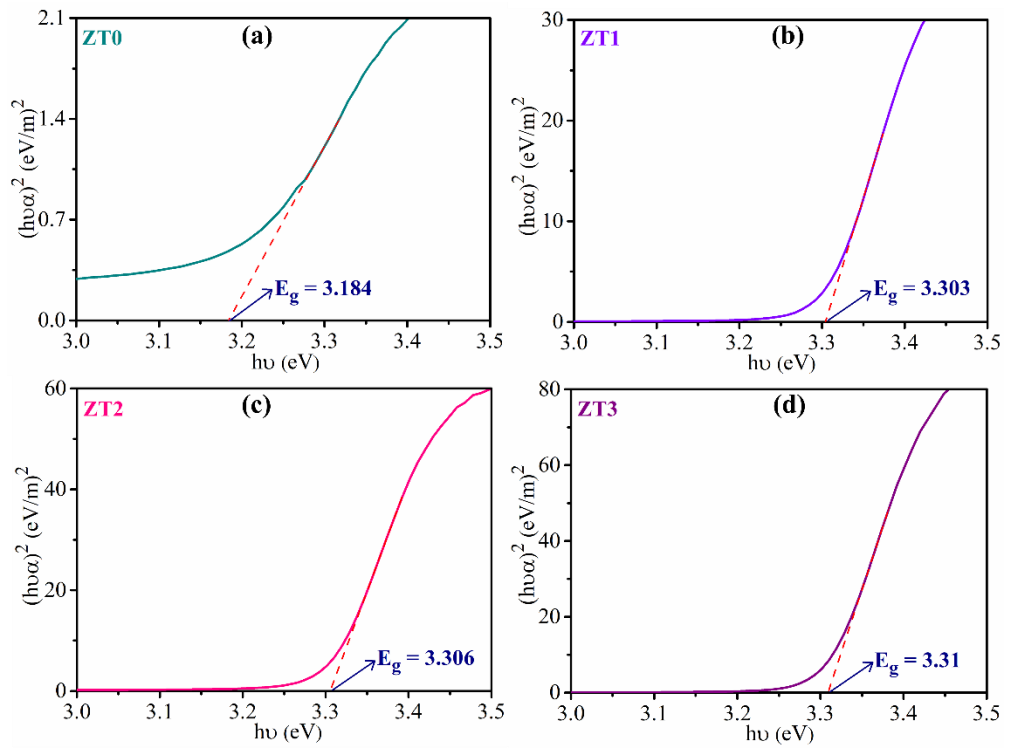
Fig. XI: Tauc's plot of (a) ZT0, (b) ZT1, (c) ZT2 and (d) ZT3 films, respectively.

APPENDIX IV

The peak of Carbon 1s (C 1s), which is positioned at 284.6 eV, is applied for the calibration of the XPS spectra. The peak fitting of the C 1s peak is implemented to determine the position of the C-H peak for the charge correction. The fitting of the XPS was executed as mentioned in Appendix I. Fig. XII (a to d) display the C 1s XPS peak fitting of TO, NTO, TO-V and NTO-V films, respectively. Table VIII, IX, X and XI present the peak position constraints and parameters of C1s deconvoluted peaks of TO, NTO, TO-V and NTO-V, respectively.
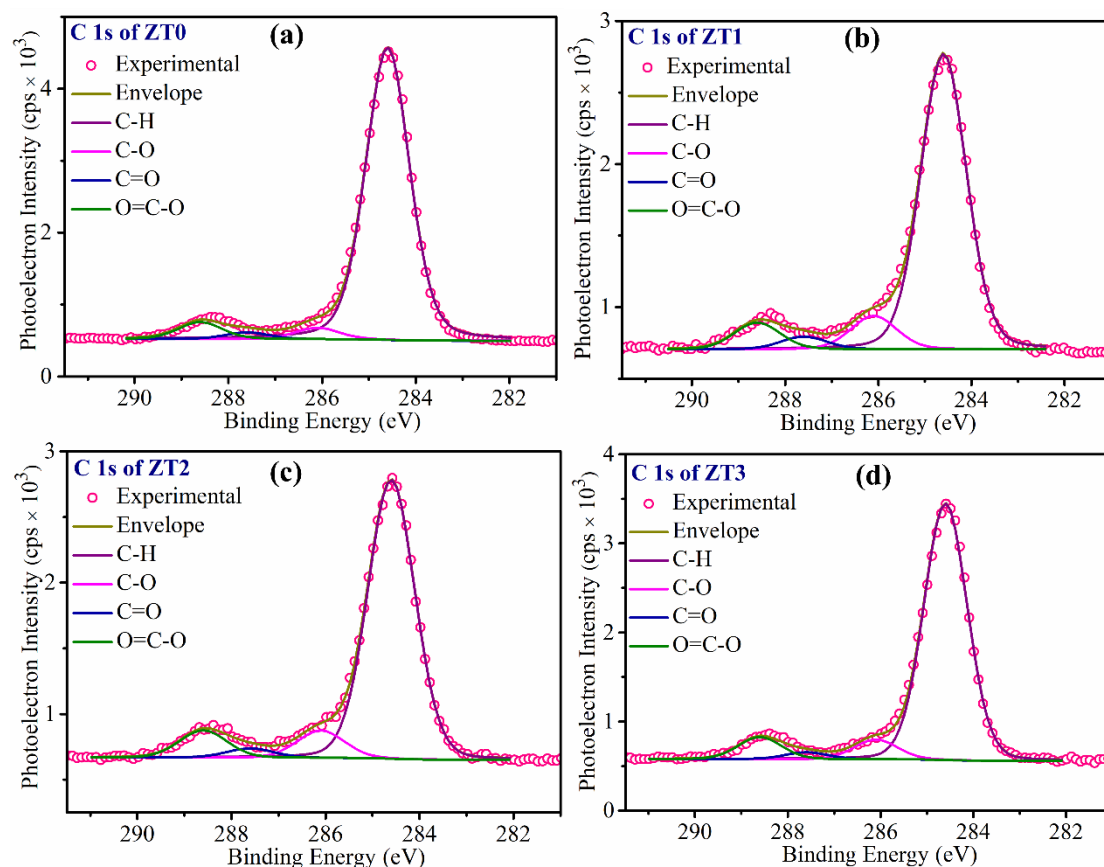

Fig. XII: C 1s high-resolution XPS peak fitting of (a) TO, (b) NTO, (c) TO-V and (d) NTO-V films, respectively.

Table VIII: C 1s XPS peak fitting parameters of the TO film.

Deconvoluted peaks	Position constraints	Position (eV)	G/L ratio	FWHM constraints	FWHM
C-H (peak I)	--	284.6	5	--	1.11
C-O (peak II)	Peak I + 1.5 eV	286.1	5	(Peak I) × 1	1.11
C=O (peak III)	Peak I + 3.0 eV	287.6	5	(Peak I) × 1	1.11
O=C-O (peak IV)	Peak I + 4.0 eV	288.6	5	(Peak I) × 1	1.11

Table IX: C 1s XPS peak fitting parameters of the NTO film.

Deconvoluted peaks	Position constraints	Position (eV)	G/L ratio	FWHM constraints	FWHM
C-H (peak I)	--	284.6	7	--	1.12
C-O (peak II)	Peak I + 1.5 eV	286.1	7	(Peak I) × 1	1.12
C=O (peak III)	Peak I + 3.0 eV	287.6	7	(Peak I) × 1	1.12
O=C-O (peak IV)	Peak I + 4.0 eV	288.6	7	(Peak I) × 1	1.12

Table X: C 1s XPS peak fitting parameters of the TO-V film.

Deconvoluted peaks	Position constraints	Position (eV)	G/L ratio	FWHM constraints	FWHM
C-H (peak I)	--	284.6	5	--	1.45
C-O (peak II)	Peak I + 1.5 eV	286.1	5	(Peak I) × 1	1.45
C=O (peak III)	Peak I + 3.0 eV	287.6	5	(Peak I) × 1	1.45
O=C-O (peak IV)	Peak I + 4.0 eV	288.6	5	(Peak I) × 1	1.45

Table XI: C 1s XPS peak fitting parameters of the NTO-V film.

Deconvoluted peaks	Position constraints	Position (eV)	G/L ratio	FWHM constraints	FWHM
C-H (peak I)	--	284.6	10	--	1.2
C-O (peak II)	Peak I + 1.5 eV	286.1	10	(Peak I) × 1	1.2
C=O (peak III)	Peak I + 3.0 eV	287.6	10	(Peak I) × 1	1.2
O=C-O (peak IV)	Peak I + 4.0 eV	288.6	10	(Peak I) × 1	1.2
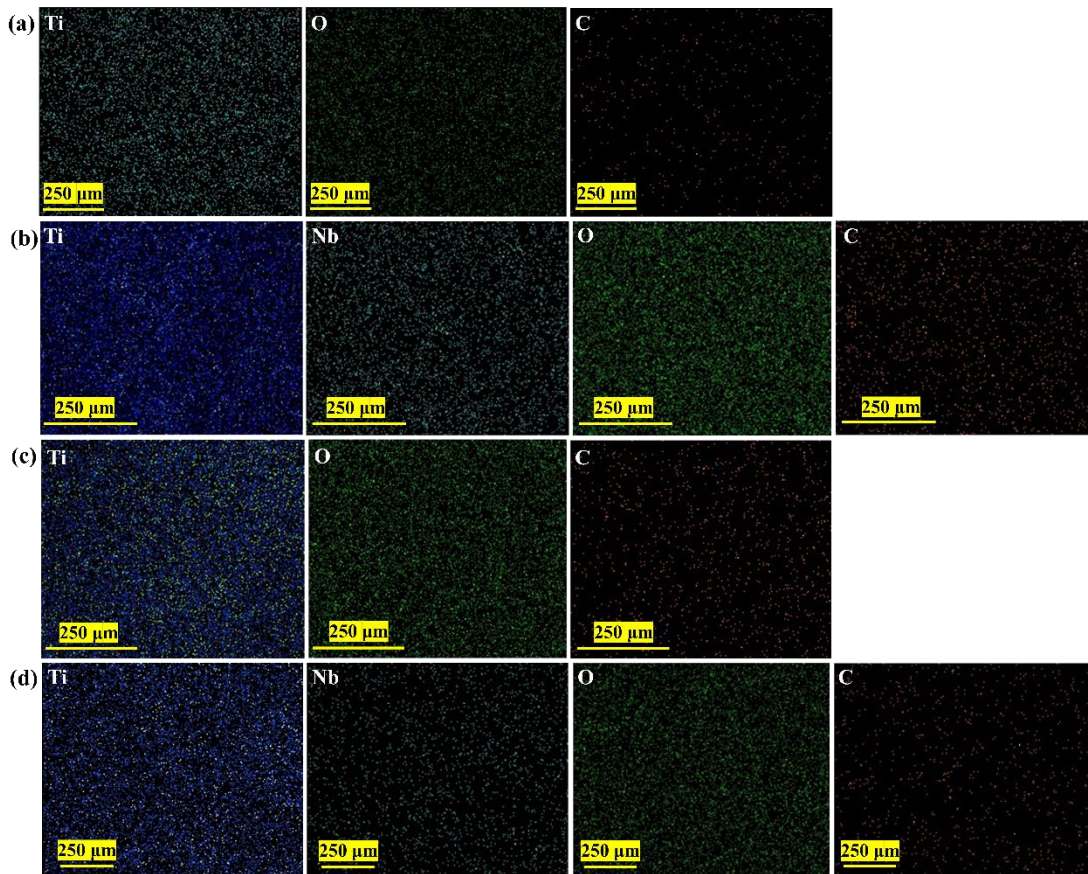
Fig. XIII: EDAX elemental mapping showing the distribution of respective elements that are present in (a) TO, (b) NTO, (c) TO-V and (d) NTO-V films.
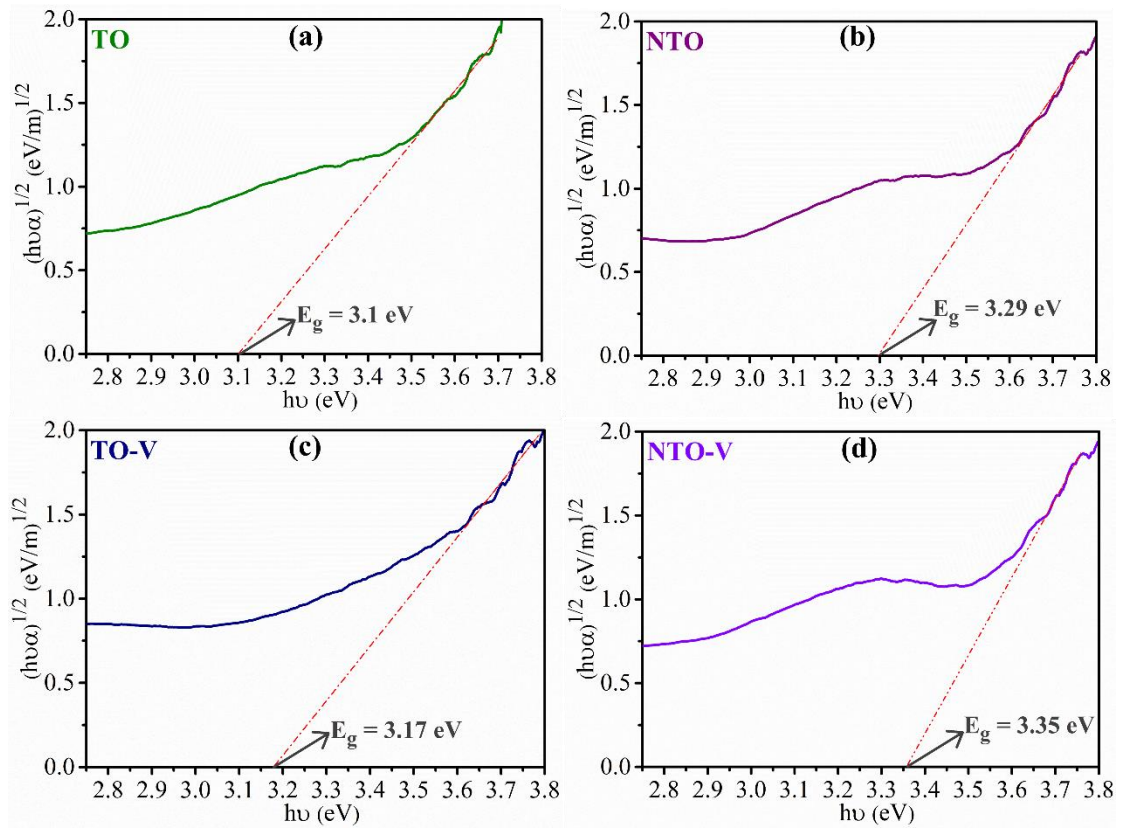
Fig. XIV: Tauc's plot of (a) TO, (b) NTO, (c) TO-V and (d) NTO-V films, respectively.

APPENDIX V

The peak of Carbon 1s (C 1s), which is situated at 284.6 eV, is used for the XPS spectra calibration. The peak fitting of the C 1s peak is conducted to determine the position of the C-H peak for the charge correction. The fitting of the XPS was executed as mentioned in Appendix I. Fig. XV (a to d) show the C 1s XPS peak fitting of IO, ITO, IZO and ITZO films, respectively. Table XII, XIII, XIV and XV provide the peak position constraints and parameters of C1s deconvoluted peaks of IO, ITO, IZO and ITZO films, respectively.
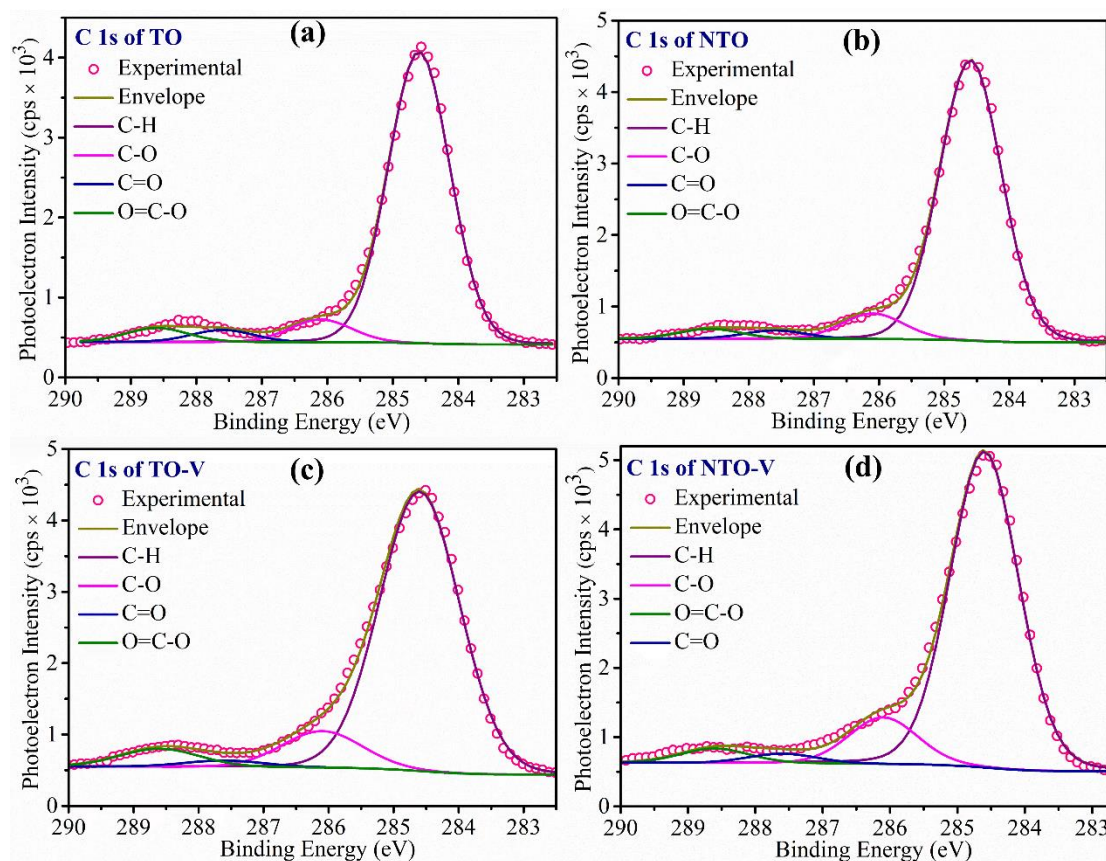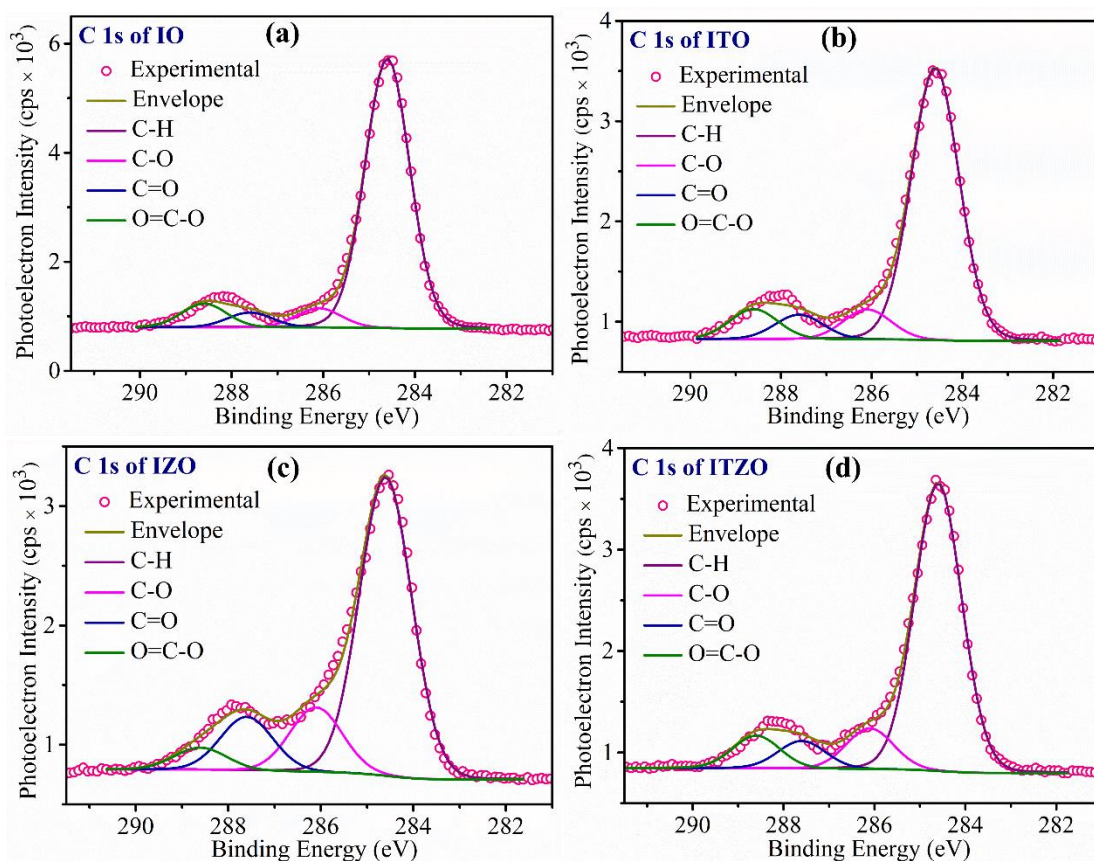

Fig. XV: C 1s high-resolution XPS peak fitting of (a) IO, (b) ITO, (c) IZO and (d) ITZO films, respectively.

Table XII: C 1s XPS peak fitting parameters of the IO film.

Deconvoluted peaks	Position constraints	Position (eV)	G/L ratio	FWHM constraints	FWHM
C-H (peak I)	--	284.6	7	--	1.15
C-O (peak II)	Peak I + 1.5 eV	286.1	7	(Peak I) × 1	1.15
C=O (peak III)	Peak I + 3.0 eV	287.6	7	(Peak I) × 1	1.15
O=C-O (peak IV)	Peak I + 4.0 eV	288.6	7	(Peak I) × 1	1.15

Table XIII: C 1s XPS peak fitting parameters of the ITO film.

Deconvoluted peaks	Position constraints	Position (eV)	G/L ratio	FWHM constraints	FWHM
C-H (peak I)	--	284.6	7	--	1.24
C-O (peak II)	Peak I + 1.5 eV	286.1	7	(Peak I) × 1	1.24
C=O (peak III)	Peak I + 3.0 eV	287.6	7	(Peak I) × 1	1.24
O=C-O (peak IV)	Peak I + 4.0 eV	288.6	7	(Peak I) × 1	1.24

Table XIV: C 1s XPS peak fitting parameters of the IZO film.

Deconvoluted peaks	Position constraints	Position (eV)	G/L ratio	FWHM constraints	FWHM
C-H (peak I)	--	284.6	4	--	1.33
C-O (peak II)	Peak I + 1.5 eV	286.1	4	(Peak I) × 1	1.33
C=O (peak III)	Peak I + 3.0 eV	287.6	4	(Peak I) × 1	1.33
O=C-O (peak IV)	Peak I + 4.0 eV	288.6	4	(Peak I) × 1	1.33

Table XV: C 1s XPS peak fitting parameters of the ITZO film.

Deconvoluted peaks	Position constraints	Position (eV)	G/L ratio	FWHM constraints	FWHM
C-H (peak I)	--	284.6	6	--	1.22
C-O (peak II)	Peak I + 1.5 eV	286.1	6	(Peak I) × 1	1.22
C=O (peak III)	Peak I + 3.0 eV	287.6	6	(Peak I) × 1	1.22
O=C-O (peak IV)	Peak I + 4.0 eV	288.6	6	(Peak I) × 1	1.22
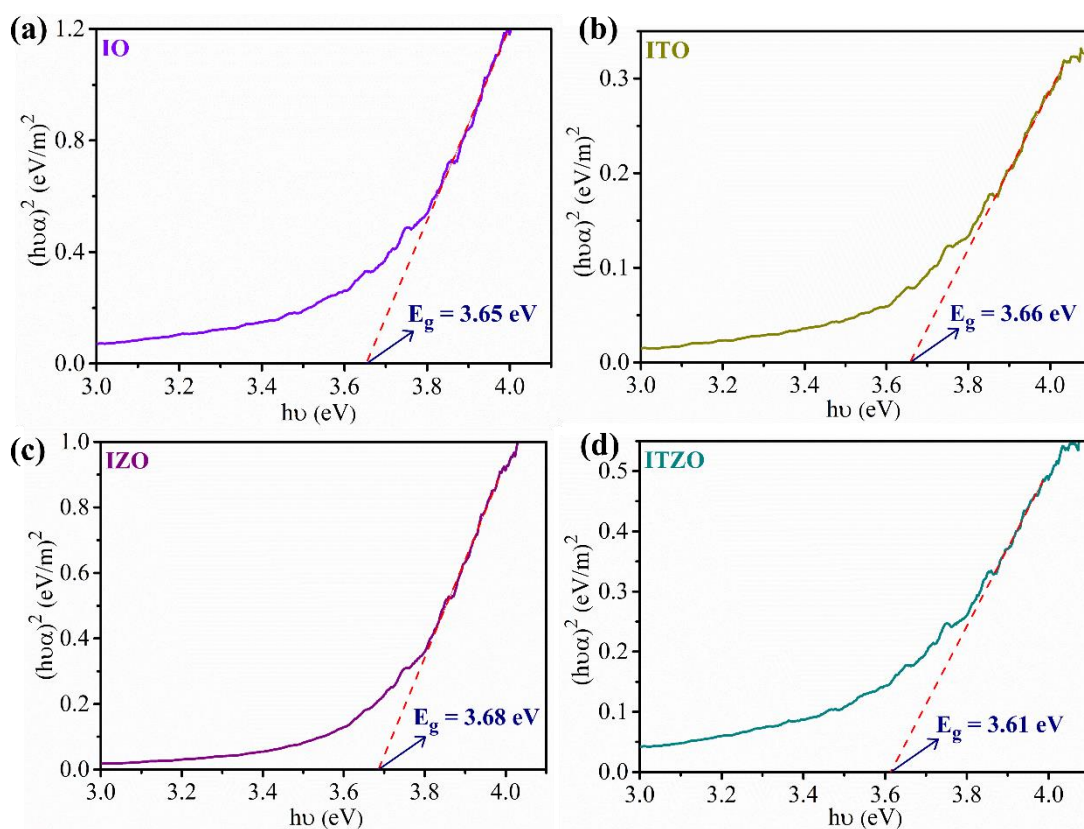
Fig. XVI: Tauc's plot of (a) IO, (b) ITO, (c) IZO, and (d) ITZO screen-printed films, respectively.

APPENDIX VI

The Carbon 1s (C 1s) peak situated at 284.6 eV is used for the for calibration of the XPS spectra. The peak fitting of the C 1s peak is conducted to determine the C-H peak position for accounting the charge correction. The fitting of the XPS was performed as mentioned in Appendix I. Fig. XVII shows the C 1s XPS peak fitting of $x = 0$ and $x = 0.05$ powders, respectively. Table XVI and XVII provide the details of C1s deconvoluted peaks of $x = 0$ and $x = 0.05$ powders, respectively.
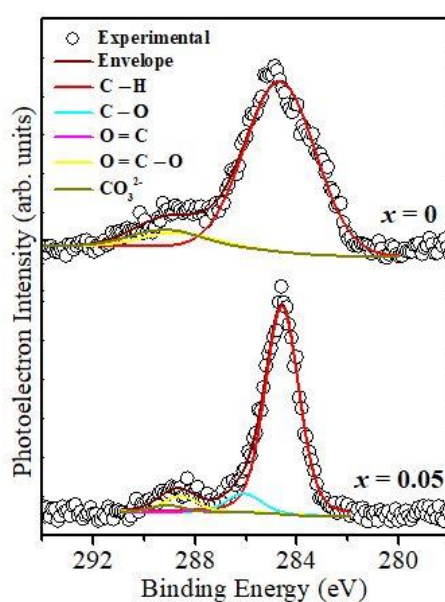
Fig. XVII: C 1s high-resolution XPS peak fitting of (a) $x = 0$ and (b) $x = 0.05$ powders synthesized at 900 °C.

Table XVI: Peak fitting parameters of C 1s for $x = 0$ powder synthesized at 900 °C.

Deconvoluted peaks	Position constraints	Position (eV)	G/L ratio	FWHM constraints	FWHM
C-H (peak I)	--	284.6	0	--	3.26
O=C-O (peak IV)	Peak I + 4.0 eV	288.6	0	(Peak I) × 1	3.26
CO_3^{2-} (peak V)	Peak I + 4.5 eV	289.1	0	(Peak I) × 1	3.26

Table XVII: Peak fitting parameters of C 1s for $x = 0.05$ powder synthesized at 900 °C.

Deconvoluted peaks	Position constraints	Position (eV)	G/L ratio	FWHM constraints	FWHM
C-H (peak I)	--	284.6	25	--	1.57
C-O (peak II)	Peak I + 1.5 eV	286.1	25	(Peak I) × 1	1.57
C=O (peak III)	Peak I + 3.0 eV	287.6	25	(Peak I) × 1	1.57
O=C-O (peak IV)	Peak I + 4.0 eV	288.6	25	(Peak I) × 1	1.57
CO_3^{2-} (peak V)	Peak I + 4.5 eV	289.1	25	(Peak I) × 1	1.57

REFERENCES

Alomair, A. A., and Alqaheem, Y. (2019). "The implementation of a carbon precursor to produce ZSM-5 membranes for the separation of isomers in the pervaporation system." *ACS Omega*, 4, 19005–19010.

Ahn, D. B., Jeon, H. J., Sheng, J., Park, J., and Park, J. S. (2015). "A review on the recent developments of solution processes for oxide thin film transistors." *Semicond Sci Technol*, 30 064001.

Al-Fori, M., Dobretsov, S., Myint, M. T. Z., and Dutta, J. (2014). "Antifouling properties of zinc oxide nanorod coatings." *Biofouling*, 30, 871–882.

Al-Gaashani, R., Radiman, S., Tabet, N., and Razak Daud, A. (2011). "Synthesis and optical properties of CuO nanostructures obtained via a novel thermal decomposition method." *J Alloys Compd*, 509, 8761–8769.

Aluri, G. S., Motayed, A., Davydov, A. V., Oleshko, V. P., Bertness, K. A., Sanford, N. A., and Rao, M. V. (2011). "Highly selective GaN-nanowire/TiO_2-nanocluster hybrid sensors for detection of benzene and related environment pollutants." *Nanotechnology*, 22, 295503.

Anand, K., Kaur, J., Singh, R. C., and Thangaraj, R. (2016). "Structural, optical and gas sensing properties of pure and Mn-doped In_2O_3 nanoparticles." *Ceram Int*, 42, 10957–10966.

Ansaree, M. J., and Upadhyay, S. (2015). "Electrical characterization of porous La-doped $BaSnO_3$ using impedance spectroscopy." *Ionics*, 21, 2825–2838.

Aswal, D. K., Lenfant, S., Guerin, D., Yakhmi, J. V., and Vuillaume, D. (2006). "Self assembled monolayers on silicon for molecular electronics." *Anal Chim Acta*, 568, 84–108.

Augustin, A., Huilgol, P., Udupa, K. R., and Bhat, U. (2016). "Effect of current density during electrodeposition on microstructure and hardness of textured Cu coating in the application of antimicrobial Al touch surface." *J Mech Behav Biomed Mater*, 63, 352–360.

Ayeshamariam, A., Kashif, M., Bououdina, M., Hashim, U., Jayachandran, M., and Ali, M. E. (2014). "Morphological, structural, and gas-sensing characterization of tin-doped indium oxide nanoparticles." *Ceram Int*, 40, 1321–1328.

Banerjee, I., Pangule, R. C., and Kane, R. S. (2011). "Antifouling coatings: recent developments in the design of surfaces that prevent fouling by proteins, bacteria, and marine organisms." *Adv Mater*, 23, 690–718.

Barreca, D., Carta, G., Gasparotto, A., Rossetto, G., Tondello, E., and Zanella, P. (2003). "A study of nanophase tungsten oxides thin films by XPS." *Surf Sci Spectra*, 8, 258–267.

Beamson, G., Clark, D. T., Hayes, N. W., and Law, D. S. L. (1994). "Effect of crystallinity on the XPS spectrum of poly(ethylene terephthalate)." *Surf Sci Spectra*, 3, 357–365.

Beegan, D., Chowdhury, S., and Laugier, M. T. (2007). "Comparison between nanoindentation and scratch test hardness (scratch hardness) values of copper thin films on oxidised silicon substrates." *Surf Coat Technol*, 201, 5804–5808.

Benayoun, S., Fouilland-Paillé, L., and Hantzpergue, J. J. (1999). "Microscratch test studies of thin silica films on stainless steel substrates." *Thin Solid Films*, 352, 156–166.

Bergum, K., Hansen, P. A., Fjellvåg, H., and Nilsen, O. (2014). "Structural, electrical and optical characterization of Ti-doped ZnO films grown by atomic layer deposition." *J Alloys Compd*, 616, 618–624.

Besozzi, E., Dellasega, D., Russo, V., Conti, C., Passoni, M., and Beghi, M. G. (2019). "Thermomechanical properties of amorphous metallic tungsten-oxygen and tungsten-oxide coatings." *Mater Des*, 165, 107565.

Bhalla, A. S., Guo, R., and Roy, R. (2016). "The perovskite structure—a review of its role in ceramic science and technology." *Mater Res Innov*, 4, 3–26.

Bhowmik, B., Manjuladevi, V., Gupta, R. K., and Bhattacharyya, P. (2016). "Highly selective low-temperature acetone sensor based on hierarchical 3-D TiO_2 nanoflowers." *IEEE Sens J*, 16, 3488–3495.

Birnie, D. P. (2001). "Rational solvent selection strategies to combat striation formation during spin coating of thin films." *J Mater Res*, 16, 1145–1154.

Brinker, C. J., Frye, G. C., Hurd, A. J., and Ashley, C. S. (1991). "Fundamentals of sol-gel dip coating." *Thin Solid Films*, 201, 97–108.

Burrell, M. C., Liu, Y. S., and Cole, H. S. (1986). "An X-ray photoelectron spectroscopy study of poly(methylmethacrylate) and poly(α-methylstyrene) surfaces irradiated by excimer lasers." *J Vac Sci Technol A*, 4, 2459–2462.

Callow, J. A., and Callow, M. E. (2011). "Trends in the development of environmentally friendly fouling-resistant marine coatings." *Nat Commun*, 2, 1–9.

Cantalini, C., Wlodarski, W., Sun, H. T., Atashbar, M. Z., Passacantando, M., and Santucci, S. (2000). "NO_2 response of In_2O_3 thin film gas sensors prepared by sol–gel and vacuum thermal evaporation techniques." *Sens Actuators B Chem*, 65, 101–104.

Cao, Y. Q., Wang, S. S., Liu, C., Wu, D., and Li, A. D. (2019). "Atomic layer deposition of ZnO/TiO_2 nanolaminates as ultra-long life anode material for lithium-ion batteries." *Sci Rep*, 9, 1–9.

Cao, Y., Zou, X., Wang, X., Qian, J., Bai, N., and Li, G. D. (2016). "Effective detection of trace amount of explosive nitro-compounds by ZnO nanofibers with hollow structure." *Sens Actuators B Chem*, 232, 564–570.

Carlos, E., Martins, R., Fortunato, E., and Branquinho, R. (2020). "Solution combustion synthesis: towards a sustainable approach for metal oxides." *Eur J Chem*, 26, 9099–9125.

Celia, E., Darmanin, T., de Givenchy, E. T., Amigoni, S., and Guittard, F. (2013). "Recent advances in designing superhydrophobic surfaces." *J Colloid Interface Sci*, 402, 1–18.

Che, Y., Feng, G., Sun, T., Xiao, J., Guo, W., and Song, C. (2021). "Excellent gas-sensitive properties towards acetone of In_2O3 nanowires prepared by electrospinning." *Colloid Interface Sci Commun*, 45, 100508.

Chen, C., Kedler, E. M., van der Put P. J. J. M., and Schoonman, J. (1996). "Morphology control of thin $LiCoO_2$ films fabricated using the electrostatic spray deposition (ESD) technique." *J Mater Chem*, 6, 765–771.

Chen, X., Deng, N., Zhang, X., Yang, Y., Li, J., Hong, B., Fang, J., Xu, J., Jin, D., Peng, X., Wang, X., and Jin, H. (2019). "Preparation of Fe-doped In_2O_3 gas sensing semiconductor by one-step impregnation with enhanced ethanol sensing." *Chem Phys Lett*, 722, 96–103.

Chen, Y., Xu, X. L., Zhang, G. H., Xue, H., and Ma, S. Y. (2010). "Blue shift of optical band gap in Er-doped ZnO thin films deposited by direct current reactive magnetron sputtering technique." *Physica E Low Dimens Syst Nanostruct*, 42, 1713–1716.

Chinh, N. D., Kim, C., and Kim, D. (2019). "UV-light-activated H_2S gas sensing by a TiO_2 nanoparticulate thin film at room temperature." *J Alloys Compd*, 778, 247–255.

Choi, S. W., Park, J. Y., and Kim, S. S. (2011). "Dependence of gas sensing properties in ZnO nanofibers on size and crystallinity of nanograins." *J Mater Res*, 26, 1662–1665.

Chung, F. C., Zhu, Z., Luo, P. Y., Wu, R. J., and Li, W. (2014). "Au@ZnO core–shell structure for gaseous formaldehyde sensing at room temperature." *Sens Actuators B Chem*, 199, 314–319.

Chung, J., Chen, J., and Tseng, C. (2008). "Preparation of TiO_2-doped ZnO films by radio frequency magnetron sputtering in ambient hydrogen – argon gas." *Appl. Surf. Sci.* 255, 2494–2499.

Chung, W. Y., Sakai, G., Shimanoe, K., Miura, N., Lee, D. D., and Yamazoe, N. (1998). "Preparation of indium oxide thin film by spin-coating method and its gas-sensing properties." *Sens Actuators B Chem*, 46, 139–145.

Claros, M., Setka, M., Jimenez, Y. P., and Vallejos, S. (2020). "AACVD synthesis and characterization of iron and copper oxides modified ZnO structured films." *Nanomaterials*, 10, 1–16.

Cui, J., Shi, L., Xie, T., Wang, D., and Lin, Y. (2016). "UV-light illumination room temperature HCHO gas-sensing mechanism of ZnO with different nanostructures." *Sens Actuators B Chem*, 227, 220–226.

Darezereshki, E., Alizadeh, M., Bakhtiari, F., Schaffie, M., and Ranjbar, M. (2011). "A novel thermal decomposition method for the synthesis of ZnO nanoparticles from low concentration $ZnSO_4$ solutions." *Appl Clay Sci*, 54, 107–111.

Das, R., and Soni, R. K. (2017). "Synthesis and surface-enhanced Raman scattering of indium nanotriangles and nanowires." *RSC Adv*, 7, 32255–32263.

Deepa, A. S., Vidya, S., Manu, P. C., Solomon, S., John, A., and Thomas, J. K. (2011). "Structural and optical characterization of $BaSnO_3$ nanopowder synthesized through a novel combustion technique." *J Alloys Compd*, 509, 1830–1835.

Deng, J., Fu, Q., Luo, W., Tong, X., Xiong, J., Hu, Y., and Zheng, Z. (2016). "Enhanced H_2S gas sensing properties of undoped ZnO nanocrystalline films from QDs by low-temperature processing." *Sens Actuators B Chem*, 224, 153–158.

Dey, A. (2018). "Semiconductor metal oxide gas sensors: A review." *Mater Sci Eng B*, 229, 206–217.

Dhahri, R., Hjiri, M., Mir, L. E., Bonavita, A., Iannazzo, D., Latino, M., Donato, N., Leonardi, S. G., and Neri, G. (2016). "Gas sensing properties of Al-doped ZnO for UV-activated CO detection." *J Phys D Appl Phys*, 49, 135502.

Dhahri, R., Hjiri, M., Mir, L. E., Bonavita, A., Iannazzo, D., Leonardi, S. G., and Neri, G. (2015). "CO sensing properties under UV radiation of Ga-doped ZnO nanopowders." *Appl Surf Sci*, 355, 1321–1326.

Dhivya, P., and Sridharan, M. (2014). "Nanostructured ZnO films for room temperature ammonia sensing." *J Electron Mater*, 43, 3211–3216.

Diebold, U., and Madey, T. E. (1996). "TiO$_2$ by XPS." *Surf Sci Spectra*, 4, 227–231.

Dineshram, R., Subasri, R., Somaraju, K. R. C., Jayaraj, K., Vedaprakash, L., Ratnam, K., Joshi, S. V., and Venkatesan, R. (2009). "Biofouling studies on nanoparticle-based metal oxide coatings on glass coupons exposed to marine environment." *Colloids Surf B Biointerfaces*, 74, 75–83.

Do, J. S., Yu, S. H., and Cheng, S. F. (2003). "Thick-film nickel–metal-hydride battery based on porous ceramic substrates." *J Power Sources*, 117, 203–211.

Dojahn, J. G., Wentworth, W. E., and Stearns, S. D. (2001). "Characterization of formaldehyde by gas chromatography using multiple pulsed-discharge photoionization detectors and a flame ionization detector." *J Chromatogr Sci*, 39, 54–58.

Dollen, P. V., and Barnett, S. (2005). "A study of screen printed yttria-stabilized zirconia layers for solid oxide fuel cells." *J Am Ceram Soc*, 88, 3361–3368.

Duta, M., Predoana, L., Calderon-Moreno, J. M., Preda, S., Anastasescu, M., Marin, A., Dascalu, I., Chesler, P., Hornoiu, C., Zaharescu, M., Osiceanu, P., and Gartner, M. (2016). "Nb-doped TiO$_2$ sol–gel films for CO sensing applications." *Mater Sci Semicond Process*, 42, 397–404.

Eadi, S. B., Kim, S., Jeong, S. W., and Jeon, H. W. (2017). "Novel preparation of Fe doped TiO$_2$ nanoparticles and their application for gas sensor and photocatalytic degradation." *Adv Mater Sci Eng*, 2017, 1–7.

Elshof, J. E. T., Abadal, C. R., Sekulić, J., Chowdhury, S. R., and Blank, D. H. A. (2003). "Transport mechanisms of water and organic solvents through microporous silica in the pervaporation of binary liquids." *Microporous Mesoporous Mater*, 65, 197–208.

Enriquez-Carrejo, J. L., Ramos, M. A., Mireles-Jr-Garcia, J., and Hurtado-Macias, A. (2016). "Nano-mechanical and structural study of WO$_3$ thin films." *Thin Solid Films*, 606, 148–154.

Er, I. K., Çağırtekin, A. O., Ajjaq, A., Yıldırım, M. A., Ateş, A., and Acar, S. (2021). "Complex electrical impedance and modulus characterizations of ZnO:Sn thin films in a wide temperature range." *J Mater Sci Mater Electron*, 32, 13594–13609.

Eranna, G., Joshi, B. C., Runthala, D. P., and Gupta, R. P. (2004). "Oxide materials for development of integrated gas sensors - A comprehensive review." *Crit Rev Solid State Mater Sci*, 29, 111–188.

Eshaghi, A., Hakimi, M. J., and Zali, A. (2015). "Fabrication of titanium zinc oxide (TZO) sol-gel derived nanostructured thin film and investigation of its optical and electrical properties." *Optik (Stuttg)*, 126, 5610–5613.

Faddoul, R., Reverdy-Bruas, N., and Blayo, A. (2012a). "Formulation and screen printing of water based conductive flake silver pastes onto green ceramic tapes for electronic applications." *Mater Sci Eng B*, 177, 1053–1066.

Faddoul, R., Reverdy-Bruas, N., and Bourel, J. (2012b). "Silver content effect on rheological and electrical properties of silver pastes." *J Mater Sci Mater in Electron*, 23, 1415–1426.

Fallah, M., Zamani-Meymian, M. R., Rahimi, R., and Rabbani, M. (2014). "Effect of annealing treatment on electrical and optical properties of Nb doped TiO_2 thin films as a TCO prepared by sol-gel spin coating method." *Appl Surf Sci*, 316, 456–462.

Fan, F., and Stebe, K. J. (2005). "Size-selective deposition and sorting of lyophilic colloidal particles on surfaces of patterned wettability." *Langmuir*, 21, 1149–1152.

Fan, F., Tang, P., Wang, Y., Feng, Y., Chen, A., Luo, R., and Li, D. (2015). "Facile synthesis and gas sensing properties of tubular hierarchical ZnO self-assembled by porous nanosheets." *Sens Actuators B Chem*, 215, 231–240.

Feng, L., Li, S., Li, Y., Li, H., Zhang, L., Zhai, J., Song, Y., Liu, B., Jiang, L., and Zhu, D. (2002). "Super-hydrophobic surfaces: from natural to artificial." *Adv Mater*, 14, 1857–1860.

Feng, Z., Zhang, L., Chen, W., Peng, Z., and Li, Y. (2020). "A strategy for supportless sensors: fluorine doped TiO_2 nanosheets directly grown onto Ti foam enabling highly sensitive detection toward acetone." *Sens Actuators B Chem*, 322, 128633.

Fomekong, R. L., Kelm, K., and Saruhan, B. (2020). "High-temperature hydrogen sensing performance of Ni-doped TiO_2 prepared by co-precipitation method." *Sensors,* 20, 5992.

Gakhar, T., and Hazra, A. (2020). "Oxygen vacancy modulation of titania nanotubes by cathodic polarization and chemical reduction routes for efficient detection of volatile organic compounds." *Nanoscale*, 12, 9082–9093.

Gan, L., Wu, C., Tan, Y., Chi, B., Pu, J., and Jian, L. (2014). "Oxygen sensing performance of Nb-doped TiO_2 thin film with porous structure." *J Alloys Compd*, 585, 729–733.

Ganesh, R. S., Navaneethan, M., Mani, G. K., Ponnusamy, S., Tsuchiya, K., Muthamizhchelvan, C., Kawasaki, S., and Hayakawa, Y. (2017). "Influence of Al

doping on the structural, morphological, optical, and gas sensing properties of ZnO nanorods." *J Alloys Compd*, 698, 555–564.

Gao, X., Li, Y., Zeng, W., Zhang, C., and Wei, Y. (2017). "Hydrothermal synthesis of agglomerating TiO_2 nanoflowers and its gas sensing." *J Mater Sci Mater in Electron*, 28, 18781–18786.

Ge, H. L., Wang, X. Q., Han, Y. B., Jin, H. X., Jin, D. F., Zeng, Y. X., and Peng, X. L. (2022). "Enhanced formaldehyde gas-sensing response based on indium oxide nanowires doped with same-valence metal cations." *Mater Adv*, 3, 7043–7052.

Ge, W., Jiao, S., Chang, Z., He, X., and Li, Y. (2020). "Ultrafast response and high selectivity toward acetone vapor using hierarchical structured TiO_2 nanosheets." *ACS Appl Mater Interfaces*, 12, 13200–13207.

Gönüllü, Y., Haidry, A. A., and Saruhan, B. (2015). "Nanotubular Cr-doped TiO_2 for use as high-temperature NO_2 gas sensor." *Sens Actuators B Chem*, 217, 78–87.

Gopala Krishnan, V., Elango, P., and Ganesan, V. (2018). "Surface characterization and gas sensing performance of yttrium doped TiO_2 nanofilms prepared by automated nebulizer spray pyrolysis (ANSP)." *J Mater Sci Mater in Electron*, 29, 392–401.

Greenwood, O. D., Moulzolf, S. C., Blau, P. J., and Lad, R. J. (1999). "The influence of microstructure on tribological properties of WO_3 thin films." *Wear*, 232, 84–90.

Grilli, M. L. (2020). "Metal oxides." *Metals*, 10, 1–3.

Guo, L., Arafune, H., and Teramae, N. (2013). "Synthesis of mesoporous metal oxide by the thermal decomposition of oxalate precursor." *Langmuir*, 29, 4404–4412.

Hadjarab, B., Bouguelia, A., Benchettara, A., and Trari, M. (2008). "The transport and photo electrochemical properties of La-doped stannate $BaSnO_3$." *J Alloys Compd*, 461, 360–366.

Hai, Z., Wei, Z., Xue, C., Xu, H., and Verpoort, F. (2019). "Nanostructured tungsten oxide thin film devices: from optoelectronics and ionics to iontronics." *J Mater Chem C Mater*, 7, 12968–12990.

Han, J., Kong, D., Zhou, W., Gao, Y., Gao, Y., Liu, G., Liu, F., Wang, C., Sun, P., and Lu, G. (2022). "Variable dimensional structure and interface design of In_2O_3/rGO nanocomposites with oxygen vacancy for enhancing NO_2 sensing performance." *Sens Actuators B Chem*, 371, 132596.

Han, N., Chai, L., Wang, Q., Tian, Y., Deng, P., and Chen, Y. (2010). "Evaluating the doping effect of Fe, Ti and Sn on gas sensing property of ZnO." *Sens Actuators B Chem*, 147, 525–530.

Hasan, M. M., Haseeb, A. S. M. A., and Masjuki, H. H. (2012). "Structural and mechanical properties of nanostructured tungsten oxide thin films." *Surf Eng*, 28, 778–785.

Hasan, M. M., Haseeb, A. S. M. A., Masjuki, H. H., and Saidur, R. (2010). "Adhesion and wear behavior of nanostructured titanium oxide thin films." *Int J Mech Mater Eng*, 5, 5–10.

Haseeb, A. S. M. A., Hasan, M. M., and Masjuki, H. H. (2010). "Structural and mechanical properties of nanostructured TiO_2 thin films deposited by RF sputtering." *Surf Coat Technol*, 205, 338–344.

Hennek, J. W., Smith, J., Yan, A., Kim, M. G., Zhao, W., Dravid, V. P., Facchetti, A., and Marks, T. J. (2013). "Oxygen 'getter' effects on microstructure and carrier transport in low temperature combustion-processed a-InXZnO (X = Ga, Sc, Y, La) transistors." *J Am Chem Soc*, 135, 10729–10741.

Hodes, G. (2007). "Semiconductor and ceramic nanoparticle films deposited by chemical bath deposition." *Phys Chem Chem Phys*, 9, 2181–2196.

Holzwarth, U., and Gibson, N. (2011). "The Scherrer equation versus the 'Debye-Scherrer equation.'" *Nat Nanotechnol,* 6, 534.

Hsu, C. L., Gao, Y. D., Chen, Y. S., and Hsueh, T. J. (2014). "Vertical Ti doped ZnO nanorods based on ethanol gas sensor prepared on glass by furnace system with hotwire assistance." *Sens Actuators B Chem*, 192, 550–557.

Huang, C., Wang, X., Liu, X., Tian, M., and Zhang, T. (2016). "Extensive analysis of the formation mechanism of $BaSnO_3$ by solid-state reaction between $BaCO_3$ and SnO_2." *J Eur Ceram Soc*, 36, 583–592.

Hui, B., Wu, D., Huang, Q., Cai, L., Li, G., Li, J., and Zhao, G. (2015). "Photoresponsive and wetting performances of sheet-like nanostructures of tungsten trioxide thin films grown on wood surfaces." *RSC Adv*, 5, 73566–73574.

Izu, N., Shin, W., Matsubara, I., and Murayama, N. (2003). "The effects of the particle size and crystallite size on the response time for resistive oxygen gas sensor using cerium oxide thick film." *Sens Actuators B Chem*, 94, 222–227.

Jaim, H. M. I., Lee, S., Zhang, X., and Takeuchi, I. (2017). "Stability of the oxygen vacancy induced conductivity in $BaSnO_3$ thin films on $SrTiO_3$." *Appl Phys Lett*, 111, 1–6.

James, K. K., Krishnaprasad, P. S., Hasna, K., and Jayaraj, M. K. (2015). "Structural and optical properties of La-doped BaSnO$_3$ thin films grown by PLD." *J Phys Chem Solids*, 76, 64–69.

Jaworski, R., Pawlowski, L., Roudet, F., Kozerski, S., and Petit, F. (2008). "Characterization of mechanical properties of suspension plasma sprayed TiO$_2$ coatings using scratch test." *Surf Coat Technol*, 202, 2644–2653.

Jiang, T., and Guo, Z. (2016). "Robust superhydrophobic tungsten oxide coatings with photochromism and UV durability properties." *Appl Surf Sci*, 387, 412–418.

Jing, L., Xu, Z., Shang, J., Sun, X., Cai, W., and Guo, H. (2002). "The preparation and characterization of ZnO ultrafine particles.' *Mater Sci Eng A*, 332, 356–361.

Jönsson, U., Olofsson, G., Malmqvist, M., and Rönnberg, I. (1985). "Chemical vapour deposition of silanes." *Thin Solid Films*, 124, 117–123.

Joseph, A. M., Nagendra, B., Gowd, E. B., and Surendran, K. P. (2016). "Screen-printable electronic ink of ultrathin boron nitride nanosheets." *ACS Omega*, 1, 1220–1228.

Joshi, N., da Silva, L. F., Shimizu, F. M., Mastelaro, V. R., M'Peko, J. C., Lin, L., and Oliveira Jr, O. N. (2019). "UV-assisted chemiresistors made with gold-modified ZnO nanorods to detect ozone gas at room temperature." *Microchim Acta*, 186, 1–9.

Kakihana, M. (1996). "'Sol-Gel' preparation of high temperature superconducting oxides." *J Solgel Sci Technol*, 6, 7–55.

Kakihana, M., and Yoshimura, M. (1999). "Synthesis and characteristics of complex multicomponent oxides prepared by polymer complex method." *Bull Chem Soc Jpn*, 72, 1427–1443.

Kakihana, M., Yoshimura, M., Mazaki, H., Yasuoka, H., and Börjesson, L. (1992). "Polymerized complex synthesis and intergranular coupling of Bi-Pb-Sr-Ca-Cu-O superconductors characterized by complex magnetic susceptibility." *J Appl Phys*, 71, 1–8.

Kaleji, B. K., Sarraf-Mamoory, R., and Fujishima, A. (2012). "Influence of Nb dopant on the structural and optical properties of nanocrystalline TiO$_2$ thin films." *Mater Chem Phys*, 132, 210–215.

Katoch, A., Sun, G. J., Choi, S. W., Byun, J. H., and Kim, S. S. (2013). "Competitive influence of grain size and crystallinity on gas sensing performances of ZnO nanofibers." *Sens Actuators B Chem*, 185, 411–416.

Ke, Q., Li, G., Liu, Y., He, T., and Li, X. M. (2010). "Formation of superhydrophobic polymerized n-octadecylsiloxane nanosheets." *Langmuir*, 26, 3579–3584.

Kim, H. J., Kim, J., Kim, T. H., Lee, W. J., Jeon, B. G., Park, J. Y., Choi, W. S., Jeong, D. W., Lee, S. H., Yu, J., Noh, T. W., and Kim, K. H. (2013). "Indications of strong neutral impurity scattering in $Ba(Sn,Sb)O_3$ single crystals." *Phys Rev B Condens Matter Mater Phys*, 88, 125204.

Kim, H. J., Kim, U., Kim, H. M., Kim, T. H., Mun, H. S., Jeon, B. G., Hong, K. T., Lee, W. J., Ju, C., Kimy, K. H., and Char, K. (2012). "High mobility in a stable transparent perovskite oxide." *Appl Phys Express*, 5, 1–3.

Kim, M. G., Kanatzidis, M. G., Facchetti, A., and Marks, T. J. (2011). "Low-temperature fabrication of high-performance metal oxide thin-film electronics via combustion processing." *Nat Mater*, 10, 382–388.

Kolodziejczak-Radzimska, A., and Jesionowski, T. (2014). "Zinc oxide–from synthesis to application: a review." *Materials*, 7, 2833–2881.

Korotcenkov, G. (2007). "Metal oxides for solid-state gas sensors: What determines our choice?" *Mater Sci Eng B*, 139, 1–23.

Kozerski, S., Łatka, L., Pawlowski, L., Cernuschi, F., Petit, F., Pierlot, C., Podlesak, H., and Laval, J. P. (2011). "Preliminary study on suspension plasma sprayed $ZrO_2 + 8$ wt.% Y_2O_3 coatings." *J Eur Ceram Soc*, 31, 2089–2098.

Krishnan, M., Sivanandham, V., Hans-Uwe, D., Murugaiah, S. G., Seeni, P., Gopalan, S., and Rathinam, A. J. (2015). "Antifouling assessments on biogenic nanoparticles: A field study from polluted offshore platform." *Mar Pollut Bull*, 101, 816–825.

Krishnan, M., Subramanian, H., Dahms, H., Seeni, P., Gopalan, S., Mahalingam, A., and Rathinam, A. J. (2018). "Biogenic corrosion inhibitor on mild steel protection in concentrated HCl medium." *Sci Rep*, 8, 1–16.

Kulandaisamy, A. J., Reddy, J. R., Srinivasan, P., Babu, K. J., Mani, G. K., Shankar, P., and Rayappan, J. B. B. (2016). "Room temperature ammonia sensing properties of ZnO thin films grown by spray pyrolysis: Effect of Mg doping." *J Alloys Compd*, 688, 422–429.

Kulkarni, S. C., and Borse, R. Y. (2011). "Study on gas sensing performance of In_2O_3 thick film resistors prepared by screen printing technique." *Sens Transducers*, 125, 194–204.

Kumar, K. D. A., Valanarasu, S., Ponraj, J. S., Fernandes, B. J., Shkir, M., AlFaify, S., Murahari, P., and Ramesh, K. (2020). "Effect of Er doping on the ammonia sensing

properties of ZnO thin films prepared by a nebulizer spray technique." *J Phys Chem of Solids*, 144, 109513.

Kwak, G., Lee, M., and Yong, K. (2010). "Chemically modified superhydrophobic WO$_x$ nanowire arrays and UV photopatterning." *Langmuir*, 26, 9964–9967.

Kwoka, M., Galstyan, V., Comini, E., and Szuber, J. (2017). "Pure and highly Nb-doped titanium dioxide nanotubular arrays: Characterization of local surface properties." *Nanomaterials*, 7, 1–13.

Łatka, L., Cattini, A., Chicot, D., Pawłowski, L., Kozerski, S., Petit, F., and Denoirjean, A. (2013). "Mechanical properties of yttria- and ceria-stabilized zirconia coatings obtained by suspension plasma spraying." *J Therm Spray Technol*, 22, 125–130.

Łatka, L., Szala, M., Macek, W., and Branco, R. (2020). "Mechanical properties and sliding wear resistance of suspension plasma sprayed YSZ coatings." *J Adv Sci Technol Res*, 14, 307–314.

Lee, M. K., Shih, C. M., Fang, S. C., Tu, H. F., and Ho, C. L. (2007). "Preparation of niobium-doped titanium oxide film by liquid phase deposition." *Jpn J of Appl Phys*, 46, 1653–1655.

Li, C. F., Hsu, C. Y., and Li, Y. Y. (2014). "NH$_3$ sensing properties of ZnO thin films prepared via sol–gel method." *J Alloys Compd*, 606, 27–31.

Li, Z., Chen, H., and Liu, W. (2018). "Full-spectrum photocatalytic activity of ZnO/CuO/ZnFe$_2$O$_4$ nanocomposite as a photofenton-like catalyst." *Catalysts*, 8, 557.

Lin, J. Y., Chen, Z. X., He, X. L., and Xie, W. M. (2017). "Detection of H$_2$S at room temperature using ZnO sensors based on hall effect." *Int. J. Electrochem. Sci*, 12, 6465–6476.

Lin, S. S., Huang, J. L., and Šjgalik, P. (2005). "The properties of Ti-doped ZnO films deposited by simultaneous RF and DC magnetron sputtering." *Surf Coat Technol*, 191, 286–292.

Liu, D., Lei, W., Qin, S., Hou, L., Liu, Z., Cui, Q., and Chen, Y. (2013a). "Large-scale synthesis of hexagonal corundum-type In$_2$O$_3$ by ball milling with enhanced lithium storage capabilities." *J Mater Chem A Mater*, 1, 5274–5278.

Liu, G., Liu, A., Zhu, H., Shin, B., Fortunato, E., Martins, R., Wang, Y., and Shan, F. (2015). "Low-temperature, nontoxic water-induced metal-oxide thin films and their application in thin-film transistors." *Adv Funct Mater*, 25, 2564–2572.

Liu, H. R., Yang, J. H., Xiang, H. J., Gong, X. G., and Wei, S. H. (2013b). "Origin of the superior conductivity of perovskite Ba(Sr)SnO$_3$." *Appl Phys Lett*, 102, 112109.

Liu, J., Han, S., Li, J., and Lin, J. (2014). "Modification of tungsten trioxide with ionic liquid for enhanced photocatalytic performance." *RSC Adv*, 4, 37556–37562.

Liu, J., Ma, S. Y., Huang, X. L., Ma, L. G., Li, F. M., Yang, F. C., Zhao, Q., and Zhang, X. L. (2012). "Effects of Ti-doped concentration on the microstructures and optical properties of ZnO thin films." *Superlattices Microstruct,* 52, 765–773.

Liu, J., Zhao, X., Duan, L., Cao, M., Sun, H., Shao, J., Chen, S., Xie, H., Chang, X., and Chen, C. (2011). "Influence of annealing process on conductive properties of Nb-doped TiO_2 polycrystalline films prepared by sol-gel method." *Appl Surf Sci*, 257, 10156–10160.

Lu, J. J. (2007). "Conductivity enhancement and semiconductor – metal transition in Ti-doped ZnO films." *Opt Mater*, 29, 1548–1552.

Lu, W., and Schmidt, H. (2008). "Lyothermal synthesis of nanocrystalline $BaSnO_3$ powders." *Ceram Int*, 34, 645–649.

Lugscheider, E., Bärwulf, S., and Barimani, C. (1999). "Properties of tungsten and vanadium oxides deposited by MSIP – PVD process for self-lubricating applications." *Surf Coat Technol*, 121, 458–464.

Lugscheider, E., Knotek, O., Bärwulf, S., and Bobzin, K. (2001). "Characteristic curves of voltage and current, phase generation and properties of tungsten- and vanadium-oxides deposited by reactive d.c.-MSIP-PVD-process for self-lubricating applications." *Surf Coat Technol*, 142–144, 137–142.

Lugscheider, E., Knotek, O., Bobzin, K., and Bärwulf, S. (2000). "Tribological properties, phase generation and high temperature phase stability of tungsten- and vanadium-oxides deposited by reactive MSIP-PVD process for innovative lubrication applications." *Surf Coat Technol*, 133–134, 362–368.

Luo, B. C., Cao, X. S., Jin, K. X., and Chen, C. L. (2016). "Determination of the effective mass and nanoscale electrical transport in La-doped $BaSnO_3$ thin films." *Curr Appl Phys*, 16, 20–23.

Luo, B. C., Zhang, J., Wang, J., and Ran, P. X. (2015). "Structural, electrical and optical properties of lanthanum-doped barium stannate." *Ceram Int*, 41, 2668–2672.

Ma, Z. H., Yu, R. T., and Song, J. M. (2020). "Facile synthesis of Pr-doped In_2O_3 nanoparticles and their high gas sensing performance for ethanol." *Sens Actuators B Chem*, 305, 127377.

MacHado, G. S., Arízaga, G. G. C., Wypych, F., and Nakagaki, S. (2010). "Immobilization of anionic metalloporphyrins on zinc hydroxide nitrate and study of an unusual catalytic activity." *J Catal*, 274, 130–141.

Maillé, L., Sant, C., Aubert, P., and Garnier, P. (2005). "Morphological and mechanical properties study of $[WO_3/W]_n$ nanoscale multilayers." *Thin Solid Films*, 479, 201–206.

Mamun, M. A., Zhang, K., Baumgart, H., and Elmustafa, A. A. (2015). "Nanomechanical and morphological characterization of tungsten trioxide (WO_3) thin films grown by atomic layer deposition." *ECS J Solid State Sci and Technol*, 4, 398–401.

Mani, G. K., and Rayappan, J. B. B. (2015a). "A highly selective and wide range ammonia sensor—Nanostructured ZnO:Co thin film." *Mater Sci Eng B*, 191, 41–50.

Mani, G. K., and Rayappan, J. B. B. (2015b). "Facile synthesis of ZnO nanostructures by spray pyrolysis technique and its application as highly selective H_2S sensor." *Mater Lett*, 158, 373–376.

Manjunath, G., Nagaraju, P., and Mandal, S. (2020). "A comparative study on enhancer and inhibitor of glycine–nitrate combustion ZnO screen-printed sensor: detection of low concentration ammonia at room temperature." *J Mater Sci Mater Electron*, 31, 10366–10380.

Manjunath, G., Nagaraju, P., and Mandal, S. (2021a). "Ultra-sensitive clogging free combustible molecular precursor-based screen-printed ZnO sensors: a detection of ammonia and formaldehyde breath markers." *J Mater Sci Mater Electron*, 32 5713–5728.

Manjunath, G., Vardhan, R. V., Praveen, L. L., Nagaraju, P., and Mandal, S. (2021b). "Room-temperature detection of ammonia and formaldehyde gases by $La_xBa_{1-x}SnO_{3-\delta}$ ($x = 0$ and 0.05) screen printed sensors: effect of ceria and ruthenate sensitization." *Appl Phys A Mater Sci Process*, 127, 1–15.

Manohar, S., Mirzaei, A., Woo, H., and Sub, S. (2020). "Recent advances in energy-saving chemiresistive gas sensors: A review." *Nano Energy*, 79, 1–25.

Manole, A. V., Dobromir, M., Gîrtan, M., Mallet, R., Rusu, G., and Luca, D. (2013). "Optical properties of Nb-doped TiO_2 thin films prepared by sol-gel method." *Ceram Int*, 39, 4771–4776.

Mardare, C. C., and Hassel, A. W. (2019). "Review on the versatility of tungsten oxide coatings." *Phys Status Solidi A*, 216, 1–16.

Marezio, M. (1966). "Refinement of the crystal structure of In_2O_3 at two wavelengths." *Acta Crystallogr*, 20, 723–728.

Maslik, J., Kuritka, I., Urbanek, P., Krcmar, P., Suly, P., Masar, M., and Machovsky, M. (2018). "Water-based indium tin oxide nanoparticle ink for printed toluene vapours sensor operating at room temperature." *Sensors*, 18, 3246.

Mbarek, H., Saadoun, M., and Bessaïs, B. (2006). "Screen-printed Tin-doped indium oxide (ITO) films for NH_3 gas sensing." *Mater Sci Eng C*, 26, 500–504.

Mbarek, H., Saadoun, M., and Bessais, B. (2007). "Porous screen printed indium tin oxide (ITO) for NO_x gas sensing." *Phys Status Solidi C*, 4, 1903–1907.

Mehmood, A., Long, X., Haidry, A. A., and Zhang, X. (2020). "Trends in sputter deposited tungsten oxide structures for electrochromic applications: A review." *Ceram Int*, 46, 23295–23313.

Mhlongo, G. H., Shingange, K., Tshabalala, Z. P., Dhonge, B. P., Mahmoud, F. A., Mwakikunga, B. W., and Motaung, D. E. (2016). "Room temperature ferromagnetism and gas sensing in ZnO nanostructures: Influence of intrinsic defects and Mn, Co, Cu doping." *Appl Surf Sci*, 390, 804–815.

Michel, B., Bernard, A., Bietsch, A., Delamarche, E., Geissler, M., Juncker, D., Kind, H., Renault, J. P., Rothuizen, H., Schmid, H., Schmidt-Winkel, P., Stutz, R., and Wolf, H. (2001). "Printing meets lithography: Soft approaches to high-resolution printing." *IBM J Res Dev*, 45, 697–719.

Miller, D. R., Akbar, S. A., and Morris, P. A. (2014). "Nanoscale metal oxide-based heterojunctions for gas sensing: A review." *Sens Actuators B Chem*, 204, 250–272.

Miller, R. J., Lenihan, H. S., Muller, E. B., Tseng, N., Hanna, S. K., and Keller, A. A. (2010). "Impacts of metal oxide nanoparticles on marine phytoplankton." *Environ Sci Technol*, 44, 7329–7334.

Misra, D., Shari, S. M., Mukhopadhyay, S., and Chatterjee, S. (2018). "Analysis of instrumented scratch hardness and fracture toughness properties of laser surface alloyed tribological coatings." *Ceram Int*, 44, 4248–4255.

Mitzi. D. B. (2009). "Solution processing of inorganic materials." *John Wiley & Sons, Inc Hoboken NJ,* 1, 1–512.

Mizoguchi, H., Chen, P., Boolchand, P., Ksenofontov, V., Felser, C., Barnes, P. W., and Woodward, P. M. (2013). "Electrical and optical properties of Sb-doped $BaSnO_3$." *Chem Mater*, 25, 3858–3866.

Montazeri, A., and Jamali-Sheini, F. (2017). "Enhanced ethanol gas-sensing performance of Pb-doped In_2O_3 nanostructures prepared by sonochemical method." *Sens Actuators B Chem*, 242, 778–791.

Moon, H. G., Shim, Y. S., Kim, D. H., Jeong, H. Y., Jeong, M., Jung, J. Y., Han, S. M., Kim, J. K., Kim, J. S., Park, H. H., Lee, J. H., Tuller, H. L., Yoon, S. J., and Jang, H. W. (2012). "Self-activated ultrahigh chemosensitivity of oxide thin film nanostructures for transparent sensors." *Sci Rep*, 2, 1–7.

Mooney, J. B., and Radding, S. B. (1982). "Spray pyrolysis processing." *Ann Rev Mater Sci*, 12, 81–101.

Mücke, R., Büchler, O., Menzler, N. H., Lindl, B., Vaßen, R., and Buchkremer, H. P. (2014). "High-precision green densities of thick films and their correlation with powder, ink, and film properties." *J Eur Ceram Soc*, 34, 3897–3916.

Mundev, D., and Turyan, I. (1996). "Applications of self-assembled monolayers in elec troanalytical chemistry." *Electroanalysis*, 8, 207–213.

Naderi, M., Zargar Shoushtari, M., Ahmadi, M., and Kazeminezhad, I. (2017). "Effect of Ti-doping on optical and structural properties of ZnO films grown by spin coating method." *Inorg Nano-Met Chem*, 47, 1668–1674.

Narendrudu, T., Suresh, S., Kumar, A. S., Rao, M. V. S., Rao, P. S., and Rao, D. K. (2016). "Spectroscopic and dielectric investigations on the role of molybdenum ions in lead niobium germanosilicate glasses." *J Non Cryst Solids*, 442, 44–55.

Navale, S. T., Yang, Z. B., Liu, C., Cao, P. J., Patil, V. B., Ramgir, N. S., Mane, R. S., and Stadler, F. J. (2018). "Enhanced acetone sensing properties of titanium dioxide nanoparticles with a sub-ppm detection limit." *Sens Actuators B Chem*, 255, 1701–1710.

Neagu, R., Perednis, D., Princivalle, A., and Djurado, E. (2006). "Zirconia coatings deposited by electrostatic spray deposition. Influence of the process parameters." *Surf Coat Technol*, 200, 6815–6820.

Nithya, N., Bhoopathi, G., Magesh, G., and Balasundaram, O. N. (2019). "Synthesis and characterization of yttrium doped titania nanoparticles for gas sensing activity." *Mater Sci Semicond Process*, 99, 14–22.

Ok, K. C., Park, J., Lee, J. H., Ahn, B. D, Lee, J. H., Chung, K. B., and Park, J. S. (2012). "Semiconducting behavior of niobium-doped titanium oxide in the amorphous state." *Appl Phys Lett*, 100, 1–3.

Olav, T., Sunde, L., Grande, T., and Einarsrud, M. (2016). "Handbook of Sol-Gel Science and Technology." *SINTEF*, 1–30.

Ong, C. W., Wong, H. Y., Pang, G. K. H., Baba-Kishi, K. Z., and Choy, C. L. (2001). "Relationship between the microstructure and nanoindentation hardness of thermally evaporated and magnetron-sputtered electrochromic tungsten oxide films." *J Mater Res*, 16, 1541–1548.

Ozkan, E., Lee, S. H., Tracy, C. E., Pitts, J. R., and Deb, S. K. (2003). "Comparison of electrochromic amorphous and crystalline tungsten oxide films." *Sol Energy Mater Sol Cells*, 79, 439–448.

Pan, J., Tonkay, G. L., and Quintero, A. (2012). "Screen printing process design of experiments for fine line printing of thick film ceramic substrates.", 9, 203–213.

Pandeeswari, R., and Jeyaprakash, B. G. (2014). "High sensing response of β-Ga_2O_3 thin film towards ammonia vapours: Influencing factors at room temperature." *Sens Actuators B Chem*, 195, 206–214.

Park, S., Sun, G. J., Jin, C., Kim, H. W., Lee, S., and Lee, C. (2016). "Synergistic effects of a combination of Cr_2O_3-functionalization and UV-irradiation techniques on the ethanol gas sensing performance of ZnO nanorod gas sensors." *ACS Appl Mater Interfaces*, 8, 2805–2811.

Parreira, N. M. G., Carvalho, N. J. M., and Cavaleiro, A. (2006). "Synthesis, structural and mechanical characterization of sputtered tungsten oxide coatings." *Thin Solid Films*, 510, 191–196.

Parreira, N. M. G., Polcar, T., and Cavaleiro, A. (2007). "Characterization of W-O coatings deposited by magnetron sputtering with reactive gas pulsing." *Surf Coat Technol*, 201, 5481–5486.

Pasquarelli, R. M., Ginley, D. S., and O'Hayre, R. (2011). "Solution processing of transparent conductors: From flask to film." *Chem Soc Rev*, 40, 5406–5441.

Patidar, R., Burkitt, D., Hooper, K., Richards, D., and Watson, T. (2020). "Slot-die coating of perovskite solar cells: An overview." *Mater Today Commun*, 22, 100808.

Patil, K. C., Hegde, M. S., Rattan, T., and Aruna, S. T. (2008). "Chemistry of Nanocrystalline Oxide Materials." 9.

Patil, P. S. (1999). "Versatility of chemical spray pyrolysis technique." *Mater Chem Phys*, 59, 185-198.

Pechini, M. P. (1967). "Method of preparing lead and alkaline earth titanates and niobates and coating method using the same to form a capacitor." *Google Patents*, 8.

Perednis, D., and Gauckler, L. J. (2005). "Thin film deposition using spray pyrolysis." *J Electroceram*, 14, 103–111.

Phair, J. W., Lundberg, M., and Kaiser, A. (2009). "Leveling and thixotropic characteristics of concentrated zirconia inks for screen-printing." *Rheol Acta*, 48, 121–133.

Pierre, A. C. (1998). "New types of sol-gel derived materials." *Introduction to Sol-Gel Processing*, 251–278.

Pistone, A., Scolaro, C., and Visco, A. (2021). "Mechanical properties of protective coatings against marine fouling: A review." *Polymers*,13, 173.

Polcar, T., and Cavaleiro, A. (2010). "Structure, mechanical properties and tribology of W-N and W-O coatings." *Int J Refract Metals Hard Mater*, 28, 15–22.

Polcar, T., Parreira, N. M. G., and Cavaleiro, A. Ã. (2007). "Tungsten oxide with different oxygen contents: Sliding properties." *Vacuum*, 81, 1426–1429.

Poloju, M., Jayababu, N., and Ramana Reddy, M. V. (2018). "Improved gas sensing performance of Al doped ZnO/CuO nanocomposite based ammonia gas sensor." *Mater Sci Eng B*, 227, 61–67.

Pomerantz, M., Segmüller, A., Netzer, L., and Sagiv, J. (1985). "Coverage of Si substrates by self-assembling monolayers and multilayers as measured by IR, wettability and X-ray diffraction." *Thin Solid Films*, 132, 153–162.

Postiglione, W. M., and Leighton, C. (2017). "Mobility optimization in $La_xBa_{1-x}SnO_3$ thin films deposited via high pressure oxygen sputtering." 1–142.

Pujar, P., Gandla, S., Gupta, D., Kim, S., and Kim, M. G. (2020). "Trends in low-temperature combustion derived thin films for solution-processed electronics." *Adv Electron Mater*, 2000464, 1–25.

Pujar, P., Gandla, S., Singh, M., Gupta, B., Tarafder, K., Gupta, D., Noh, Y-Y., and Mandal, S. (2017). "Development of low temperature stoichiometric solution combustion derived transparent conductive ternary zinc tin co-doped indium oxide electrodes." *RSC Adv*, 7, 48253–48262.

Pujar, P., Vardhan, R. V., Gupta, D., and Mandal, S. (2018). "A balancing between super transparency and conductivity of solution combustion derived titanium doped indium oxide: Effect of charge carrier density and mobility." *Thin Solid Films*, 660, 267–275.

Pushpamalar, V., Langford, S. J., Ahmad, M., and Lim, Y. Y. (2006). "Optimization of reaction conditions for preparing carboxymethyl cellulose from sago waste." *Carbohydr Polym*, 64, 312–318.

Qi, J., Zhang, H., Lu, S., Li, X., Xu, M., and Zhang, Y. (2015). "High performance indium-doped ZnO gas sensor." *J Nanomater*, 16, 74.

Ramana, C. V., Battu, A. K., Dubey, P., and Lopez, G. A. (2020). "Phase-control-enabled enhancement in hydrophilicity and mechanical toughness in nanocrystalline tungsten oxide films for energy-related applications." *ACS Appl Nano Mater*, 3, 3264–3274.

Rawal, I. (2014). "Facial synthesis of hexagonal metal oxide nanoparticles for low temperature ammonia gas sensing applications." *RSC Adv*, 5, 4135–4142.

Reddy, C. V. G., Manorama, S. V, and Rao, V. J. (2001). "Preparation and characterization of barium stannate: application as a liquefied petroleum gas sensor." *J Mater Sci Mater Electron*, 12, 137–142.

Reddy, I. N., Reddy, C. V., Cho, M., Shim, J., and Kim, D. (2017). "Structural, optical and XPS study of thermal evaporated In_2O_3 thin films." *Mater Res Express*, 4, 1–12.

Regragui, M., Addou, M., Idrissi, B. E, Bernède, J. C., Outzourhit, A., and Ec-chamikh, E. (2001). "Effect of the annealing time on the physico-chemical properties of WO_3 thin films prepared by spray pyrolysis." *Mater Chem Phys*, 70, 84–89.

Regragui, M., Addou, M., Outzourhit, A., Bernéde, J. C., Idrissi, E. E., Benseddik, E., and Kachouane, A. (2000). "Preparation and characterization of pyrolytic spray deposited electrochromic tungsten trioxide films." *Thin Solid Films*, 358, 40–45.

Reynolds, T. D., Kalpathy, S. K., Kumar, S., and Francis, L. F. (2010). "Dip coating of charged colloidal suspensions onto substrates with patterned wettability: Coating regime maps." *J Colloid Interface Sci*, 352, 202–210.

Riemer, D. E. (1989). "The theoretical fundamentals of the screen printing process." *Microelectron Int*, 6, 8–17.

Rondinelli, J. M., May, S. J., and Freeland, J. W. (2012). "Control of octahedral connectivity in perovskite oxide heterostructures: An emerging route to multifunctional materials discovery." *MRS Bull*, 37, 261–270.

Rougier, A., Portemer, F., Quede, A., and Marssi, M. el. (1999). "Characterization of pulsed laser deposited WO_3 thin films for electrochromic devices." *Appl Surf Sci*, 153, 1–9.

Ruffolo, S. A., Macchia, A., Russa, M. F. L., Mazza, L., Urzì, C., Leo, F. D., Barberio, M., and Crisci, G. M. (2013). "Marine antifouling for underwater archaeological sites: TiO$_2$ and Ag-Doped TiO$_2$." *Int J Photoenergy*, 2013, 1–7.

Sagiv, J. (1980). "Organized Monolayers by Adsorption, 1. Formation and Structure of Oleophobic Mixed Monolayers on Solid Surfaces." *J Am Chem Soc*, 399, 92–98.

Sahu, N., Parija, B., and Panigrahi, S. (2009). "Fundamental understanding and modeling of spin coating process: A review." *Indian J Phys*, 83, 493–502.

Salavati-Niasari, M., Davar, F., and Mazaheri, M. (2008). "Preparation of ZnO nanoparticles from [bis(acetylacetonato)zinc(II)]-oleylamine complex by thermal decomposition." *Mater Lett*, 62, 1890–1892.

Salavati-Niasari, M., Mir, N., and Davar, F. (2010). "A novel precursor in preparation and characterization of nickel oxide nanoparticles via thermal decomposition approach." *J Alloys Compd*, 493, 163–168.

Sallis, S., Scanlon, D. O., Chae, S. C., Quackenbush, N. F., Fischer, D. A., Woicik, J. C., Guo, J. H., Cheong, S. W., and Piper L. F. J. (2013). "La-doped BaSnO$_3$ –degenerate perovskite transparent conducting oxide: Evidence from synchrotron x-ray spectroscopy." *Appl Phys Lett*, 103, 1–5.

Sankarasubramanian, K., Soundarrajan, P., Sethuraman, K., and Ramamurthi, K. (2015). "Chemical spray pyrolysis deposition of transparent and conducting Fe doped CdO thin films for ethanol sensor." *Mater Sci Semicond Process*, 40, 879–884.

Sarraf, M., Nasiri-Tabrizi, B., Dabbagh, A., Basirun, W. J., and Sukiman, N. L. (2020). "Optimized nanoporous alumina coating on AA3003-H14 aluminum alloy with enhanced tribo-corrosion performance in palm oil." *Ceram Int*, 46, 7306–7323.

Sarraf, M., Zalnezhad, E., Bushroa, A. R., Hamouda, A. M. S., Baradaran, S., Nasiri-Tabrizi, B., and Rafieerad, A. R. (2014). "Structural and mechanical characterization of Al/Al$_2$O$_3$ nanotube thin film on TiV alloy." *Appl Surf Sci*, 321, 511–519.

Sathe, P., Richter, J., Myint, M. T. Z., Dobretsov, S., and Dutta, J. (2016). "Self-decontaminating photocatalytic zinc oxide nanorod coatings for prevention of marine microfouling: a mesocosm study." *Biofouling*, 32, 383–395.

Satyanarayana, N., Sinha, S. K., and Srinivasan, M. P. (2005). "Friction and wear life evaluation of silane based self assembled monolayers on silicon surface." *Tribol Interface Eng Ser*, 48, 821–826.

Schoell, S. J., Oliveros, A., Steenackers, M., Saddow, S. E., and Sharp, I. D. (2012). "Multifunctional SiC Surfaces: From Passivation to Biofunctionalization." *Silicon Carbide Biotechnology*, 495.

Schraufnagel, D. E., Balmes, J. R., Cowl, C. T., Matteis, S. D., Jung, S. H., Mortimer, K., Perez-Padilla, R., Rice, M. B., Riojas-Rodriguez, H., Sood, A., Thurston, G. D., To, T., Vanker, A., and Wuebbles, D. J. (2019). "Air pollution and noncommunicable diseases: A review by the forum of international respiratory societies' environmental committee, Part 2: Air pollution and organ systems." *Chest*, 155, 417–426.

Schüler, T., Asmus, T., Fritzsche, W., and Möller, R. (2009). "Screen printing as cost-efficient fabrication method for DNA-chips with electrical readout for detection of viral DNA." *Biosens Bioelectron*, 24, 2077–2084.

Scriven, L. E. (1988). "Physics and applications of DIP coating and spin coating." *MRS Proceedings*, 121, 717.

Seeley, Z. M., Bandyopadhyay, A., and Bose, S. (2009). "Influence of crystallinity on CO gas sensing for TiO_2 films." *Mater Sci Eng B*, 164, 38–43.

Sethulakshmi, N., Unnimaya, A. N., Al-Omari, I. A., Al-Harthi, S., Sagar, S., Thomas, S., Srinivasan, G., and Anantharaman, M. R. (2015). "On magnetic ordering in heavily sodium substituted hole doped lanthanum manganites." *J Magn Magn Mater*, 391, 75–82.

Shan, C., Huang, T., Zhang, J., Han, M., Li, Y., Hu, Z., and Chu, J. (2014). "Optical and electrical properties of sol-gel derived $Ba_{1-x}La_xSnO_3$ transparent conducting films for potential optoelectronic applications." *J Phys Chem C*, 118, 6994–7001.

Shankar, P., Bosco, J., and Rayappan, B. (2016). "Gas sensing mechanism of metal oxides: The role of ambient atmosphere, type of semiconductor and gases - A review." *Sci Lett J*, 4, 126.

Shelke, V., Bhole, M. P., and Patil, D. S. (2013). "Effect of open air annealing on spin coated aluminum doped ZnO nanostructure." *Mater Chem Phys*, 141, 81–88.

Shewale, P. S., and Yu, Y. S. (2016). "H_2S gas sensing properties of undoped and Ti doped ZnO thin films deposited by chemical spray pyrolysis." *J Alloys Compd*, 684, 428–437.

Shim, E. (2018). "Coating and laminating processes and techniques for textiles." *Smart Textile Coatings and Laminates*, 11, 1–35.

Shinde, V. R., Gujar, T. P., and Lokhande, C. D. (2007). "Enhanced response of porous ZnO nanobeads towards LPG: Effect of Pd sensitization." *Sens Actuators B Chem*, 123, 701–706.

Shingange, K., Tshabalala, Z. P., Ntwaeaborwa, O. M., Motaung, D. E., and Mhlongo, G. H. (2016). "Highly selective NH_3 gas sensor based on Au loaded ZnO nanostructures prepared using microwave-assisted method." *J Colloid Interface Sci*, 479, 127–138.

Singh, S., Kaur, H., Singh, V. N., Jain, K., and Senguttuvan, T. D. (2012). "Highly sensitive and pulse-like response toward ethanol of Nb doped TiO_2 nanorods based gas sensors." *Sens Actuators B Chem*, 171–172, 899–906.

Sinha, S. K., Song, T., Wan, X., and Tong, Y. (2009). "Scratch and normal hardness characteristics of polyamide 6/nano-clay composite." *Wear*, 266, 814–821.

Sivakumar, R., Raj, A. M. E., Subramanian, B., Jayachandran, M., Trivedi, D. C., and Sanjeeviraja, C. (2004). "Preparation and characterization of spray deposited n-type WO_3 thin films for electrochromic devices." *Mater Res Bull*, 39, 1479–1489.

Slassi, A. (2015). "Ab initio study of a cubic perovskite: Structural, electronic, optical and electrical properties of native, lanthanum- and antimony-doped barium tin oxide." *Mater Sci Semicond Process*, 32, 100–106.

Somalu, M. R., and Brandon, N. P. (2012). "Rheological studies of nickel/scandia-stabilized-zirconia screen printing inks for solid oxide fuel cell anode fabrication." *J Am Ceram Soc*, 95, 1220–1228.

Somalu, M. R., Muchtar, A., Daud, W. R. W., and Brandon, N. P. (2017). "Screen-printing inks for the fabrication of solid oxide fuel cell films: A review." *Renew Sust Energ Rev*, 75, 426–439.

Sonker, R. K., Sabhajeet, S. R., Singh, S., and Yadav, B. C. (2015). "Synthesis of ZnO nanopetals and its application as NO_2 gas sensor." *Mater Lett*, 152, 189–191.

Sridhar, R., Manoharan, C., Ramalingam, S., Dhanapandian, S., and Bououdina, M. (2014). "Spectroscopic study and optical and electrical properties of Ti-doped ZnO thin films by spray pyrolysis." *Spectrochim Acta A Mol Biomol Spectrosc*, 120, 297–303.

Stampino, P. G., Omati, L., Cristiani, C., and Dotelli, G. (2010). "Characterisation of nanocarbon-based gas diffusion media by electrochemical impedance spectroscopy." *Fuel Cells*, 10, 270–277.

Stanulis, A., Sakirzanovas, S., Bael, M. van, and Kareiva, A. (2012). "Sol-gel (combustion) synthesis and characterization of different alkaline earth metal (Ca, Sr, Ba) stannates." *J Solgel Sci Technol*, 64, 643–652.

Stelzer, N. H. J., and Schoonman, J. (1996). "Synthesis of terbia-doped yttria-stabilized zirconia thin films by electrostatic spray deposition (ESD)." *J Mater Synth Process*, 4, 429–438.

Stojanovic, B. D., Dzunuzovic, A. S., and Ilic, N. I. (2018). "Review of methods for the preparation of magnetic metal oxides." *Magnetic, Ferroelectric, and Multiferroic Metal Oxides*, 17, 333–359.

Sun, Y-F., Liu, S-B., Meng, F-L., Liu, J-Y., Jin, Z., Kong. L-T., and Liu, J-H. (2012). "Metal oxide nanostructures and their gas sensing properties: A review." *Sensors*, 12, 2610–2631.

Sundararajan, M., Devarajan, M., and Jaafar, M. (2020). "Investigation of surface and mechanical properties of Anodic Aluminium Oxide (AAO) developed on Al substrate for an electronic package enclosure." *Surf Coat Technol*, 401, 126273.

Sundaresh, S., Nehate, S. D., and Sundaram, K. B. (2021). "Electrical and optical studies of reactively sputtered indium oxide thin films." *ECS J Solid State Sci Technol*, 10, 065016.

Sunde, T. O. L., Grande, T., and Einarsrud, M. A. (2016). "Modified pechini synthesis of oxide powders and thin films." *Handbook of Sol-Gel Science and Technology: Processing, Characterization and Applications*, 0373, 1–30.

Szeto, W., Leung, M. K. H., and Leung, D. Y. C. (2020). "Recent developments of titanium dioxide materials for aquatic antifouling application." *J Mar Sci Technol*, 26, 301–321.

Tesfamichael, T., Cetin, C., Piloto, C., Arita, M., and Bell, J. (2015). "The effect of pressure and W-doping on the properties of ZnO thin films for NO_2 gas sensing." *Appl Surf Sci*, 357, 728–734.

Tesler, A. B., Kim, P., Kolle, S., Howell, C., Ahanotu, O., and Aizenberg, J. (2015). "Extremely durable biofouling-resistant metallic surfaces based on electrodeposited nanoporous tungstite films on steel." *Nat Commun*, 6, 1–10.

Tian, X., Cui, X., Lai, T., Ren, J., Yang, Z., Xiao, M., Wang, B., Xiao, X., and Wang, Y. (2021). "Gas sensors based on TiO_2 nanostructured materials for the detection of hazardous gases: A review." *Nano Materials Science*, 3, 390–403.

Tong, X., Shen, W., Zhang, X., Corriou, J. P., and Xi, H. (2020). "Synthesis and density functional theory study of free-standing Fe-doped TiO_2 nanotube array film for H_2S gas sensing properties at low temperature." *J Alloys Compd*, 832, 155015.

Trari, M., Doumerc, J. P., Dordor, P., Pouchard, M., Behr, G., and Krabbes, G. (1994). "Preparation and characterization of lanthanum doped $BaSnO_3$." *J Phys Chemi Solids*, 55, 1239–1243.

Turgman-Cohen, S., Fischer, D. A., Kilpatrick, P. K., and Genzer, J. (2009). "Asphaltene adsorption onto self-assembled monolayers of alkyltrichlorosilanes of varying chain length." *ACS Appl Mater Interfaces*, 1, 1347–1357.

Udawatte, C. P., Kakihana, M., and Yoshimura, M. (1998). "Preparation of pure perovskite-type $BaSnO_3$ powders by the polymerized complex method at reduced temperature." *Solid State Ion*, 108, 23–30.

Ulman, A. (1996). "Formation and structure of self-assembled monolayers." *Chem Rev*, 96, 1533–1554.

Upadhyay, S., and Kavitha, P. (2007). "Lanthanum doped barium stannate for humidity sensor." *Mater Lett*, 61, 1912–1915.

Upadhyay, S., Parkash, O., and Kumar, D. (2004). "Synthesis, structure and electrical behaviour of lanthanum-doped barium stannate." *J Phys D Appl Phys*, 37, 1483.

Varma, A., Mukasyan, A. S., Rogachev, A. S., and Manukyan, K. V. (2016). "Solution combustion synthesis of nanoscale materials." *Chem Rev*, 116, 14493–14586.

Vasilopoulou, M., Soultati, A., Georgiadou, D. G., Stergiopoulos, T., Palilis, L. C., Kennou, S., Stathopoulos, N. A., Davazoglou, D., and Argitis, P. (2014). "Hydrogenated under-stoichiometric tungsten oxide anode interlayers for efficient and stable organic photovoltaics." *J Mater Chem A Mater*, 2, 1738–1749.

Venkatesh, K. S., Vijayalakshmi, K., Karthick, K., Krishnamoorthi, S. R., Palani, N. S., and Ilangovan, R. (2014). "Fabrication of room temperature H_2 gas sensor using pure and La: ZnO with novel nanocorn morphology prepared by sol–gel dip coating method." *J Mater Sci Mater Electron*, 25, 4339–4347.

Verho, T., Bower, C., Andrew, P., Franssila, S., Ikkala, O., and Ras, R. H. A. (2011). "Mechanically durable superhydrophobic surfaces." *Adv Mater*, 23, 673–678.

Vijayalakshmi, K., and Gopalakrishna, D. (2014). "Influence of pyrolytic temperature on the properties of ZnO films optimized for H_2 sensing application." *J Mater Sci Mater Electron*, 25, 2253–2260.

Vijayalakshmi, K., and Karthick, K. (2014). "Growth of highly c-axis oriented Mg:ZnO nanorods on Al_2O_3 substrate towards high-performance H_2 sensing." *Int J Hydrog Energy*, 39, 7165–7172.

Voon, C. H., Foo, K. L., Lim, B. Y., Gopinath, S. C. B., and Al-Douri, Y. (2020). "Synthesis and preparation of metal oxide powders." *Metal Oxide Powder Technologies*, 31–65.

Wang, C., Meinhardt, J., and Löbmann, P. (2010a). "Growth mechanism of Nb-doped TiO_2 sol-gel multilayer films characterized by SEM and focus/defocus TEM." *J Solgel Sci Technol*, 53, 148–153.

Wang, C., Yin, L., Zhang, L., Xiang, D., and Gao, R. (2010b). "Metal oxide gas sensors: Sensitivity and influencing factors." *Sensors*, 10, 2088–2106.

Wang, H., Sun, Q., Yao, Y., Li, Y., Wang, J., and Chen, L. (2016). "A micro sensor based on TiO_2 nanorod arrays for the detection of oxygen at room temperature." *Ceram Int*, 42, 8565–8571.

Wang, J., Zou, B., Ruan, S., Zhao, J., and Wu, F. (2009). "Synthesis, characterization, and gas-sensing property for HCHO of Ag-doped In_2O_3 nanocrystalline powders." *Mater Chem Phys*, 117, 489–493.

Wang, L., Xing, X., Chen, N., Zhao, R., Wang, Z., Zou, T., Wang, Z., and Wang, Y. (2020a). "W-doped nanoporous TiO_2 for high performances sensing material toward acetone gas." *J Nanostruct*, 10, 148–156.

Wang, M., Zhu, Y., Meng, D., Wang, K., and Wang, C. (2020b). "A novel room temperature ethanol gas sensor based on 3D hierarchical flower-like TiO_2 microstructures." *Mater Lett*, 277, 128372.

Wang, X., Zhang, F., Zheng, Z., Chen, L., Wang, H., Li, C., and Lui, X. (2000). "Chemical composition and structure of titanium oxide films deposited on LTI-carbon by IBED." *Thin Solid Films*, 365, 94–98.

Wannes, H. B., Zaghouani, R. B., Ouertani, R., Araújo, A., Mendes, M. J., Aguas, H., Fortunato, E., Martins, R., and Dimassi, W. (2018). "Study of the stabilizer influence on the structural and optical properties of sol-gel spin coated zinc oxide films." *Mater Sci Semicond Process*, 74, 80–87.

Wei, D., Huang, Z., Wang, L., Chuai, X., Zhang, S., and Lu, G. (2018). "Hydrothermal synthesis of Ce-doped hierarchical flower-like In_2O_3 microspheres and their excellent gas-sensing properties." *Sens Actuators B Chem*, 255, 1211–1219.

Wei, R. H., Tang, X. W., Hui, Z. Z., Luo, X., Dai, J. M., Yang, J., Song, W. H., Chen, L., Zhu, X. G., Zhu, X. B., and Sun, Y. P. (2015). "Solution processing of transparent conducting epitaxial La:$BaSnO_3$ films with improved electrical mobility." *Appl Phys Lett*, 106, 1–6.

Weinhardt, L., Blum, M., Bär, M., Heske, C., Cole, B., Marsen, B., and Miller, E. L. (2008). "Electronic surface level positions of WO_3 thin films for photoelectrochemical hydrogen production." *J Phys Chem C*, 112, 3078–3082.

Wiatrowski, A., Mazur, M., Obstarczyk, A., Wojcieszak, D., Kaczmarek, D., Morgiel, J., and Gibson, D. (2018). "Comparison of the physicochemical properties of TiO_2 thin films obtained by magnetron sputtering with continuous and pulsed gas flow." *Coatings*, 8, 1–16.

Winnicki, M., Łatka, L., Jasiorski, M., and Baszczuk, A. (2021). "Mechanical properties of TiO_2 coatings deposited by low pressure cold spraying." *Surf Coat Technol*, 405, 126516.

Wu, W., Zhang, L., Zhai, X., Liang, C., and Yu, K. (2018). "Preparation and photocatalytic activity analysis of nanometer TiO_2 modified by surfactant." *Nanomater Nanotechnol*, 8, 1–8.

Xia, W., Wang, H., Zeng, X., Han, J., Zhu, J., Zhou, M., and Wu, S. (2014). "High-efficiency photocatalytic activity of type II SnO/Sn_3O_4 heterostructures via interfacial charge transfer." *CrystEngComm*, 16, 6841–6847.

Xue, Y., Zhao, J., Qiu, R., Zheng, J., Lin, C., Ma, B., and Wang, P. (2015). "In situ glass antifouling using Pt nanoparticle coating for periodic electrolysis of seawater." *Appl Surf Sci*, 357, 60–68.

Yan, H., Zhang, X., Zhou, S., Xie, X., Luo, Y., and Yu, Y. (2011). "Synthesis of WO_3 nanoparticles for photocatalytic O_2 evolution by thermal decomposition of ammonium tungstate loading on g-C_3N_4." *J Alloys Compd*, 509, 232–235.

Yang, C. Y., Chuang, S. I., Lo, Y. H., Cheng, H. M., Duh, J. G., and Chen, P. Y. (2016). "Stalagmite-like self-cleaning surfaces prepared by silanization of plasma-assisted metal-oxide nanostructures." *J Mater Chem A*, 4, 3406–3414.

Yang, D., An, Y., Wang, S., Wu, Z., and Liu, J. (2014). "Evidence of the oxygen vacancies-induced room-temperature ferromagnetism in the $(In_{0.97-x}Fe_xSn_{0.03})_2O_3$ films." *RSC Adv*, 4, 33680–33686.

Yasukawa, M., Kono, T., Ueda, K., Yanagi, H., and Hosono, H. (2010). "High-temperature thermoelectric properties of La-doped $BaSnO_3$ ceramics." *Mater Sci Eng B*, 173, 29–32.

Yebra, D. M., Kiil, S., and Dam-johansen, K. (2004). "Antifouling technology — past, present and future steps towards efficient and environmentally friendly antifouling coatings." *Prog Org Coat*, 50, 75–104.

Y. Niu, J., B. Hong, C. Xu, J., B. Han, Y., X. Jin, H., F. Jin, D., X. Zeng, Y., L. Peng, X., L. Ge, H., and Wang, X. Q. (2022). "Enhanced formaldehyde gas-sensing response based on indium oxide nanowires doped with same-valence metal cations." *Mater Adv*, 3, 7043–7052.

Yoo, K. S., Park, S. H., and Kang, J. H. (2005). "Nano-grained thin-film indium tin oxide gas sensors for H_2 detection." *Sens Actuators B Chem*, 108, 159–164.

Yu, X., Marks, T. J., and Facchetti, A. (2016). "Metal oxides for optoelectronic applications." *Nat Mater*, 15, 383–396.

Zavareh, A. M., Abd Razak, B., Wahab, M. H. B., Goh, B. T., Mahmoodian, R., and Wasa, K. (2020). "Fabrication of $Pb(Zr,Ti)O_3$ thin films utilizing unconventional powder magnetron sputtering (PMS)." *Ceram Int*, 46, 1281–1296.

Zeng, Q., Cui, Y., Zhu, L., and Yao, Y. (2020). "Increasing oxygen vacancies at room temperature in SnO_2 for enhancing ethanol gas sensing." *Mater Sci Semicond Process*, 111, 104962.

Zhang, X., Peng, S., Hong, P., Zhao, R., Yang, Y., Xing, X., and Wang, Y. (2019). "Gas response enhancement of VOCs sensor based on Sn doped nanoporous anatase TiO_2 nanoparticles at a relative low operating temperature." *Mater Res Express*, 6, 105008.

Zhao, L., Zhao, X., Liu, J., Zhang, A., Wang, D., and Wei, B. (2010). "Fabrications of Nb-doped TiO_2 (TNO) transparent conductive oxide polycrystalline films on glass substrates by sol-gel method." *J Solgel Sci Technol*, 53, 475–479.

Zheng, H., Ou, J. Z., Strano, M. S., Kaner, R. B., Mitchell, A., and Kalantar-Zadeh, K. (2011). "Nanostructured tungsten oxide - Properties, synthesis, and applications." *Adv Funct Mater*, 21, 2175–2196.

Zhu, J., Li, H., Zhong, L., Xiao, P., Xu, X., Yang, X., Zhao, Z., and Li, J. (2014a). "Perovskite oxides: Preparation, characterizations, and applications in heterogeneous catalysis." *ACS Catal*, 4, 2917–2940.

Zhu, L., Li, Y., and Zeng, W. (2017). "Enhanced ethanol sensing and mechanism of Cr-doped ZnO nanorods: Experimental and computational study." *Ceram Int*, 43, 14873–14879.

Zhu, L., Li, Y., and Zeng, W. (2018). "Hydrothermal synthesis of hierarchical flower-like ZnO nanostructure and its enhanced ethanol gas-sensing properties." *Appl Surf Sci*, 427, 281–287.

Zhu, L., and Zeng, W. (2017). "Room-temperature gas sensing of ZnO-based gas sensor: A review." *Sens Actuators A Phys*, 267, 242–261.

Zhu, T., Chong, M. N., and Chan, E. S. (2014b). "Nanostructured tungsten trioxide thin films synthesized for photoelectrocatalytic water oxidation: A review." *ChemSusChem*, 7, 2974–2997.

Ziakhodadadian, S., and Ren, T. (2020). "Structural and tribological properties of tungsten oxide thin film on a silicon substrate." *J Chem Res*, 44, 744–749.

Zidi, N., Omeiri, S., Hadjarab, B., Bouguelia, A., Akroun, A., and Trari, M. (2010). "Transport properties and photo electrochemical characterization of oxygen-deficient $ASnO_{3-\delta}$ (A=Ca, Sr and Ba)." *Physica B Condens Matter*, 405, 3355–3359.

Zou, A. L., Qiu, Y., Yu, J. J., Yin, B., Cao, G. Y., Zhang, H. Q., and Hu, L. Z. (2016). "Ethanol sensing with Au-modified ZnO microwires." *Sens Actuators B Chem*, 227, 65–72.

The page was left intentionally blank

LIST OF PUBLICATIONS

Robbi Vivek Vardhan, Manjunath G, Saumen Mandal, "Fabrication of solution combustion based transparent semiconducting titanium and zinc co-doped indium oxide (ITiZO) films" **Materials Science Forum** 969, 260-265 (2019).

Robbi Vivek Vardhan, Mayur Jiyalal Prajapati, Saumen Mandal, "Effect of lanthanum on the phase evolution of perovskite barium stannate synthesized through polymerized complex method" **Ceramics International** 45, 17420-17428 (2019). (Equal Contribution).

Robbi Vivek Vardhan, Subodh Kumar, Saumen Mandal, "A facile, low temperature spray pyrolysed tungsten oxide (WO_3): an approach to antifouling coating by amalgamating scratch resistant and water repellent properties" **Bulletin of Materials Science** 43, 1-12 (2020).

Robbi Vivek Vardhan, Subodh Kumar, Saumen Mandal, "Fabrication of minimal capital-intensive scratch-resistant and hydrophobic tungsten oxide film on stainless steel through spray pyrolysis" **Surface and Interface Analysis** 54, 510-523 (2022).

Robbi Vivek Vardhan, Manjunath G, P. Nagaraju, Saumen Mandal, "Room temperature ammonia gas detection by solution combustion-processed pristine and Ti-doped ZnO transparent films: A study on depletive effects on the gas response after doping" **Journal of Materials Science: Materials in Electronics** (Revision to be submitted).

Robbi Vivek Vardhan, Manjunath G, P. Nagaraju, Saumen Mandal, "Tracing of ammonia gas by solution-combustion derived pristine and Nb-doped TiO_2 films: Beneficial impact of crystallinity and adsorbed oxygen on the gas response" (Submitted to **Journal of Electronic Materials**).

Robbi Vivek Vardhan, Manjunath G, Lakkimsetti Lakshmi Praveen, P. Nagaraju, Saumen Mandal, "Fabrication of screen-printable particle-free aqueous combustible inks-derived In_2O_3-based films: Response to ethanol gas at room temperature" (Manuscript under preparation).

OTHER PUBLICATIONS

G Manjunath, **Robbi Vivek Vardhan**, Ashritha Salian, Rashi Jagannatha, Mayank Kedia, Saumen Mandal, "Effect of annealing-temperature-assisted phase evolution on conductivity of solution combustion processed calcium vanadium oxide films" **Bulletin of Materials Science** 41, 1-9 (2018).

Robbi Vivek Vardhan, Manjunatha M, Saumen Mandal, "Stoichiometric redox reaction-controlled, combustion assisted spray pyrolyzed zirconia films on stainless steel" **IOP SciNotes** 1, 1-6 (2020) (Equal Contribution).

G Manjunath, **Robbi Vivek Vardhan**, Lakkimsetti Lakshmi Praveen, P Nagaraju, Saumen Mandal, "Room-temperature detection of ammonia and formaldehyde gases by $La_xBa_{1-x}SnO_{3-\delta}$ ($x = 0$ and 0.05) screen printed sensors: effect of ceria and ruthenate sensitization" **Applied Physics A** 127, 1-15 (2021).

Robbi Vivek Vardhan, Nitesh Eknath Chaudhari, Pavan Pujar, Saumen Mandal, "A revisit to solution-processed zirconia and its stabilized derivatives as protective coatings for base-stainless steel" **Critical Reviews in Solid State and Materials Sciences** (2022).

Sameer Sunil Karle, Karakavalasa Kailasam, **Robbi Vivek Vardhan**, Saumen Mandal, "Anti-biofouling evaluation of vacuum-assisted hydrophobic ytterbium oxide (Yb_2O_3) coating on stainless steel by facile spray combustion" **Bulletin of Materials Science** (Submitted to the journal).

Ashritha Salian, Pavan Pujar, **Robbi Vivek Vardhan**, Haewon Cho, Sunkook Kim, Saumen Mandal, "Evolution of high dielectric permittivity in low-temperature solution combustion processed phase-pure high entropy oxide (CoMnNiFeCr)O for thin film transistors" **ACS Applied Electronic Materials** (Submitted to the journal).

LIST OF PATENTS

Saumen Mandal, Bikesh Gupta, Pavan Pujar, Komalakrushna Hadagalli, **Robbi Vivek Vardhan**, "Fabrication of high conductive metallic films at low temperature" **Indian Patent**, 347677 (2020) (Granted).

LIST OF CONFERENCE PRESENTATIONS

Robbi Vivek Vardhan, Subodh Kumar, Saumen Mandal, "Development of low cost antifouling tungsten oxide (WO_3) coatings on glass and steel substrates via spray pyrolysis", International Conference on Surface Engineering (INCOSRF 2018), August 9-11, 2018, IISc Bangalore, India. (Poster) **(Best Poster Award)**.

Robbi Vivek Vardhan, G Manjunath, Saumen Mandal, "Fabrication of solution combustion based transparent semiconducting titanium and zinc co-doped indium oxide (ITiZO) films" International Conference on Recent Advances in Materials and Manufacturing Technologies (ICRAMMT 2018), November 19-20, 2018, MLRITM Hyderabad, India (Oral).

Robbi Vivek Vardhan, Mayur Jiyalal Prajapati, Saumen Mandal, "Study of structural, compositional and morphological properties of lanthanum doped barium stannate through solution processing", National Conference on Emerging Trends in Science, Technology & Application of Electron Microscopy (STAEM-2018) and 5th Annual Meeting of the Academy of Microscope Science & Technology (AMST), December 19-21, 2018, CSIR-NIIST, Trivandrum, India. (Equal Contribution) (Poster).

Robbi Vivek Vardhan, Subodh Kumar, Saumen Mandal, "Low temperature solution processed tungsten oxide based robust and water repellant coating on stainless steel", 2nd International Conference on Metallurgy & Materials Technology – Emerging trends, Development & Applications, June 29-30, 2021, MatCorr, India (Oral).

Robbi Vivek Vardhan, Sameer Karle, Karakavalasa Kailsam, Subodh Kumar, Saumen Mandal, "A comparative study of solution-processed tungsten oxide and ytterbium oxide coatings on stainless steel for marine antifouling applications" International Conference on Global Trends in Traditional to Space Ceramics (GT-TSC'22), 2022, IIT-BHU, India (Oral).

G Manjunath, **Robbi Vivek Vardhan**, Ashritha Salian, Rashi Jagannatha, Mayank Kedia, Saumen Mandal "Development of combustion synthesized high conductive calcium vanadium oxide ($CaVO_3$) thin film electrodes", International Conference on Nanoscience and Technology (ICONSAT 2018), IISc Bangalore, India (Poster).

Ashritha Salian, **Robbi Vivek Vardhan**, Lakkimsetti Lakshmi Praveen, Santhra Krishnan P, Pavan Pujar, Saumen Mandal, "Development of low temperature processed high dielectric constant high entropy oxide for electronic applications", XXI International Workshop on Physics of Semiconductor Devices (IWPSD 2021), IIT Delhi, India (Poster).

Karakavalasa Kailasam, **Robbi Vivek Vardhan,** Saumen Mandal, "Low-cost fabrication of hydrophobic ceramic coating (Yb_2O_3) at low temperature on SS substrate by solution combustion technique", National Symposium on Electrochemical Science and Technology (NSEST 2021), IISc Bengaluru, India (Oral) **(Best Paper Award)**.

The page was left intentionally blank

BIODATA

Name	:	Robbi Vivek Vardhan
Father's name	:	Robbi Hemarao
Date of birth	:	27th August 1993
Permanent Address	:	#3-67B, Rotary Nagar 1,
		Tekkali, Srikakulam District,
		Andhra Pradesh, India.
Mobile	:	+91-9640488868
E-mail	:	robbivivekvardhan@gmail.com

Academic qualification:

Bachelor of Technology (B.Tech.) in Mechanical Engineering from Gudlavalleru Engineering College, Andhra Pradesh (75.39 % out of 100 %).

Master of Technology (M.Tech.) in Materials Engineering from National Institute of Technology Karnataka, Surathkal (CGPA: 8.28 out of 10).